Diamond turning of glassy polymers

Citation for published version (APA):
Gubbels, G. P. H. (2006). *Diamond turning of glassy polymers*. [Phd Thesis 1 (Research TU/e / Graduation TU/e), Mechanical Engineering]. Technische Universiteit Eindhoven. https://doi.org/10.6100/IR613637

DOI:
10.6100/IR613637

Document status and date:
Published: 01/01/2006

Document Version:
Publisher's PDF, also known as Version of Record (includes final page, issue and volume numbers)

Please check the document version of this publication:

• A submitted manuscript is the version of the article upon submission and before peer-review. There can be important differences between the submitted version and the official published version of record. People interested in the research are advised to contact the author for the final version of the publication, or visit the DOI to the publisher's website.
• The final author version and the galley proof are versions of the publication after peer review.
• The final published version features the final layout of the paper including the volume, issue and page numbers.

Link to publication

General rights
Copyright and moral rights for the publications made accessible in the public portal are retained by the authors and/or other copyright owners and it is a condition of accessing publications that users recognise and abide by the legal requirements associated with these rights.

- Users may download and print one copy of any publication from the public portal for the purpose of private study or research.
- You may not further distribute the material or use it for any profit-making activity or commercial gain
- You may freely distribute the URL identifying the publication in the public portal.

If the publication is distributed under the terms of Article 25fa of the Dutch Copyright Act, indicated by the "Taverne" license above, please follow below link for the End User Agreement:

www.tue.nl/taverne

Take down policy
If you believe that this document breaches copyright please contact us at:

openaccess@tue.nl

providing details and we will investigate your claim.

Download date: 16. Nov. 2023

Diamond Turning of Glassy Polymers

Guido Gubbels

Diamond Turning of Glassy Polymers

Guido P.H. Gubbels

21st August 2006

Gubbels, Guido P.H.

Diamond Turning of Glassy Polymers
by Guido P.H. Gubbels – Eindhoven: Technische Universiteit Eindhoven, 2006.
Proefschrift.

A catalogue record is available from the Library Eindhoven University of Technology

ISBN-10: 90-386-2918-4
ISBN-13: 978-90-386-2918-6

NUR 978

Subject headings: diamond turning / glassy polymers / thermal modelling / surface / tribo-electric tool wear / tribo-chemical tool wear / oxidative etching

This thesis was prepared with the $\LaTeX\,2_{\varepsilon}$ documentation system.

Printed by PrintPartners Ipskamp, Enschede, The Netherlands.
Cover: Lichtenberg figure through the diamond tool.

Copyright © 2006 by G.P.H. Gubbels

All rights reserved. No parts of this publication may be reproduced, utilised or stored in any form or by any means, electronic or mechanical, including photocopying, recording or by any information storage and retrieval system, without permission of the copyright holder.

Diamond Turning of Glassy Polymers

PROEFSCHRIFT

ter verkrijging van de graad van doctor aan de
Technische Universiteit Eindhoven, op gezag van de
Rector Magnificus, prof.dr.ir. C.J. van Duijn, voor een
commissie aangewezen door het College voor
Promoties in het openbaar te verdedigen
op dinsdag 31 oktober 2006 om 16.00 uur

door

Guido Petrus Herman Gubbels

geboren te Urmond

Dit proefschrift is goedgekeurd door promotor:

prof.dr.ir. P.H.J. Schellekens

Copromotoren:
dr.ir. F.L.M. Delbressine
en
dr.ir. L.E. Govaert

Dedicated to

Astrid,
Lieke and Thomas
and
my parents

Samenvatting

De optische industrie krijgt steeds grotere interesse in de toepassing van kunststoffen als optische componenten. De reden hiervoor is dat er kunststoffen met steeds hogere brekingsindex ontwikkeld worden en dat deze bovendien een lagere soortelijke massa hebben dan glas. Het is mogelijk om kunststoffen tot optische kwaliteit te draaien in één opspanning: dit is een proces dat in de contactlenzenindustrie al toegepast wordt. De voordelen hiervan zijn kostenbesparing, omdat er minder machines nodig zijn en verhoogde nauwkeurigheid door afwezigheid van omstelfouten.

In dit onderzoek is gekeken naar het precisiedraaiproces van glasachtige (transparante) kunststoffen. In het algemeen worden voor het precisiedraaien mono-kristallijne diamantbeitels gebruikt. Voor procesoptimalisatie van het verspaningsproces van kunststoffen is het van groot belang dat men weet in welke fase zich het kunststof bevindt tijdens het draaien en hoe de relatief hoge diamantslijtage ontstaat.

In de literatuur op het gebied van precisiedraaien van kunststoffen wordt aangenomen dat men de beste oppervlaktekwaliteit behaalt als men een temperatuurstijging tot de glastransitietemperatuur (T_g) van het polymeer kan bereiken door meer adiabatische verspaningscondities toe te passen. De oppervlaktekwaliteit werd in alle onderzoeken direct gekoppeld aan het wel of niet bereiken van T_g. Ook zijn er afschattingen van de temperatuurstijging gemaakt tijdens het verspanen, maar hiervoor zijn nooit daadwerkelijk krachtmetingen uitgevoerd.

In het eerste deel van deze dissertatie wordt het aangepaste temperatuurmodel van Hahn toegepast. De invoer voor dit model zijn de verspaningskrachten, die in dit onderzoek daadwerkelijk gemeten zijn. De belangrijkste aanpassing van het temperatuurmodel voor dit onderzoek bestaat uit de toevoeging van de conversieratio η van mechanische arbeid naar warmte. Op basis van literatuur en uitgevoerde temperatuurmetingen blijkt dat deze voor kunststoffen op 0,5 gesteld mag worden tijdens het verspaningsproces.

Door toepassing van het temperatuurmodel blijkt dat de temperatuur tijdens het verspaningsproces van kunststoffen niet de glastransitietemperatuur bereikt. Dit geeft aan dat de behaalde oppervlaktekwaliteit na diamantdraaien niet beïnvloed wordt door de hoogte van T_g. Een andere implicatie is dat naast thermisch geactiveerde vloei een deel spanningsgeactiveerde vloei optreedt tijdens

het verspanen. De spanningsgeactiveerde vloei kan ketenbreuk in de primaire deformatiezone tot gevolg hebben, wat bij PMMA het geval is en bij polycarbonaat (PC) niet.

Het temperatuurmodel is ook gebruikt voor de bestudering van de invloed van diverse verspaningsparameters. Hieruit blijkt bijvoorbeeld dat een verhoging van de snijsnelheid weinig invloed heeft op de maximale temperatuur in de primaire deformatiezone. Wel leidt een grote negatieve spaanhoek ($-20°$) tot een aanzienlijke temperatuurstijging. Echter, deze is ook niet voldoende om T_g te bereiken tijdens het draaien van PC.

Zowel gestoken als vlakgedraaide oppervlakken zijn bestudeerd. De oppervlakken na het steken (met een rechte snijkant) van PC vertoonden sterke overeenkomsten met plooien gevormd in een viskeuze laag op een viskeuze matrix belast onder compressie. PMMA vertoonde dit gedrag niet, wat verklaard kan worden door het feit dat PMMA een gesegmenteerde spaan vormt en PC een volledig ductiele spaan.

Alhoewel plooivorming een significante invloed kan hebben op de oppervlakteruwheid tijdens steken, is dit effect verwaarloosbaar bij het precisiedraaien met radiusbeitels vanwege de zeer kleine spaandoorsnedes. Het blijkt dat de oppervlakteruwheid van precisiegedraaide kunststof oppervlakken gedomineerd wordt door de beitelafdruk en optimalisatie kan hier het beste toegepast worden middels aanpassing van de voeding.

De thermo-mechanische geschiedenis van een kunststof is niet van invloed op de haalbare oppervlaktekwaliteit. Daarnaast blijkt ook de crosslinkdichtheid géén direkte factor voor haalbare oppervlaktekwaliteit te zijn. Dit is onderzocht met behulp van verschillend gecrosslinkte PMMA materialen. Weliswaar veranderde de oppervlaktestructuur bij toenemende crosslinkdichtheid, maar de *Ra* waarde bleef nagenoeg gelijk. Het lijkt erop dat niet zonder meer verondersteld mag worden dat thermoharders niet tot optische kwaliteit te verspanen zijn.

Het tweede deel van deze dissertatie beschrijft de twee dominante slijtagemechanismen tijdens het diamantdraaien van kunststoffen. Voor tribo-elektrische slijtage is een sterke oplading nodig met een bepaalde polariteit. Als de beitel als anode fungeert kunnen positieve Lichtenberg figuren in de beitel ontstaan. Als de beitel als kathode fungeert, zijn er veel grotere veldsterktes nodig om Lichtenberg figuren te laten ontstaan. Hierdoor hoeft tribo-elektrische slijtage dan niet als het dominante slijtagemechanisme aanwezig te zijn.

Een ander dominant slijtagemechanisme is tribo-chemische slijtage. Experimenten hebben duidelijk gemaakt dat het hier om een oxidatief etsproces gaat. Dit etsen leek alleen op te treden bij kunststoffen die makkelijk hydrolyseerbaar zijn. Als spaanvlak wordt veelal de (110) oriëntatie gebruikt, welke naar een (111) vlak toeëtst. De invloed van de relatieve luchtvochtigheid is hierbij een belangrijke parameter en dit duidt op een OH-stabilisatie tijdens het etsen. Er is een reactiemechanisme opgesteld voor de oxidatie tijdens het diamantdraaien van kunststoffen met als basis een nucleofiele aanval op een carbonyl getermineerd diamantoppervlak, uiteindelijk resulterend in CO-desorptie en OH-terminatie aan het diamantoppervlak. Op deze manier kan etsen als dominant slijtagemechanisme optreden.

Berekeningen hebben aangetoond dat er voldoende energie vrijkomt om dit etsproces te laten verlopen en dat er ook voldoende nucleofielen aanwezig zijn om dit proces te kunnen initiëren.

Abstract

Optical industries become more and more interested in the application of optical polymers. The reason for this is that polymers can be made with high refractive indices and that polymers have a low specific mass. It is possible to precision turn polymers to optical quality on one turning machine, which is already done in the fabrication of contacts. The benefits are: lower production costs and higher accuracies.

This research investigated the precision turning process of optical, glassy polymers. In general mono-crystalline diamond tools are used for the turning process. For process optimisation it is necessary to know in what phase the polymer is during turning. Another aspect is how the diamond tool wears during turning of these polymers.

Literature shows that it is assumed that the best surface qualities can be achieved when the glass transition temperature (T_g) of the polymer is reached. Estimates of cutting temperatures have been made, but true cutting temperature measurements were not found.

The first part of this thesis applies the modified temperature model of Hahn. The input parameters of this model are the cutting forces, which have been measured in this research. The most important modification of the model is the introduction of the work to heat conversion ratio η. Based on literature and experiments it was found that in diamond turning of polymers this value is 0.5.

The application of the temperature model shows that in polymer turning for the investigated polymers T_g is not reached. This indicates that it is not the height of T_g that determines whether optical quality can be achieved in diamond turning of polymers. Another implication of not reaching T_g is that not just thermally activated flow, but also stress activated flow is important in polymer turning. Stress activated flow may result in chain scission in the primary shear zone, which is probably the case during turning of PMMA. For polycarbonate (PC), no chain scission was found to occur during turning.

Also, the temperature model is used for studying the influence of several turning parameters. It was found that an increase in cutting speed has little effect on the temperature rise in the primary shear zone. A large negative rake angle (-20°) has more effect, but is not enough for reaching T_g in PC. Also, crack formation in front of the tool becomes important.

Experiments with both faceted (straight cutting edge) and radius tools have been used for studying surface formation. Surfaces formed in plunge turning with a straight cutting edge and a rake angle of 0° on PC showed strong resemblance with fold formation in a viscous layer on a viscous matrix under compression. PMMA did not show such behaviour, which may be explained by its segmented chip type, while PC has a fully ductile chip.

Although fold formation can have a significant influence on the achievable surface roughness value, it is not of importance in the precision turning process. The main reason for this is that in precision turning only small uncut chip thicknesses are used. It appears that in precision turning operations the surface roughness is dominated by the footprint of the radius tool and optimisation should be performed by this.

The thermo-mechanical history of the polymer does not have any influence on the achieved surface roughness. The influence of crosslink density was investigated by differently crosslinked PMMA grades. With increasing crosslink density the surface structure changed, but the *Ra* value remained approximately the same. Simply saying that thermosets cannot be machined to optical quality is therefore not correct.

The second part of this thesis described the two possible dominant wear mechanisms of the diamond tool in polymer turning. For tribo-electric tool wear to be dominant, a sufficiently high charge with a certain polarity has to be produced. When the tool acts as an anode in the cutting system positive Lichtenberg figures can be created, damaging the tool and possibly the cutting edge. This way, tribo-electric tool wear can be dominant.

Tribo-chemical tool wear is another dominant wear mechanism in polymer turning. It was found that oxidative etching of the diamond tool can occur. It appeared that polymers that can easily by hydrolyzed (polymers containing esters) resulted in much tribo-chemical tool wear. In diamond turning, the rake face is generally the (110) orientation, which will etch to a (111) orientation. Experiments showed the influence of relative humidity, meaning that OH stabilization occurs. A hypothesis for the oxidative etch mechanism during diamond turning of polymers is given. It starts with a nucleophilic attack on the carbonyl group on the diamond surface, finally resulting in CO desorption and OH stabilization on the diamond surface. This way, tribo-chemical wear can be dominant.

Calculations showed that during the diamond turning process enough energy is present for oxidative etching to occur, and that enough nucleophiles are present to initiate the etching process.

Contents

Samenvatting **vii**

Abstract **xi**

1 Introduction **1**

1.1 Polymers for optical applications . . . 1
1.1.1 Lens production . . . 1
1.1.2 Optical properties . . . 2
1.2 The turning process . . . 6
1.2.1 Precision turning lathe . . . 6
1.2.2 The precision turning process . . . 6
1.2.3 Tool force models . . . 10
1.2.4 Surface formation . . . 12
1.2.5 Diamond tool wear . . . 14
1.3 Material behaviour of polymers . . . 15
1.3.1 Linear deformations . . . 15
1.3.2 Plastic deformation in the solid state . . . 18
1.3.3 Fracture . . . 21
1.4 Short literature review on polymer turning . . . 25
1.5 Research goals . . . 27
1.6 Outline . . . 27

2 Properties of polymer turning **29**

2.1 Differences between metal and polymer turning . . . 29
2.2 Cutting forces in polymer turning . . . 33
2.3 Thermal model of the polymer turning process . . . 34
2.3.1 Introduction . . . 34
2.3.2 Shear plane temperature . . . 36
2.3.3 Temperature rise at the chip-tool interface . . . 43
2.3.4 Temperature rise in the diamond tool . . . 47
2.4 Experimental verification . . . 49
2.4.1 Development of a tool with embedded thermocouple . . . 49
2.4.2 Verification experiments . . . 50
2.4.3 Infrared measurements . . . 51

2.5 Conclusions 53

3 Influence of cutting conditions and material properties 55
3.1 Introduction 55
3.2 Turning parameters 55
3.2.1 Plunge turning 56
3.2.2 Face turning with a radius tool 72
3.3 Influence of thermo-mechanical history 77
3.3.1 Experimental 77
3.3.2 Results 79
3.4 Influence network density 84
3.4.1 Experimental 84
3.4.2 Results 85
3.5 Conclusions 88

4 Tribo-electric diamond tool wear 91
4.1 Introduction 91
4.2 Charging in polymer cutting 93
4.2.1 Charging at low cutting speeds 93
4.2.2 Charging at higher cutting speeds 96
4.3 Luminescence observations 97
4.3.1 Observations 97
4.3.2 Spectral measurements 98
4.4 Conditions influencing charging in polymer turning 102
4.4.1 Influence of cutting speed 102
4.4.2 Influence of feed rate 103
4.4.3 Influence of depth of cut 104
4.4.4 Influence of humidity 104
4.4.5 Influence of chain scission 106
4.5 Tool life experiments 107
4.5.1 Expectations 107
4.5.2 Experiments and results 110
4.5.3 Dominance of tribo-electric tool wear 114
4.6 Tool life improvements 116
4.7 Conclusions 117

5 Tribo-chemical diamond tool wear 119
5.1 Introduction 119
5.2 Material selection 122
5.3 Experiments 124
5.3.1 Results 124
5.3.2 Conclusions from experiments 130
5.4 Influence of water on diamond tool wear 131
5.4.1 Results 132

5.5 Proposed tribo-chemical reaction mechanism 134
  5.5.1 Creation of reactive elements 134
  5.5.2 Oxidative etching mechanism 136
  5.5.3 Discussion 137
5.6 Conclusions 139

6 Conclusions and recommendations 141
6.1 Conclusions 142
  6.1.1 Cutting mechanics 142
  6.1.2 Diamond tool wear 144
6.2 Recommendations 146
  6.2.1 Cutting mechanics 146
  6.2.2 Diamond tool wear 147
  6.2.3 Optical materials 148

Bibliography 149

A List of used Nomenclature, Acronyms and Symbols 161
A.1 Abbreviations 161
A.2 Symbols 162
A.3 Values of some fundamental constants 165

B Cutting edge measurement 167

C Material Properties 171

D Calibration of diamond tool with embedded thermocouple 173
D.1 Calibration 173
D.2 Error sources 176
  D.2.1 Conduction to tool shank 176
  D.2.2 Forced convection 178
  D.2.3 Radiation 179
  D.2.4 Total heat loss 180
  D.2.5 Heat transport by chip movement 181

E Cutting force data 183

F Tool wear during turning of Sil-O-Flex 185
F.1 Experiment and results 186

G Electrostatic measurements 189
G.1 Electrostatics 189
  G.1.1 Static electrification 189
  G.1.2 Electrostatics of charged insulators 190
G.2 Measurement of electrostatic charging 191

G.2.1 Non-contacting voltmeter 191
G.2.2 Vibrating electrostatic voltmeter 193
G.3 Measurement results of electrostatic charging 194
G.3.1 Electrostatic charges after turning with 1 m/s 194
G.3.2 Signs of charges on chip and tool 195

H Discharge chemistry 197

Curriculum vitae 201

Dankbetuiging 203

Chapter 1

Introduction

This chapter describes the increasing use of polymeric materials for optical applications. Further, it will give some general background information about the turning process and in particular the diamond turning process, polymer material behaviour, and a short literature review on polymer turning. Finally the research goals will be presented.

1.1 Polymers for optical applications

1.1.1 Lens production

Polymeric optical materials are increasingly used in optical applications. Examples are car lights, traffic lights, displays of mobile telephones, contacts, spectacle lenses, laser lenses, micro-structured arrays, projection lenses and drums in copier machines. A lot of these products are manufactured in mass production and therefore it is convenient to produce them by injection moulding. However, some products have to be produced customer-specific. The example here is the production of lenses. Contacts, intra-ocular lenses (IOL's) and spectacle lenses have to be produced according to the eye dioptry of the customer. People needing spectacles or contacts have different eye dioptries and they also have different wishes for their lenses, such as bi- or multi-focal. Multi-focal lenses have a large range of changing dioptries on their contour, especially designed for people who want to use their lenses for both near and far sight viewing. This means that all these lenses have to be produced customer-specific.

The current production process of lenses consists of rough cutting the so-called ”blank”. This process creates the rough form of the lens, but not the correct optical quality. If the surface roughness of the rough cut blank is too high for immediate polishing, the blank is first transported to a grinding machine. After grinding a better surface quality is achieved, but still not the correct optical quality. To achieve this the blank is transported to the polishing machine for polishing to optical quality.

The process of transporting and fixing the blank on other machines introduces inaccuracies in the final product [1]. Another source of inaccuracies originates from the grinding and polishing processes itself. The use of fixed stamps for grinding and polishing results in contact pressure distributions over the blank [2, 3]. At higher contact pressures more material is being removed than at lower contact pressures. This inherently leads to a flattening of high spots and round-off at the edges [4]. This attributes to form and shape uncertainties.

Also, the above mentioned manufacturing process has the disadvantage of being environmental unfriendly. Use of grinding and polishing powders pollutes the water that is used in these processes. It is obvious from the foregoing that the manufacturing process of these optical lenses can be improved.

The precision cutting process enables a high flexibility in the production process [5] and an increased production rate of asymmetric products [6]. Especially the non-rotational symmetric lenses can be produced with high flexibility by using a so called ”fast tool servo” [7]. Higher form and shape accuracies can be achieved by the turning process than with conventional grinding and polishing techniques [8, 9, 10]. It may be obvious that performing rough cutting and precision cutting on one machine will decrease the uncertainties of the final product and can increase the throughput.

1.1.2 Optical properties

Most common optical materials used for spectacle lenses are mineral glasses, and polymers such as allyl diglycol carbonate (ADC) and polycarbonate (PC). The biggest benefit of ADC and PC, which are polymers, is their relatively low specific mass. Their specific masses are approximately 1300 $\mathrm{kg/m^3}$, which is half the density of glass.

In Europe, mineral glasses have a share of approximately 35% in spectacle lenses and PC approximately 5%. Looking at the United States of America, no mineral glasses are being used for spectacle lenses, while PC has a share of approximately 35%. The rest are mainly ADC’s [11]. These polymers are low index materials (< 1.55). Also higher index (> 1.6) polymers can be found, up to refractive indices of 1.74. In fact, PC is a mid index material with a refractive index of 1.58, but it has a bad chromatic aberration. Chromatic aberration arises from the fact that the refractive index is a function of the wavelength of the light, $n = n(\lambda)$. The thin-lens equation is given by Hecht [12] as:

$$\frac{1}{f} = (n_l - 1)\left(\frac{1}{r_1} - \frac{1}{r_2}\right) \tag{1.1}$$

with f the focal length of the lens, n_l the refractive index of the lens material, and r_1 and r_2 the radius of curvature of the two lens surfaces. Since the refractive index is a function of wavelength, it can be seen that the focal length of a lens, see the thin lens equation, is dependent on the wavelength too. In general $n(\lambda)$ decreases with wavelength over the visible region, and thus $f(\lambda)$ increases with λ [12].

At this moment also polyamides (PA) and polyurethanes (PU) are more and

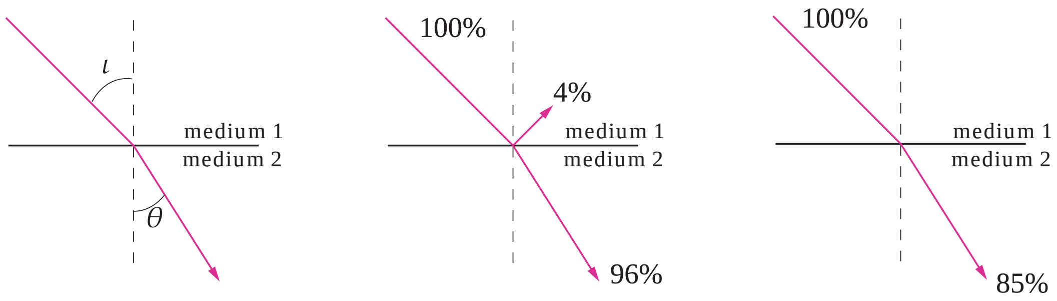

a) Refraction b) Reflection c) Absorption

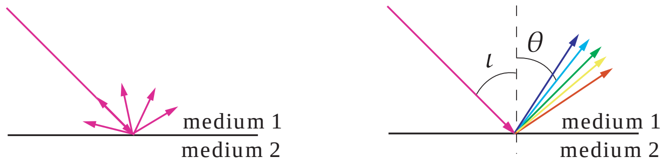

d) Diffusion e) Diffraction

Figure 1.1: The optical properties of a lens are determined by refraction, reflection, absorption, diffusion and diffraction.

more applied for optical lenses. These materials have good impact resistance and better optical properties than PC.

The following five optical properties can be distinguished.

- **Refraction** When a light beam travels non-perpendicular from one material to another material that has a different refractive index, see Figure 1.1(a), the light beam changes direction according to

  $$\sin \iota = n \cdot \sin \theta \tag{1.2}$$

  with ι the angle between surface normal and incident light beam, n the refractive index of the material and θ the angle between surface normal and refracted light beam. The refraction index n of a material is determined by $n = c/v_m$ in which c is the speed of light in vacuum and v_m is the speed of light in the specific material, therefore $n > 1$.

  The refractive index is dependent on the wavelength of the used light. A different wavelength results in a different v_m, since $v_m = f \cdot \lambda$ with f the frequency of light and λ the wavelength. The dependence between n and λ is called dispersion and results in chromatic aberration. It is characterized by the Abbe number V_d and defined as [12]:

  $$V_d = \frac{n_{yellow} - 1}{n_{blue} - n_{red}} \tag{1.3}$$

with n_{yellow}, n_{blue} and n_{red} the refractive indices for yellow (λ = 587.6 nm), blue (λ = 486.1 nm) and red (λ = 656.3 nm) light. When a material has a low Abbe value, it has a lot of dispersion and chromatic aberration. Generally, in optics the dispersion is not a big influence parameter [13], however, PC is known as a material with a bad chromatic abberation: its Abbe number is approximately 30, which is bad. This in contrast to the thermoset CR39, which is an allyl diglycol carbonate (ADC). It has an Abbe value of nearly 60, which results in less chromatic abberation [13].

- **Reflection** Reflection, shown schematically in Figure 1.1(b), always occurs on a surface and is also material dependent. The higher the refractive index, the higher the reflection. In [13] can be found that for an n=1.5 material the reflection for a perpendicular incident light beam is 7.8% and for an n=1.9 material the reflection increases to 18%. A way of omitting this reflection is applying an anti-reflection coating on the surface.

- **Absorption** Atoms and molecules contain electrons. It is often useful to think of these electrons as being attached to the atoms by springs. The electrons and their attached springs have a tendency to vibrate at specific frequencies, called their natural frequencies. When a light wave of a given frequency strikes a material with electrons having the same vibrational frequencies, these electrons will absorb the energy of the light wave and transform it into vibrational motion. During their vibrations, the electrons interact with neighbouring atoms converting the vibrational energy into thermal energy. Subsequently, the light wave with that given frequency is absorbed by the object, Figure 1.1(c). Absorption is a material property.

- **Diffusion** Diffusion appears at the surface of a material. Therefore, this is not a material property. It is dependent on the surface roughness. An incident light beam ”scatters” at the surface, see Figure 1.1(d). The reflected light does not totally leave the surface under the same angle as the incident beam, but leaves the surface under all angles.

  A relation between diffusion and surface roughness is given by the total integrated scatter (TIS) equation [14, 15]:

$$TIS = \left(\frac{4\pi Rq}{\lambda}\right)^2 \tag{1.4}$$

  In this equation, TIS is the amount of scattered light with respect to the total intensity of the incident beam on the surface, Rq is the root mean square roughness of the surface, and λ is the wavelength of the incident beam. It may be obvious from this equation that the TIS value is highly dependent on the used wavelength, and that for larger wavelengths, the amount of scatter becomes negligible. However, for the visual spectrum, with its shortest wavelength of approximately 300 nm, an Rq roughness of

2.4 nm has to be achieved to have only 1% loss of intensity by scattering. Therefore, high surface qualities are needed for optics that are to be used in the visual spectrum.

- **Diffraction** Diffraction is the bending and spreading of waves when they meet an obstruction. It may be a result of regularly spaced patterns with dimensions in the order of the wavelength of the used light. In fact, diffraction is an interference phenomenon that can only occur for coherent light waves. Diffraction for optics is best described by the far field solution, defined as Fraunhofer diffraction. It is described by the grating equation for oblique incidence [12] as:

  $$\sin\theta = \sin\iota + \frac{m\lambda}{d} \tag{1.5}$$

  with m the order of the interference line ($m = 0, \pm 1, \pm 2, ...$), λ the wavelength of the used light, d the grating distance, ι the angle between surface normal and incident light beam, and θ the angle between surface normal and diffracted light beam.

  Diffraction is given schematically in Figure 1.1(e). When a white light ray incidents on a surface with a regularly spaced pattern a ”rainbow” image can be seen. This is also a problem for turned optics, since a regular pattern is formed by the footprint of the tool during turning. If a constant feed rate f was used, it holds that $d = f$. This way, the amount of diffraction can be calculated using Equation 1.5. Notice that when a feed rate smaller than the wavelength of light is used, no diffraction occurs. However, this means increasing production times for optics.

From the above description it is clear that the different optical phenomena can either be determined by material properties or manufacturing properties. This is summarized in Table 1.1.

Table 1.1: Influencing properties on optical phenomena.

phenomenon	material property	manufacturing property
refraction	×	
reflection	×	
absorption	×	
diffusion		×
diffraction		×

Equations 1.4 and 1.5 can be used for the determination of turning parameters that should be used to achieve certain optical properties with respect to the amount of allowable scattering and diffraction of an optical system.

1.2 The turning process

1.2.1 Precision turning lathe

This thesis describes aspects of the diamond turning process of glassy polymers. An important factor in diamond turning is the precision lathe used [16]. The experiments described in this thesis were all performed on a precision turning machine, called ”Colath”, that was developed at Philips Natlab [17] in the 1980’s. The used configuration is an upgraded version from the original turning lathe.

The setup of the machine consist of two hydrostatic slides and an air bearing spindle. The slides were actuated by linear motor actuators (LIMA’s) [17] and recently upgraded with voice-coil actuators for higher accuracy. Also, the laser interferometer measurement system has been replaced by Heidenhain nanometer scales. The accuracy of the Colath is better than 1 μm [17].

1.2.2 The precision turning process

The precision turning process with a nose radius tool is schematically shown in Figure 1.2. It can be seen that the tool penetrates the workpiece at a certain depth of cut h with a relative cutting speed v_c with the workpiece. Further, the tool moves perpendicular to its cutting speed and parallel with the workpiece surface to be cut. This is the feed rate f. Because the tool penetrates the workpiece, a chip is formed that slides over the rake face of the tool, as depicted in Figure 1.3. The chip formation process is a process with strong plastic deformation. True strains of 1-3 are normal in the turning process [18]. The strain rate during cutting can be estimated by [19]:

$$\dot{\gamma} = \frac{v_c}{h_{cu}} \cdot \gamma \tag{1.6}$$

with γ and h_{cu} the shear strain respectively the uncut chip thickness. Using common precision turning parameters it can be calculated, see Equations 1.16 and 1.17, that the uncut chip thickness is approximately 1 μm. Generally cutting speeds $v_c > 1$ m/s are applied. For such cutting speeds it can be calculated that the strain rates in the precision turning process are of order 10^6 s^{-1} or higher. These high strain rates will result in an adiabatic process. This has some consequences for the turning process. Adiabatic conditions raise the temperature in the deformation zone. For metallic materials it is known that temperature rises of several hundred degrees Celsius may occur. This results in a softening behaviour of the material in front of the tool.

In most precision turning processes diamond tools are being used, since they can be made accurately and have sharp cutting edges. Because of the temperature increase in front of the tool and because of frictional heating at the rake face, thermal wear of cutting tools may occur. This is one of the reasons why diamond wears so quickly when machining steel, since the cutting temperatures exceed

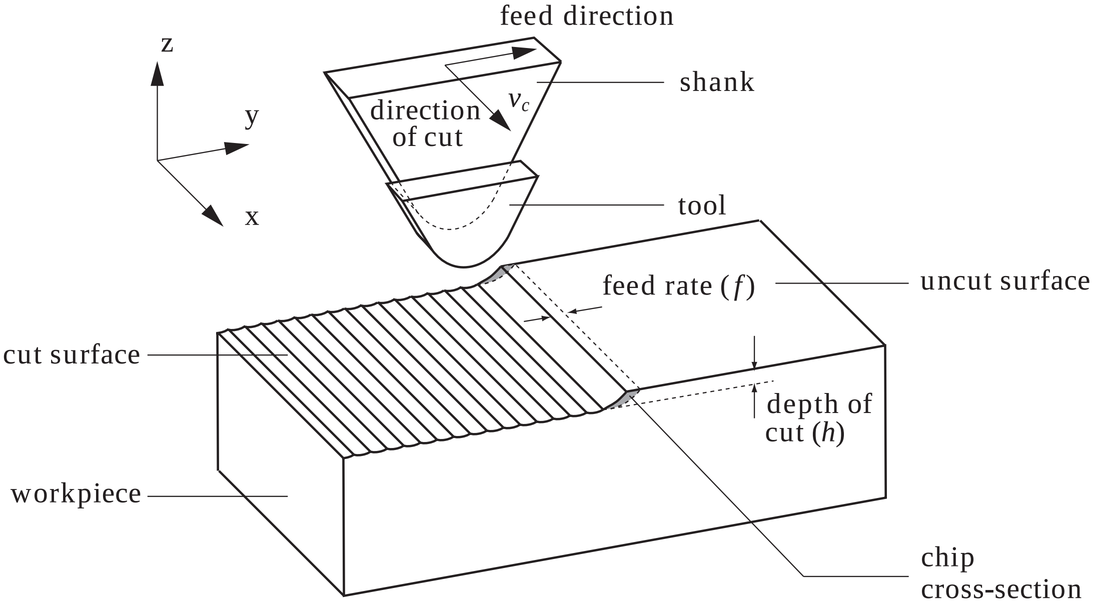
feed direction
z
shank
y
direction of cut
v_c
x
tool
feed rate (f)
uncut surface
cut surface
depth of cut (h)
workpiece
chip cross-section

Figure 1.2: Cutting geometry in precision turning operations.

the oxidation temperature of diamond (> 500 °C) and rapid tool wear occurs e.g. [20].

The turning process is generally simplified as an orthogonal cutting process. In orthogonal cutting the cutting edge direction is set orthogonally to the motion of the tool and orthogonal to the generated surface. If, in this orthogonal cutting process a large ratio exists of cutting width to undeformed chip thickness, the cutting can be considered as plane strain, or two dimensional, see Figure 1.3(a).

This figure shows the plane strain setup of the turning process, represented

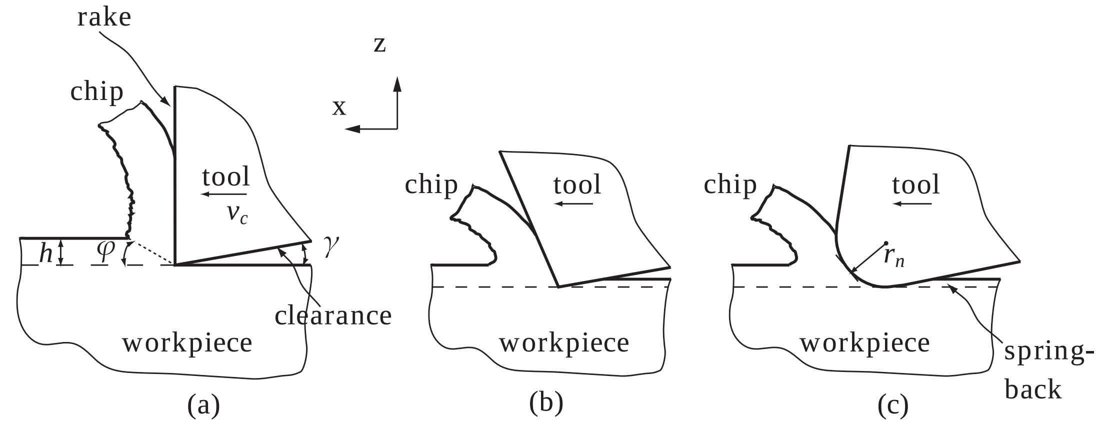
rake
z
chip
x
tool
v_c
h
φ
γ
clearance
workpiece
(a)
chip
tool
workpiece
(b)
chip
tool
r_n
workpiece
spring-back
(c)

Figure 1.3: (a) Orthogonal cutting process, an ideal situation, (b) and (c) the ploughing action of a tool with negative rake respectively a tool with a cutting edge radius of size depth of cut.

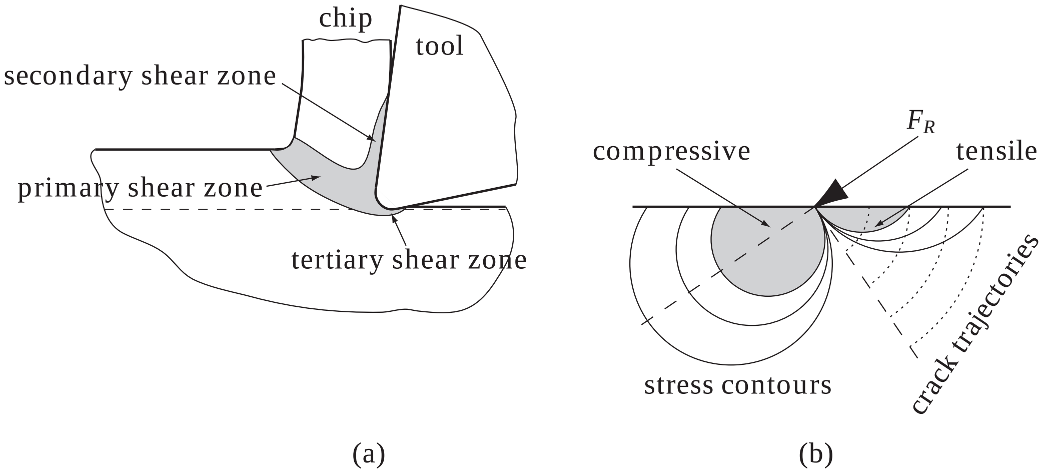

Figure 1.4: Figure (a) shows the different shear zones encountered in turning operations. Figure (b) shows the stress zones in turning operations.

by the dotted line at an inclined angle φ, the shear angle. This figure shows an ideal turning process: the workpiece layer to be cut is totally removed. In reality this will not be the case, because of the finite cutting edge of the diamond tool.

Deformation zones Generally the turning process is modeled as shearing deformation in a narrow zone. However, cutting processes are more complicated than that. This is illustrated in Figure 1.4(a) showing the deformation zones encountered in turning operations. Since the main deformation mechanism in these zones is shear, these deformation zones are generally called shear zones. Besides the primary shear zone that is generally modeled for analytical calculations, a secondary and tertiary shear zone are formed.

The secondary shear zone originates from friction between chip and rake. The tertiary shear zone originates from the material transported underneath the tool. The size of the tertiary shear zone depends on the cutting edge radius, but also on the amount of flank wear [4].

It can be seen in Figure 1.2 that a chip with an increasing thickness over its cross-section is produced in the diamond turning process. At the smallest chip side, the undeformed chip thickness is of the order of the size of the cutting edge of the tool. This means that one can no longer assume that a sharp cutting edge exists in that part of the cutting zone. Still, the exact influence of this region on the surface to be formed is not well understood. It may be understood that the workpiece material is transported underneath the tool, while at the bigger undeformed chip thicknesses the material is being sheared into the chip. The effect of relative bluntness of the tool is bigger when a negative rake angle is used or a large cutting edge radius, see Figures 1.3(b) and (c). The material that is transported underneath the tool will be deformed and elastic springback behind the tool will occur; this material rubs on the clearance face of the tool [21, 22]. When cutting polymers, this rubbing can be substantial, because the polymer will be heated above the glass transition temperature by the friction between cut surface and clearance face, which was shown clearly by Carr and Feger [21].

Not only the material at the smallest chip side will be transported underneath the tool, but this occurs over the entire chip width too. Research about the thickness of the layer to be transported underneath the tool was carried out by e.g. [23, 24, 25]. Also the resulting springback layer, resulting from elastic recovery of the material transported underneath the tool has been modeled, e.g. [4, 24, 25].

Figure 1.4(b) shows schematically the stress fields in precision turning [26]. This stress field solution follows from the line force F_R acting on a half space. The line force F_R is the combined action of main cutting force and thrust force. The stress field is radial, with compressive and tensile stresses occurring in front respectively behind the tool, of a line projected normal to the line force F_R. Plastic deformation zones occur in the shaded zones (based on Von Mises criteria). In the tensile stress field, mode I fracture can occur along the crack trajectories.

It is known from metal cutting that different kinds of chips can be formed in turning operations. Figure 1.5(a) shows a homogeneous flow chip. Wavy chips, see Figure 1.5(b), are formed by an oscillation of the shear angle. The segmented or shear chip, see Figure 1.5(c), is formed by adiabatic shear localization. Brittle materials lead to discontinuous chips in turning, see Figure 1.5(d). The segments are fully separated from each other by (brittle) fracture of the material in or in front of the shear zone.

It is generally known that when continuous (ductile) chips, Figure 1.5(a), are produced better surface qualities are achieved than when discontinuous (brittle) chips, Figure 1.5(d), are produced. Generally when brittle materials like ceramics are cut, a crack is produced in front of the tool, which causes a fractured surface and a bad surface quality. If one knows how to achieve ductile and stable cutting

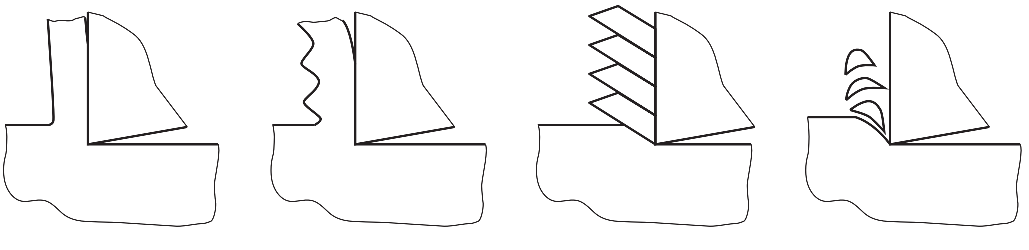

(a) (b) (c) (c)

Figure 1.5: Schematic representation of chip types known from metal cutting [27]: (a) homogeneous flow chip, (b) non homogeneous wavy chip, (c) non-homogeneous segmented or shear chip, and (d) non-homogeneous discontinuous chip.

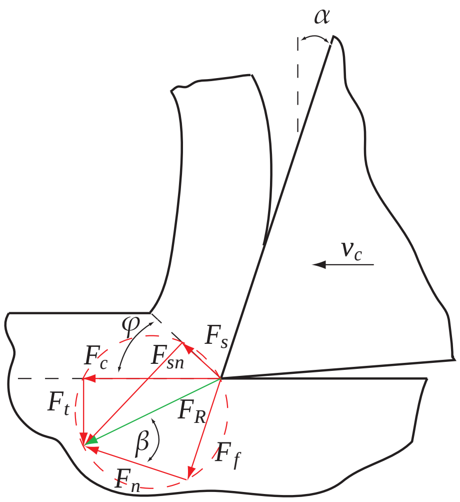

Figure 1.6: Tool force diagram for orthogonal cutting [31], with main cutting force F_c, thrust force F_t, resultant force F_R, shear plane force F_s, shear plane normal force F_{sn}, frictional force on the rake face F_f and normal force on the rake face F_n.

conditions, one is capable of achieving high surface qualities and high accuracies. From cutting research on highly brittle materials, such as single crystal silicon [28], germanium [29] and quartz [30], it is known that there is a brittle-to-ductile transition. This means that there is a depth of cut where the process changes from brittle to ductile. It is known that a brittle-to-ductile transition occurs if the hydrostatic pressure in front of the tool is high enough to favour a ductile chip formation instead of a brittle one.

1.2.3 Tool force models

Figure 1.6 shows a model that can be used for the prediction of cutting forces. The figure shows a chip that is considered to be in equilibrium. The equilibrium forces are a resultant force on the chip at the rake face of the tool and a resultant force at the base of the chip on the rake face. From the figure it can be seen that the resultant force F_R can be subdivided in different pairs of forces. In general the main cutting force F_c and the thrust force F_t can be measured by a dynanometer. From the figure it follows that:

$$\vec{F_R} = \vec{F_c} + \vec{F_t} = \vec{F_s} + \vec{F_{sn}} = \vec{F_f} + \vec{F_n} \tag{1.7}$$

with F_s the shear plane force, F_{sn} the shear plane normal force, F_f the frictional force on the rake face and F_n the normal force on the rake face. For these forces the following geometrical relations can be derived with the aid of the cutting force diagram given in Figure 1.6.

$$\begin{aligned} F_s &= F_c \cos\varphi - F_t \sin\varphi && (1.8)\\ F_{sn} &= F_c \sin\varphi + F_t \cos\varphi && (1.9)\\ F_f &= F_c \sin\alpha + F_t \cos\alpha && (1.10)\\ F_n &= F_c \cos\alpha - F_t \sin\alpha && (1.11) \end{aligned}$$

with α the rake angle and φ the shear angle. From these equations and Figure 1.6 it becomes clear that the key parameter in the turning process is the shear angle. If the shear angle can be predicted (and the shear flow stress τ_y is known), the cutting forces can be determined:

$$F_c = \tau_y \cdot b \cdot h \cdot \frac{\cos(\beta - \alpha)}{\cos(\varphi + \beta - \alpha)\sin\varphi} \tag{1.12}$$

$$F_t = \tau_y \cdot b \cdot h \cdot \frac{\sin(\beta - \alpha)}{\cos(\varphi + \beta - \alpha)\sin\varphi} \tag{1.13}$$

with width of cut b, depth of cut h and friction angel β defined as $\beta = F_f/F_n$. In the past several analytical cutting force models have been derived. One of the best known models are Ernst and Merchant's [32] and Lee and Shaffer's [33]. These models assume the occurrence of a maximum shear stress on the shear plane. Using different assumptions, different solutions were derived for the shear angle:

$$\varphi = \frac{\pi}{4} - \frac{\beta}{2} + \frac{\alpha}{2} \tag{1.14}$$

and

$$\varphi = \frac{\pi}{4} - \beta + \alpha \tag{1.15}$$

with Equation 1.14 and 1.15 Ernst and Merchant's respectively Lee and Shaffer's solution. Ernst and Merchant's model is known as an upper bound model [18]. The derivation of turning forces in the precision turning process may differ from these derived for conventional turning. This will be described in the next section.

Applicability of tool force models for precision turning

One of the problems concerned with the precision turning process is the use of radius tools that result in a varying uncut chip thickness along the radius of the tool, see Figure 1.2 and 1.7. The maximum uncut chip thickness (dimension perpendicular to the cutting edge) is defined as:

$$\begin{aligned} h_{cu} &= R - \sqrt{R^2 - 2f(b-f)} \quad \text{, with} && (1.16)\\ b &= R \cdot \arccos\left(\frac{R-h}{R}\right) && (1.17) \end{aligned}$$

This means that the chip thickness in precision turning increases from zero to approximately 1.3 μm at the uncut surface at ”normal” precision turning conditions with feed rate 10 μm/rev, depth of cut 10 μm and tool nose radius 1 mm. The value of the cutting edge radius for a newly lapped diamond tool is approximately 50 nm (see Appendix B). Because of this finite cutting edge radius it may be understood that the influence of the cutting edge can be significant at the smallest chip cross-section in precision turning operations. Because of this cutting edge radius the conventional analytical models may not be applicable for precision turning processes, since they assume a sharp cutting edge radius.

In general it can be said that the energy in conventional turning is dissipated by chip formation (shearing in the primary shear zone and friction in the secondary shear zone) and by sliding occurring from flank wear and/or elastic recovery of the workpiece material. When using a negative rake or a finite cutting edge, see Figure 1.3, an additional ploughing occurs contributing to the energy dissipation. During precision turning the effect of the cutting edge may result in an additional ploughing when the chip thickness becomes the size of the cutting edge radius [25, 34, 35, 36].

The question is how much this ploughing effect will be present. In Lucca and Seo’s research [35] a tool with a cutting edge radius of 250 nm was used. They measured that during precision turning of Te-Cu significant differences occurred in the specific energy for uncut chip thicknesses below 1 μm. The used cutting edge radius was relatively large compared to newly lapped mono-crystalline diamond tools of approximately 50 nm. Taking a rough estimate, this could mean that the specific energy for precision turning with sharp tools increases significantly for depths of cut below $4 \cdot 50$ nm = 200 nm. Considering the above, it will be assumed in this research that the normal tool force models can be applied.

1.2.4 Surface formation

Surface formation can be considered as the most important aspect of the precision turning process. The reason for this is that turning is a material removing process to obtain a finished product. This means that the surface quality has to fulfill certain requirements. Generally, precision turning is used when a high surface quality is needed, such as optical quality with Ra roughness values less than 10 nm, but preferably below 5 nm.

Surface formation is a process that is generally considered as a two dimensional problem. Looking at Figure 1.7(b) it can be seen that the tool leaves a ”footprint” at the cut surface. For the ideal cutting process the following relation holds for the theoretical Rt roughness during diamond turning for $R >> h$ [31, 37]:

$$Rt = \frac{f^2}{8R} \tag{1.18}$$

with f the feed rate and R the tool nose radius. The Ra roughness is defined as the arithmetic mean of all absolute deviations from the profile in respect to its mean

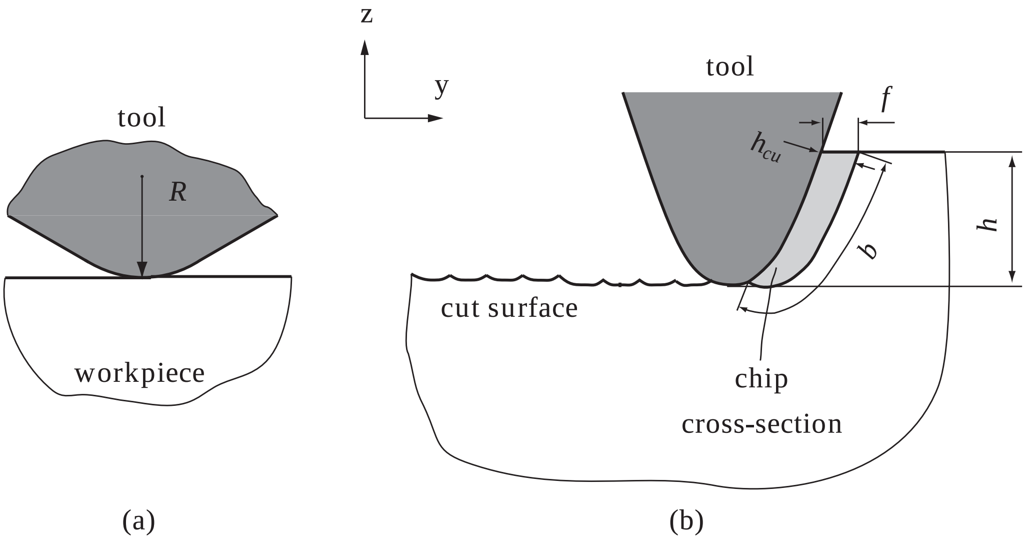

Figure 1.7: Figure (a) shows the diamond turning process on scale with a tool nose radius of 1 mm, depth of cut 10 μm and feed rate 10 μm/rev. Figure (b) shows an exaggerated schematic view.

line. In the case of a nose radius tool, the mean line is $Rt/8$ from the bottom of the profile. Using this mean line, the arithmetic roughness Ra is defined as [38]:

$$Ra \approx \frac{0.032 \cdot f^2}{8R} \tag{1.19}$$

Notice that these two equations give theoretical values. In practice, these roughness values will generally be higher. The reason for this is that the cutting process is a complex process. No ideal material removal will occur and the cutting process is always accompanied by vibrations, either from the surroundings or the chip formation process itself. Concerning the effect of vibrations on surface formation, modelling is presented in [37], while a good overview of chatter is described in e.g. [39].

Looking at the influence of the chip formation process, it can be said that a brittle or ductile process influences the surface formation to a large extent. Using the split-workpiece technique of Arcona [24] the photos shown in Figure 1.8 were made. The figure shows cross-sections of a thermosetting ADC material and a thermoplastic PC.

It can be seen in figure (a) that the ADC material behaves rather brittle, resulting in a discontinuous chip formation process. Cracks originate at the tool tip, advancing the tool. In an ideal situation these cracks would propagate toward the free surface. However, as can be seen, the cracks may also propagate below the depth of cut, resulting in a fractured surface after cutting. This results in a bad surface quality after diamond turning. PC in figure (b) shows a ductile flow chip. In contrast to the ADC material, no cracks are formed in front of the tool. Due

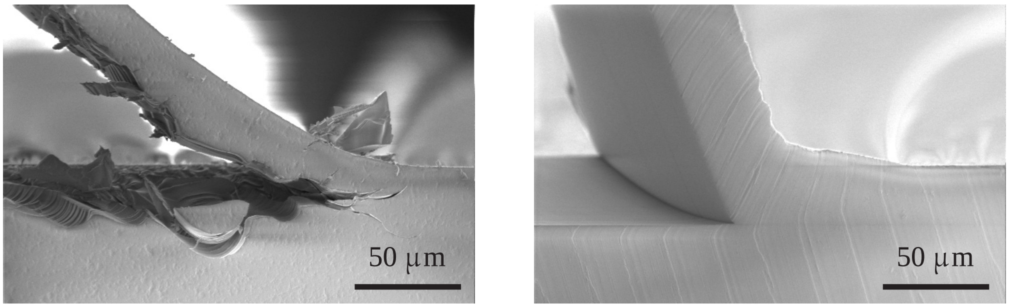

(a) (b)

Figure 1.8: Brittle chip and surface formation of a thermosetting ADC (a), and ductile chip formation in thermoplastic PC (b) at a cutting speed of 2.5 mm/s. These pictures were taken using Arcona's technique for chip visualization [24].

to the ductile chip formation process, a better surface roughness can be achieved, as shown in the figure. Generally when ductile chips are produced, good surface qualities can be expected [28].

1.2.5 Diamond tool wear

In precision turning processes the tools are generally made of mono-crystalline diamond. Mono-crystalline tools are preferred above poly-crystalline, since they can be manufactured with sharper and more accurate cutting edge radii. Mono-crystalline diamond tools can be manufactured with edge radii of approximately $20 - 75$ nm, see Appendix B. Poly-crystalline diamond tools are made of small grains with radii of approximately 2 µm. The cutting edge of a poly-crystalline diamond tool will always have a certain waviness as a result of these grains. Although mono-crystalline diamond tools can be made with sharp edge radii, tools will always become dull during turning. Depending on the workpiece material the tool will wear only little, e.g. copper [40], or a lot, e.g. steel [20].

Not only the initial cutting edge is important for achieving high quality products, but tool life also. When a tool wears, the accuracy of the product becomes questionable, unless the tool wear behaviour is known and can be predicted. A good example of this is the use of synthetic mono-crystalline diamond tools in the production of contacts. These tools have a more predictable tool life behaviour than natural diamond [40, 41] and therefore it can be very well predicted how many lenses can be turned. Natural diamond tools show more spread on their tool lives, making it harder to predict their tool life. This indicates the economical importance of the knowledge of tool life behaviour.

Kobayashi mentions in [42] that "cutting edges of tools used in the [cutting] process have failed by chipping or have worn excessively, limiting their further use". Kobayashi concludes that frictional heat (in conventional cutting!) causes

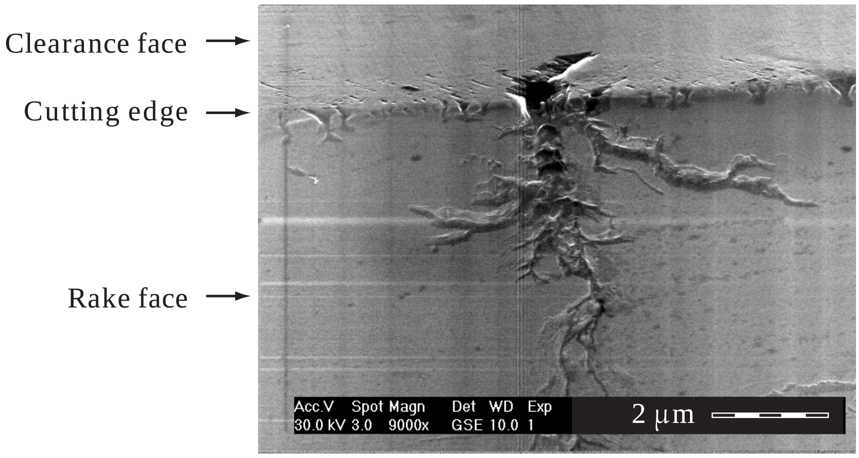

Figure 1.9: Scanning electron microscope photo of diamond tool wear. This phenomenon, a so-called ”Lichtenberg tree”, is ascribed to electric discharging resulting from tribo-electric charging between polymer and diamond.

softening and annealing of the high speed steel (HSS), and is responsible for the high amount of tool wear during conventional cutting of a polymer. This indicates that thermal wear may be important. However, from the contact lens manufacturing industry it is known that tribo-electric tool wear may be an important wear mechanism for diamond tools.

Figure 1.9 shows damage that would occur after discharging between workpiece and tool. Although it is believed that this damage occurs because of discharging and it is known to occur more in winter when the air is dry, it seems difficult to reproduce this wear. Another known wear mechanism is the presence of hard particles in the base material of contacts for achieving higher oxygen transport through the lens. These hard particles may cause abrasive wear to the diamond. Looking at literature, it can be stated that little is published on tool wear phenomena during diamond turning of polymers. For instance, no literature is found about a wear description of tribo-electric tool wear during turning of polymers, although industry claims this is a problem during diamond turning of polymers.

1.3 Material behaviour of polymers

In the precision turning process the material in front of the tool is deformed. This section will describe some material properties of glassy, amorphous polymers during deformation.

1.3.1 Linear deformations

Generally, glassy polymers are solid at room temperature, this is called the glassy state. Figure 1.10 shows the elasticity modulus as a function of temperature. It

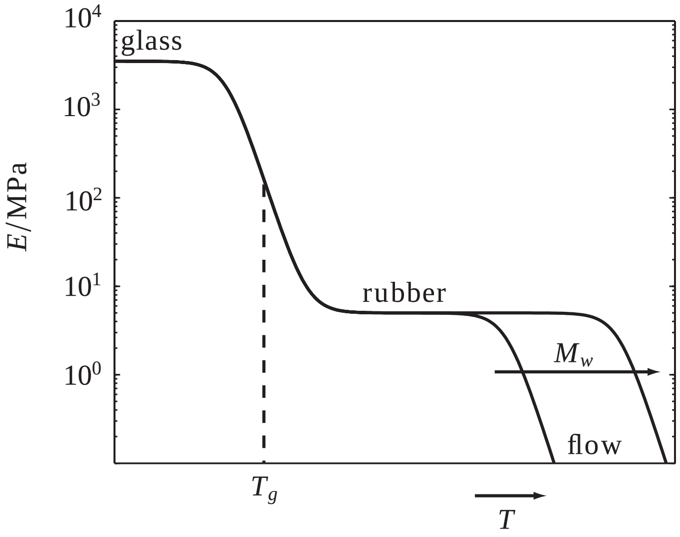

Figure 1.10: Elastic modulus as a function of temperature for a glassy polymer. For T_g values, see Table C in Appendix C.

can be seen that the polymer has a relatively high Young's modulus (E) in the glassy state. In the glassy state only side-group motions are possible. When the temperature is increased, a transition region occurs. This is the region around the glass transition temperature T_g. This transition region is the onset of main chain segmental mobility of the polymer chains. It is characterised by its visco-elastic behaviour. The polymer comes into the rubber state upon further heating. In this region the rubber plateau is caused by the entanglements between the polymer chains. By further heating, the polymer enters the region where the chains are capable of full reptation. This is called the flow regime. Where this flow regime occurs is dependent on the molecular weight (M_w) of the polymer, as can be seen in Figure 1.10.

In literature on polymer turning, e.g. [21, 44], it is generally said that the polymer can reach the glass transition temperature and enters the flow regime during turning. Notice, however, that it is not the flow regime that the polymer enters, but the rubber plateau, which should be seen as a softened state instead of a flow state. When the polymer comes in the flow regime, the molecular weight of the polymer chains should become important for the description of the cutting mechanics. At very low rates of deformation polymer melts have a Newtonian behaviour. The shear viscosity of the polymer melt is then characterized by the symbol η_0, the zero shear viscosity. Figure 1.11 shows the influence of the molecular weight on this zero shear viscosity.

If the polymer chains have a molecular weight smaller than the polymer's critical molecular weight M_c, then the zero shear viscosity scales by the first power of the molecular weight. When the polymer chains have a molecular weight above M_c, then the zero shear viscosity scales by a power of 3.4 of the

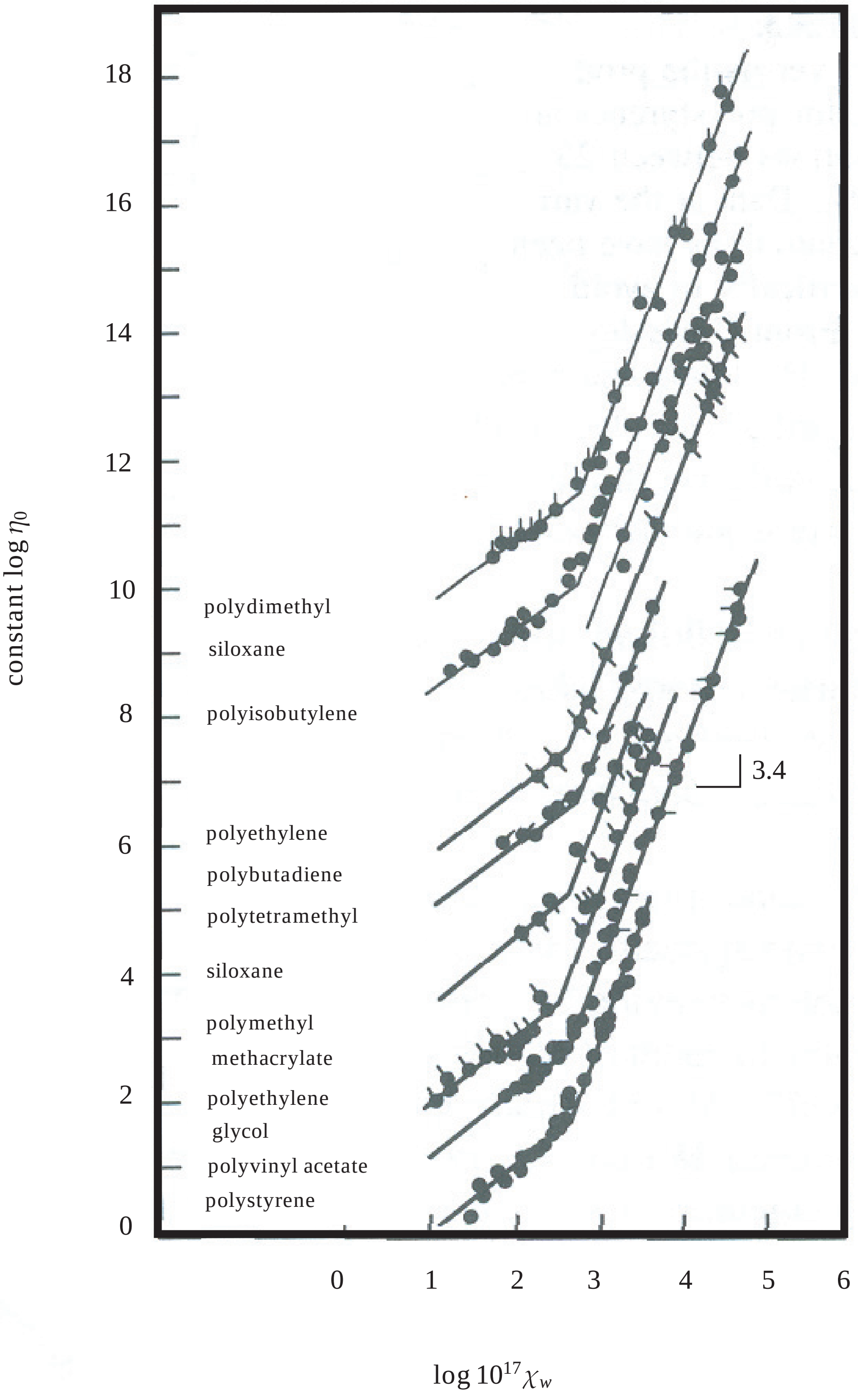

Figure 1.11: Typical viscosity versus molecular weight dependence for molten polymers; χ_w is proportional to the number of backbone atoms and M_w (reproduced from [43]).

molecular weight. For the zero shear viscosity, the following relation holds:

$$\eta_0 = \eta_0(M_w) \tag{1.20}$$

The stress necessary for linear deformations is then defined by:

$$\sigma = \eta_0(M_w) \cdot \dot{\gamma} \tag{1.21}$$

which indicates that higher stresses are needed with increasing molecular weights for small linear deformations. However, in turning processes large deformations occur [18], and also material separation in front of the tool. The next sections give more information on these two topics.

1.3.2 Plastic deformation in the solid state

In previous research on polymer turning, e.g. [21, 44], it was concluded that polymers can be machined in the thermal flow regime. However, before adiabatic heating can occur, the polymer deforms in the solid-state.

Intrinsic material behaviour

Figure 1.12 depicts the solid-state material behaviour of a polymer during deformation. When the polymer is strained, it will first deform (visco-)elastically, until the initial yield point is reached. In fact, this yield point can be seen as a stress induced mobility of the polymer chains. It is the onset of main chain segmental mobility.

The polymer network is formed by physical and/or chemical entanglements. Beyond the yield point, the polymer chains under stress have segmental mobility. During deformation the chains align in the direction of the applied stress, which leads to a decrease of chain entropy, and results in a rubber-elastic stress contribution. Therefore, the entanglements forming the polymer network result in strain hardening during deformation.

During plastic deformation of polymers, another effect has to be taken into account: physical aging. When a polymer is in the molten state it is in a thermodynamic equilibrium. This means that the polymer chains can freely move by main chain motion and stay in a stress-free situation. During cooling, around T_g main chain segmental motion becomes too slow, and the polymer gets out of its thermodynamic equilibrium. Figure 1.13 shows this behaviour by plotting the specific volume as a function of temperature. When the polymer is out of its thermodynamic equilibrium it will strive in time for this thermo-dynamic equilibrium. This process is called ”physical aging” [45].

Physical aging is known to lead to an increase in initial yield stress. From Meijer [47] it is known that during physical aging the local attraction of individual atoms to their neighbours in the polymer material increases, leading to an increasing enthalpy peak near the glass transition temperature. This peak has to

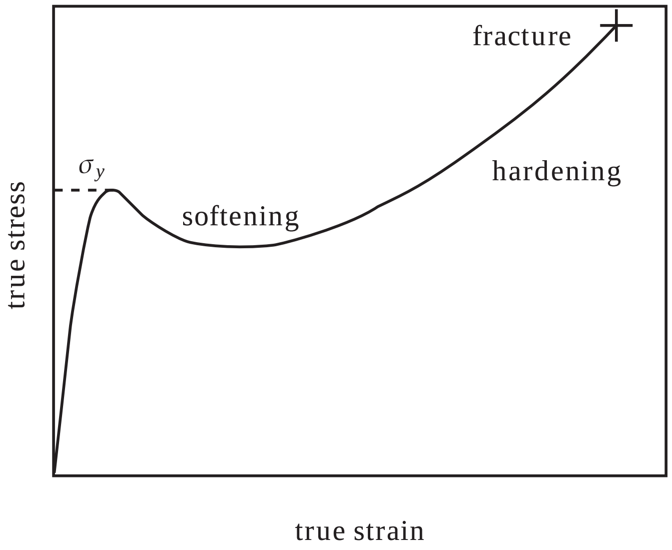

Figure 1.12: General stress-strain behaviour of glassy polymers. The initial yield point, for polymers typically in the range of 60 – 120 MPa, is the onset of stress induced main chain segmental mobility.

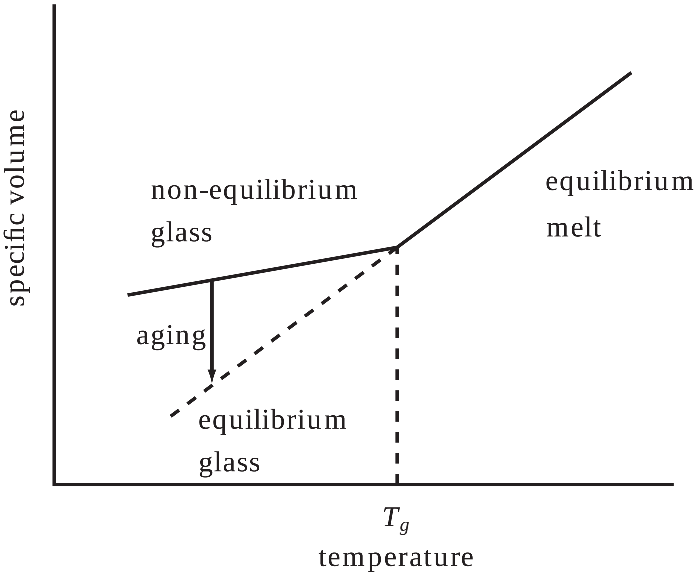

Figure 1.13: Schematic representation of specific volume as a function of temperature for glassy polymers [46]. See Appendix C for T_g values of several glassy polymers.

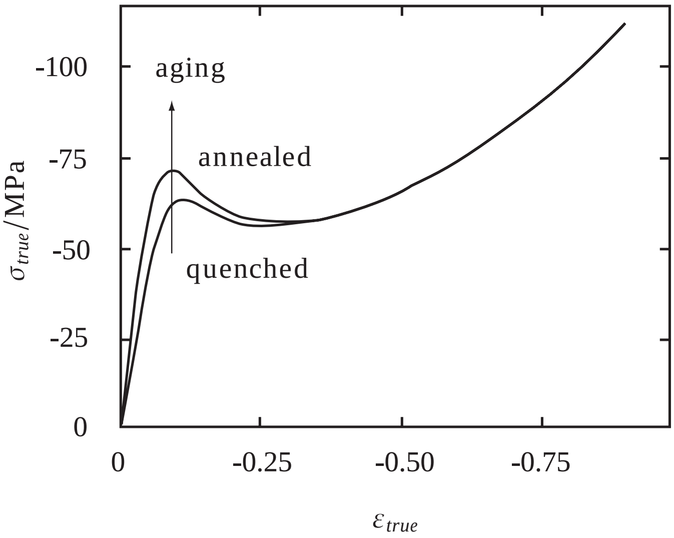

Figure 1.14: Influence of thermal history on the compressive behaviour of PC, reproduced from van Melick [48]. Physical aging leads to increasing initial yield stress.

be overcome to have segmental mobility of a polymer chain. This can be done by thermal energy or by deformation energy. If segmental mobility is increased, not by temperature but by stress, this can be envisaged as an increase in initial yield stress for overcoming the increasing enthalpy peak, see Figure 1.14.

Softening

Figure 1.14 shows that physical aging leads to an increasing initial yield stress. It can also be seen that with increasing physical aging the stress drop behind the initial yield stress increases too. This stress drop is called ”strain softening” or shorter ”softening”, see Figure 1.12 too.

The amount of softening has its consequence for the macroscopic material response of the polymer [49]. Intrinsic strain softening leads to a localization of strain. The evolution of the localized plastic zone depends on the stabilizing effect of the strain hardening, i.e. the polymer network. When a localized deformation zone cannot be stabilized by sufficient strain hardening the material will fail in a macroscopically brittle way. A good example is PS, which has a strong strain softening and a very low strain hardening. Therefore, upon stretching PS will fail macroscopically brittle. The opposite case is PC, which has a moderate strain softening, and a strong strain hardening behaviour. PC will generally behave ductile [48, 49].

Thermo-mechanical treatments

It was described that polymers are susceptible to physical aging and that this process leads to a changing macroscopic material behaviour. Generally, aging can take a long time, but it can be enhanced by a thermal treatment called ”annealing” or ”aging”. During this process, the polymer is heated to a temperature approximately 20 °C below its T_g and slowly cooled to room temperature again.

When the polymer is aged, the initial yield stress is raised, as shown in Figure 1.14. Aging does not influence the post-yield behaviour, and therefore strain softening increases. This will lead to strain localization and subsequently, if strain hardening cannot stabilize the strain localization, to a brittle material response. Aging can even lead to brittle fracture in PC [48, 49].

The opposite of aging is ”rejuvenation”. Rejuvenation is generally performed by a thermo-mechanical treatment. Quenching is only a thermal treatment, in which the polymer is rapidly cooled from a temperature above to far below its glass transition temperature. Mechanical rejuvenation is performed by applying a pre-deformation to the material [50, 51]. Quenching and thermo-mechanical rejuvenation lead to a lower initial yield stress, decreasing the strain softening, and leading to a more ductile macroscopic response of the polymer during deformation, see e.g. [48, 50, 51].

When the polymer is further strained, see Figure 1.14, the influence of thermo-mechanical history is erased by plastic deformation. This means that strain hardening is not influenced by the thermo-mechanical history of the polymer.

Influence of strain rate

Figure 1.15 shows true stress-true strain curves of PC for different strain rates. It can be seen that with increasing strain rate the yield curves shift upwards. This means that at higher strain rates higher stresses are needed for deformations to occur.

1.3.3 Fracture

In cutting, in front of the tool, material separation has to occur, since a chip has to be formed. When a polymer is strained, it can fail by two possible mechanisms: 1) by disentanglement, or 2) by disentanglement and chain scission. Distinction has to be made here between microscopic and macroscopic behaviour.

Microscopic behaviour

The main interest in dealing with the microscopic failure behaviour of polymers is the interest in whether chain scission occurs during failure. A theoretical review of maximum strain is given.

From [46] it is known that the root mean square end-to-end distance of an unperturbed freely-jointed chain is:

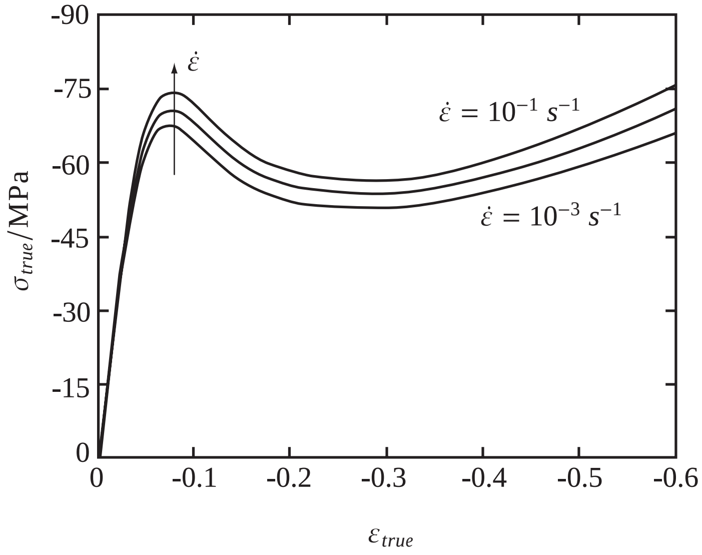

Figure 1.15: Influence of strain rate on the compressive behaviour of PC [52].

$$\left\langle r^2 \right\rangle_f^{1/2} = n^{1/2} \cdot l \tag{1.22}$$

where r is the end-to-end distance of the freely-jointed polymer chain, n is the number of segments of the polymer chain, l is the bond length (for C-C bonds $l = 0.154$ nm). The subscript f indicates that it is the end-to-end distance for the freely-jointed chain. It has to be noted here that $\langle\rangle$ indicates an averaged value with respect to time. Taking into account the structure of chemical bonds, this equation is adapted to:

$$\left\langle r^2 \right\rangle_{fa} = n \cdot l^2 \cdot \frac{1 - \cos\theta}{1 + \cos\theta} \tag{1.23}$$

where subscript fa indicates chains whose bonds rotate freely about a fixed bond angle θ, i.e. the valence angle between two bonds. In general, $180° > \theta > 90°$, resulting in $\cos\theta$ to be negative and therefore

$$\left\langle r^2 \right\rangle_{fa} > \left\langle r^2 \right\rangle_f \tag{1.24}$$

For $C-C$ back bone bonds, $\theta \approx 109.5°$, from which it follows that $\cos\theta \approx -1/3$. Then, it can be derived that for polyethylene (PE), the RMS end-to-end distance increases by a value of approximately $\sqrt{2}$.

Another factor that has to be taken into account is the steric hindrance. Equation 1.23 is then adapted to [46]:

$$\left\langle r^2 \right\rangle_0 = n \cdot l^2 \cdot \frac{1 - \cos\theta}{1 + \cos\theta} \cdot \frac{1 - \langle\cos\varphi\rangle}{1 + \langle\cos\varphi\rangle} \tag{1.25}$$

and $\langle\cos\varphi\rangle$ is the average value of steric hindrances. Due to short-range steric hindrances, $\left|\varphi\right| < 90^\circ$ are favoured [46], so that $\langle\cos\varphi\rangle$ is positive and $\langle r^2\rangle_0$ is greater than $\langle r^2\rangle_{fa}$. Equation 1.25 is quite often expressed as:

$$\left\langle r^2\right\rangle_0 = n \cdot l^2 \cdot C_\infty \tag{1.26}$$

where C_∞ is called the characteristic ratio, defined as [46]:

$$C_\infty = \frac{1-\cos\theta}{1+\cos\theta} \cdot \frac{1-\langle\cos\varphi\rangle}{1+\langle\cos\varphi\rangle} \tag{1.27}$$

Using Equation 1.26, it is possible to estimate the maximum extension ratio λ_{max} of a polymer chain:

$$\lambda_{max} = \frac{L_{max}}{L_0} = \frac{n \cdot l \cdot \cos\alpha}{\langle r^2\rangle_0^{1/2}} = \frac{n \cdot l}{\sqrt{C_\infty \cdot n \cdot l^2}} \cdot \cos\alpha = \sqrt{\frac{n}{C_\infty}} \cdot \cos\alpha \tag{1.28}$$

with L_0 the initial end-to-end distance and L_{max} the maximum length of the stretched chain. This maximum extension ratio is dependent on $\cos(\alpha)$, and $\alpha = 90^\circ - \theta/2$, with θ the valence angle between successive bonds. For $\theta \approx 109.5^\circ$, $\cos\alpha \approx 0.8$.

It has to be noted here, that this relation is only valid if the entanglement points are considered as fixed points [53]. From this equation it becomes clear that fracture of a chain during extension scales with the number of monomers between entanglements. With M_e the molecular weight between entanglements and M_0 the molecular weight of the chain, n is defined as:

$$n = \frac{M_e}{M_0} \tag{1.29}$$

For thermosets, M_e is to be replaced by M_c, the molecular weight between chemical entanglements (crosslinks).

Looking at this equation, it can be understood that a heavily crosslinked material, like ADC, will only have a small λ_{max} since n is small. For ADC M_c is estimated to be $800 - 1600$ g/mol and M_0 is approximately 274 g/mol. Using Equation 1.29 it can be calculated that $3 < n < 6$. From [54] it appears that C_∞ is always larger than 2. Then, using Equation 1.28, for ADC $\lambda_{max} \ll 1.4$.

From several references [48, 53, 54, 55, 56, 57] and some calculations with the above equations Table 1.2 can be derived.

Looking at this table, it can be seen that when a polymer has a low entanglement density ν_e, a high maximum extension ratio λ_{max} between entanglements can be achieved. When this segment becomes strained to its full extension, the molecular bonds will be subjected to more intense stress. When this stress exceeds the bond strength chain scission will occur.

PS shows, according to Table 1.2, a large extension ratio. This is in contrast to the general observation that PS behaves brittle in tension. However, this

Table 1.2: Material properties for several glassy polymers.

Material	ρ in kg/m^3	ν_e in chains/m^3	M_e in kg/mol	M_0 in kg/mol	n	C_∞	λ_{max} (theoretical)
PS	1050	$0.35 \cdot 10^{26}$	17851	104	172	9.9	3.7
PMMA	1180	$0.77 \cdot 10^{26}$	9200	100	92	6.9	3.0
PC	1220	$2.94 \cdot 10^{26}$	2495	254	10	2.4	1.6
PSU	1240	$2.37 \cdot 10^{26}$	3150	443	7	2.0	1.5

behaviour is a macroscopic behaviour. On microscale, so-called crazes are formed. Crazes are super drawn fibrils. Thus, on a microscopic level PS behaves very ductile.

Macroscopic behaviour

Looking at the research of Vincent [58] and van Melick [48], it can be said that when the polymer has an initial yield strength that is higher than the fracture strength, it will show a brittle macroscopic fracture. This does not automatically mean that the main chain bonds of the polymer are broken by chain scission. Chain slip may also result in a brittle failure, which is known from PS.

Figure 1.16 shows experimental data from References [58, 59, 60]. Fits are made according to the relationship [59]:

$$\sigma = \sigma_\infty (1 - M_c/M_n) \tag{1.30}$$

with σ the tensile stress, σ_∞ the limiting tensile strength for high molecular weights, M_c the critical molecular weight (defined as $M_c = 2M_e$), and M_n the number averaged molecular weight.

It can be seen in this figure that an increasing molecular weight increases the brittle strength of the polymer to a certain maximum value, which is polymer specific. It can be understood that at this brittle strength the polymer fails macroscopically. Whether this failure appears by disentanglement and/or chain scission cannot be concluded from this figure.

In Figure 1.16, two curves for PS are given. One for room temperature and one for $T = -196\,^\circ\mathrm{C}$. The time-temperature equivalence principle states in its simplest form that the visco-elastic behaviour at one temperature can be related to that at another temperature by a change in time-scale only [61]. Based on the time-temperature equivalence principle, it can be said that the curve of $-196\,^\circ\mathrm{C}$ corresponds to the same curve taken at room temperature, but with a strain rate several decades higher. As a rough approximation, it can be said that $10\,^\circ\mathrm{C}$ decrease in temperature corresponds to an increase of one decade in strain rate. This would imply that the curves given for a temperature of $-196\,^\circ\mathrm{C}$ can correspond to the strain rates encountered in precision turning ($\dot{\epsilon} \approx 10^7\ \mathrm{s}^{-1}$).

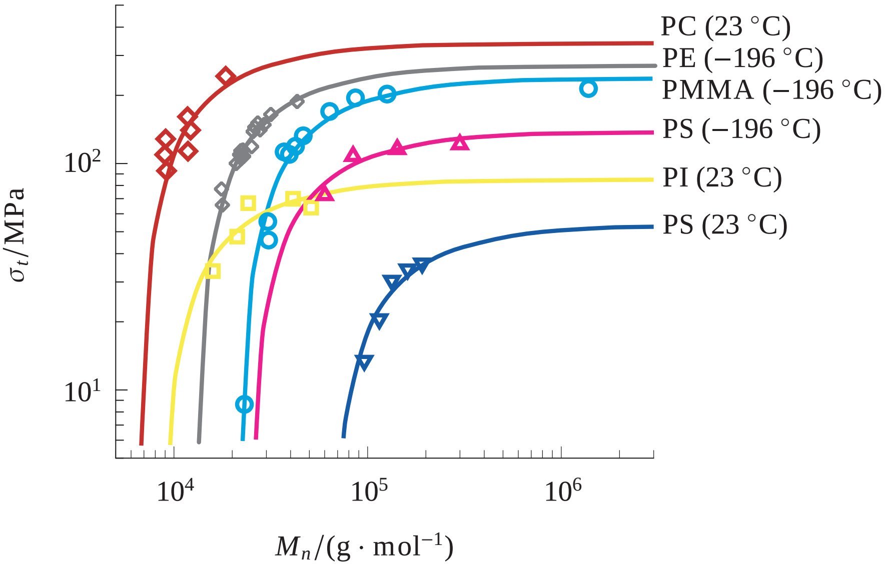

Figure 1.16: Influence of molecular weight on the macroscopic tensile strength of several polymers. Above the curves brittle fracture occurs. Measurement data are derived from References [58, 59, 60].

Section 1.3 gave a short overview of polymer material behaviour. This section can be used as a reference through the rest of this thesis.

1.4 Short literature review on polymer turning

Several researches about cutting behaviour of polymers have been performed. The first researchers were Kobayashi and Saito e.g [62]. Their research focused on the influence of the visco-elastic effect of polymers. When cutting at low speeds (order mm/min), the viscous part of the material behaviour is applied and a smooth and ductile chip can be achieved. By increasing the speed, the elastic part of the polymer will become more important, resulting in a more brittle process. Notice that this research was focussed on the conventional turning process and not on the diamond turning process.

Smith's research [44] focused on the relationship between the glass transition temperature of the polymer and the achievable surface roughness. Better surface qualities can be achieved if a ductile chip is formed during turning [28]. Since polymers behave more ductile around T_g, Smith's hypothesis was that an increasing cutting speed results in more adiabatic heating and therefore a more thermally ductile chip being formed. This hypothesis was proven by measured surface roughness values of several polymers (PS, PMMA and PC) after turning with different cutting conditions. Also, estimates of the temperature increase in the deformation zone during different cutting conditions were made using Boothroyd's model [63], supporting her research. Smith's research is a very good reference for the different types of surface structures that can be formed in diamond turning of several glassy polymers. Since the diamond turned surfaces of this research were similar to those given by Smith, the reader is referred to Smith's research for pictures of diamond turned PS, PMMA and PC.

Carr and Feger [21, 64] investigated several polymers. They interpreted the research of Kobayashi and Saito [62] on the precision turning process, mainly by applying the time-temperature equivalence principle. Carr and Feger showed the effect of the time-temperature equivalence principle by turning Vespel, a polyimide, over a large range of cutting speeds. They described that when the cutting speed was increased, the increased adiabatic temperature rise resulted in a more viscous effect (i.e. lowered the deformation rate). However, with more increased cutting speed the deformation rate became too high and the elastic effect of the polymer prevailed, resulting in a fractured surface and increased surface roughness.

Also, Carr and Feger [21] investigated the influence of the rake angle on the resulting surface finish for the brittle material Vespel. It was shown that the rake angle influences the direction of the resulting cutting force F_R. When the rake angle is large and negative, F_R points into the workpiece and the cut material will show a lot of pits. When the rake angle is almost zero, the force vector F_R will be directed along the uncut surface. The best effect is reached when the rake angle is slightly positive (around +2°). The reason is that F_R is pointing slightly to the uncut surface. Cracks that are formed in front of the tool will not penetrate the cutting plane, leaving a nice cut surface. When the rake angle is further increased, ”islands” will be formed in front of the tool, because of the cracks, and they are pressed underneath the tool, resulting in a worse surface topography.

Based on the results of Smith [44], Carr and Feger also investigated the influence of molecular weight on the achievable surface roughness. When a polymer is cut in the thermal flow regime, the viscous effect will play a significant role in the cutting process, since viscosity is dependent on the molecular weight (M_w) of the polymer, see Figure 1.10. Carr and Feger [21] argued that with increasing molecular weight higher surface roughness values should occur. Therefore they cut different PMMA grades with narrow molecular weight distributions ($M_w/M_n \approx 1$), and showed that with increasing molecular weight a higher surface roughness value was achieved. Based on these results they concluded that cutting of polymers occurs in the thermal flow regime.

An interesting aspect in all literature found on diamond turning of polymers is the big absence of a tool wear description, although industry claims that this is a major problem, e.g [41]. Carr and Feger [21] hardly described it, half a page on a total of 17 pages. However, they remarked that the (qualitative) diamond tool wear was five to ten times higher in polymer turning than in copper turning under the same turning conditions. The observed diamond tool wear was attributed to a thermally induced wear.

Notice that this remark of Carr and Feger is in contrast with the research of

Paul et al. [65], who showed that no wear is to be expected during diamond turning of polymers, since polymers do not contain unpaired d-electrons.

1.5 Research goals

The main objective of this research is to find out which parameters can be used or adapted to improve the precision turning process as a finishing process for polymeric optics. To investigate this, the problem is split up in two parts: 1) the description of the precision turning process of polymers and the relation to cut optical quality, typically defined as $Ra < 5$ nm, with respect to material properties and cutting conditions, and 2) the description and reduction of the relatively high amount of diamond tool wear, during precision turning of glassy polymers.

Literature shows that some polymers can be cut in the thermal regime above T_g, and that certain parameters may influence this cutting state. From Smith [44] it is known that polycarbonate (PC) cannot be cut in this thermal regime because of its high T_g. The application of a thermal model can give some new insights about the thermal state of polymers during precision turning and the influence of cutting conditions on the thermal state during turning. In Smith's research [44] no cutting forces were measured as input for the thermal model. In this research they will be measured and the forces will be used as input for the thermal model. Also, the thermal model will be verified by true temperature measurements during diamond turning of polymers.

Another important factor determining the applicability of diamond turning for optics is tool life. Based on the fact that diamond is the hardest material known and that polymers are (relatively) soft, no tool wear could be expected, but industry considers tool wear as the main problem in diamond turning of polymers. More specific: industry says that tool wear by discharging is a major problem [41]. Since little is found in literature about diamond tool wear in polymer turning, this research focussed on possible wear processes.

1.6 Outline

The introduction, about precision turning process, polymer material behaviour and known literature about diamond turning of polymers, was given in Chapter 1.

Chapter 2 presents the thermal model known from metal cutting. It is shown that it needs an adaption for the application of polymers. Input for the model are cutting force measurements. Also, cutting temperature measurements are given for the validation of the thermal model.

The influence of changing cutting conditions is described in Chapter 3. The thermal model is used here for visualizing the temperature contours. Besides the adaption of cutting parameters, also the influence of the thermo-mechanical history, and the crosslink density of a polymer is investigated. The achieved surface qualities will be described.

In Chapter 4 tribo-electric tool wear is described. Besides measurements of electrostatic charging, luminescence observations are presented. It is described when tribo-electric tool wear can be dominant in diamond turning of polymers.

Another possible dominant diamond tool wear mechanism, tribo-chemical wear, will be described in Chapter 5. Also, it presents tool wear rates, estimated from measurements. Several wear patterns for different polymers are shown in this chapter. A description and calculation of the possible chemical wear reactions are presented at the end of this chapter.

Conclusions and recommendations about the diamond turning process of polymers are given in Chapter 6.

Chapter 2

Properties of polymer turning

Current literature on polymer turning e.g. [21, 44] states that the most important aspect for achieving an optical surface quality in polymer turning is the adiabatic heating in the primary shear zone. If the temperature rise is enough for reaching T_g, a more ductile chip should be formed and a good surface quality should result from this.

Smith [44] made some estimates of the temperature rise in the primary shear zone. However, she did not make any force measurements. This chapter will first discuss some differences between metal and polymer turning. Then some force measurements for different polymers are presented, which will be used in a thermal model. The thermal model is derived from metal cutting, but is adapted for the polymer turning process.

The thermal model will be used in Chapter 3 for investigating the influence of cutting parameters on the temperature rise in the primary deformation zone.

2.1 Differences between metal and polymer turning

Cutting temperatures Perhaps the first thing that comes to mind about differences between polymers and metals is the difference in melting temperatures. Metals generally have a melting temperature in excess of 500 °C, while glassy polymers generally have a melting, or better said a thermal flow temperature, around 250 °C (PS respectively PC has a thermal flow temperature of approximately 200 °C respectively 300 °C).

Figure 1.10 showed that when T_g is reached, the rubber plateau is reached. This can be considered as a temperature region where the polymer is in a softened state and can be more easily deformed. It is this region that is generally assumed to be reached in polymer turning, see references [21, 44], and not the melt temperature.

Better surface qualities can be achieved when a ductile chip is produced during turning [28]. Since polymers are more susceptible to plastic deformation close to the glass transition temperature, surface qualities should improve when the cutting temperature reaches T_g. In Smith's research [44] it was concluded that an increase in cutting speed, and therefore an increase in adiabatic heating in the cutting zone mostly led to a better surface roughness for PS and PMMA, but not for PC. The latter has the highest glass transition temperature and the adiabatic heating could not reach T_g. Smith made an estimate of the temperature rise in the shear zone using Boothroyd's model [63], although she did not perform force measurements. She used three amorphous polymers, PS, PMMA and PC, all having different glass transition temperatures. The cutting conditions and results are summarized in Table 2.1.

Table 2.1: Estimates of temperature rise by Smith [44].

Smith's set	$v_c/(\mathrm{m \cdot s^{-1}})$	R/mm	$f/(\mathrm{\mu m \cdot rev^{-1}})$	$h/\mathrm{\mu m}$	Temperature rise in		
					PS	PMMA	PC
1	0.3	3.175	50.80	12.7	59 K	50 K	70 K
	1.5	3.175	50.80	12.7	91 K	88 K	92 K
2	0.3	0.762	50.80	12.7	64 K	64 K	65 K
	1.5	0.762	50.80	12.7	97 K	97 K	103 K
3	0.4	0.762	10.16	12.7	42 K	25 K	23 K
	4.0	0.762	10.16	12.7	88 K	85 K	87 K
	10.0	0.762	10.16	12.7	96 K	100 K	105 K
5	0.4	0.762	3.81	12.7	7 K	5 K	1 K
	4.0	0.762	3.81	12.7	73 K	66 K	68 K
	10.0	0.762	3.81	12.7	91 K	90 K	94 K

It can be seen in this table that for some materials and conditions the predicted temperature rise is close to T_g. Notice however, that all calculated temperatures are well below the thermal flow temperatures of these polymers, which are around or above 200 °C. It can therefore be concluded that all polymers and metals are cut by plastic deformation and not by a thermal viscous flow.

Cutting forces Another important difference between metals and polymers is their difference in initial yield stress. For non-ferrous metals initial yield stresses are typically more than 100 MPa and for glassy polymers typically less than 100 MPa. Table 2.2 on page 34 shows the initial yield stresses (σ_y) of several glassy polymers.

It was described in Section 1.3.2 that the value of the initial yield strength of a polymer is dependent on its thermo-mechanical history. The consequences of the thermo-mechanical history of the polymer on the cutting behaviour will be discussed in Chapter 3.

Tool wear During metal cutting a built-up edge (BUE) may form. The work-piece material that builds-up, will strain harden and heavily stick/adhere to the diamond tool. At some point this BUE will become unstable and may damage the diamond tool by a fracture of the tool material. BUE formation is ascribed to strong strain hardening, high friction and possible other factors [18]. It is assumed, since glassy polymers generally show strain softening prior to strain hardening, that tool wear due to unstable BUE formation will not appear in polymer turning. Also, it was not observed during this research.

Abrasive tool wear may occur in diamond turning of some metals such as copper [66]. When polymers containing hard abrasive particles are diamond turned, they might show abrasive tool wear. Budinski reports such wear on steel dies [67].

For the diamond tools used in precision turning it is known that high temperatures (> 500 °C) are needed for thermal wear to occur [68, 69]. Since polymers have a lower thermal flow temperature than metals it is expected that thermal tool wear does not play an important role in the wearing process of the diamond tool. Ferrous metals cannot be cut, because of the affinity of carbon (C) with iron (Fe), which is a carbide former [20, 65, 70]. This results in a dramatic diamond tool wear. Glassy polymers do not contain such carbide formers and therefore this kind of chemical tool wear cannot occur.

A big difference between metals and polymers is the electrical conductivity. Polymers are electrical insulators. Since the used natural diamond tool is an electrical insulator as well, static electrification may occur during diamond turning of polymers. Tribo-electric tool wear can generally be assumed to be absent in metal cutting.

Carr and Feger [21] mentioned that the diamond tool wear can be five to ten times as high in polymer turning than in copper turning during the same conditions.

Energy dissipation In metal cutting it is generally assumed that in the deformation zone approximately 100% of the mechanical work is converted into heat [31]. However, for polymers lower values are known. Adams and Farris [71] found values of only 50-80% of the work of deformation being dissipated as heat. The remainder of the work is being stored in the material as a change in internal energy. They found that the amount of work to heat conversion was strain rate dependent. However, values differ in literature between different researchers, as can be read in [53] and [72].

In Godovsky [72] possible contributions of energy storage in amorphous polymers are given. These storage mechanisms in polymers can be more diverse than in metals and can be summarized as:

1. Mechanism of internal dissipation. It can be described as energy needed to overcome intermolecular attraction forces between the polymer chains. It consist e.g. of disrupture of hydrogen bonds and change of conformation.

2. Entropy changes. Deformation results in polymer orientation, which means that energy is used to decrease the entropy of the system.

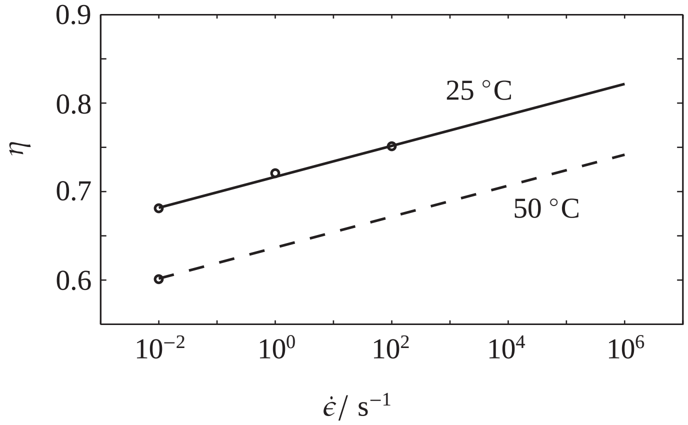

Figure 2.1: Heat dissipation factor for PMMA after Boyce et al. [73]. (o) Data from Boyce et al. The solid line is the fit and extrapolated line for 25 °C, and the dashed line is the shifted line from 25 °C to 50 °C.

In general, conversion rates in literature are given for relatively low strain rates ($10^{-6} - 10^{-3}$ s^{-1}) compared to the strain rates that occur in precision turning. Therefore the research of Boyce et al. [73] is used. In this research relatively high strain rates of deformation are investigated, namely up to 10^{2} s^{-1}. It is described that the amount of dissipation is dependent on strain, strain rate and temperature. In fact, the amount of dissipation increases with increasing strain rate and decreases with increasing temperature and strain.

Figure 2.1 shows data derived from [73] for PMMA at a true strain of 1.0 and at different strain rates and different temperatures. It also shows the fitted least-squares curve for 25 °C which has been extrapolated to higher strain rates as encountered in precision turning (> 10^{6} s^{-1}).

It will be shown later by measurements (Section 2.4) that a work to heat ratio of $\eta = 0.5$ can be assumed during diamond turning of polymers. This value differs from the extrapolated value of $\eta = 0.85$ derived from the research of Boyce et al. [73] in Figure 2.1.

Summary Several differences can be expected between metal and polymer turning. Although a brief description is given of these differences, this research does not try to resolve these differences, but tries to find a better understanding of the diamond turning process of glassy polymers. The main problem in this description is the occurring cutting temperature that determines whether cutting is performed in the solid state or in the thermal flow regime.

The next section deals with the cutting forces in polymer turning. These are necessary for the heat input for the used model in Section 2.3.

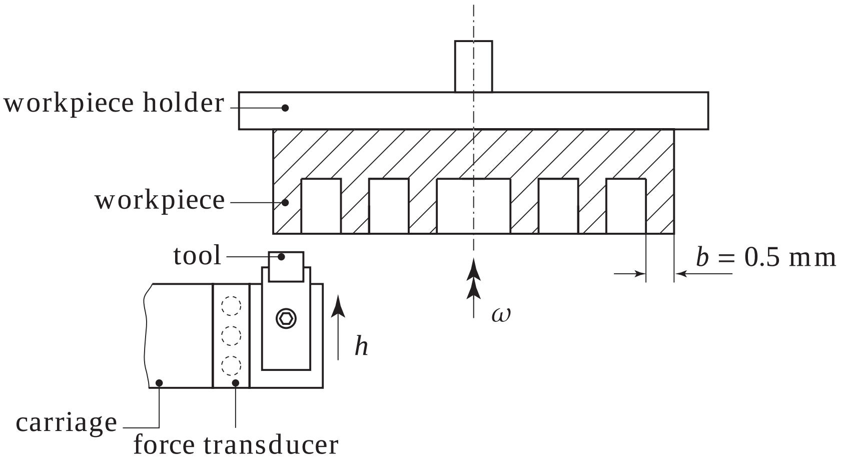

Figure 2.2: Schematic representation of the used cutting setup for force measurements.

2.2 Cutting forces in polymer turning

In literature on diamond turning of polymers, e.g. [21, 44, 74, 75], only little references are found with cutting force data. Since force data are required for the analytical estimation of cutting temperatures in Section 2.3, force measurements have been performed.

Setup The measurement data are obtained by cutting the polymers with a faceted, mono-crystalline diamond tool, rake angle $\alpha = 0°$ and clearance angle $\gamma = 15°$. The cutting forces were measured using a three-component Kistler dynanometer (type 9251A) in plunge turning conditions, see Figure 2.2. The following cutting conditions were used: cutting speed $v_c = 0.3$ m/s, depth of cut $h = 10\ \mu$m and width of cut $b = 0.5$ mm. Dry cutting was applied. Also, the chips were collected for measuring the chip length, necessary for determining the chip compression ratio.

Results The results of these measurements can be found in Table 2.2, where the main cutting force F_c, thrust force F_t and resultant cutting force F_R are given (see also Figure 1.6). The resultant cutting force F_R was determined using Equation 1.7. The result of PMMA is in agreement with the value of the specific cutting force found in literature [76].

The reciprocal of r_c is the chip compression ratio. The value of r_c can be found as:

$$\frac{1}{r_c} = \frac{h_c}{h} = \frac{L}{L_{chip}} = \frac{v_c}{v_{chip}} \tag{2.1}$$

Table 2.2: Measured cutting forces during diamond turning of several polymers (v_c = 0.3 m/s, h = 10 μm and b = 0.5 mm).

Material	σ_y/MPa	F_c/N	F_t/N	F_R/N	r_c
PS	100	1.27	0.64	1.91	0.57
PMMA	115	2.46	0.63	3.09	0.67
PC	70	2.20	1.35	3.55	0.61
PSU	75	2.10	1.42	3.52	0.50

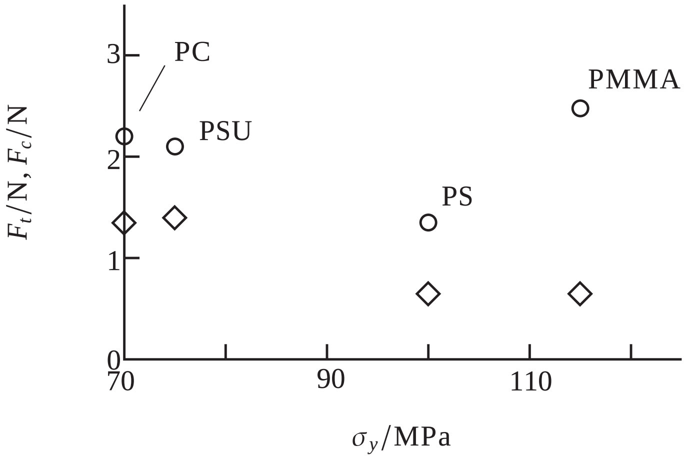

Figure 2.3: Graphical representation of main cutting force F_c (o) and thrust force F_t (◇) versus initial yield strength σ_y.

with h_c chip thickness, h depth of cut, L length of cut, L_{chip} length of the deformed chip, v_c cutting speed and v_{chip} speed of the chip.

Figure 2.3 shows the measured main cutting force F_c (o) and thrust force F_t (◇) in respect to the initial yield stress σ_y known from literature for these polymers [57]. It can be seen that there is no linear relationship between cutting forces and initial yield stress. This is also known from Drescher's research on specific cutting forces [4]. He states that it is not only the initial yield stress that is important for the (specific) cutting force, but the combination of material ductility and strength. In this thesis, the relation between the mentioned combination and specific cutting forces was not investigated.

2.3 Thermal model of the polymer turning process

2.3.1 Introduction

Section 1.4 described in short what is known about the diamond turning process of polymers. Based on this literature it can be said that polymer turning is performed in the thermal flow regime. Smith [44] made an estimate of the temperature rise in the primary deformation zone by application of Boothroyd's model [63]. She made the following assumptions:

1. No cutting forces were measured, therefore an estimate was made based on the hardness of the polymers multiplied by the cross-section of the undeformed chip.

   Using Smith's hardness values for PS, PMMA and PC, given as 155, resp. 199 and 186 MPa, the following cutting forces can be derived for a cross-section of the uncut chip of 0.5 mm × 0.010 mm: 0.78 N resp. 1.0 N and 0.93 N. Looking at the measured values in this research, the estimated values given by Smith [44] seem to be underestimated.

2. The friction force on the rake face is estimated as $F_f = \mu F_c$ with $\mu = 0.2$. The cutting force was derived from the hardness as described before. The value of 0.2 lies in the range of friction coefficients for diamond mentioned in Wilks and Wilks [69]. Therefore, this seems a reasonable assumption. From the force measurements in this research and Equation 1.10 for the calculation of the friction force, the following $\mu = F_f/F_c$ is derived for PS, PMMA, PC and PSU: 0.50, 0.27, 0.61 respectively 0.68. This could mean that the assumed friction coefficient was too low in Smith's research.

3. Smith used Boothroyd's thermal model, which incorporates Weiner's solution for the estimation of the fraction of heat B that is conducted into the workpiece. Using Smith's set 2 conditions, see Table 2.1, with $v_c = 0.3$ m/s, a heat partition fraction of approximately 0.4 can be estimated. Section 2.3.2 will show that the fraction of heat conducted into the workpiece for the given cutting speed of 0.3 m/s is approximately $B = 0.2$ for polymers. Therefore, Smith overestimated the heat partition fraction, resulting in an overestimate of the temperature rise.

4. A mean undeformed chip thickness is assumed. However, a radius tool is used, implying a changing chip thickness over the cutting zone, see Figure 1.2. This may have overestimated the calculated temperature rise values.

5. A conversion of mechanical work to heat of 100% is assumed. As described in Section 2.1 a conversion of 50% can be assumed for polymers in diamond turning applications. This indicates that she overestimated her temperature rise with this assumption as well.

The influence of the work to heat ratio η is not considered in Smith's research [44]. Therefore, it was thought that temperature rise values may have been significantly different than those calculated by Smith. The research of Komanduri and Hou [77, 78, 79] is used at the base of this research. Their research considers the effects of two heat sources in the cutting process:

1. The heat generated in the primary shear zone, and
2. The heat generated at the rake face caused by friction between chip and rake face.

The model will be made applicable for polymer turning by using the assumed dissipation factor η given in Section 2.1. Then verification experiments will be presented for the validation of the adapted model.

2.3.2 Shear plane temperature

Smith used Boothroyd's model for estimating the temperature increase in the deformation zone. However, most thermal models for cutting, including Boothroyd's, assume the material on either side of the shear zone as two separate bodies in sliding contact. This is of course not the case, since the material in front and behind the shear (heat) zone is the same. The main differences in thermal models are the used assumptions, such as the nature of the heat source, the estimation of the heat partition fraction, the direction of the motion of the heat source and the applied boundary conditions. For a good summary of the many models that are known and their pros and cons the reader is referred to Komanduri and Hou's research [77].

Model

The heat generated at the shear zone is considered as an oblique moving band heat source with the uncut surface. Komanduri and Hou [77] use an adapted model from Hahn [80], which will further be referred to as "Hahn's model". The model is depicted in Figure 2.4(a).

Shown is a moving coordinate system with $X - z$ axes. This model assumes that the moving band heat source $\overline{oA}$ of length L is divided into infinitely small differential segments dl_i. Each of these segments is considered as an infinitely long moving line heat source (i.e. perpendicular to the plane of the drawing). The solution for calculating the temperature rise at any point M, caused by a differential segment dl_i is [81, 82]:

$$\Theta_M = \frac{\dot{q}_l}{2\pi\lambda} e^{-X_i v/2\kappa} \cdot K_0\left(Rv/2\kappa\right) \tag{2.2}$$

where Θ_M is the temperature rise in any point M, expressed by the coordinates of the moving coordinate system at time t, of the coordinate system given in Figure 2.4(a). X_i is the projection of the distance R in the direction of motion, v the speed of the moving heat source (here $v = v_c$), κ the thermal diffusivity, λ the thermal conductivity and $\dot{q}_l$ the heat generation intensity, i.e. the amount of heat generated in the primary shear zone by the cutting action. K_0 is the modified Bessel function of the second kind and order zero. Equation 2.2 is the solution for steady-state conditions, which are reached in cutting in approximately 0.1 s for

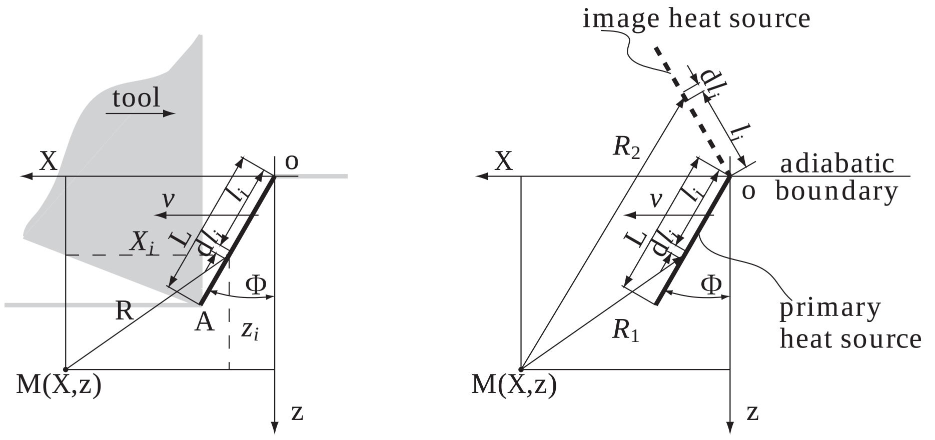

(a) (b)

Figure 2.4: Figure (a) shows the schematic of an oblique moving heat source $\overline{oA}$ in an infinite medium. Figure (b) shows the application of an image heat source when an adiabatic boundary is present.

continuous chip formation [77]. Therefore this equation can be used as the base of the thermal analysis of the cutting process.

However, the equation has to be adapted for the amount of mechanical work that is converted into heat, defined by $\eta = \frac{\text{amount of heat generated}}{\text{amount of work done}}$. Then Equation 2.2 becomes:

$$\Theta_M = \eta \cdot \frac{\dot{q}_l}{2\pi\lambda} e^{-X_i v/2\kappa} \cdot K_0\left(Rv/2\kappa\right) \tag{2.3}$$

Consider a segmental oblique moving line heat source as depicted in Figure 2.4(a). Using Equation 2.3, the heat generation intensity of this heat source $\dot{q}_l = \dot{q}_{pl} \cdot dl_i$. When the heat source is positioned at an angle Φ, the distance R between point M and the segmental line heat source is given by

$$R = \sqrt{(X - l_i \sin\Phi)^2 + (z - l_i \cos\Phi)^2} \tag{2.4}$$

The projection of R on the X-axis is then

$$X_i = X - l_i \sin\Phi \tag{2.5}$$

The temperature rise at any point $M(X, z)$ caused by any of the segmental line heat sources can then be derived by substituting Equations 2.4 and 2.5 into 2.3. This results in

$$d\Theta_M = \eta \cdot \frac{\dot{q}_{pl}\, dl_i}{2\pi\lambda} e^{-(X - l_i \sin\Phi)v/2\kappa} \cdot K_0\left[\frac{v}{2\kappa}\sqrt{(X - l_i \sin\Phi)^2 + (z - l_i \cos\Phi)^2}\right] \tag{2.6}$$

From this the temperature rise at any point M for the entire oblique moving heat source can be determined as

$$\Theta_M = \eta \cdot \frac{\dot{q}_{pl}}{2\pi\lambda} \int_{l_i=0}^{L} e^{-(X-l_i \sin\Phi)v/2\kappa} \cdot K_0 \left[\frac{v}{2\kappa} \sqrt{(X - l_i \sin\Phi)^2 + (z - l_i \cos\Phi)^2} \right] dl_i \quad (2.7)$$

This equation is Hahn's solution for an oblique plane heat source moving in an infinite medium. However, in orthogonal machining the shear plane heat source is moving in a semi-infinite medium with the work surface and the chip surface being the boundaries of the semi-infinite media. Therefore, Hahn's oblique moving heat source solution has to be modified with consideration of the boundaries.

The uncut surface of the workpiece and the free side of the chip can be considered as adiabatic boundaries in the (dry!) turning process. This means that no heat is lost at these surfaces. Looking at Hahn's model applied to the cutting process, this means that at the adiabatic boundary of the semi-infinite body an image heat source with the same heat generation intensity can be applied, see Figure 2.4(b). Using this figure, the following solution for the temperature rise at any point M caused by moving heat source and image heat source can be derived:

$$\Theta_M = \eta \cdot \frac{\dot{q}_{pl}}{2\pi\lambda} \int_{l_i=0}^{L} e^{-(X-l_i \sin\Phi)v/2\kappa} \cdot \left[K_0 \left(R_1 v/2\kappa \right) + K_0 \left(R_2 v/2\kappa \right) \right] \, dl_i \quad (2.8)$$

and

$$R_1 = \sqrt{(X - l_i \sin\Phi)^2 + (z - l_i \cos\Phi)^2}, \text{ and } \quad R_2 = \sqrt{(X - l_i \sin\Phi)^2 + (z + l_i \cos\Phi)^2} \quad (2.9)$$

When Hahn's model is being applied to the cutting process, the problem is split up in two separate problems. This is depicted in Figure 2.5. Figures (a) and (c) show the moving shear plane heat source for the workpiece part respectively the chip part. Although a separation is made in the calculations, the oblique moving band heat source model considers the material in front and behind the heat source as a continuous body. To achieve this an imaginary part $\overline{eocd}$ is introduced in Figures 2.5(b) and (d).

Figures 2.5(a) and (b) show the shear plane heat source moving continuously with the cutting velocity v_c at an oblique angle $\Phi = -(90 - \varphi)$. Figures 2.5(c) and (d) show the shear plane heat source moving continuously with the chip velocity v_{chip}, but in opposite direction with the chip. It moves at an oblique angle, defined as $\Phi = (\varphi - \alpha)$.

By applying the correct boundary conditions and subsequently the correct image heat sources, the temperature rise can be determined for polymeric materials.

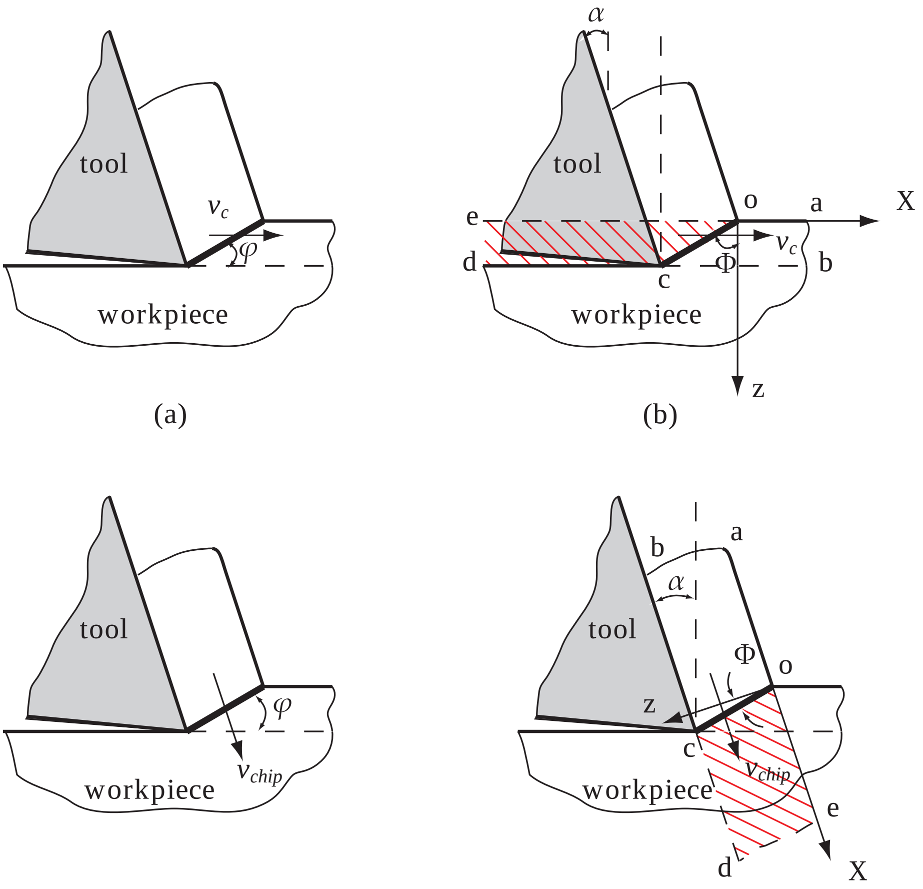
tool
v_c
φ
workpiece
α
tool
e
o
a
X
v_c
d
Φ
b
c
workpiece
z
tool
φ
v_{chip}
workpiece
b
a
α
tool
Φ
o
z
c
v_{chip}
workpiece
e
d
X

(a) (b)

(c) (d)

Figure 2.5: Schematics of Hahn's oblique moving heat source model for continuous chip formation, from [77].

Thermal model applied to polymer turning

The cutting force data of Table 2.2 and the equations of Section 1.2.3 have been used for the determination of the input for the thermal model. The shear angle in cutting can be determined by the relation

$$\tan\varphi = \frac{h\ \cos\alpha}{h_c - h\ \sin\alpha} \tag{2.10}$$

For zero rake angle this equation becomes $\tan\varphi = h/h_c$. The heat generation intensity of the heat source is defined as $\dot{q}_{pl} = F_s v_s/(L_s \cdot b)$ with F_s, v_s, L_s and b the shear force, shear velocity, length respectively width of the shear plane. For the analysis of the temperature rise in the chip, the chip velocity is determined by $v_{chip} = r_c \cdot v_c$. Using the cutting force data from Table 2.2 the parameters for the thermal model were determined and they are given in Table 2.3.

Using this cutting data, the temperature rise isotherms of Figure 2.6 were

Table 2.3: Input for thermal model of shear plane temperature distribution.

	PS	PMMA	PC	PSU
v_c	0.26 m/s	0.28 m/s	0.27 m/s	0.27 m/s
h	10 μm	10 μm	10 μm	10 μm
b	0.5 mm	0.5 mm	0.5 mm	0.5 mm
φ	30°	34°	31°	27°
r_c	0.57	0.67	0.61	0.50
L_c	50 μm	80 μm	30 μm	50 μm
$L = L_s$	20.2 μm	18.0 μm	19.2 μm	22.4 μm
η	0.5	0.5	0.5	0.5
$\dot{q}_{pl}$	$2.3 \cdot 10^7$ W/m^2	$6.4 \cdot 10^7$ W/m^2	$3.9 \cdot 10^7$ W/m^2	$3.4 \cdot 10^7$ W/m^2

made by calculating the temperature rise for workpiece and chip separately and combining the plots without the imaginary parts. The thermal properties of the polymers have been corrected for the temperature increase. In [83] the following relation for change of heat capacity with temperature for solid polymers is given:

$$\frac{1}{c_s(298)}\frac{dc_s}{dT} = 3 \cdot 10^{-3} \tag{2.11}$$

with c_s the heat capacity for the solid polymer. This relation is based on mean values derived for several polymers. For polymers above T_g the following mean relation holds:

$$\frac{1}{c_l(298)}\frac{dc_l}{dT} = 1.2 \cdot 10^{-3} \tag{2.12}$$

with c_l the heat capacity of the polymer above T_g. The heat capacity can be used for determining the heat conduction of the polymer as:

$$\lambda = \rho \cdot c \cdot u \cdot L_{thermal} \tag{2.13}$$

with u the velocity of sound in the material and $L_{thermal}$ the distance between adjacent thermal layers. For the thermal diffusivity the following relation holds

$$\kappa = \frac{\lambda}{\rho \cdot c} \tag{2.14}$$

It can be seen in Figure 2.6 that for all cases the glass transition temperature T_g is not reached during cutting. This indicates that for the given turning conditions no thermal flow regime is reached. Therefore, chip formation is also dominated by stress activated flow, which was described in Section 1.3.

It can also be seen that steep temperature gradients exist in front of the tool. This is the result of the low thermal diffusion of polymers. The heat affected zone is less than 30 μm below the cut surface. The maximum temperature behind the

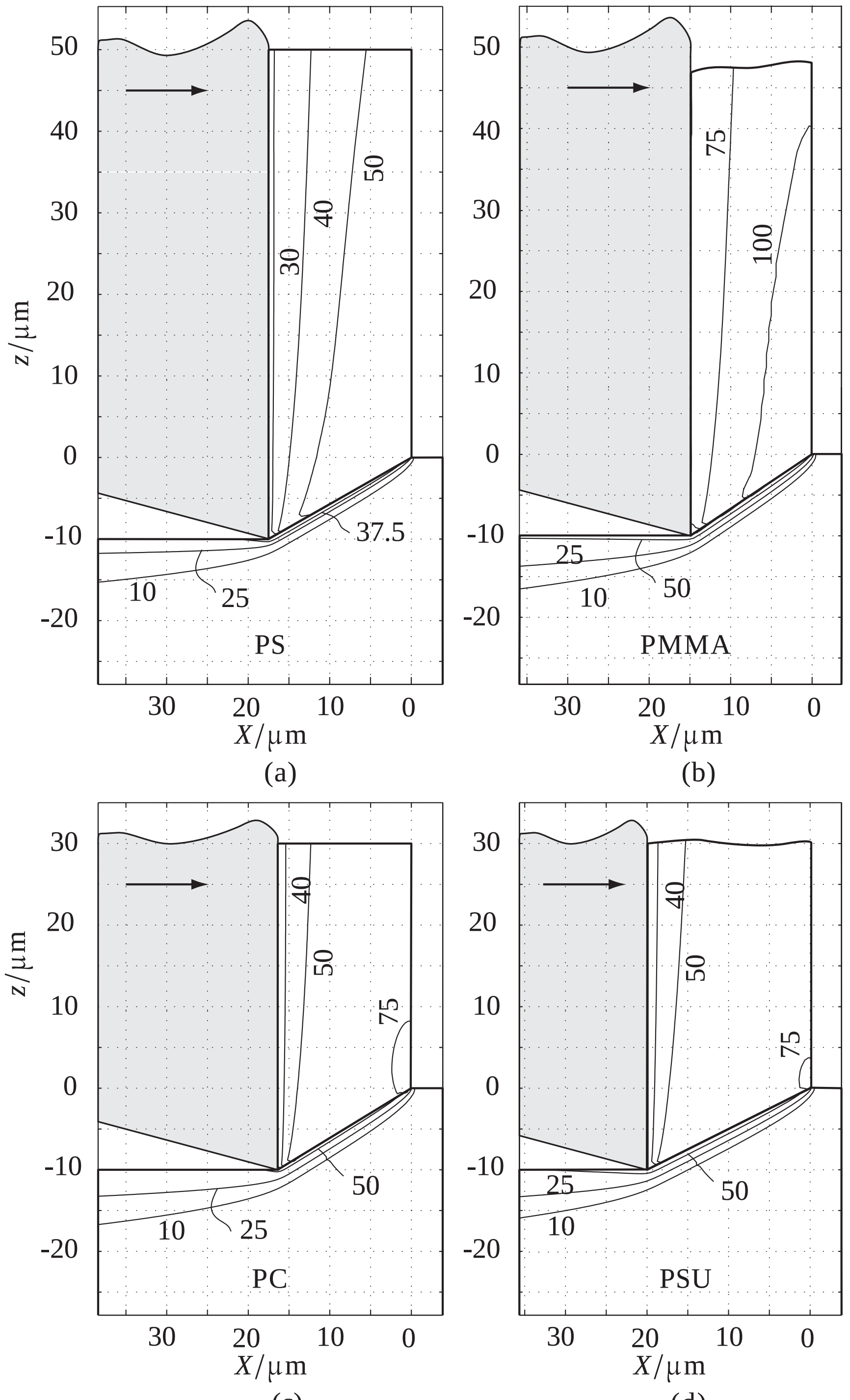

(a) (b) (c) (d)

Figure 2.6: Calculated temperature rise isotherms during polymer turning with $\eta = 0.5$, for (a) PS, (b) PMMA, (c) PC and (d) PSU ($v_c = 0.3$ m/s, $h = 10$ µm, $b = 0.5$ mm).

tool is not sufficiently high for thermal flow to occur behind the tool at the cut surface.

The calculated temperature rises in the chip are higher than those in the workpiece, which is mainly caused by the lower chip velocity. Notice that this is not interesting for determining whether cutting is performed in the solid or thermal flow regime. However, it can be interesting for tool wear research. It can also be seen that the isotherms in the chip at the shear zone do not totally overlap with the isotherms of the workpiece. This can also be seen in the research of Komanduri and Hou [77]. The reason is given by Komanduri and Hou [77] who indicate that this is caused by the non-uniform temperature distribution encountered in the chip during turning operations.

Heat partition fraction The use of the described thermal model does not require an *a priori* assumption regarding the partitioning of heat between workpiece and chip, although other models generally require this heat partitioning [77]. The calculated mean temperature rise in the chip ($\overline{\Theta}_{chip}$) can be used to calculate this heat partition fraction B of the workpiece and $(1-B)$ of the chip. Notice that the heat partition value obtained in this way, includes all the heat, namely by conduction and by heat energy flow due to material flow.

The mean temperature rise can be used to calculate the heat necessary for causing this temperature increase as:

$$\dot{Q} = \dot{m} \cdot c \cdot \overline{\Theta}_{chip} \tag{2.15}$$

with $\dot{Q}$ the heat rate, $\dot{m}$ the mass rate, c the heat capacity of the material (assumed to be constant), and $\overline{\Theta}_{chip}$ the mean temperature rise in the chip. This can be rewritten to the heat flux:

$$\dot{q} = \rho \cdot c \cdot v_{chip} \cdot \overline{\Theta}_{chip} \tag{2.16}$$

Then the heat partition fraction follows from:

$$B = 1 - \frac{\dot{q}}{\dot{q}_{pl}} \tag{2.17}$$

Using these equations for calculating the temperature rise in the chip, Table 2.4 was constructed.

Table 2.4: Calculated heat partition fractions.

Material	$\overline{\Theta}_{chip}$	B	$(1-B)$
PS	51 K	0.19	0.81
PMMA	80 K	0.24	0.76
PC	66 K	0.21	0.79
PC	66 K	0.22	0.78

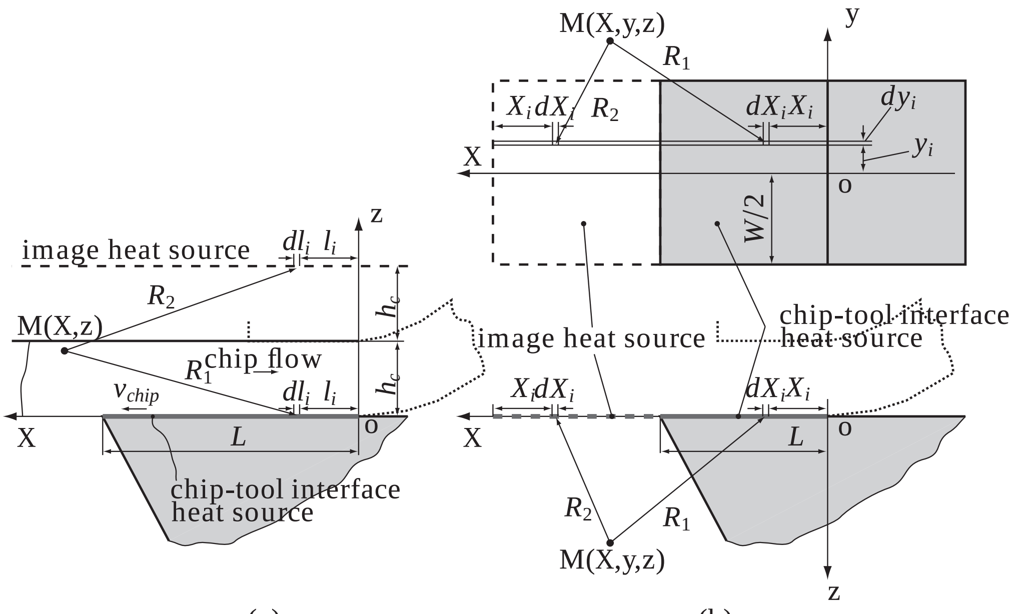
image heat source
dl_i
l_i
z
R_2
M(X,z)
h_c
chip flow
R_1
v_{chip}
dl_i
l_i
h_c
X
o
L
chip-tool interface heat source
M(X,y,z)
y
R_1
$X_i dX_i$
R_2
$dX_i X_i$
dy_i
y_i
X
o
$W/2$
image heat source
chip-tool interface heat source
$X_i dX_i$
$dX_i X_i$
X
L
o
R_2
R_1
M(X,y,z)
z

(a) (b)

Figure 2.7: Schematics showing the used model for calculating the effects of the frictional heat source at the chip-tool interface, from [78]. Figure (a) is used for the chip and (b) for the tool.

It can be seen in this table that the heat partition fraction *B* of the workpiece, i.e. the amount of heat conducted into the workpiece from the shear zone, is approximately 0.2. Approximately 80% of the heat produced in the shear zone is removed by the chip.

Looking at the values calculated by Komanduri and Hou [77] for diamond turning of aluminium (experimental data of Ueda et al. [84]), it can be seen that aluminium had a heat partition fraction of the chip of only 0.35, and this was even found for a cutting speed of more than 8 m/s! These results clearly indicate that during turning of polymers most of the heat generated in the primary shear zone is removed by the chip.

2.3.3 Temperature rise at the chip-tool interface

Model

Besides the heat generated in the primary shear zone, there is generally an additional heat source at the chip-tool interface. Because of friction between chip and rake face, see e.g. [18, 31], heat is generated in this zone. The solution of this heat problem changes, since we are now dealing with two different bodies: (1) the moving chip and (2) the stationary tool.

Figure 2.7(a) shows the model with appropriate coordinate system for the chip side. For the calculation of the temperature rise at the chip side, the same approach will be used as in the previous section. For the frictional heat source at the moving chip side, Jaeger's semi-infinite solution on an infinitely long moving line heat source is used [78, 81] for calculating the temperature rise, supplemented with the dissipation factor η:

$$\Theta_M = \eta \cdot \frac{\dot{q}_l}{\pi\lambda} e^{-X_i v/2\kappa} \cdot K_0 \left(Rv/2\kappa\right) \tag{2.18}$$

This equation for the differential temperature rise at any point $M(X, z)$ caused by the differential segmental line heat source, located at a distance l_i from the origin, is used for the calculation. Taking into account the image heat source, since the frictional heat source is located at the boundary of the body, the following relation is derived from [78] with addition of the work to heat conversion ratio η:

$$d\Theta_M = \eta \cdot \frac{\dot{q}_{pl}\, dl_i}{\pi\lambda} e^{-X_i v/2\kappa} \cdot \left[K_0 \left(R_1 v/2\kappa\right) + K_0 \left(R_2 v/2\kappa\right)\right] \tag{2.19}$$

where $\dot{q}_{pl} = \dot{q}_l\, dl_i$ and

$$R_1 = \sqrt{(X - l_i)^2 + z^2}, \quad \text{and} \quad R_2 = \sqrt{(X - l_i)^2 + (2h_c - z)^2} \tag{2.20}$$

Then the total temperature rise in the chip at any point $M(X, z)$ caused by the chip-tool interface frictional heat source and the appropriate image heat source is given by

$$\Theta_M = \eta \cdot \frac{\dot{q}_{pl}}{\pi\lambda} \int_{l_i=0}^{L} e^{-X_i v/2\kappa} \cdot \left[K_0 \left(R_1 v/2\kappa\right) + K_0 \left(R_2 v/2\kappa\right)\right]\, dl_i \tag{2.21}$$

For the stationary tool, Jaeger's stationary rectangular heat source solution is applied. Here the effect of the clearance face will be taken into account [78]. The interface frictional heat source is considered as a stationary rectangular heat source with width W and length L. Considering the heat partition fraction of the tool to be $(1 - B)$, then the heat generation rate $(1 - B)\dot{q}$ of the stationary rectangular heat source is considered to be transfered totally into the tool. Therefore, the interface is considered adiabatic and the solution used is that for a semi-infinite body. The semi-infinite solution is obtained by multiplying by two the value of the infinite solution.

Further, the clearance face should be considered adiabatic as well. Therefore an image heat source is used as depicted in Figure 2.7(b). The heat generation of this image heat source is the same as that of the frictional heat source.

The objective of the analysis is to determine the temperature rise at any point $M(X, y, z)$ in the tool. Referring to Figure 2.7(b), the chip-tool interface heat source of length L and width W and its image heat source can be considered as a combination of series of differential segmental line heat sources of width dy_i and length dX_i. Each segment $dX_i \times dy_i$ can then be considered as a point heat source with heat generation intensity $\dot{q}_{point}$ given by

$$\dot{q}_{point} = \dot{q}_0 \, dX_i \, dy_i/(L \cdot W) = \eta \cdot \dot{q}_{pl} \, dX_i \, dy_i \tag{2.22}$$

where $\dot{q}_0$ is the heat generation intensity for the rectangular heat source. The semi-infinite solution of a continuous point heat source is [78, 81]

$$\Theta = \frac{\dot{q}_{point}}{2\pi\lambda R} \tag{2.23}$$

Using this solution, the differential temperature rise at any point $M(X, y, z)$ caused by one of the point heat sources located at (X_i, y_i) is given by

$$d\Theta_M = \eta \cdot \frac{\dot{q}_{pl}}{2\pi\lambda}\left(\frac{1}{R_1} + \frac{1}{R_2}\right) dX_i \, dy_i \tag{2.24}$$

where

$$R_1 = \sqrt{(X - X_i)^2 + (y - y_i)^2 + z^2} \tag{2.25}$$

and

$$R_2 = \sqrt{(X - 2L + X_i)^2 + (y - y_i)^2 + z^2} \tag{2.26}$$

The total temperature rise at any point $M(X, y, z)$ in the tool caused by the whole stationary rectangular interface heat source and its image heat source is then given by

$$\Theta_M = \eta \cdot \frac{\dot{q}_{pl}}{2\pi\lambda} \int\limits_{y_i=-W/2}^{W/2} dy_i \int\limits_{X_i=0}^{L} \left(\frac{1}{R_1} + \frac{1}{R_2}\right) dX_i \tag{2.27}$$

for cutting with a sharp tool.

Considering Blok's heat partition principle [85], the calculated temperature rise on both sides of the interface should be the same. Using Equations 2.21 and 2.27 and considering $z = 0$, the local temperature rise can be calculated for both sides of the interface, using an assumed heat partition fraction B. An iterative procedure results in a correct value of B for equal average temperatures on both sides of the interface.

Application to PMMA

The model has been applied for PMMA with the cutting forces mentioned in Table 2.2. Table 2.5 summarizes the parameters used for the input of the thermal model.

By an iterative procedure, a heat partition fraction $B = 0.005$ is found for the PMMA chip and diamond tool combination. This seems a reasonable value if one considers that $\kappa_{polymer} << \kappa_{diamond}$. The calculated temperature rise for the moving chip and the stationary tool are given in Figure 2.8. It can be seen that the mean temperature rise is less than 0.5 K at the interface.

Table 2.5: Input for temperature rise calculations at the chip-tool interface for diamond turning PMMA.

Input for the chip-tool interface model	
$v_{chip} = v_c \cdot r_c$	0.19 m/s
$h_c = h/r_c$	15 µm
b	0,5 mm
φ	33.8°
$L = L_c$	80 µm
η	0.5
$\dot{q}_{pl} = F_f \cdot v_{chip}/(b \cdot h_c)$	$4.7 \cdot 10^6$ W/m^2

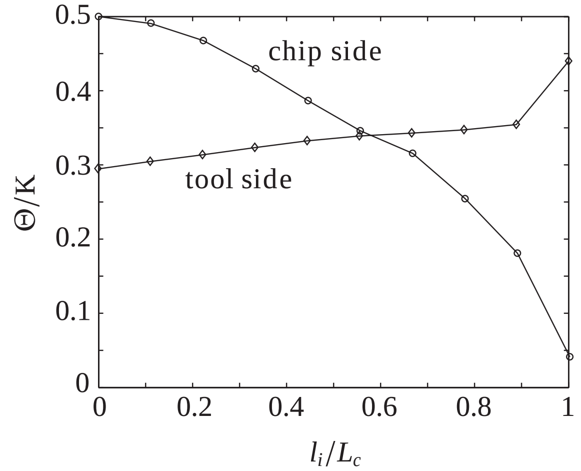

Figure 2.8: Calculated temperature rise at the chip-tool interface for the frictional heat source ($\eta = 0.5$).

The low temperature rise caused by the frictional heat source indicates that only little heat is transported here. From Tables 2.3 and 2.5 it becomes clear that the amount of heat generated at the chip-tool interface is only 7% of the heat generated at the primary shear zone. Based on this result, no further effort is put in shifting the local heat partition value for matching the temperature curves of the tool and the chip side, as was done by Komanduri and Hou in [78].

Since the frictional temperature rise is small compared to the temperature rise in the shear zone, this effect will be neglected. This is in agreement with Komanduri and Hou [79] who showed that in diamond turning generally the primary shear heat zone has the biggest contribution to the temperature rise in the tool. The next section describes the model used for determining the temperature rise in the tool.

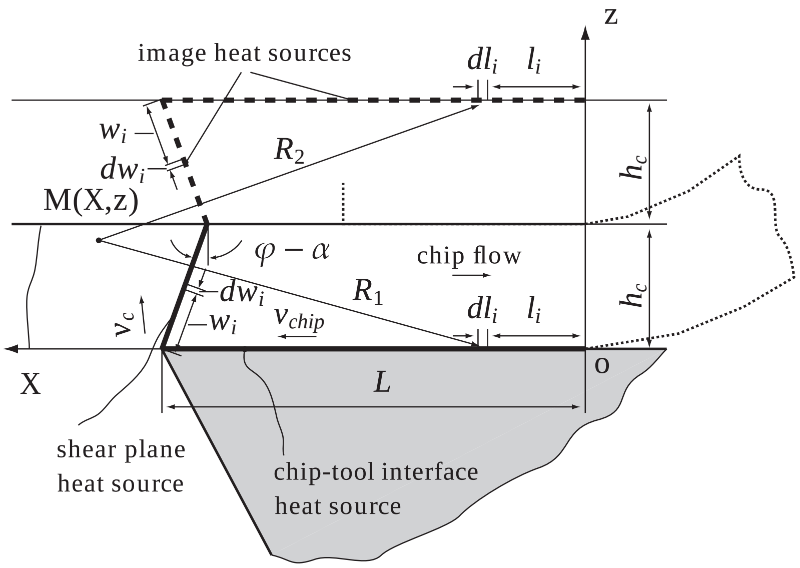
z
image heat sources
dl_i
l_i
w_i
dw_i
R_2
M(X,z)
h_c
$\varphi - \alpha$
chip flow
dw_i
R_1
w_i
v_{chip}
v_c
dl_i
l_i
h_c
X
L
o
shear plane
heat source
chip-tool interface
heat source

Figure 2.9: Schematic showing the used model for calculating the effects of the frictional heat source at the chip-tool interface, from [79].

2.3.4 Temperature rise in the diamond tool

The research of Komanduri and Hou [79] described the combined effect of shear plane heat source and frictional heat source. For diamond turning of PMMA, and probably for most polymers, the temperature rise caused by the frictional heat source can be neglected, as was shown in Section 2.3.3. Therefore, the model presented in this section is simplified for the application of polymer turning.

Model applied to diamond turning of PMMA

For ease of application, the model given in Section 2.3.2 will be given in another coordinate system, see Figure 2.9.

The temperature rise at any point $M(X, z)$ in the chip, including the points along the chip-tool interface, using the solution of an infinitely long moving line heat source for an infinite medium was given by Equation 2.8. In Section 2.3.3 it was shown that the frictional temperature rise at the chip-tool interface was less than 1 K. Therefore, this temperature rise will be neglected for the calculation of the temperature rise in the chip. For the new coordinate system it can be derived that the temperature rise for any point $M(X, z)$ in the chip, neglecting the frictional heat source, is given by:

$$\begin{aligned}\Theta_M \quad &= \eta \cdot \tfrac{\dot{q}_{pls}}{2\pi\lambda} \int_{w_i=0}^{h_c/\cos(\varphi-\alpha)} e^{-(X-X_i)v/2\kappa} \cdot \Bigl\{ K_0\Bigl[\frac{v}{2\kappa}\sqrt{(X-X_i)^2+(z-z_i)^2}\,\Bigr] \\ &\qquad + K_0\Bigl[\frac{v}{2\kappa}\sqrt{(X-X_i)^2+(2h_c-z-z_i)^2}\,\Bigr]\Bigr\}\, dw_i \end{aligned} \tag{2.28}$$

where η is the work to heat conversion ratio and $\dot{q}_{pls}$ is the heat generation of the shear plane. Further,

$$X_i = L_s - w_i \sin(\varphi - \alpha) \quad \text{and} \quad z_i = w_i \cos(\varphi - \alpha)\ . \tag{2.29}$$

Although the shear zone can be considered as a moving heat source for the calculation of the temperature rise in the chip, this is not the case for the calculation of the temperature rise in the tool. The reason for this is that the shear zone has to be considered as a stationary heat source in respect to the tool. Therefore, the above equations cannot be used for the calculation of the temperature rise in the tool, since they are based on a moving heat source.

A heat transfer method for the calculation of the temperature rise in the tool, caused by the shear plane heat source, is to consider that part of the heat coming from the shear plane heat source through the chip and the chip-tool interface into the tool, acting as a stationary heat source located at the chip-tool interface. This heat source can then be considered as an induced stationary rectangular heat source [79].

The total temperature rise at any point $M(X, z)$ in the tool caused by the induced heat source is given by [79]:

$$\Theta_M = \frac{B_{ind} \cdot \dot{q}_{pli}}{2\pi\lambda} \int_{y_i=-W/2}^{W/2} dy_i \int_{X_i=0}^{L} \left(\frac{1}{R_1} + \frac{1}{R_2}\right) dX_i \tag{2.30}$$

where R_1 and R_2 are given by Equations 2.25 and 2.26, and $X_i = l_i$. B_{ind} is the fraction of heat flow to the tool caused by the induced heat source, and $\dot{q}_{pli}$ is the average intensity of the induced heat source.

Initially, the heat intensity $\dot{q}_{pli}$ of this induced heat source is unknown. But the average temperature at the chip-tool interface is known from Equation 2.28. Assuming that $B_{ind} = 1$, the computer program that was developed for the calculations of Section 2.3.3 can be used for the calculation of the average intensity of the induced heat source $\dot{q}_{pli}$, and it was found to be $3.0 \cdot 10^8$ W/m^2.

Due to continuity of the heat flow, the mean temperature on chip side and tool side have to be the same, resulting in an estimate of B_{ind}. It was found that the best fit occurs when $B_{ind} = 1$. No better distribution can be found by the application of non-uniform distributions. The average temperature rise at the tool/chip interface is found to be 52 K.

Using these values, the isotherms of the temperature rise in the tool can be calculated, see Figure 2.10.

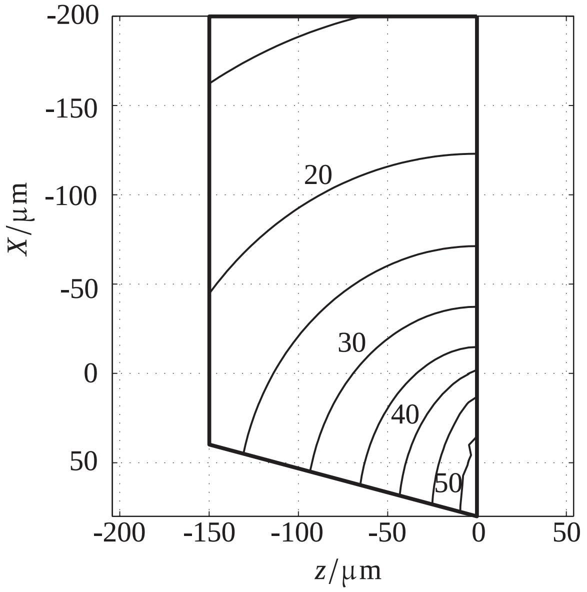

Figure 2.10: Isotherms of the temperature rise in the tool during diamond turning of PMMA with $v_c = 0.3$ m/s, $h = 10$ µm and $b = 0.5$ mm.

It can be seen that a maximum temperature rise of approximately 50 K occurs near the cutting edge. Further, a steep temperature gradient can be seen in the diamond tool, which is in accordance with the high thermal diffusivity of diamond ($4 - 11$ cm^2/s). These low temperatures indicate that thermal wear is not an issue in polymer turning.

2.4 Experimental verification

In the previous section the analytical temperature rise in diamond turning of PMMA was determined. To verify the adapted thermal model, temperature measurements were performed.

2.4.1 Development of a tool with embedded thermocouple

Diamond has a high thermal conductivity. In diamond, thermal conductivity is caused by lattice vibration, instead of electron transport as is the case in metals [86, 87]. Diamond conducts heat very quickly and this makes it an interesting material for applications where a high heat conduction is needed. Therefore, it is believed that diamond is a very good material for a tool with an embedded thermocouple, since a short time constant can be achieved and a stable temperature profile in the tool can be achieved quickly.

For the production of dies for the wire-drawing industry holes are drilled in diamond by excimer laser technology. These holes have the shape of a cone. For

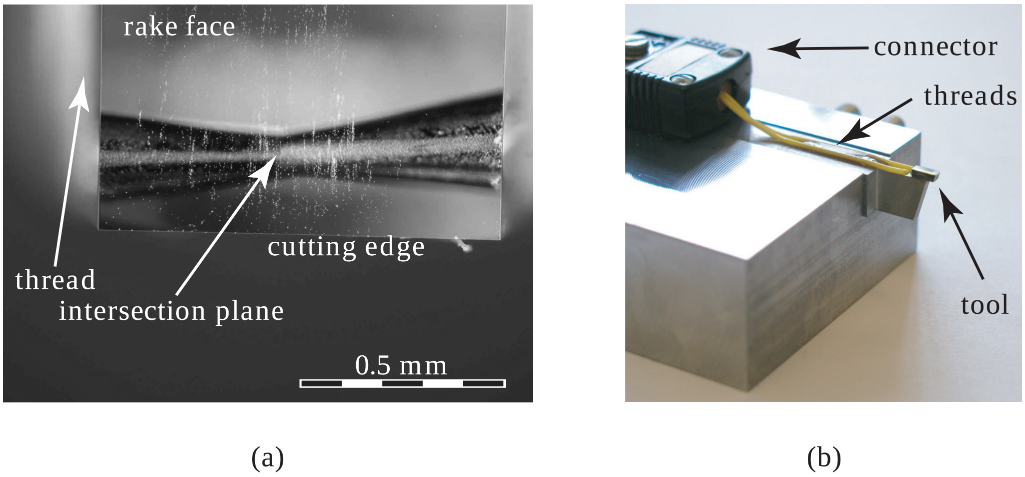

(a) (b)

Figure 2.11: (a) Dark field photo of the diamond tool with embedded thermocouple, and (b) shows the assembly of the tool.

the production of the embedded thermocouple tool a synthetic mono-crystalline diamond tool was used. A faceted tool geometry was chosen in order to get a good two dimensional heat profile in the tool. Figure 2.11(a) shows a dark field microscope photo of the developed diamond tool with embedded thermocouple. For the placement of the thermocouple, holes were drilled from both side faces of the tool and the cones intersect in the middle of the tool. In this intersection plane a J-type thermocouple is placed and fixed by a thermally conductive epoxy. The diameter of the threads of the thermocouple is 25 μm and the junction is approximately 75 μm. In the photo the two cones are clearly visible, intersecting each other almost in the middle of the tool. The smallest diameter of the hole is approximately 100 μm, positioned at approximately 200 μm from the cutting edge and approximately 150 μm under the rake face. Out of focus are the two leads at the side faces of the tool. Also visible is some dust on the rake face. Because the threads of the thermocouple are fragile they are led to a connector near the tool, see Figure 2.11(b). From this connector a connection is made to a data-acquisition system. A calibration method is necessary to estimate the error that originates from the distance between cutting edge and thermocouple. This can be found in Appendix D. It is described in the appendix that the calibration has to be performed on a material with approximately the same thermal properties as those of the workpiece material to be cut. This was done prior to the measurements.

2.4.2 Verification experiments

The embedded thermocouple is used for the verification measurements of the thermal cutting model described in Section 2.3. Table 2.6 shows the measured temperatures during turning of PS, PMMA and PC, with the error estimation of the fit found by the calibration procedure. It shows the calculated temperature rise at the chip/rake interface and the shear zone for a work to heat conversion ratio $\eta = 0.5$ too. The fifth column shows the ratio of measured temperature rise and the calculated temperature rise for $\eta = 1$, which is equal to $2 \cdot \Theta_{\eta=0.5}$.

The value in the fifth column indicates how good the assumption of $\eta = 0.5$ was. Taking into account the error of the calibration data for the actual temperature measurement, for PS and PMMA a reasonable agreement is found between calculation with $\eta = 0.5$ and thermocouple measurement. For PC, a relatively high value of η is found, compared to PS and PMMA. Notice that the value of $\eta = 0.5$ is at the lower side of the values reported in literature e.g. [71, 73], where η is given as 50-80%.

Table 2.6: Temperature measurements on PS, PMMA and PC.

Material	$\Theta_{measured}$	$\Theta_{chip/tool}$ for $\eta = 0.5$	$\Theta_{shear\ zone}$ for $\eta = 0.5$	$\frac{\Theta_{measured}}{2\Theta_{chip/tool}}$
PS	21 ± 4 K	26 K	37 K	0.40
PMMA	58 ± 4 K	52 K	75 K	0.56
PC	45 ± 4 K	33 K	52 K	0.68

Although the measured values can be related to conversion rates of mechanical work to heat known from literature, a second verification experiment was performed to find out if the thermocouple tool and calibration procedure were correctly applied for measuring the cutting edge temperatures.

2.4.3 Infrared measurements

The additional measurement is performed with an infrared (IR) camera. This measurement consists of measuring the cutting process of PMMA simultaneously with the embedded thermocouple tool and an IR camera. Although polymers can be highly transparent for IR radiations, PMMA has a high absorption in the wavelength range of approximately $7.8 - 8.8\ \mu$m [88]. This is in the spectral range of the used camera (Flir Systems, type Thermovision A40). The setup is schematically shown in Figure 2.12(a). The infrared camera was positioned under a small angle with the uncut surface and almost perpendicular to the chip's free surface. For the infrared measurements an emissivity value of 0.84 was taken [89].

The same cutting conditions as described in the previous section were used, except width of cut. The width of cut in this experiment increased from 0.36 mm at the beginning to 0.64 mm at the end of the experiment. This means that a width of cut of half a millimeter is reached in the middle of the cutting time.

Figure 2.12(b) shows the results of the measurements. The temperature given by the embedded thermocouple tool is the temperature at the cutting edge as derived by the application of the calibration data. The temperature measured by the infrared camera is the maximum temperature at the chip's free side in the shear zone region. It can be seen that the temperature at the cutting edge as derived by the thermocouple and the chip free side as measured by the IR camera,

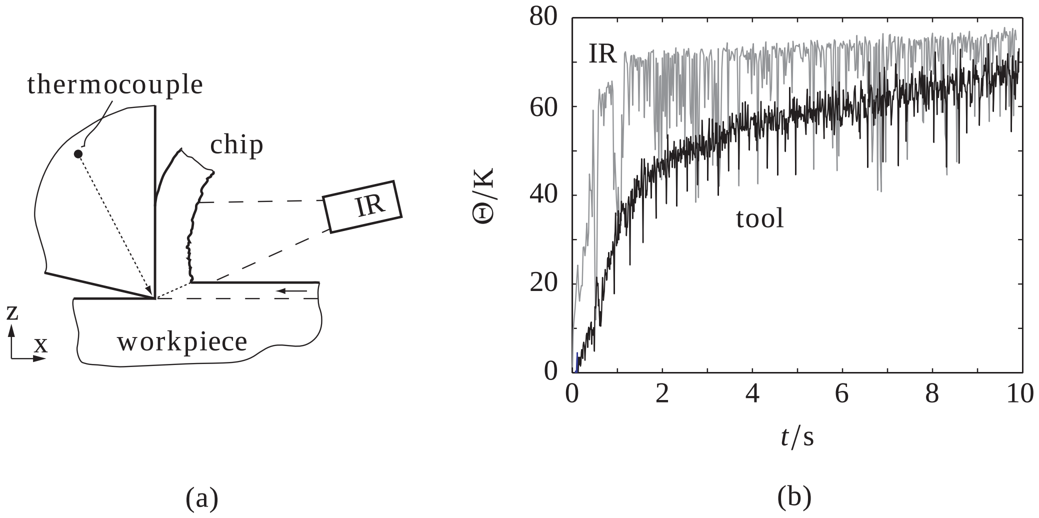

(a) (b)

Figure 2.12: Verification experiment on PMMA. Figure (a) showing schematically the used setup, and (b) showing the measurement result for v_c = 0.3 m/s and h = 10 µm.

are in accordance with each other. The thermocouple tool shows a time constant in the beginning of the measurement, while this is absent in the IR measurement, which is logical.

Also, peak fluctuations can be seen in both measurements. Since these peaks were not present in measurements with other cutting conditions, it was concluded that the peaks are a result of the turning process, and mainly the chip formation process.

Both measurements give comparable temperatures and trend, therefore it is assumed that the temperatures measured with the embedded thermocouple tool and the IR camera are the temperatures as they were in the cutting process.

The results of the calculations and the different measurements are summarized in Table 2.7. For the calculated values, see also Figure 2.6(b).

Table 2.7: Comparison of temperature rise calculations (η = 0.5) and measurements for PMMA.

Chip-tool interface		Chip's free side	
Calculated	Measured by thermocouple	Calculated	Measured by IR
Θ = 52 K	Θ = 58 K	Θ = 115 K	Θ = 73 K

Looking at this table, a big difference can be seen: the big overestimation of the thermal model of the temperature rise at the chip's free side in respect to the IR measurement. Whether this is an artifact of the assumption of the adiabatic boundary in the thermal model should be investigated. Another possibility is that the emissivity value of the PMMA was higher than that used in the measurement.

However, this does not yield such a big difference.

In Section 2.3.4 the temperature rise distribution in the tool was calculated. Looking at the point ($X = -200$ µm, $z = -150$ µm), a temperature rise of 11 K was found. This point is approximately the spot were the embedded thermocouple was positioned. Looking in the appendix at Figure D.1 the calibration profile is given for an applied temperature at the cutting edge of approximately 60 °C. In that case a temperature rise of approximately 10 K can be seen for the thermocouple. The difference between theory and experiment is acceptable.

Although a big difference exists between calculated temperature rise at the chip's free side and measured temperature by IR, the trend of the measurements seems good. Also taking into account the agreement between calculated temperature rise of the thermocouple and that actually measured, the adapted thermal model derived in this chapter is considered applicable for polymers.

2.5 Conclusions

In this chapter a thermal model was used for determining the temperature rise during turning. The model was based on a thermal model for metal cutting operations, but was adapted for calculations of polymer turning processes. This was done by the introduction of the heat dissipation factor η in the model. It was shown, using this adapted model, that the temperature rise in polymer turning is in the order of several ten degrees.

For the used model no heat partition fraction has to be assumed *a priori* . This heat partition value can be determined from the calculated temperature rise in the chip. It was shown that for the given diamond turning process of polymers typically 80% of the heat formed in the primary shear zone is removed by the chip. Only 20% of this heat is conducted into the workpiece.

Using a heat conversion ratio of mechanical work to heat of $\eta = 0.5$ in the model, which is in agreement with literature and performed experiments, it was found that for the investigated polymers a temperature rise below T_g occurred. This is in contrast with other researches [21, 44], however, in this research cutting forces were actually measured as input for the thermal model and verification experiments were performed to validate the results of the applied thermal model. The influence of a change in cutting conditions on the temperature rise will be described in chapter 3.

It was calculated with the adapted thermal model that approximately 20% of the heat formed in the primary shear zone is conducted back into the workpiece. This indicates that 80% of the heat is removed by the chip for the given conditions. Notice that these values were obtained as part of the outcome of the calculations and that they are not based on an *a priori* assumption.

A diamond tool with embedded thermocouple was developed for measuring the temperature rise during polymer turning. A calibration procedure was used for determining the error between cutting edge temperature and the temperature of the embedded thermocouple. It was described in Appendix D that the thermal contact resistance is important for the calibration procedure. The measurements with the embedded thermocouple tool were in good agreement with the calculated cutting temperatures. Besides measurements with the embedded thermocouple tool, measurements with an infrared camera were performed. These IR measurements indicated a higher temperature at the chip's free side, which was in accordance with theory, but the temperature was approximately 30 °C lower than calculated. Despite the big difference between calculated and IR measured temperature rise at the chip's free side, the trend of the measurements seems good. Based on the agreement between thermocouple measurement, IR measurement and calculated temperature rise, the adapted thermal model derived in this chapter is considered applicable for polymers.

Using the embedded thermocouple tool, it was shown that the used heat dissipation factor in the thermal model is chosen properly. For turning processes of polymers a work to heat conversion ratio of 0.5 can be assumed. Notice that this is different from the metal cutting process where almost 100% conversion of mechanical work to heat can be seen.

From this chapter it follows that care has to be taken with the interpretation of the available literature that is known on polymer turning. The main reason for this is not taking into account the storage of internal energy during deformation of polymers. This can be as high as 50%, thus lowering the final cutting temperature reached in the primary shear zone during turning. Also, the heat partition fraction B to the workpiece is smaller than that used in the calculations of Smith [44], indicating that until now overestimates were made.

Chapter 3

Influence of cutting conditions and material properties

3.1 Introduction

This chapter describes the influence of several cutting parameters on the results of the diamond turning process of glassy polymers. For the investigation of machining modifications the thermal model derived in the previous chapter is used for visualizing the temperature profiles. Besides changing cutting conditions, also workpiece material modification is investigated. It includes changes of thermo-mechanical history and crosslink density of polymers.

The next section deals with two different turning setups, namely a plunge turning setup where a straight cutting edge is used, and a face turning setup that uses a nose radius tool. Section 3.3 presents the influence of thermo-mechanical history of the workpiece material on the surface quality. The effect of increasing crosslink density is investigated in Section 3.4. The chapter ends with conclusions about the diamond turning process of polymers.

3.2 Turning parameters

One of the most used methods for improving surface quality is the adaption of cutting parameters. It is the easiest way of improving cutting results, such as surface quality.

This section is split in two parts with different turning setups: 1) plunge turning with a faceted, straight edged diamond tool, and 2) face turning with a nose radius tool.

The plunge turning is used for investigating the effect of cutting parameters on the temperature rise. It is known from the previous chapter that the glass transition temperature was not reached for the given turning conditions. However, in literature about polymer turning such as Smith's research [44], it is assumed that with an increase in cutting speed, more adiabatic heating results in a higher

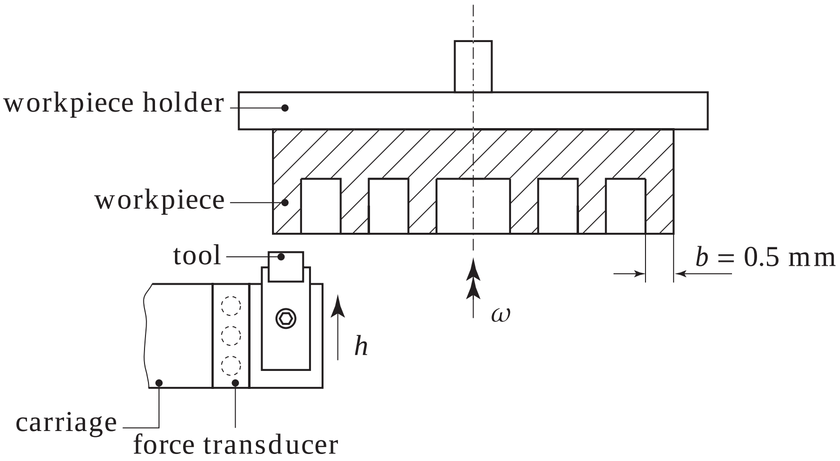

Figure 3.1: Schematic representation of the used cutting setup for the plunge turning experiments.

temperature rise. This will be investigated in the first part of this section. Also, it includes aspects of surface formation.

The face turning setup is used for investigating the effects of changing turning parameters on achieved surface quality. In this process a nose radius tool is used, since it is the most used tool in precision turning operations for optics.

3.2.1 Plunge turning

A. Experimental

The plunge turning setup was given in Figure 2.2, but is depicted again in Figure 3.1. It is mainly used for investigating the influence of cutting parameters during turning of PC. A faceted, natural, mono-crystalline diamond tool was used. Different rake angles were used for the (110) oriented rake face, see Table 3.1. In all sets, the clearance angle was 15°, however, for sets 6 and 7, see Table 3.1, the tool was rotated to achieve the required rake angle, thus changing the 15° clearance angle likewise.

The cutting forces were measured using a three-component force transducer (Kistler type 9251). The main cutting force F_c and thrust force F_t were used as input for the thermal model given in Chapter 2. Also, the length of the chip L_c after cutting was compared to the theoretical length of cut L. This gave the r_c value given by Equation 2.1, needed for determining the shear angle as given by Equation 2.10.

Sets 1 to 5, given in Table 3.1, were chosen for investigating the effect of cutting speed and depth of cut on the temperature rise distribution. Set 8 was chosen to investigate how a large negative rake angle influences the temperature distribution. Smith [44] used in her research the same negative rake angle of $-20°$, but did not make any temperature estimate for it, although her assumption was

Table 3.1: Turning sets used for PC.

set	α	$v_c/(\mathrm{m \cdot s^{-1}})$	$h/\mu\mathrm{m}$	b/mm	F_c/N	F_t/N	r_c
1	0°	0.3	10	0.8	3.20	2.05	0.60
2	0°	0.3	5	0.74	1.30	0.65	0.58
3	0°	0.3	2	0.8	0.83	0.51	0.56
4	0°	3.0	10	0.8	2.85	1.65	0.63
5	0°	3.0	2	0.8	0.67	0.37	0.63
6	3.6°	0.3	10	0.75	2.00	1.03	0.65
7	– 3.6°	0.3	10	0.72	2.25	1.40	0.59
8	– 20°	0.3	10	0.8	5.00	4.80	0.57

that such a negative rake angle would increase the temperature rise significantly. Since some interesting surface effects were seen in the experiments of sets 1 to 5, sets 6 and 7 were also introduced.

B. Cutting forces

Figure 3.2 shows the measured cutting forces for sets 1, 3, 4 and 5. For clarity, these forces are depicted as

$$F_c^* = \frac{F_c}{b \cdot h} \quad \text{and} \quad F_t^* = \frac{F_t}{b \cdot h} \tag{3.1}$$

It can be seen that the cutting forces for 2 μm depth of cut are higher than those for 10 μm depth of cut. This is in accordance with literature about specific cutting forces, such as [34, 76].

It can also be seen that with an increase in cutting speed, the measured cutting forces decrease. Although this may be expected intuitively, this does not have to be the case, since the volumetric work energy is independent of the cutting speed [4]. It was shown by Moriwaki and Okuda [90] that for copper, the cutting forces do not change over a cutting speed range of 2 – 20 m/s. Drescher [4] mentions that only at high speeds material softening may affect the cutting forces. Possibly, softening influences the cutting forces for the investigated PC. Whether this is thermal or intrinsic softening cannot be concluded from these results.

C. Thermal aspects

C1. Cutting speed For the investigation of the influence of cutting speed on the cutting temperature distribution, cutting experiments were performed with different cutting speeds, namely $v_c = 0.3$ m/s and $v_c = 3$ m/s. From Smith's research [44] it is known that an increase in cutting speed should result in an increased temperature rise in the primary shear zone.

Figure 3.3 shows the isotherms of the calculated temperature rise for different conditions, sets 1, 3, 4 and 5. It can be seen in this figure that a steep temperature gradient occurs in front of the primary shear zone. At high cutting speed $v_c =$

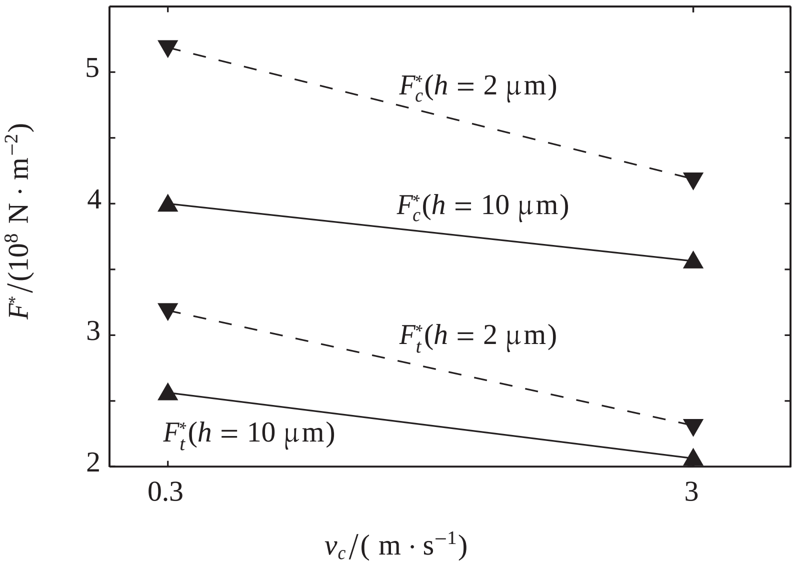

Figure 3.2: Cutting forces F_c^* and F_t^* as a function of cutting speed for plunge turning of PC, sets 1, 3, 4 and 5.

3 m/s the tool movement is too high for thermal diffusion to occur in front of this shear zone. Also, a temperature gradient occurs behind the tool at the cut surface. A possible consequence of this will be discussed later on page 67.

Table 3.2 gives the maximum calculated value in the shear plane found by the thermal model given in Section 2.3.2.

Table 3.2: Calculated maximum shear plane temperature rise during diamond turning of PC with different v_c and h.

set	$v_c/(\mathrm{m \cdot s^{-1}})$	$h/\mu\mathrm{m}$	Θ_{sp}/K
1	0.3	10	70
2	0.3	5	65
3	0.3	2	70
4	3.0	10	75
5	3.0	2	70

It can be seen in this table that the maximum temperature at the shear plane is approximately the same for all situations. This is in contrast with the available literature on polymer turning, and specifically Smith's calculations as given in Table 2.1. It is generally assumed that an increase in cutting speed results in more adiabatic heating of the cutting zone [21, 44].

This contrast is also visible in Figure 3.4 that shows the temperature rise isotherms for PMMA cut with $v_c = 0.3$ m/s respectively $v_c = 3$ m/s and depth of cut 10 μm. It can be seen in this figure too, that an increase in cutting speed does not result in an increase in temperature rise in the primary shear zone. The glass transition temperature is not reached in the primary shear zone for both

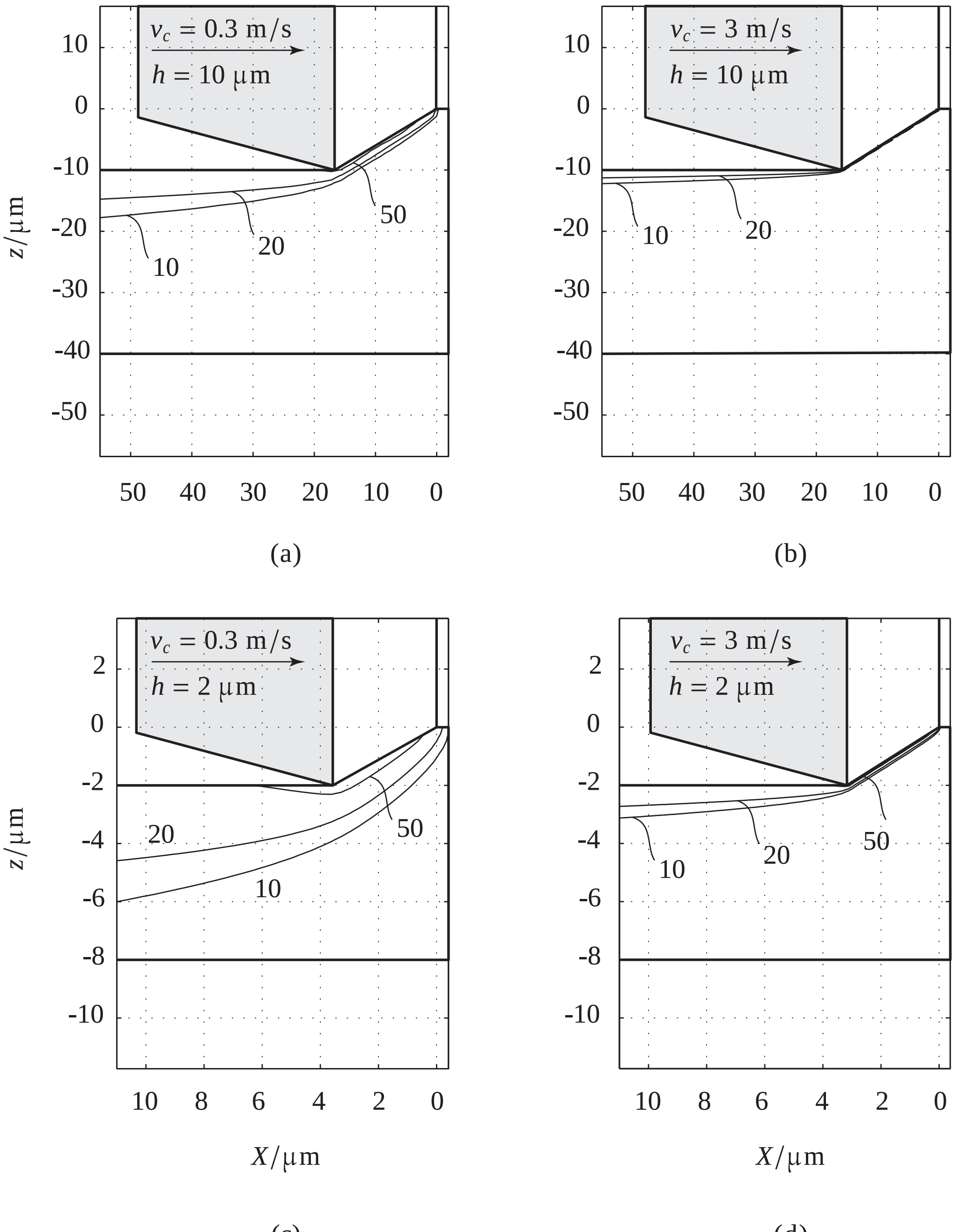

(a) (b)

(c) (d)

Figure 3.3: Isotherms of calculated temperature rise for PC ($\eta = 0.5$) cut with (a) set 1, (b) set 4, (c) set 3, and (d) set 5.

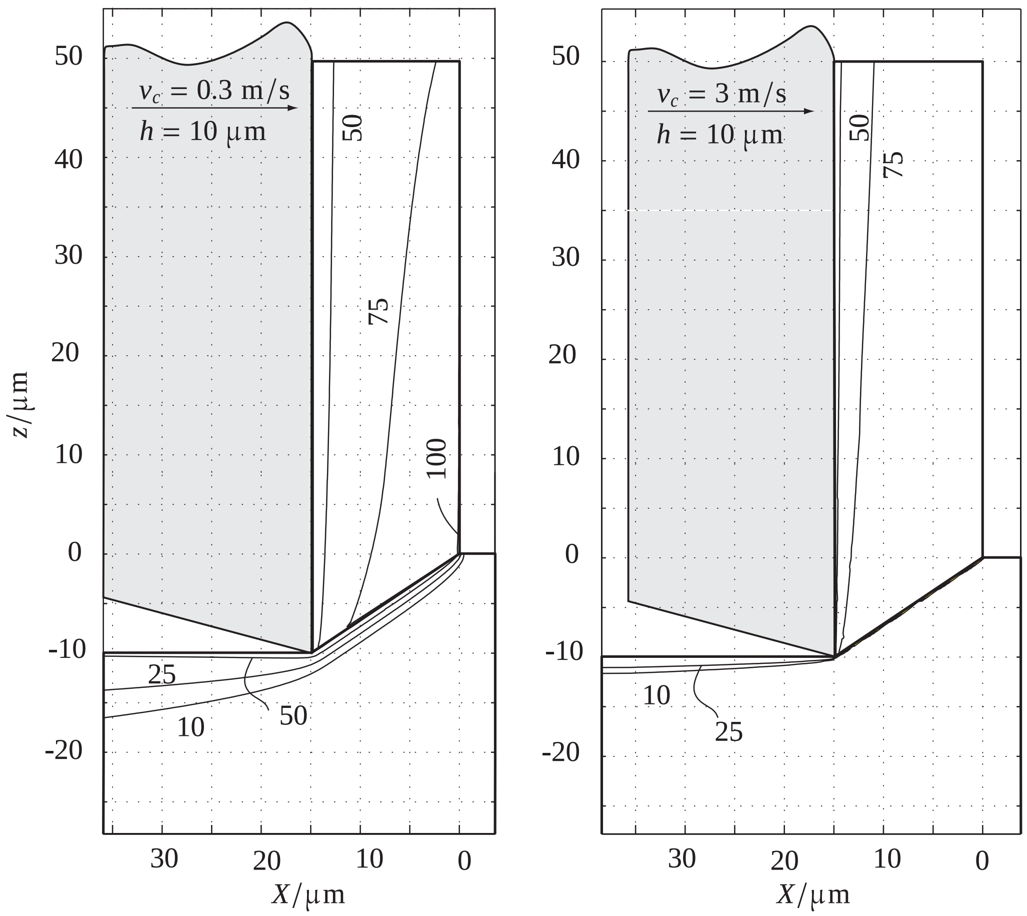

(a) (b)

Figure 3.4: Calculated temperature rise distributions ($\eta = 0.5$) during turning of PMMA with $h = 10$ µm, $b = 0.5$ mm, and cutting speed (a) $v_c = 0.3$ m/s and (b) $v_c = 3$ m/s.

machining conditions. In fact, the temperature rise is less for the high speed situation, and the maximum calculated chip temperature is lower too. The latter is caused by the higher chip removal speed and the amount of heat moved away from the shear zone by material flow. This is also reflected in the heat partition fraction of workpiece and chip for the higher cutting speed: $B = 0.11$ respectively $(1 - B) = 0.89$. For the lower cutting speed these were determined as $B = 0.24$ respectively $(1 - B) = 0.76$, see Table 2.4.

These values confirm that the heat diffusion is too small to influence the material in front of the tool. This indicates that the turning process of PC and PMMA will consist of the combined action of thermal and stress activated flow in the narrow primary shear zone. In fact, for higher cutting speeds of order meter per second, the thermal diffusion is too small to result in more adiabatic heating. The thermal layer at the cut surface decreases with a factor three for the higher cutting speed.

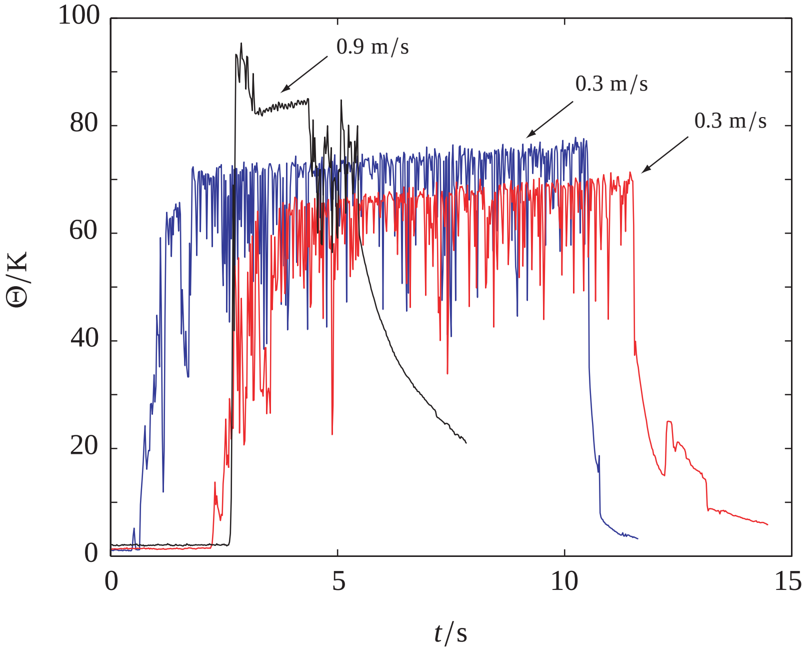

Figure 3.5: Infrared thermography measurement results on PMMA for different cutting speeds $v_c = 0.3$ m/s respectively $v_c = 0.9$ m/s, and width of cut approximately 0.5 mm.

Figure 3.5 shows the results of IR thermography on PMMA. It shows two measurements for $v_c = 0.3$ m/s and one measurement at an increased cutting speed $v_c = 0.9$ m/s. The measurements were taken at a room temperature of 20 °C. It can be seen that a higher temperature is achieved in the latter case.

The IR measurements show a trend of increasing cutting temperatures with increasing cutting speed. However, this cannot be seen in the results of the calculations made by the thermal model, as given in Figures 3.3 and 3.4 for PC respectively PMMA.

Possible explanations for these errors can be:

- Measurement error of the chip length after cutting. This influences directly the determination of r_c and φ. The shear angle φ is used again in the determination of $\dot{q}_{pl}$ through $\dot{q}_{pl} = F_s v_s / (L_s \cdot b)$. Calculations showed, however, that with a measurement error of the chip length of ±10 mm, the total calculated temperature rise error is only 10 K.

- Changing cutting speed means changing strain rate. Figure 2.1 showed that an increase in strain rate results in an increase in the work to heat ratio η. Assuming a strain rate increase of one order for the different cutting speeds (Equation 1.6), this would increase η by approximately 0.02. This is to less to cause a dramatic increase in calculated temperature rise too.

- The used workpieces with rills, given schematically Figure 3.1, were manufactured manually. During the fabrication of these rills by turning, frictional heating at the side walls may have caused different heating effects per rill, resulting in different thermo-mechanical histories. A different thermo-mechanical history has its influence on the cutting forces, which are necessary for the calculation of the temperature rise.

- During temperature measurements overlapping cuts occur. From the calculated temperature rise distributions it becomes clear that a heat effected zone exists at the cut surface behind the tool. If cooling of this zone does not occur quick enough within one revolution, this offset temperature will be present in the IR measurement, while this is not included in the calculation for the temperature rise. This may result in a higher temperature measured for overlapping cuts at the higher cutting speed.

The above showed that different initial conditions may have been present in the different workpieces, leading to differences in measured and calculated temperatures. The difference between the two IR measurements made at v_c = 0.3 m/s is already 10 K. Unfortunately only one IR measurement was made at a cutting speed of 0.9 m/s, which temperature rise is approximately 10 K higher as the highest temperature measured with $v_c = 0.3$ m/s.

Based on the previous considerations, and mainly the possible higher temperature offset of the workpiece material at higher cutting speeds, it is assumed that the temperature model predicts the accurate values, since offset temperature is not included in the temperature rise calculation.

An interesting aspect is whether chain scission occurs in front of the cutting edge, since stress activated flow is also present. If chain scission occurs in turning, the molecular weight of the material in the chip must be lower than the molecular weight of the bulk material of the workpiece. To measure this, gel permeation chromatography can be used. Gel permeation chromatography (GPC) can determine the molecular weight of a polymer by using a size-exclusion technique. For further reading about this technique, see e.g. [83]. Although the measurement error is smaller than 2%, variations in the bulk material may be larger (up to 10%).

The molecular weights of the bulk material prior to cutting and the collected chips after cutting were determined. This was done for PMMA and PC. Table 3.3 shows the results of the used PMMA and PC for cutting conditions $v_c = 2.4$ m/s, $f = 0.25$ µm/rev and $h = 5$ µm.

It can be seen that the cut PC has a higher M_n than the uncut PC, but this can be ascribed to variations in the bulk. Uncut PMMA has an M_n-value higher than 10^6 g/mol, since it was not measurable by the used GPC instrument. However, after cutting the GPC distribution was measurable, showing a decreased molecular weight for the chip material. The results clearly indicate that chain scission occurs during turning of this PMMA grade and not during turning of this PC grade.

Table 3.3: Results of GPC measurements.

	$M_n/(\mathrm{g}\cdot\mathrm{mol}^{-1})$	$M_w/(\mathrm{g}\cdot\mathrm{mol}^{-1})$	PDI
PC uncut	$16.3\cdot10^3$	$41.5\cdot10^3$	2.54
PC cut	$16.7\cdot10^3$	$43.2\cdot10^3$	2.58
PMMA uncut	$> 1.0\cdot10^6$	-	
PMMA cut	$38.9\cdot10^3$	$284.5\cdot10^3$	7.31

C2. Depth of cut Figure 3.3 on page 59 showed the calculated isotherms of the temperature rise for different depths of cut. It can be seen that the temperature profiles are approximately the same for 2 μm and 10 μm. This is confirmed by the maximum values of the calculated temperature rise in Table 3.2 on page 58. This is in contrast with the trend given by Smith [44] for decreasing chip thickness.

However, the following should be considered: the specific cutting forces for depth of cut 2 μm are higher than those for 10 μm, see Figure 3.2. Using Merchant's equation for the shear stress [34]:

$$\tau = \frac{F_c \sin\varphi\cos\varphi - F_t \sin^2\varphi}{b\cdot h} \tag{3.2}$$

and looking at the data given in Table 3.1, the values given in Table 3.4 can be used for calculating the shear stress in the primary shear zone:

Table 3.4: Calculated shear stresses for set 1 and 3 conditions.

set	1	3
$h/\mu\mathrm{m}$	10	2
b/mm	0.8	0.8
F_c/N	3.20	0.83
F_t/N	2.05	0.51
φ	31°	29°
τ/MPa	108	145

It follows from this table that the calculated shear stress is approximately 1.5 times higher for the smaller depth of cut (set 3). This also becomes clear from the amount of heat liberated in the shear zone, as derived in the thermal model: for set 1: $\dot{q}_{pl} = 1.9\cdot10^7\ \mathrm{W/m^2}$, and for set 3: $\dot{q}_{pl} = 2.5\cdot10^7\ \mathrm{W/m^2}$.

The increase in shear stress can be attributed to a higher specific cutting force, but also to the fact that $\dot{\gamma} \propto h^{-1}$, indicating that at smaller depth of cut the strain rate is higher. Figure 1.15 showed that the yield stress of polymers increases with higher strain rates. These effects were not taken into account in Smith's research [44] and may explain the difference in trends as predicted in Smith's research and in this research. They also indicate that with decreasing depth of cut the temperature rise does not have to decrease as well.

A depth of cut of 2 μm in these experiments shows similarities with the maximum uncut chip thickness in precision turning, see Section 1.2.3. Figures 3.3(c) and (d) can therefore be regarded as representative for the achieved cutting temperatures in the precision turning process of PC with a radius tool of $R = 1$ mm, and turning conditions $f = 10$ μm and $h \approx 20$ μm. In that case the biggest uncut chip cross-section is 2 μm.

C3. Rake angle Figure 3.6 shows the temperature rise contours in the workpiece calculated with the aid of the thermal model derived in Chapter 2. It can be seen that the temperature rise for rake angles deviating little from zero are approximately the same. However, when a large negative rake angle (−20°) is used a higher temperature rise is determined, see Figure 3.6(d). This is in accordance with literature on polymer turning, like Smith's [44]. It confirms Smith's statement that a negative rake increases the amount of heating in the shear zone. It also confirms that even a large negative rake cannot raise the temperature high enough to reach T_g during diamond turning of PC.

A remark has to be made here on the temperature rise calculated for set 1 conditions, see Table 3.5. For set 1 conditions, the temperature rise is 10 K lower than that given for set 1 in Table 3.2. The most probable reason for this is the use of a different workpiece, giving rise to different cutting forces, necessary for the input of the thermal model.

Table 3.5: Calculated shear plane temperatures for different rake angles.

α	set	Θ_{sp}/K
3.6°	6	50
0°	1	60
− 3.6°	7	55
− 20°	8	90

D. Surfaces in plunge turning

D1. Cutting speed From the calculations of the thermal model it follows that both PC and PMMA are not cut in the thermal flow regime for set 1 and 4 conditions. The temperature rise distributions for PC were given in Figure 3.3(a) and (b) and for PMMA in Figure 3.4(a) and (b). Based on these results only little differences in surface quality should be expected.

However, looking at Figure 3.7 it can be seen that for set 1 and 4 conditions, a wavy pattern originates at the surfaces of PC and PMMA. Table 3.6 shows some roughness values for the shown surfaces. It can be seen that for PC the roughness decreases with increasing cutting speed, while for PMMA the opposite is the case. Looking at the wavelength of the patterns, it can be seen that both decrease with increasing cutting speed. This means that the frequency of the pattern increases.

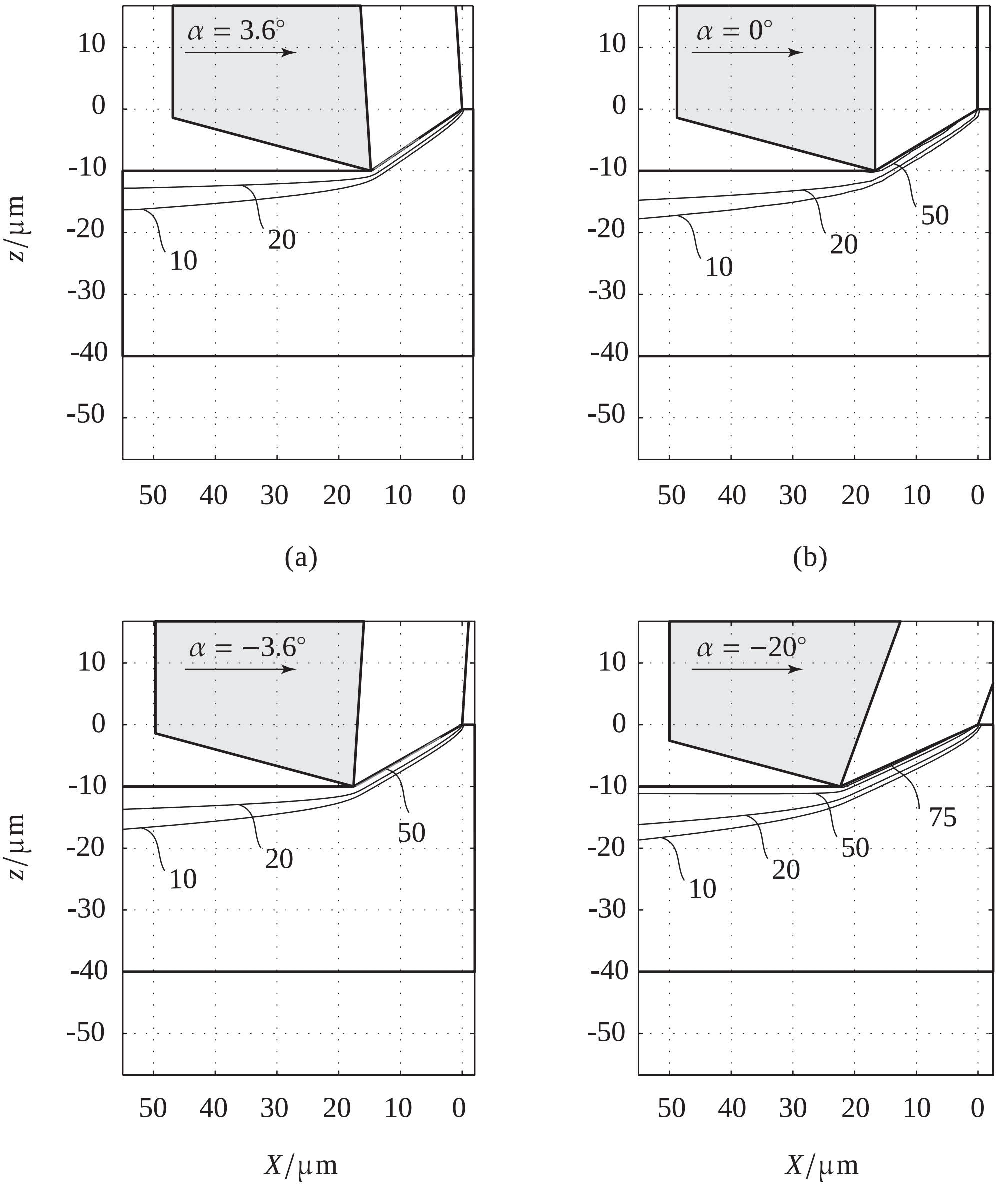

(a) (b)

(c) (d)

Figure 3.6: Temperature rise contours for PC ($\eta = 0.5$) cut with $v_c = 0.3$ m/s and $h = 10$ µm.

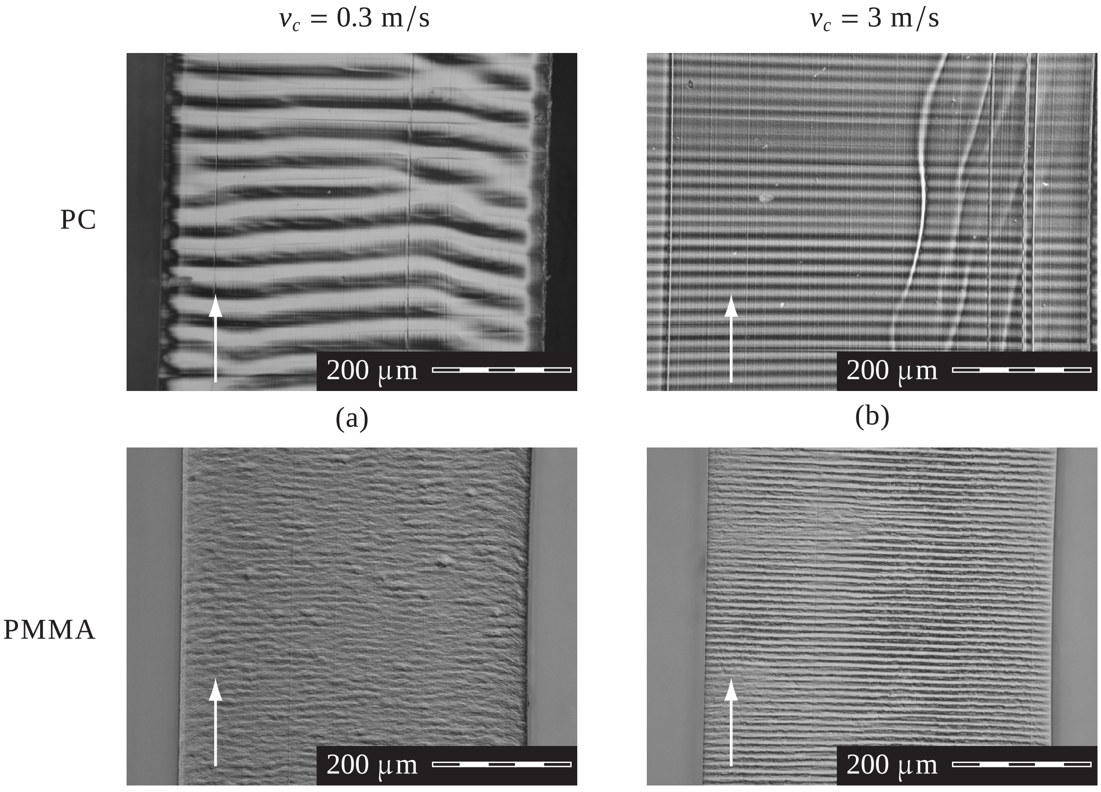

(c) (d)

Figure 3.7: Surfaces of PC (upper) and PMMA (lower). Photos on the left were obtained with set 1 conditions and on the right with set 4 conditions. Direction of cut is indicated by the arrows.

Table 3.6: Surface characteristics for set 1 and 4 conditions for PC and PMMA.

		PC		PMMA	
cutting speed	$v_c/(\mathrm{m \cdot s^{-1}})$	0.3	3	0.3	3
roughness	Ra/nm	256	11	18	69
amplitude	A/nm	923	33	91	220
wavelength	λ/μm	46.7	17.4	13.0	10.4
frequency	f/kHz	6.4	172	23	290

The increase in frequency was independent of the increase in rotational speed of the spindle of the turning machine.

The difference in surface pattern and response to an increase in cutting speed of PC and PMMA may originate from differences in chip formation: Table 3.3 showed that PC forms ductile chips without chain scission, while PMMA forms semi-ductile/segmented chips accompanied with chain scission in the cutting zone. This indicates a difference in chip formation process, which can be a reason for the observed differences in cut surface and the different response to an increase in cutting speed.

Tool vibration It is expected that the combination of frequencies and amplitudes cannot be ascribed to machine vibrations. An estimate is made for the volume of the material that should vibrate for achieving a pattern with an amplitude of frequency 6.4 kHz. The frequency of a vibrating machine part is given by:

$$f = \sqrt{\frac{C}{m}} \tag{3.3}$$

with C the stiffness and m the mass. For an estimate of the total mass moving, this can be rewritten to

$$m = \frac{C}{f^2} \tag{3.4}$$

Now assuming that $C = 10^7$ N/m, which is a common stiffness used in machinery design, specific mass $\rho = 7.8 \cdot 10^3$ kg/m^3 for steel, and $m = \rho \cdot V$, then the volume that should be moving at a frequency of 6.4 kHz is calculated as:

$$V = \frac{C}{\rho \cdot f^2} = \frac{10^7}{7.8 \cdot 10^3 \cdot (6.4 \cdot 10^3)^2} = 3.1 \cdot 10^{-5}\ \text{m}^3 \tag{3.5}$$

This volume (31 cm^3) can have dimensions that are approximately equal to a part of the force measurement system. Assuming this stiffness, and looking at the thrust force activating this eigenfrequency, an amplitude of $A = F_t/C = 2/10^7 = 2 \cdot 10^{-7}$ m (200 nm) can be calculated. This is less than the measured amplitude of 923 nm for PC turned with set 1 conditions.

Viscous folding Another explanation for the surface characteristics after turning PC can be found in viscous folding. Since chain scission (non-ductile failure) occurs during cutting of PMMA a different surface formation mechanism can be active.

Viscous folding can occur in two situations. Figure 3.8(a) shows the first situation where a matrix material with viscosity η_M and a top layer with viscosity $\eta_L < \eta_M$ are compressed with a compressive stress σ_{compr}. Folds as shown schematically in gray will form.

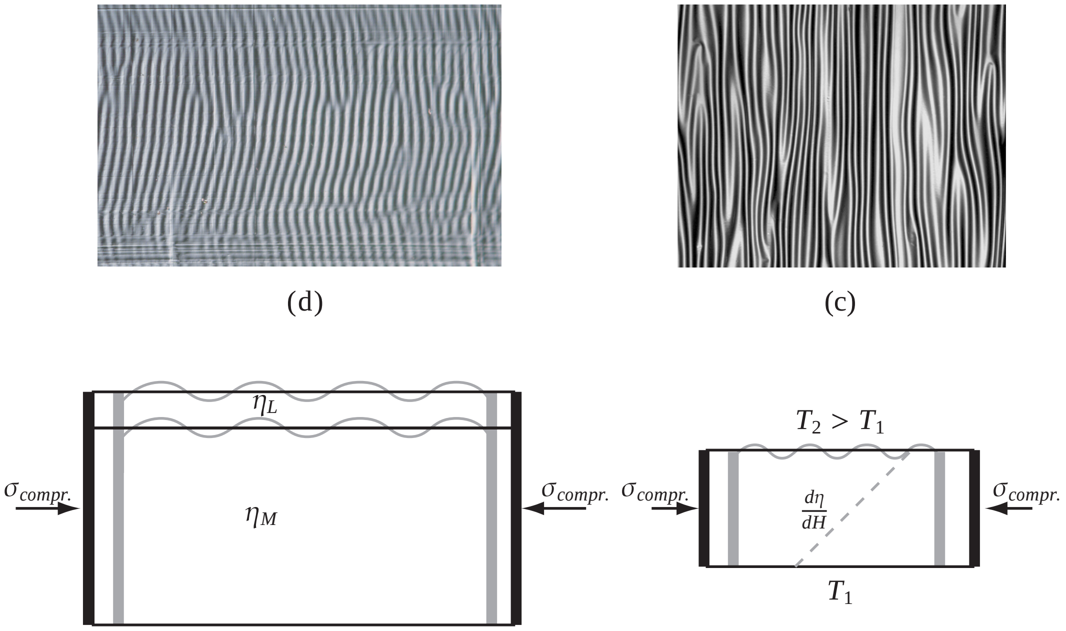

(a) (b)

Figure 3.8: Schematic representation of viscous folding as a result of a viscosity difference between layer and matrix (a), and a viscosity gradient caused by a thermal gradient in the polymer (b). Figure (c) shows a preliminary result of Feldman [91] created with setup (b). Figure (d) shows a similar surface structure, but after turning PC. For (c) and (d) the direction of strain was in the horizontal plane of the page.

Another situation that can result in viscous folding is when a material, like a polymer, has a temperature gradient over its thickness H. This can be caused by applying two different temperatures at the upper and lower side of the material. Figure 3.8(b) shows such a setup. Due to the temperature gradient a viscosity gradient $d\eta/dH$ will occur as well. When this material is subjected to a compressive stress folds will be formed at the surface. Figure 3.8(c) shows such a folding pattern (preliminary result of Feldman [91]) that originated by applying a temperature gradient (and therefore a viscosity gradient) over a polymer.

Figure 3.8(d) shows a similar pattern as in (c), but it was formed by plunge turning PC with set 3 conditions. Figure 3.3 showed the calculated temperature rise isotherms during cutting of PC. It can be seen that behind the tool a temperature gradient is present in the top layer of the workpiece. This is a similar situation as depicted in Figure 3.8(b), indicating that viscous folding can occur in turning processes of polymers. Notice that compressive stresses are present behind the tool when the tensile region behind the tool , see Figure 1.4(b), has passed and the material returns to a ”stress-free” state again.

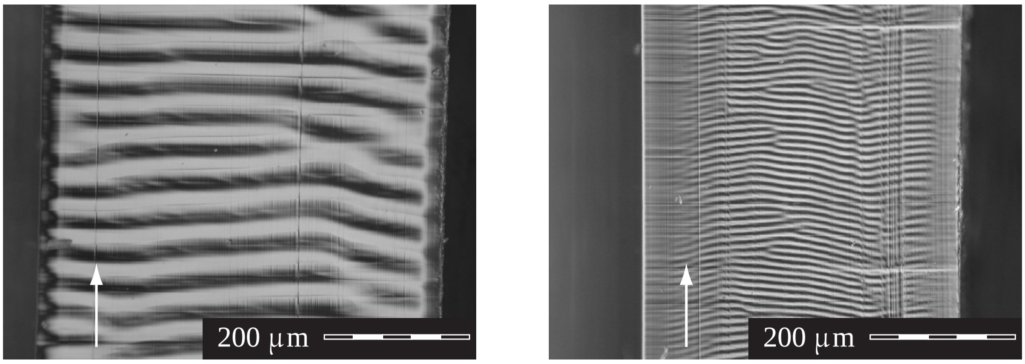

(a) (b)

Figure 3.9: Cut surfaces of PC with cutting speed $v_c = 0.3$ m/s, and depth of cut (a) $h = 10$ μm and (b) $h = 2$ μm. Cutting direction is indicated by the arrow.

D2. Depth of cut Figure 3.9 shows the surfaces obtained after turning with two different depths of cut on PC in plunge turning setup (set 1 and 3). It can be seen that a decrease in depth of cut results in a decrease of wavelength. Table 3.7 shows measurement data for set 1, 2, 3, 4 and 5 conditions. It can be seen that the Ra and λ values decrease with decreasing depth of cut, but also for increasing cutting speeds.

Table 3.7: Surface characteristics for different sets after cutting PC.

set		1	2	3	4	5
cutting speed		$v_c = 0.3$ m/s			$v_c = 3$ m/s	
depth of cut	h	10 μm	5 μm	2 μm	10 μm	2 μm
roughness	Ra/nm	256	76	52	11	15
amplitude	A/nm	923	246	154	33	16
wavelength	λ/μm	46.7	20.4	11.0	17.4	3.7
frequency	f/kHz	6.4	14.7	27.2	172	811

Figure 3.10(a) shows a logarithmic plot of the calculated temperature rise at a distance L_s from the cutting edge versus depth underneath the cut surface of PC for cutting sets 1, 3, 4 and 5. The distance L_s is taken as a reference for comparing the different conditions.

It can be seen in figure (a) that the maximum temperature rise is approximately the same for all cutting conditions, however, the slope of the curves is different. In figure (b) the slope of the curves, determined by a least-squares first order fit, is given on the x-axis. It appears that an increasing slope, thus an increasing temperature gradient near the cut surface, results in a decreasing amplitude of the pattern. The same is true for the wavelength of the pattern.

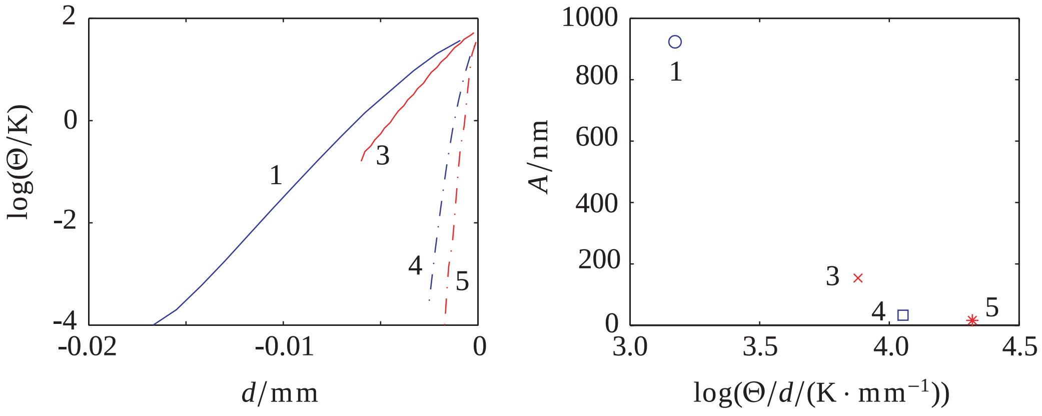

(a) (b)

Figure 3.10: Influence of temperature gradient on the amplitude of the pattern. The numbers correspond to the sets given in Table 3.1.

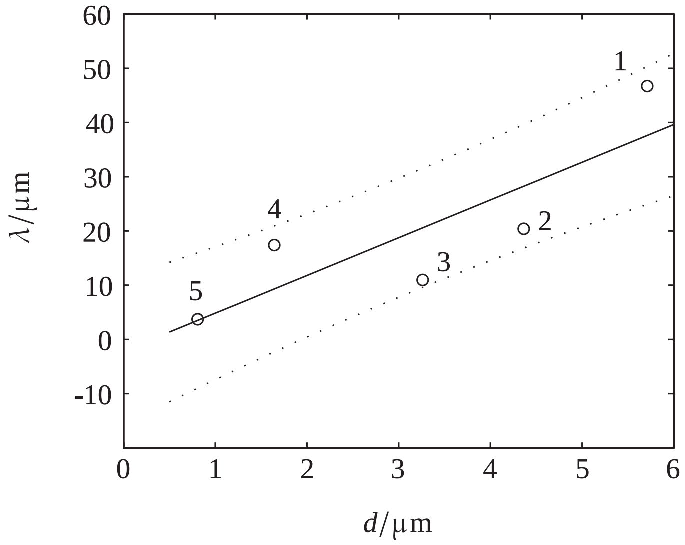

Figure 3.11: Dependence between the thickness d of the $\Theta = 10\,\mathrm{K}$ layer and the dominant wavelength in plunge turning. The solid line is an LSQ fit and the dashed lines indicate the 95% confidence area.

In case of viscous folding, it is known from references [92, 93] that the dominant wavelength of a folding pattern will always scale linear with the thickness d of the viscous layer. Although the exact thickness of the viscous layer is not known, the thickness of the $\Theta = 10\,\mathrm{K}$ layer is taken here as a reference. Figure 3.11 shows a plot of the thickness d of the $\Theta = 10\,\mathrm{K}$ layers, calculated with the thermal model, for different cutting conditions. The fit given in the figure shows a linear behaviour, indicating that viscous folding occurred in turning PC.

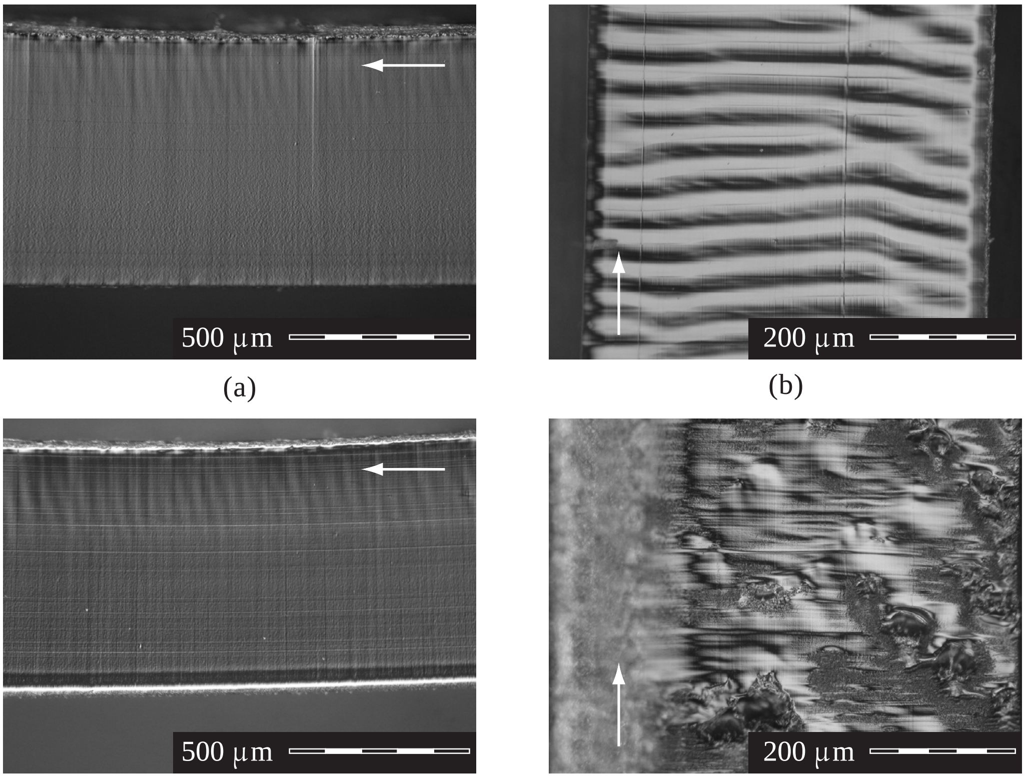

(a) (b)

(c) (d)

Figure 3.12: Cut surfaces of PC at $v_c = 0.3$ m/s, $h = 10$ µm, and (a) rake 3.6°, (b) rake 0°, (c) rake −3.6° and (d) rake −20°. Cutting directions are indicated by the arrows.

D3. Rake angle Figure 3.12 shows the surfaces obtained on PC for the different turning sets 1, 6, 7 and 8. It can be seen that the surfaces cut with rake angles of 0° and −20° have the worst surface qualities. The surface turned with a rake angle of −20° shows a very irregular surface, formed by tearing/fracturing of the workpiece material in front/underneath the tool. The surface formed by cutting with a zero rake angle shows the possible viscous folding pattern.

The gradients of the temperature rise profiles at a distance L_s are given in Figure 3.13 for the three different rake angles of sets 1, 6 and 7. Since no continuous chip is formed for set 8 conditions ($\alpha = -20°$), this is not used for comparison. From Figures 3.6 and 3.13(a) it is clear that there is little difference between the temperature gradients behind the tool for the different rake angles of sets 1, 6 and 7, and that the depth of the $\Theta = 10$ K line is approximately the same for these three sets.

In contrast with this similarity in temperature rise is the big difference in surface structures seen in Figure 3.12. The measured amplitudes of the patterns are given in Table 3.8. It was expected that a positive rake resulted in a decreasing temperature gradient, while the negative rake was expected to result in an increa-

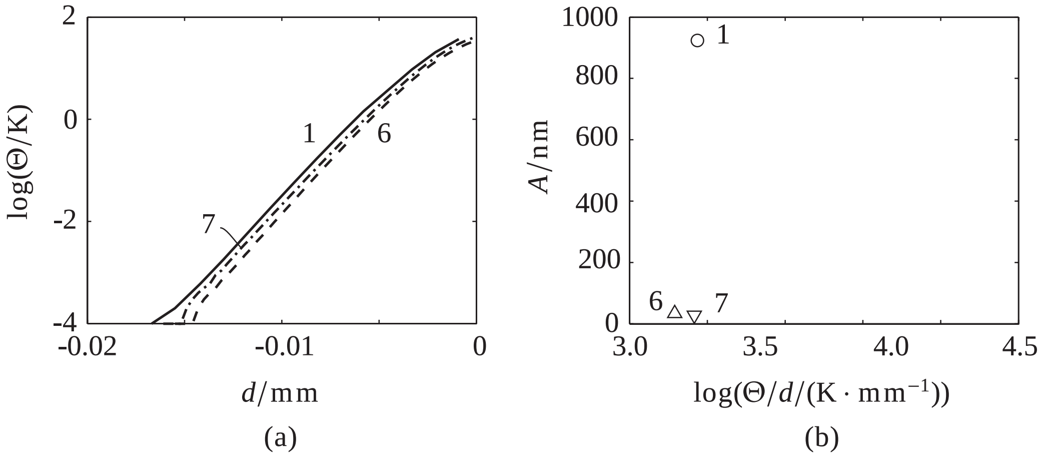

(a) (b)

Figure 3.13: Influence of temperature gradient on the amplitude of the pattern. The numbers correspond to the sets given in Table 3.1.

sing temperature gradient. This should have decreased respectively increased the folding behaviour. Instead, a small non-zero rake angle decreases the folds significantly, indicating that possibly the turning process changes dramatically. A big decrease in surface roughness value can be seen in Table 3.8 for small non-zero rake angles, whether they are positive or negative.

From the previous section it could be stated that viscous folding can be important in diamond turning, but the results also indicate that the process is very sensitive to changes in rake angle, or better said, changes in cutting geometry.

Table 3.8: Surface characteristics for different rake angles when cutting PC at v_c = 0.3 m/s and h = 10 μm.

rake	α	3.6°	0°	−3.6°
roughness	Ra/nm	10	256	16
amplitude	A/nm	34	923	28
wavelength	λ/μm	5.9	46.7	2.4
frequency	f/kHz	50.8	6.4	125

3.2.2 Face turning with a radius tool

A. Experimental

Face turning experiments are performed, since face turning is a normal finishing operation, although the optical industry mostly applies face turning operations as a contouring operation. Contouring operations are necessary for producing lenses. The difference between face turning and contouring is that in contouring, a part or the whole of the perimeter of the radius tool is used, while in face turning only one spot on the perimeter is used. For the investigation of the

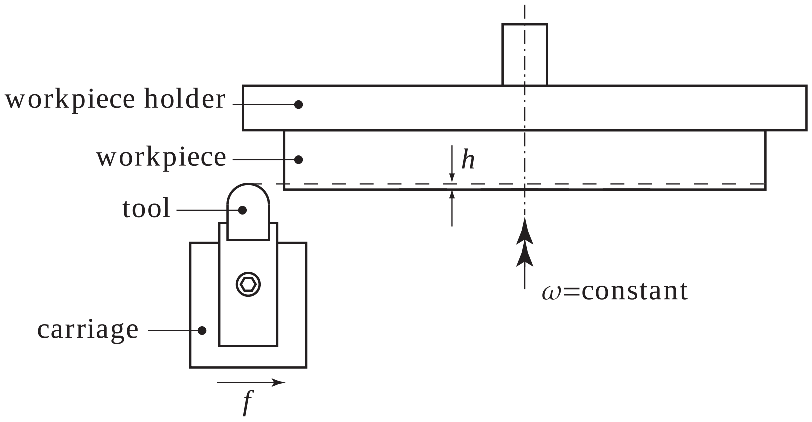

Figure 3.14: Schematic representation of the used cutting setup for face turning experiments.

turning process and its response to changing cutting parameters, the face turning operation satisfies.

The experimental setup is shown in Figure 3.14. In these experiments a natural, mono-crystalline diamond tool was used. It had a nose radius of 1 mm. Unless stated otherwise, rake angle $\alpha = 0°$, and clearance angle $\gamma = 15°$. No force measurements were performed. Surfaces were studied with Nomarski DIC and by atomic force microscopy. For a good description of surface patterns formed for PS, PMMA and PC, the reader is referred to Smith's research [44].

B. Surface formation

B1. Cutting speed The influence of cutting speed was investigated for PMMA and PC. The cutting conditions that were used are given in Table 3.9. Since a constant rotational speed ω was applied, the cutting speed in the center of the workpiece equals zero. Evaluation of the surface roughness was performed from nearly the center of the workpiece to the outer diameter.

Table 3.9: Cutting speed variation in face turning.

nose radius	R	1 mm
cutting speed	v_c	0.14 – 5.7 m/s
feed rate	f	10 μm/rev
depth of cut	h	10 μm
workpiece diameter	d	60 mm

Figure 3.15 shows the results of the cutting speed variation during turning of PMMA and PC. It can be seen that the surface roughness values of PC are higher than those of PMMA. Both materials cannot be machined to the theoretical value given by Equation 1.19. It can also be seen that for PMMA the surface roughness values at higher cutting speeds (above 2 m/s) are lower than those at lower cutting

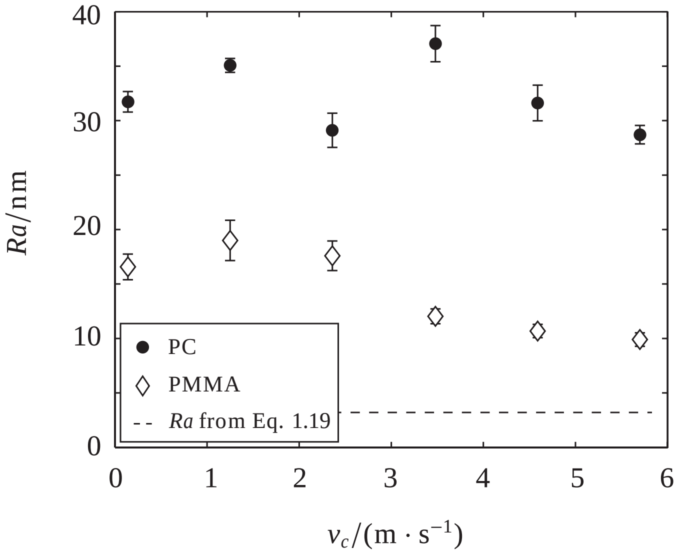

Figure 3.15: *Ra* values versus cutting speed for precision turned PC and PMMA ($f = 10$ µm/rev, $h = 10$ µm and $R = 1$ mm).

speeds. This is in contrast with the results for the faceted tool. The results are, however, in agreement with the results of Smith [44] concerning the increase of surface quality with increasing cutting speed for PMMA. But, notice, that this does not say anything about the achieved cutting temperatures in the shear zone.

For PC there appears to be no relation between increasing cutting speed and achievable surface roughness in the investigated range of cutting speeds. This is also in accordance with the research of Smith [44].

B2. Depth of cut Figure 3.16 shows the influence of the depth of cut on the surface roughness of precision turned PC and PMMA. It can be seen in this figure that the depth of cut has little effect on the achieved surface roughness for PC and PMMA, although the exception seems to be 0.5 µm depth of cut for PC. In general it can be said that a change in depth of cut in the range 1 − 10 µm cannot be used as a parameter for increasing surface quality of a precision turned polymer workpiece.

B3. Feed rate Figure 3.17 shows the influence of changing feed rate on the surface roughness after precision turning PC and PMMA. According to Equation 1.19 the relation between *Ra* roughness and feed rate is quadratic. Both for PC and PMMA fits are made according to the relation:

$$A \cdot \frac{f^2}{8R} + B = Ra \tag{3.6}$$

Using a least-squares fit, and with R the used tool nose radius, this results in

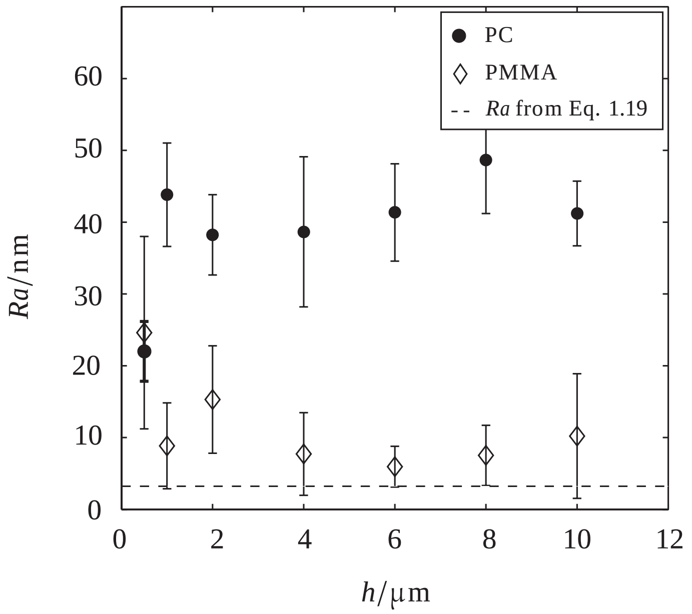

Figure 3.16: *Ra* values versus depth of cut for precision turned PC and PMMA ($v_c = 1,18$ m/s, $f = 10$ µm/rev and $R = 1$ mm).

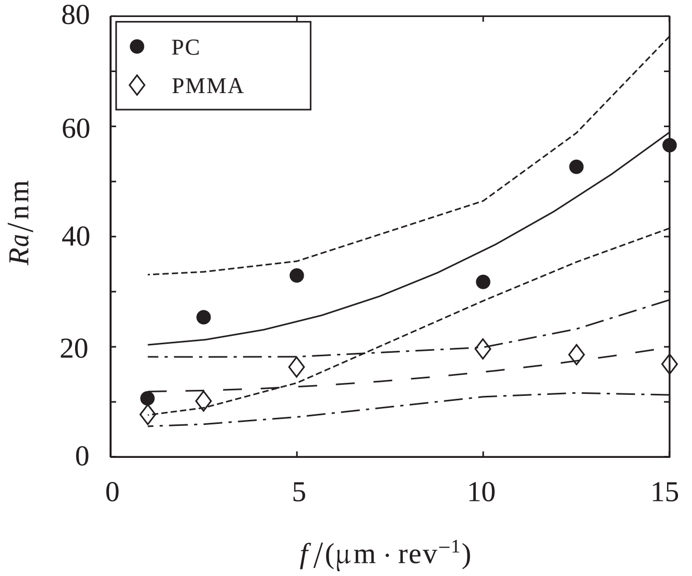

Figure 3.17: *Ra* values versus feed rate for turned PC and PMMA. ($v_c = 1.18$ m/s, $h = 10$ µm and $R = 1$ mm). Also given are the fits according to Equation 3.6 and the 95% confidence intervals for PC (solid) and PMMA (dashed).

the parameters given in Table 3.10. The offset values of the fits are 20 nm for PC and 12 nm for PMMA. The figure shows the 95% confidence intervals of the fits

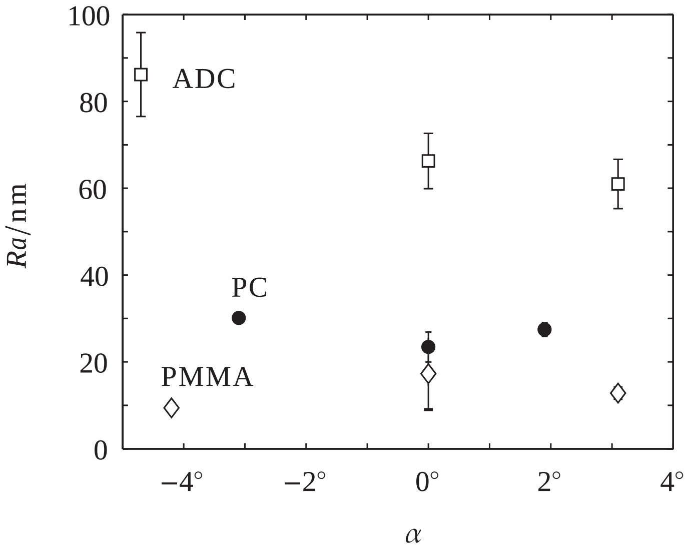

Figure 3.18: *Ra* values versus rake angle for turned ADC, PC and PMMA, v_c = 1.18 m/s, f = 10 µm/rev and h = 10 µm.

too. It can be seen in this figure, that PMMA can more easily be machined to an *Ra* value of less than 10 nm than PC.

Table 3.10: Fitted parameters for PC and PMMA for a tool nose radius R = 1000 µm. These values are only valid if f and R in Equation 3.6 are expressed in *µm*.

	A	B/µm
PC	1.3776	0.0202
PMMA	0.2865	0.0118

B4. Rake angle It was described in Section 3.2.1 that a small non-zero rake angle in plunge turning of PC resulted in a significant decrease in surface roughness. Figure 3.18 shows the results of turning experiments with different rake angles on PC and PMMA. The results of ADC, a thermoset that is often used as a material for spectacle lenses, are given too. The following cutting conditions were used: v_c = 1.18 m/s, f = 10 µm/rev and h = 10 µm.

It can be seen in this figure that for ADC, a positive rake angle has a positive effect on the achievable *Ra* value. However, the surface is still too bad for optical quality to be achieved. How the effect of a rake angle of e.g. 20° would be has to be further investigated.

Looking at PC, it can be said that with a rake angle α = 0° the best surface quality is reached. In fact, it is just below 20 nm, which was less than the values given in Figures 3.15 and 3.16. The exact reason for this is not known, but it may be attributed to a different workpiece. However, when a small positive or negative rake angle is used, not such a significant effect as described in the plunge turning experiment, Table 3.8, can be seen. This indicates that in precision turning the surface roughness determining factor appears to be in radial direction and not in tangential direction.

For PMMA it can be seen that a small positive or negative rake angle works beneficial for the achievable surface roughness.

3.3 Influence of thermo-mechanical history

In Section 1.3.2 it was described that the thermo-mechanical history of a polymer determines its macroscopic material behaviour. Shearing deformation occurs during cutting, but this does not influence the intrinsic material properties.

In general PS behaves brittle since it ages quickly [48]. The question arises whether rejuvenated PS, which behaves ductile, behaves differently in the cutting process than aged PS, or is process manipulation possible by changing the thermo-mechanical history of a polymer? This is interesting to know, since generally good surface qualities are achieved when cutting in a ductile regime [28]. To investigate if process manipulation is possible experiments on polystyrene were performed.

3.3.1 Experimental

The materials used in these experiments were general purpose polystyrene Styron 648 and Styron 660 from Dow Plastics (Dow Chemical Company). Table 3.11 shows the molecular weights of these two grades. From this table it can be concluded that Styron 648 has longer chains than Styron 660.

Table 3.11: Molecular weights of the used PS grades.

Material	$M_w/(\text{kg}\cdot\text{mol}^{-1})$	$M_n/(\text{kg}\cdot\text{mol}^{-1})$	PDI
Styron 648	318	107	2.97
Styron 660	203	66	3.09

The two granulates were injection moulded to plates with a thickness of 3 mm and surface 60×60 mm^2. Half of the samples were cut into workpieces of approximately 20×20 mm^2 and then placed into an oven at 80 °C for three days and subsequently cooled to room temperature at a low cooling rate (5 °C/hr). These samples are annealed, which means that they were thermally aged.

The rest of the injection moulded plates were rolled with a thickness reduction of 30% in order to mechanically rejuvenate them [51]. After rolling the plates were cut into workpieces of approximately 20×20 mm^2 and immediatly tested, since aging of PS is on a minutes time-scale [51].

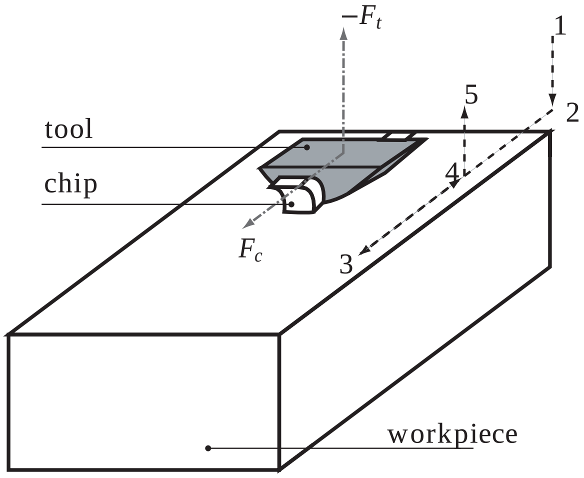

Figure 3.19: Tool movements for the experiments shown by the dotted arrows.

The idea of the used experimental setup for cutting originates from Arcona and Dow's research [94]. The idea is to have the spindle fixed and make the cutting movement with the carriage. This is schematically depicted in Figure 3.19. Disadvantage of this approach is that only relatively low cutting speeds can be achieved. In these experiments a cutting speed of 2 mm/s was used. This cutting speed is approximately three orders lower than in normal turning operations. The distance L that heat diffuses in a material is given by [95]:

$$L = \sqrt{\kappa \cdot t} \tag{3.7}$$

with κ the thermal diffusivity and t the time of deformation. The latter is given by $t = 1/\dot{\epsilon}$ with $\dot{\epsilon}$ the strain rate. Isothermal conditions prevail if

$$\dot{\epsilon} < \frac{\kappa}{L^2} \tag{3.8}$$

The strain rate encountered in cutting was given by Equation 1.6. Using these equations, it can be calculated that with a cutting speed of 2 mm/s isothermal conditions prevail, while in normal turning adiabatic conditions prevail.

The tool is moved to a certain depth of cut (from point 1 to 2) and then moved in one stroke to position 3 (stroke of 15 mm). A dwell time is used before the tool is moved backwards for 7 mm (point 4), where it is retracted from the workpiece (to point 5). Since it is not known what the effect of the cutting process is on the newly created surface (sub-surface damage may be present), the workpieces are not precision turned to a flat surface prior to the actual experiment (this in contrast with the research of Arcona and Dow). Another reason for not doing this is that the aging process would go on while the surface would be turned flat. This turning to a flat surface would take several minutes and the rejuvenated PS would have become aged by that time.

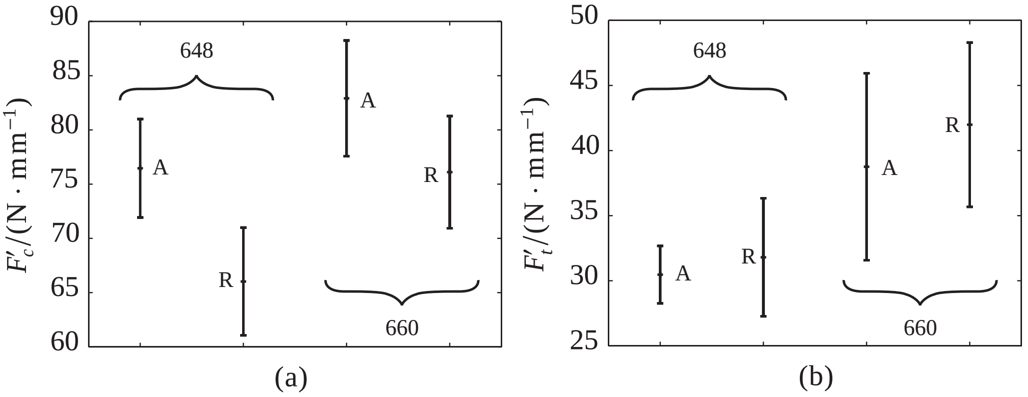

(a) (b)

Figure 3.20: Measured cutting forces of PS Styron 648 and Styron 660 grades in aged (A) and rejuvenated (R) condition.

The main cutting force F_c and thrust force F_t are measured during the experiments with a 3D-component (Kistler 9251A) force transducer. Cuts were made on 10 workpiece samples for each material and material condition.

3.3.2 Results

Force measurements

Since the surfaces were not flat during the experiment, the actual depth of cut changed between 20 and 30 μm. The measured cutting forces are therefore divided by the depth of cut of the formed groove. The assumption here is that the amount of springback is independent of the actual depth of cut, which is true according to Equation 3.9 on page 81.

Figure 3.20(a) depicts the measured main cutting force $F'_c = F_c/h$, and (b) the measured trust force $F'_t = F_t/h$. It shows the values for the two PS grades, both in aged condition (denoted by A) and rejuvenated condition (denoted by R). This figure shows the mean force values plus/minus one standard deviation of the measurement data of all samples for that grade and condition.

It can be seen in Figure 3.20(a) that the cutting force F_c decreases as the material is rejuvenated. This is true for both PS grades. The differences between the mean cutting forces of the two grades was found to be caused by differences in initial yield stress between Styron 648 and Styron 660, which were a result of different cooling times in the injection moulding machine. Figure 3.21 shows the differences in initial yield stresses for the PS grades. These curves were obtained by indentation experiments and subsequent simulations. For the simulations the so-called compressible Leonov model was used. This model uses elasto-viscoplastic constitutive equations for describing the non-linear and rate dependent deformation behaviour of polymers [96]. It leads too far to discuss it here. For further reading about the Leonov-model, see e.g references [50, 97, 98].

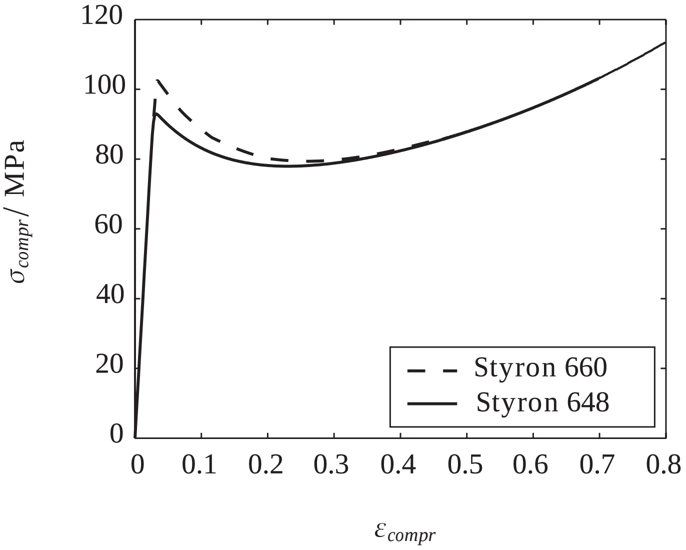

Figure 3.21: Yield curves for both PS grades in aged conditions.

Table 3.12 shows some data of all these experiments. Looking at the calculated ratios between the two grades, it can be concluded that the height of the initial yield stress of a single polymer directly influences the resultant cutting force F_R, and the main cutting force F_c. Remember from Section 2.2 that it is the combination of strength and ductility that determines the cutting forces. This means that for a single polymer grade (like the Stryron 648 used here) the height of the initial yield stress does determine the cutting force, since the post-yield behaviour is the same for the rejuvenated and aged samples.

Table 3.12: Measured cutting forces for (mean) $h = 25$ µm.

Condition		PS Styron 648	PS Styron 660	ratio
aged	σ_y/MPa	93	103	0.90
aged	$F'_c/(\mathrm{N \cdot mm^{-1}})$	76.5	82.9	0.92
	$F'_t/(\mathrm{N \cdot mm^{-1}})$	30.5	38.8	0.79
	$F'_R/(\mathrm{N \cdot mm^{-1}})$	107.0	121.7	0.88
	$\beta = F'_t/F'_c$	0.40	0.47	0.85
rejuvenated	$F'_c/(\mathrm{N \cdot mm^{-1}})$	66.0	76.1	0.87
	$F'_t/(\mathrm{N \cdot mm^{-1}})$	31.1	42.0	0.74
	$F'_R/(\mathrm{N \cdot mm^{-1}})$	97.1	108.1	0.90
	$\beta = F'_t/F'_c$	0.47	0.55	0.85

It can be seen that rejuvenation leads to smaller cutting forces, while the ratios between the two PS grades remain approximately the same. However, the ratio for β, the friction angle, increases upon rejuvenation. This indicates that the thrust force increases (since $\alpha = 0°$). From Figure 3.20(b) a relative increase in the measured thrust forces for the rejuvenated samples can be seen, although the mean values are within each other's standard deviation.

Concerning the differences for β between the two grades, it is interesting to have a look at the amount of material transport underneath a tool. Arcona [24] gives the following experimental relation for metal cutting operations:

$$\delta = 43 \cdot r_n \cdot \frac{H}{E} \tag{3.9}$$

When using $H = 3 \cdot \sigma_y$, $E = 3300$ MPa and σ_y from Table 3.12, it can be seen that the amount of material transport δ underneath the tool is only 10% smaller for the 648 grade than for the 660 grade. Using the research of Zhang and Zhang [99] the normal force on the clearance face (during cutting) due to material springback can be described as:

$$N = \frac{1}{2} \cdot \delta \cdot E^* \cdot b \tag{3.10}$$

with E^* the effective modulus and b width of cut. It is known that E^* can decrease as a result of cracks formed in the sublayer in the previous cut [99]. Combining Equations 3.9 and 3.10 and assuming that $H = 3 \cdot \sigma_y$, it can be derived that:

$$N = 64.5 \cdot b \cdot r_n \cdot \sigma_y \cdot \frac{E^*}{E} \tag{3.11}$$

Based on the 10% lower yield stress of Styron 648, it follows from this equation that the normal force as a result of springback should also be 10% lower when $E^* = E$.

This equation yields $N = 60$ mN for Styron 648 ($\sigma_y = 93$ MPa) respectively $N = 66$ mN for Styron 660 ($\sigma_y = 103$ MPa) with $r_n = 50$ nm and an average $b = 200$ µm.

Figure 3.22 shows that in the back stroke the rebound forces are higher than those calculated: approximately 100 mN for Styron 648 and 250 mN for Styron 660. The differences in measured thrust forces and calculated ones can be a result of a different cutting edge radius r_n. The big difference between thrust forces in backward stroke between the Styron 648 and Styron 660 may be caused by a change in effective modulus E^*. For future research it will be necessary to measure the cutting edge radius accurately prior to each cutting test. Also, micro-indentations can be performed in the cut groove to find out if the effective modulus deviates from the elastic modulus and if it varies per PS grade.

Chip and surface formation

One of the prime interests in the influence of thermo-mechanical history on the cutting behaviour was the question whether aged PS would show a brittle chip formation and rejuvenated PS would show a ductile chip formation, and whether changes in surface quality could be observed.

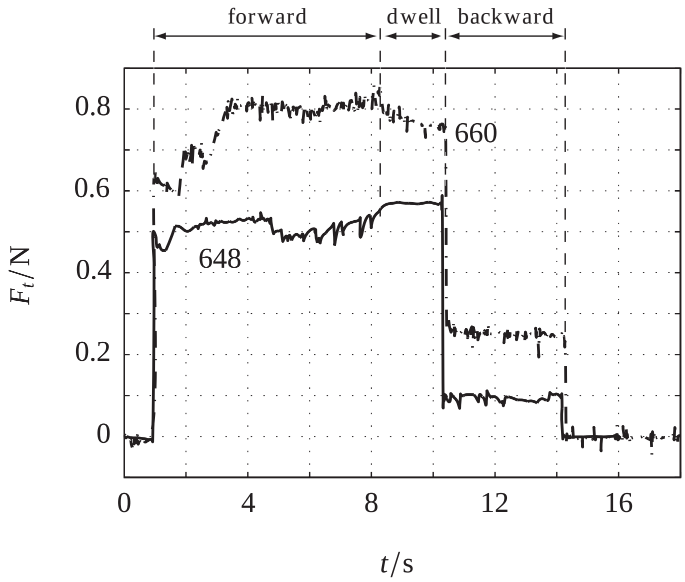

Figure 3.22: Measured thrust forces of an aged Styron 648 grade (solid) and an aged Styron 660 (dash-dot) grade; $v_c = 2$ mm/s, $h = 20$ µm and $R = 1$ mm.

No differences in chip morphology between rejuvenated and aged samples were found by scanning electron microscopy (SEM). All chips, whether they were aged or rejuvenated, were the ductile type. The back sides of the chips were all very smooth; an example is shown in Figure 3.23. Therefore, it seems normal to expect the same kind of surface quality independent of aging time. To validate this one thermo-mechanically rejuvenated PS Styron 660 sample was used. It is known that renewed brittle fracture occurs 1 hour after thermo-mechanical rejuvenation [48]. Figure 3.24(a) shows the used setup. Surface 1, a stroke of 10 mm, was cut 6 minutes after the rejuvenation process. At the end of the stroke a groove was cut, for defining the end of the stroke, and the beginning of the next stroke. All strokes were cut with a radius tool $R = 1$ mm, cutting speed $v_c = 2.4$ m/s, feed rate $f = 10$ µm/rev, and depth of cut $h = 30$ µm. Surface 2 was cut 15 minutes after rejuvenation and surface 3 one day after rejuvenation.

Figure 3.24(b) shows the results of these cuts. Although aging has its influence on the cutting forces, no relation can be seen between *Ra* roughness and aging time in precision turning conditions. Using atomic force microscopy on the turned samples, no differences in topographies could be found. It can therefore be concluded that thermo-mechanical treatments cannot be used for improving the final diamond turned surface quality.

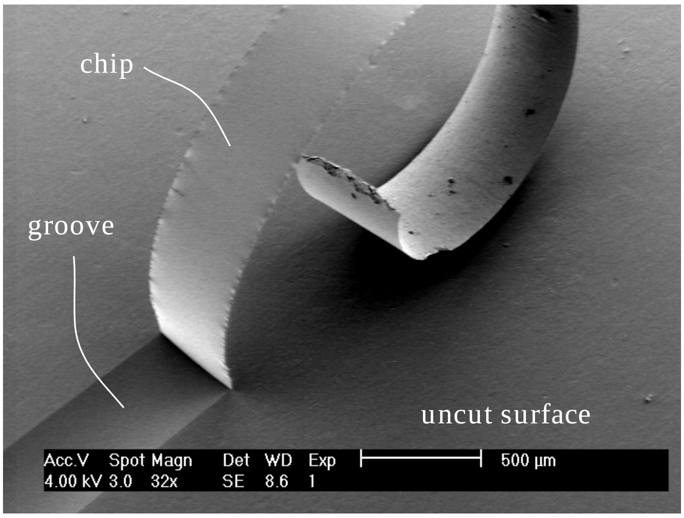
chip
groove
uncut surface
Acc.V Spot Magn Det WD Exp
4.00 kV 3.0 32x SE 8.6 1
500 µm

Figure 3.23: ESEM photo of a ductile PS chip. No brittle/ductile differences were found in the chip morphology between aged and rejuvenated PS samples.

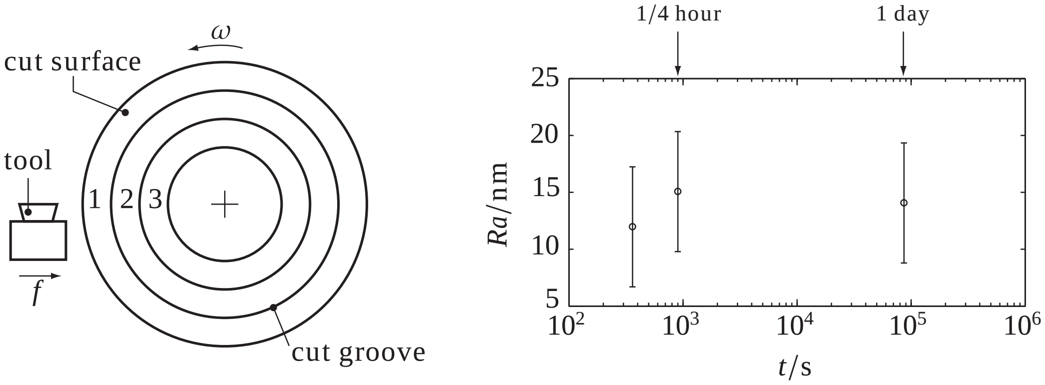

(a) (b)

Figure 3.24: Figure (a) shows the used cutting setup. It was used for determining the influence of aging time on achieved *Ra* roughness value for PS, as depicted in figure (b).

Table 3.13: Measured crosslink densities of several PMMA grades and estimated crosslink density of ADC.

grade number	Material	crosslink density
1	PMMA	$0.46 \cdot 10^{26}$ m^{-3}
2	PMMA	$1.58 \cdot 10^{26}$ m^{-3}
3	PMMA	$2.40 \cdot 10^{26}$ m^{-3}
4	PMMA	$2.83 \cdot 10^{26}$ m^{-3}
5	PMMA	$3.50 \cdot 10^{26}$ m^{-3}
6	ADC	$5.10 \cdot 10^{26}$ m^{-3}

3.4 Influence network density

3.4.1 Experimental

As shown in Figure 1.8 chip and surface formation appear to be dependent on the fact whether one cuts a thermoset or a thermoplast. In fact, Carr and Feger [21] stated that thermosets cannot be machined with good surface qualities, because of their brittle behaviour.

ADC materials, which are thermosets, are often used for spectacle lenses. It is known that they behave very brittle and that they cannot be machined to optical quality, not even by ultrasonic vibration cutting as researched by Kim and Choi [100]. Still, ADC's are interesting for the optical industry, because of their good optical properties. Therefore it may be interesting to find out how crosslink density influences cutting behaviour.

To investigate the influence of crosslink density on achievable surface roughness, experiments were performed on differently crosslinked PMMA grades. These grades have been made by adding ethylene glycol dimethacrylate (EGDM) and initiators Trigonox C, AIBN and V70 to the MMA prior to polymerization. This mixture was poured into a die and placed in an oven for polymerization. Depending on the amount of initiator the crosslink density of the resulting PMMA differed. The amount of crosslink density for the PMMA grades was determined by Dynamic Mechanical Thermal Analysis (DMTA). The results are given in Table 3.13. For ADC an estimate was made, based on data available from Nouriset NS200, an ADC formerly supplied by Akzo Nobel.

Prior to cutting the grades were first heated above their T_g and subsequently cooled to room temperature at a rate of 5 °C/hour in order to achieve samples without frozen-in stresses. Cutting was performed with a diamond tool, rake angle 0° and nose radius 1 mm. Cutting speed was 1.5 m/s, depth of cut 20 µm and feed rate 10 µm/rev. The used samples were all rectangular (approximate dimensions $L \times W = 30 \times 10$ mm^2) and all mounted on the same workpiece holder to enable the same cutting conditions, see Figure 3.25(a). This way, it was possible to measure the cutting forces of all samples in one revolution. This was done with a Kistler dynanometer, type 9251A.

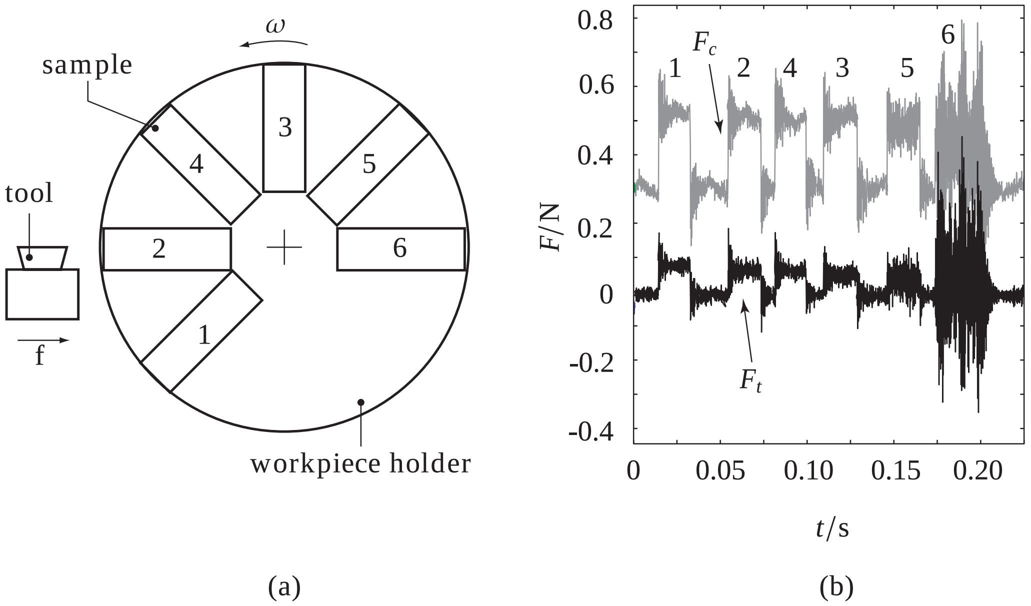

(a) (b)

Figure 3.25: Figure (a) shows the used setup for force measurements on differently crosslinked samples, for numbering see Table 3.13. Figure (b) shows the measured force signal during one revolution. F_c is shifted +0.3 N for clarity. Cutting parameters: v_c = 1.5 m/s, h = 20 µm, f = 10 µm/rev and R = 1 mm.

3.4.2 Results

From the unfiltered force signals in Figure 3.25(b), it is concluded that there is no direct relation in force amplitude and crosslink density. The ADC signal, however, shows significant chatter. This chatter signal is likely to originate from the very brittle chip formation process, as shown in Figure 1.8(a), which is also evident from the measured AFM topography of Figure 3.27(c).

The PMMA grade with the lowest crosslink density, Figure 3.27(a), shows a surface that is very characteristic for normal thermoplastic PMMA. The surface shows a tearing and smearing like behaviour and the footprint left by the tool can be seen clearly. Since only little crosslinker was added to this material it seems normal that it shows such a good similarity with thermoplastic PMMA. Commercially available PMMA is known to have an entanglement density of approximately $\nu_e = 0.77 \cdot 10^{26}$ chains/m^3.

Looking at the surface of the PMMA with the highest crosslink density in Figure 3.27(b), one can see that the surface no longer shows the tearing and smearing like behaviour. The feed marks of the tool are still visible, but the surface shows more small craters, most probably resulting from a more brittle cutting behaviour. Although the surface seems to be formed by a more brittle process, this cannot be seen in the measured roughness value as given in Figure 3.26.

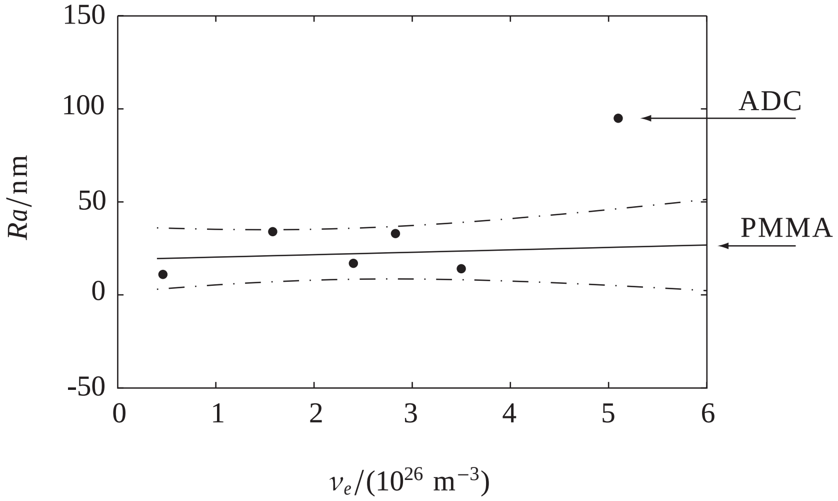

Figure 3.26: Measured *Ra* roughness values for all crosslinked materials. ADC with the highest crosslink density has an extremely high *Ra* value, compared to the different PMMA grades. Cutting parameters: v_c = 1.5 m/s, h = 20 µm, f = 10 µm/rev and R = 1 mm.

Figure 3.26 shows that for all PMMA grades relatively low *Ra* values can be achieved. It was expected that the *Ra* roughness was proportional to the crosslink density. However, ADC shows a very high *Ra* value, which deviates significantly from the expected proportionality. This is mainly caused by the huge amount of cracks that were formed during the cutting process of ADC, see Figure 3.27(c). Because of these cracks no optical quality could be achieved on this sample, only a milky appearance at the surface, while all PMMA grades had a good optical surface quality.

Carr and Feger [21] indicated that crosslinked materials cannot be turned to a good optical quality, because of their brittle behaviour. However, the PMMA with the highest crosslink density, resulted in a good optical quality and low *Ra* value. Obviously another material ”parameter” than thermoplast or thermoset defines the outcome of the surface roughness and surface quality. Which one that is, needs to be investigated in future research.

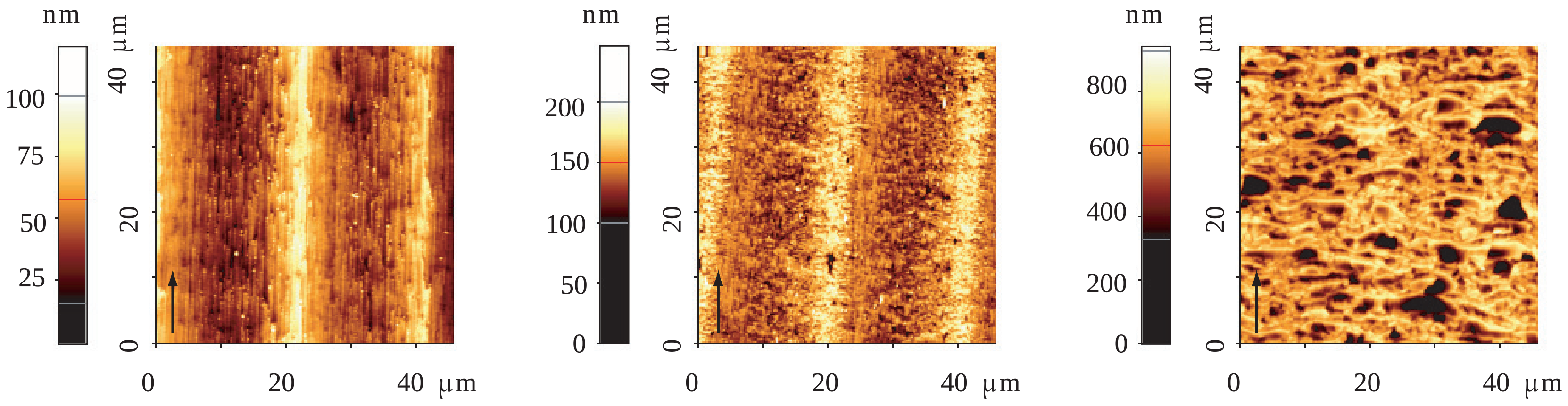
nm
100
75
50
25
µm
40
20
0
0
20
40 µm
nm
200
150
100
50
0
µm
40
20
0
0
20
40 µm
nm
800
600
400
200
0
µm
40
20
0
0
20
40 µm

(a) (b) (c)

Figure 3.27: Measured surface topographies for differently crosslinked samples; (a) PMMA with $\nu_e = 0.46 \cdot 10^{26}$ chains/m^3, (b) PMMA with $\nu_e = 3.50 \cdot 10^{26}$ chains/m^3 and (c) ADC with $\nu_e = 5.10 \cdot 10^{26}$ chains/m^3. With increasing crosslink density the surface topography appears to be formed by a more brittle process. For PMMA this does not lead to a higher *Ra* roughness value. However, ADC behaves very brittle and results in a heavily fractured surface and bad optical quality.

3.5 Conclusions

If one wants to manufacture polymeric optical lenses, it is interesting to know which parameters can be adapted to obtain optical quality. One of the first and most applied solutions is the adaption of cutting conditions, like cutting speed or feed rate. Less thought of is the adaption of the workpiece material. This chapter focussed on the influence of cutting parameters on the cutting temperatures and the adaption of the workpiece material during diamond turning of polymers. Surface properties after turning were described as well.

Looking at the adaption of cutting speed in literature, e.g. Smith's research [44], it is found that an increase in cutting speed will result in more thermal softening. Generally this has always been concluded by the assumption that a better surface quality is achieved when the thermal softening point of the polymer is reached during turning. Section 3.2.1 of this thesis presented the results of the adapted thermal model for polymer turning, and it was found that an increase in cutting speed does not lead to a significant additional increase in temperature rise in the primary shear zone. It was found that with increasing cutting speed the amount of heat transported from the primary shear zone to the chip, which is the combined action of heat conduction and material transport, increases up to 90%! This indicates that adiabatic heating is counteracted by the higher amount of heat removed by the chip.

IR measurements indicated that a higher temperature rise may occur during turning at higher cutting speeds. However, this higher temperature measured by the IR system may have been caused by heating effects of previous cuts. Since higher turning speeds were used, less time for cooling was present during the measurements, resulting in a higher ”offset” temperature. This offset temperature was not used in the calculation of the temperature rise. This makes it difficult to compare the different results; further research would be needed for this.

The results of the adapted thermal model showed that a decreasing depth of cut does not lead to a changing temperature rise in the primary shear zone. Neither does the application of a small non-zero rake angle. A large negative rake angle ($\alpha = -20°$) however, resulted in an additional temperature rise of 30 K in the primary shear zone during plunge turning of PC. Still, this was too less to get the PC into a thermal flow regime, which is in accordance with the conclusion of Smith [44].

Gel permeation chromatography (GPC) on collected chips and bulk workpiece material showed that the used PMMA grade formed chips by a combined mechanism of chain scission and chain slip, while the used PC did not show any chain scission during turning. Firstly, this indicates that it is not the height of the glass transition temperature that determines whether chain scission occurs in turning operations. Secondly, it can be said that the PC chip is formed by a ductile fracture mechanism. It also shows that stress activated flow is a very important parameter in the description of the turning process, which may be a subject for future research.

Looking at the surfaces formed during turning operations on PC in plunge turning, a new surface pattern resembling viscous folding (see Figure 3.8) was observed. It was shown that for zero rake angle the wavelength of the surface pattern scaled linearly with the thickness of the viscous layer, which is in accordance with literature on the subject of viscous folding [92, 93]. However, the appearance of viscous folding is very sensitive to changing cutting geometry, i.e. rake angle.

PMMA did not show viscous folding patterns after plunge turning. The difference between PC and PMMA can be explained by the difference in chip and surface formation processes: PMMA chips are formed by chain scission and chain slip, while PC chips are formed without chain scission.

In face turning processes with a radius tool $R = 1$ mm, feed 10 μm/rev and depth of cut 10 μm, an uncut chip thickness of 1.3 μm is achieved. Looking at the folded surfaces of PC after plunge turning with depth of cut 2 μm, it can be said that the effect of viscous folding in precision turning of PC, i.e. with maximum uncut chip thicknesses smaller than 2 μm, will be small.

Face turning experiments with a nose radius tool and variation of cutting speed, depth of cut, feed rate and rake angle, indicate that the best parameter for improving surface quality is a decreasing feed rate. Further, it appears that for PMMA a small change in rake angle from zero to non-zero seems beneficial. It does not matter whether this non-zero rake angle is positive or negative. Notice that Carr and Feger [21] showed that for turning Vespel a small, positive non-zero angle was beneficial for the achievable surface roughness. For ADC, an optics material and thermoset, a large positive rake angle decreases the surface roughness, although optical quality is not achieved.

Looking at the adaption of the workpiece material, two material states/properties have been investigated. The first is the influence of thermo-mechanical history on the achievable surface roughness. It was found for two PS grades that the thermo-mechanical history had its influence on the cutting forces, but not on the cutting regime, i.e. brittle or ductile mode. Whether the material was aged or rejuvenated, chip formation was always in a ductile manner. Also, the surface roughness value was not influenced by the age of the polymer.

The second workpiece property investigated was the influence of crosslink density. Differently crosslinked PMMA grades and one ADC material were cut in the same experiment. Although a linear relation between crosslink density and *Ra* surface roughness was expected, this was not found. For the PMMA grades, the *Ra* value was found to be 21 ± 13 nm for all PMMA grades. ADC, a thermoset with a 1.5 times higher crosslink density than the PMMA with the highest crosslink density, showed a four times higher surface roughness than was expected by the difference in crosslink density with the PMMA. This indicates that it is not just crosslink density, or the fact that a material is a thermoset, that determines the outcome of the turning operation for thermosets.

Chapter 4

Tribo-electric diamond tool wear

4.1 Introduction

Much research on diamond tool wear has been performed in the past, e.g. [20, 25, 40, 65, 66, 70, 84, 101, 102, 103, 104], but only few references are found on tool wear mechanisms during diamond turning of glassy polymers [21, 40, 103, 104]. Evans [101] used the following classification for diamond tool wear: adhesion, abrasion, tribo-thermal and tribo-chemical. In [40] and [104] tribo-electric tool wear were added to the list for diamond turning of polymers.

Usually more than one wear mechanism is active. However, generally only one is dominant for a certain tool/workpiece combination and a certain cutting regime.

Adhesive tool wear can be excluded as a dominant diamond tool wear mechanism, since adhesive wear always occurs on the softer material of the two adhering materials, which in this case is the polymer and not the diamond.

Looking at abrasive tool wear it can be stated that this can only be excluded by chemical investigation of the polymer. It is known from the production of contact lenses [105, 106] that relatively hard silicon particles can abrade the diamond tool during turning. Appendix F describes the investigation of the wear behaviour of Sil-O-Flex, a contact lens material, that was expected to result in abrasive wear. However, no abrasive wear was found for this material. The materials that are described in this chapter were chemically investigated by energy dispersive X-ray (EDX) analysis and they contained no elements that could cause abrasive tool wear.

Thermal wear of the diamond occurs in vacuum at approximately 1700 °C [107]. At this temperature the diamond structure, which is meta-stable, converts from diamond to graphite. In air thermal wear is enhanced by the presence of oxygen, which causes the diamond carbon to oxidize into CO or CO_2. Oxidation of the diamond structure proceeds quickly above 500 °C [69]. In chapter 2 the temperatures that occur in diamond turning of polymers were described. It was shown that temperatures can increase to approximately 100 °C during turning. This is not enough for thermal wear to occur, and therefore it will be excluded as

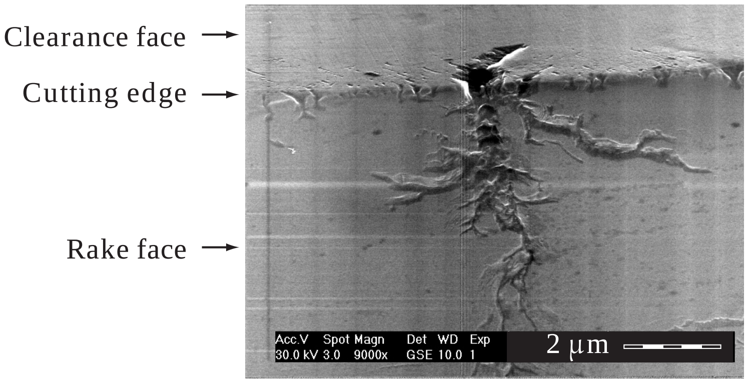

Figure 4.1: SEM photo of tribo-electric wear on a diamond tool. This phenomenon, a so-called ”Lichtenberg figure”, originates from electric discharging.

a dominant wear mechanism too.

Tribo-electric tool wear can occur in two different ways:

1. Tool wear by discharging. This results in so-called Lichtenberg figures [108]. A Lichtenberg figure that damaged a diamond cutting tool during polymer turning is shown in Figure 4.1. Generally, these Lichtenberg figures originate when a dielectric is irradiated with electrons. These electrons get trapped inside the material and accumulate. The depth of penetration is determined by the beam’s energy and the dielectric properties of the material. A huge number of electrons accumulates in the material, forming a space charge. As the material is an electrical insulator, the electrons cease to move free in the material and become trapped. As the space charge builds up, the electric field locally increases until the point is reached where the breakdown strength of the material is reached. When the breakdown occurs, fractal geometries are formed. This process is well known for producing Lichtenberg figures in e.g. PMMA [109].

2. Another, and less instantaneous tool wear that may occur by the presence of electric fields is the detachment of diamond atoms by impinging electrons or ions. When an electric field is present, electrons and ions will be accelerated, increasing their kinetic energy. Assuming that an electron or ion is present in a uniform electric field, the energy U during acceleration of this particle can be derived from the work done on that particle:

   $$U = F \cdot \lambda \tag{4.1}$$

   with λ the mean free path of the particle and F the force exerted on that particle by the electric field E, given by:

   $$F = E \cdot Q \tag{4.2}$$

> with Q the charge of the particle. Then the energy of the particle acquired by travelling a mean free path λ can be given by:
>
> $$U = E \cdot Q \cdot \lambda \tag{4.3}$$
>
> For an electron in atmospheric air the mean free path is $\lambda_e = 10^{-5}$ m, and for an ion in atmospheric air the mean free path is $\lambda_i = 10^{-7}$ m [110]. The acquired energy can be used for damaging the diamond surface by impingement of the particle and detachment of a carbon atom, which requires an energy of 7.4 eV.
>
> Since the mean free path of ions is smaller than that of electrons, ions need a higher electric field strength than electrons before they can damage a surface. During discharges the electric field strength can easily be a factor 100 more than calculated by Equation 4.3 [111]. This implies that the energy of ions will be sufficiently high for damaging the tool by impact as well. Because of the higher mass, ions can more easily damage a surface by impact than electrons.

Equation 4.3 is at the base for quantifying tribo-electric tool wear. Therefore, this chapter will present measurements for determining the electric field strengths in diamond turning of polymers. It can be expected that turning parameters, such as cutting speed, feed rate and depth of cut, will directly influence the electric field strength during turning. Besides these turning parameters, workpiece properties may also influence the amount of charging. The environmental effect of relative humidity on charging is also known.

This chapter will present measurements that were performed to describe the tribo-electric tool wear in diamond turning of glassy polymers. It presents the influence of turning parameters on charging, the effect of material properties, and the effect of relative humidity. The experiments described in this chapter indicate when tribo-electric wear can be dominant.

4.2 Charging in polymer cutting

4.2.1 Charging at low cutting speeds

In this section the charges generated at the cut surface of PMMA, PC and PSU will be derived. PMMA was chosen since it can easily be machined to optical quality and it is quite often used. PC is known to be used as spectacle lens material. PSU was chosen since it was observed to result in a clear luminescence in prior cutting experiments.

In the experiment a relatively low cutting speed (100 mm/min) was used. Although the cutting speed is relatively low compared with normal turning conditions, this experiment creates the possibility of making non-overlapping cuts on

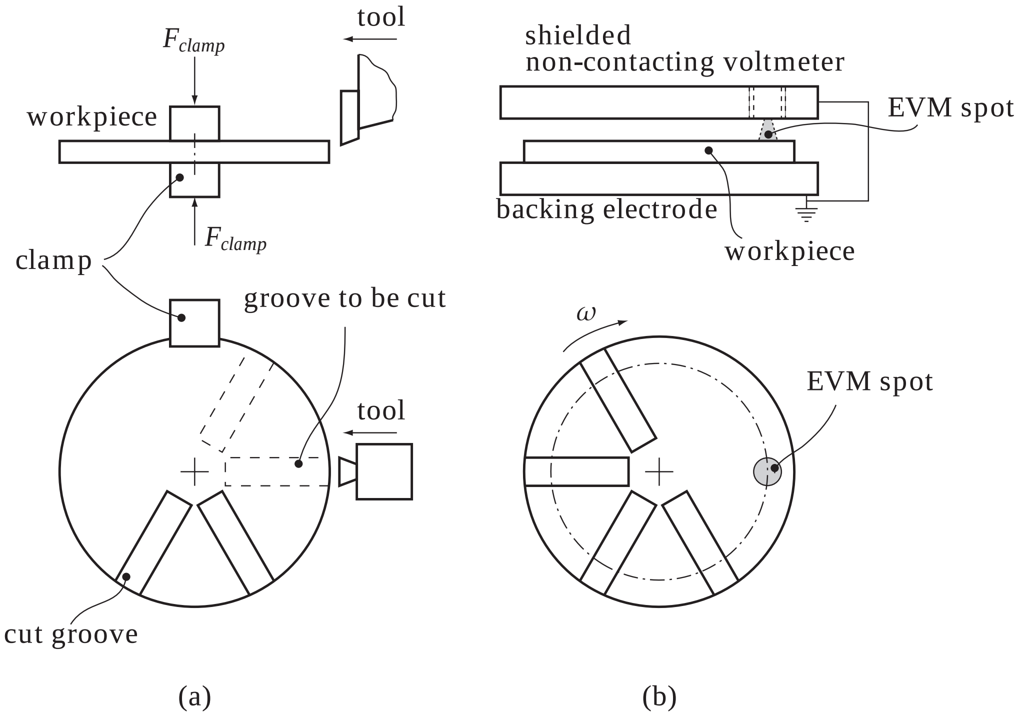

Figure 4.2: Schematic setup for measuring surface potentials; (a) shows the cutting of the grooves and (b) the measurement setup with the electrostatic voltmeter.

one workpiece. This way, the reproducibility can be checked. The main idea of this setup was to investigate the difference in charging of the used polymers.

Setup

Figure 4.2 shows schematically the used setup for these measurements. Prior to the experiments, the workpiece surface is flattened by turning it twice with a nose radius tool of 1 mm at a feed rate of 20 μm/rev and depth of cut of 20 μm. Subsequently, the workpiece was discharged with a wet tissue and it was verified that the measured surface potential was zero before the cutting experiment was started. The spindle was fixated against rotation with a clamp, see Figure 4.2(a). A faceted tool, width 2.7 mm, was used for making cuts at a cutting speed of 100 mm/min and depth of cut of 5 μm. Four single cuts were made per workpiece, by rotating the workpiece after each cut.

After cutting the spindle was released, so it could rotate free again. A revolution speed of approximately 0.25 Hz was used. This rotation speed was small enough in comparison to the response time of < 2.5 ms of the used electrostatic voltmeter: a Monroe Electronics Electrostatic Voltmeter, type 244A, in combination with a high resolution Kelvin probe (type 1017AEH). Such a Kelvin probe can be used for determining surface charges at insulators [112].

Notice that insulators are volume charged, but that they behave, as far as their external field is concerned, as if they have surface charge densities on their exterior surfaces. These quantities are referred to as ”projected” or ”effective” surface charge densities. A Kelvin probe can only measure the effective charge density and not the charge distribution withing the thickness of the insulator [112].

The measurement of the electrostatic voltage was performed using a shielded electrostatic voltmeter and a backing electrode for the polymer workpiece. This is schematically depicted in Figure 4.2(b). The surface charges were determined, using the equations presented in Appendix G.

From the surface charge σ the electric field strength E can be calculated using Equation 4.4, which can be used for a uniform electric field between two infinite parallel plates:

$$E = \frac{\sigma}{\epsilon_0 \epsilon_r} \tag{4.4}$$

with ϵ_0 the absolute dielectric constant in vacuum and ϵ_r the relative dielectric constant, which is material dependent.

Results

Table 4.1 gives the results of the measurements and the calculations for deriving the electric field strength. It can be seen that PMMA shows little charging compared to PC and PSU.

Table 4.1: Measured surface charges and electric field strengths at v_c = 100 mm/min, h = 5 µm, b = 2.7 mm and $RH \approx 50\%$.

Material	$\sigma/(\mathrm{C \cdot m^{-2}})$	$E/(\mathrm{kV \cdot mm^{-1}})$
PMMA	$-3.4 \cdot 10^{-6}$	-0.4
PC	$-4.4 \cdot 10^{-5}$	-5.0
PSU	$+6.8 \cdot 10^{-5}$	$+7.7$

Further it can be seen, that both PC and PSU reach electric field strengths above the critical field strength of air given by van Veldhuizen [113] as 1 kV/mm, while PMMA stays below this critical value.

Notice in this table that the signs of the measured surface charge of PMMA and PC are opposite to that of PSU. Based on the tribo-electric series and the value of the relative dielectric constant of PMMA, PC and PSU, see Table 4.3, polymers should charge negative when brought into contact with diamond. Although relative humidity can have a significant effect on the relative dielectric constant of a polymer, see [83], the RH-value in all experiments was 50% ± 2%. Therefore, the different sign of charging for PSU must have another origin.

The best explanation derived from literature is the difference in polymer structure. Although no general rule is available yet, a summary is given next.

Sharma and Pethrick [114] showed that PMMA grades with different tacticities charge different and even with opposite sign with respect to each other. Tacticity means the way side groups are positioned to the polymer main chain. This positioning can be regular or irregular. When the side groups are regularly positioned, meaning that they are positioned at one side of the main chain, the polymer is called ”isotactic”. When the side groups alternate from one side of the main chain to the other side, the polymer is called ”syndiotactic”. Full irregular positioning of the side groups leads to an ”atactic” polymer.

The work of Sharma and Pethrick is partly supported by Dickinson et al. [115], who came to the same conclusion concerning the effect of tacticity. However, they performed experiments in vacuum, showing that water had no influence on the sign of charging, which was in contrast with the results of Sharma and Pethrick. This indicated that the sign and amount of charging is mainly determined by the chemical structure of the polymer.

Taylor et al. [116] measured electrostatic charging during capillary extrusion. They found that the sign of charging of PS was dependent on filler materials, where impurities can have an influence as well. The presence of additives of low molecular weight commonly found in commercial polymers [117] can also be a reason. Besides frictional charging at an interface consisting of two different solids, Taylor et al. [116] indicate that charge can also be generated by internal slip in the polymer.

Shashoua [118, 119] concludes that whether a polymer charges positive or negative is dependent on the decay of both negative and positive charges. The slowest decaying one determines the sign of charging. This effect is polymer dependent. Shashoua [118] also noted that this charge selectivity of the electrostatic charging of polymers can easily be ”reversed through contamination by inorganic and organic ions”.

Based on these findings, it can be said that the differences in charging can be a result of differences in both polymer structure and contaminations in the polymers.

Although most research seems to indicate that the sign and amount of charging is dependent on the polymer structure, no general rule has been found yet. Further research is needed for this, but for this research that was not necessary, since the goal is to find out what parameter(s) determine(s) the amount of tribo-electric tool wear.

4.2.2 Charging at higher cutting speeds

Charging at higher cutting speeds (1 m/s) and with overlapping cuts is investigated, since this is ”common practice” in industry.

For the charge measurements at higher cutting speed only PMMA and PC were tested. PSU was not tested in this setup, but results for PSU, turned under different conditions, are presented within the next sections as well. Based on the findings of the low speed cutting test, an estimate is made for PSU. These three materials are also used in the tool life tests described in Section 4.5.

The surface charges generated during cutting with a radius tool (R = 1 mm), constant cutting speed 1 m/s, feed rate 2.5 mm/min and depth of cut 20 µm were determined. The results are given in Table 4.2. It can be seen in this table that PC charges more with these cutting conditions than PMMA.

Table 4.2: Surface charges for PMMA, PC and PSU after face turning with a radius tool $R = 1$ mm, $v_c = 1$ m/s, $f = 2.5$ mm/min, $h = 20$ µm and $RH = 44\%$.

Material	$\sigma/(\mathrm{C} \cdot \mathrm{m}^{-2})$	$E/(\mathrm{kV} \cdot \mathrm{mm}^{-1})$
PMMA	$+8 \cdot 10^{-6}$	0.9
PC	$+28 \cdot 10^{-6}$	3.2
PSU	$-43 \cdot 10^{-6}$	-4.8

Based on this table, it can be concluded that PMMA will most probably not result in electric breakdown of air during diamond turning, since the electric field strength is less than the electric breakdown strength of air. Based on the electric field strengths found for PC and PSU it is expected that they result in electric breakdown and luminescence. This will be discussed in the next section.

4.3 Luminescence observations

It has been shown in the previous section that the charges generated during cutting can be sufficient for electric breakdown in air to occur during diamond turning of polymers. If breakdown in air occurs, one should be able to see luminescence, like lightning from the sky.

4.3.1 Observations

Table 4.3 presents some luminescence observations by the author during precision turning of several polymeric materials. Not all materials showed luminescence during the diamond turning process. PMMA was not observed to show luminescence during diamond turning with these conditions, but Grabchenko et al. [120] did see it. The reason for this deviation is not known, but may be a result of different polymer and/or turning conditions.

Cutting with a faceted tool on tubular PC (width of cut 2 mm) in a dark environment resulted in the luminescence shown in Figure 4.3. This photo shows the luminescence appearing near the cutting edge and at the rake face of the tool, but it is not exactly clear where the luminescence appears, since the recording rate of the camera was not high enough for shooting a ”stand-still” photo. Observations of the recorded movies showed a very clear luminescence around the produced chip and the rake face, and less intensity at the cut surface.

The luminescence observations of PC and PSU are in accordance with the calculations of Section 4.2, indicating that for PC and PSU the breakdown strength

Table 4.3: Luminescence observations by the author during diamond turning of several polymers.

Material	Luminescence?	ϵ_r
PMMA	no	2,6-3,7
PC	yes	2,6-3,0
PSU	yes	3,1

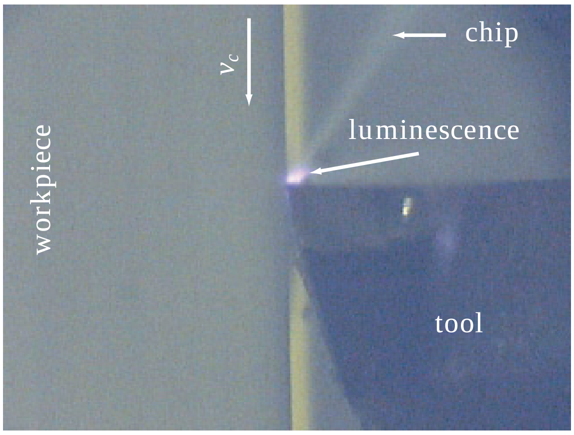

Figure 4.3: Luminescence during turning of PC.

of air was reached. For PMMA no luminescence was observed, confirming the calculations too.

To verify that breakdown in air can occur during diamond turning of polymers, spectral measurements were performed. The other reason for spectral measurements is to find out whether luminescence occurs during turning of PMMA as well, since spectrometers are very sensitive. Also, longer observation/registration times can be used than by the human eye. The results of the spectrometer measurements may concur the luminescence observations for PMMA of Grabchenko et al. [120].

4.3.2 Spectral measurements

Prior to the spectral measurements the diamonds were placed underneath an ultraviolet (UV) lamp. This was done to exclude diamonds having a band gap excitation from the nitrogen inclusions at 5.5 eV[1] [69]. When a diamond has such a band gap excitation, this will be visible in the recorded spectrum as well, making the analysis of the spectrum more difficult. The used diamonds did not have a band gap excitation.

Spectral measurements are performed using a spectrometer (Ocean Optics

---

[1] 1 eV = $1.60219 \cdot 10^{-19}$ J

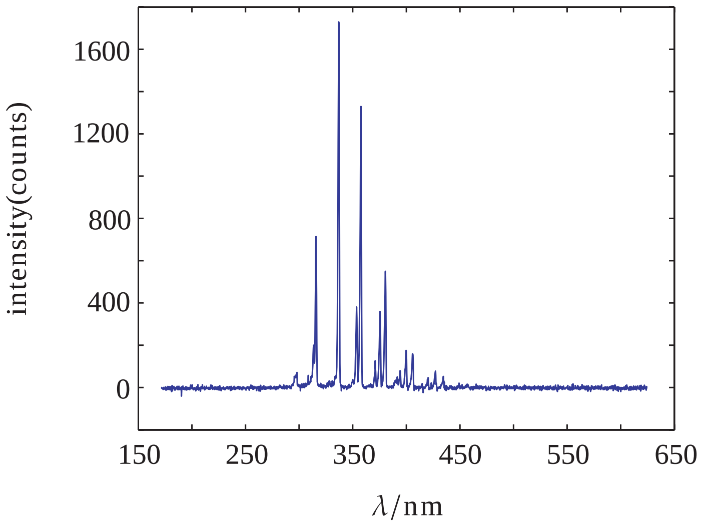

Figure 4.4: Full recorded spectrum during turning of PC (v_c = 1.6 m/s, f = 10 µm/rev and h = 0.12 mm), mainly showing the peaks resulting from excited nitrogen.

HR2000) with a measurement range of 171 nm to 624 nm and a resolution of approximately 0.2 nm. The spectrometer is used in combination with an optical fiber and a collimating lens. The turning machine was shielded from environmental light by a thick black polymer foil.

Measurements were made for both PMMA and PC with a mono-crystalline diamond tool (R = 1 mm). No luminescence was detected during precision turning of PMMA, indicating that the electric field is indeed too small for discharging to occur around the tool. As expected from the naked eye observations, PC shows a spectrum. The recorded spectrum is shown in Figure 4.4 for a relatively large depth of cut.

Analysis showed that this spectrum originates from excited nitrogen [121], with a characteristic wavelength of 337 nm. This wavelength belongs to the vibrational state of the nitrogen molecule [122], which is the so-called second positive system of excited nitrogen [123][2].

The existence of excited nitrogen in the spectrum can only be ascribed to a plasma in air, since PC has no nitrogen in its polymer chains. Therefore, it can be concluded that the luminescence must occur from discharging and not from (deformation) mechano-luminescence in the polymer, as described by Grabchenko et al. [120]. This is confirmed by the observations of Fuhrmann et al. [124] who observed only little emission phenomena (photons, neutral and/or charged particles) during shearing of PC.

Figure 4.5 shows a detail of a measurement from which it was concluded that OH radicals are present in the spectrum [125]. The possible consequence

---

[2] The second positive system is ascribed to the $C^3\Pi_u \rightarrow B^3\Pi_g$ transition [123].

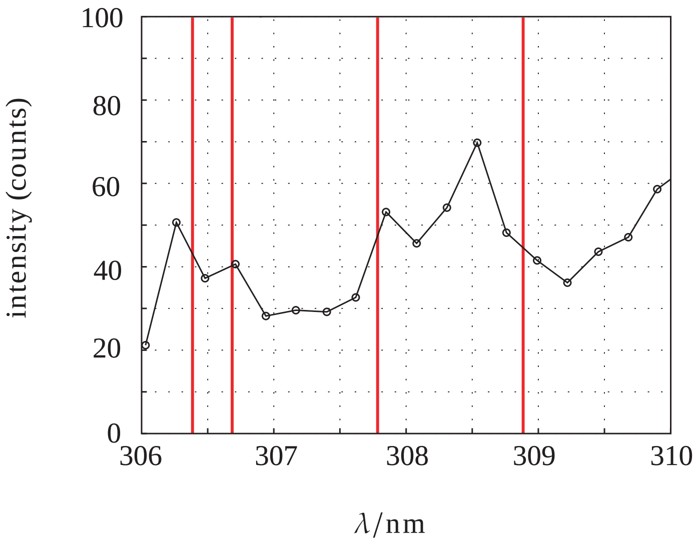

Figure 4.5: Measured spectrum during diamond turning of PC, showing the *OH* contribution to the spectrum. Vertical lines indicate characteristic wavelengths of *OH* radicals.

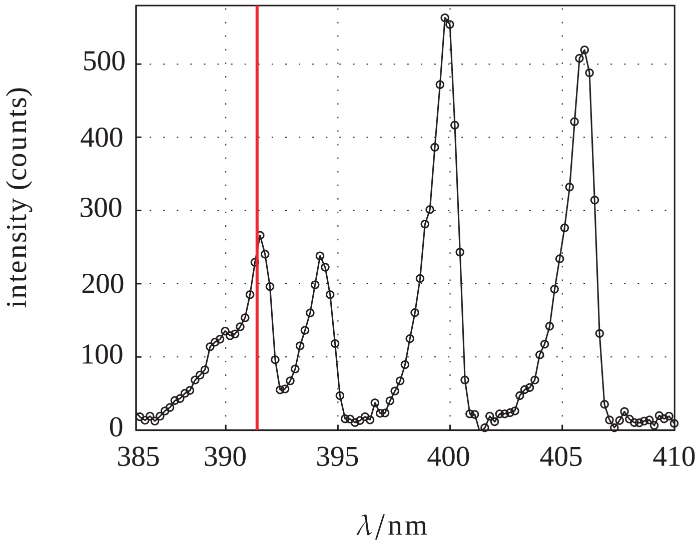

Figure 4.6: Measured spectrum during diamond turning of PC, showing the N_2^+ peak at $\lambda = 391.4$ nm.

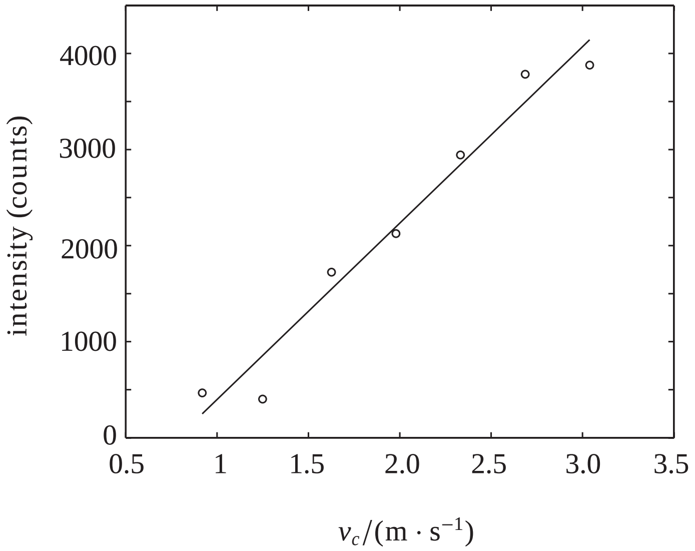

Figure 4.7: Measured intensities at $\lambda = 337$ nm for different cutting speeds during turning of PC ($f = 10$ µm/rev and $h = 0.12$ mm). The solid line (least-squares fit) is drawn as a guide to the eye.

of these OH radicals on tool wear will be discussed in Section 4.5.1. Another detail of a measurement is given in Figure 4.6, where the peak at $\lambda = 391.4$ nm is characteristic for the presence of the N_2^+ nitrogen ion [113].

Generally oxygen molecules cannot be visualized that easily, because of their weak emission intensities. Ozone cannot be measured in emission, but only in absorption. Therefore, nothing can be concluded from the spectral measurements concerning the presence of reactive ozone.

Influence of cutting speed Figure 4.7 shows the relation between the recorded intensity at a wavelength of 337 nm and the applied cutting speed. It can be seen that there exists a linear relation between the applied cutting speed and the luminescence that was detected. Notice that for this depth of cut and feed rate there appears to be a certain critical cutting speed ($v_c \approx 0.75$ m/s) for luminescence to occur. As will be shown in Section 4.4, the amount of electrostatic charging is also depended of the applied cutting speed. Combining these results indicates that a certain cutting speed is necessary for producing enough surface charge for electric breakdown to occur. The observed dependence of the luminescence intensity and speed was also observed by Nakayama for sliding experiments of diamond on sapphire [126].

Nakayama et al. [127, 128] showed that no correlation exists between friction coefficient and tribo-emission intensity. The reason for this is that tribo-emission intensity is mainly dominated by the electrical resistivity of the solid. This was concluded after measurements on different conductors, semi-conductors and insulators. The experiment included the (crystalline) polymers teflon and nylon.

They found that the amount of tribo-emission is dependent on the amount of surface damage. The amount of damage was dependent on sliding speed, radius of the diamond slider and the hardness of the tested material. They found a decreasing tribo-emission intensity with increasing hardness of the tested materials.

Based on the general assumption that the hardness of a material can be described as:

$$H = 3 \cdot \sigma_y \tag{4.5}$$

and using σ_y given in Table 2.2, it can be seen that PMMA has a significantly higher hardness value than PC and PSU. Therefore, from Nakayama's point of view, PMMA should show less luminescence than PC and PSU, which was indeed observed.

4.4 Conditions influencing charging in polymer turning

This section presents measurements that were performed in order to obtain the factors that influence the charging behaviour in the diamond turning process of polymers. This can be used to decrease tool wear provided that tribo-electric tool wear is dominant.

4.4.1 Influence of cutting speed

Surface charges for PSU were measured at two different rotational speeds, namely 1000 rpm and 2000 rpm, on the same workpiece in subsequent turning experiments. Turning was performed with feed rate $f = 20$ µm/rev, depth of cut $h = 50$ µm, tool nose radius $R = 1$ mm and relative humidity $RH \approx 50\%$.

When plotting the measured surface charges against actual cutting speed instead of rotational speed the curves overlap, see Figure 4.8. This indicates that cutting speed is indeed an important factor in the charging behaviour. It can be seen that with increasing cutting speed the amount of generated charge increases too.

A possible explanation is given by Taylor et al. [116] who indicate that in extrusion processes charge is generated within the polymer. It is known that the charging behaviour during capillary extrusion is speed dependent too. Increasing speed may lead to an increased (internal) frictional charge generation. Such a generated charge will be measured by the used electrostatic voltmeter. Another explanation is given by Nakayama et al. [128], who indicate that the increase in charging is a result of increasing surface damage with higher sliding speeds. Turning can be considered as a process that continuously creates a fresh surface. This can be considered as a damaged surface.

Kumar and Perlman [129] indicate that local heating effects facilitate charge transfer too. From Chapter 3 it became clear that increasing cutting speed does

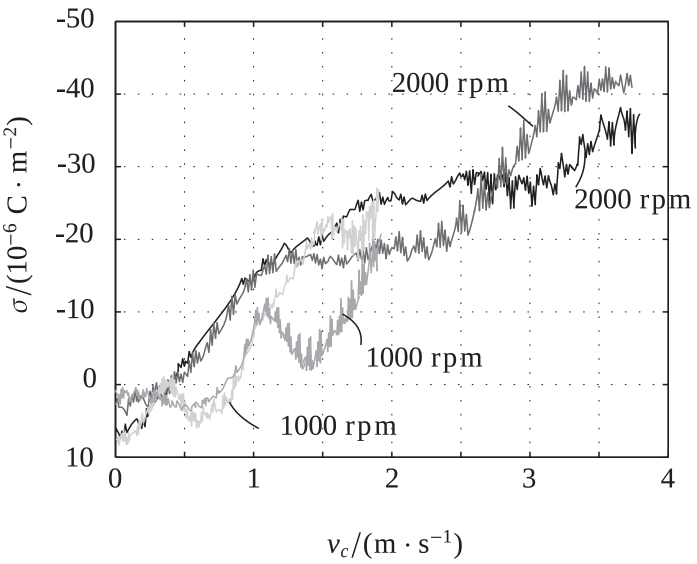

Figure 4.8: Measured surface charges on PSU for $f = 20$ µm/rev, $h = 50$ µm, $R = 1$ mm and $RH \approx 50\%$.

not significantly influence the maximum temperature rise in the primary shear zone. However, it influences the temperature rise distribution. This may have an influence on the charging behaviour in cutting.

Notice in these experiments, that for smaller cutting speeds the sign of the charge changes. This is in accordance with the low cutting speed measurements of Section 4.2.1, where a positive charge was measured for PSU.

Another important aspect during these experiments was that the luminescence disappeared at a certain distance from the center, or better said at a certain cutting speed, since a constant rotational speed was used. Depending on the used rotational speed, this location shifted. Therefore, it can be concluded that luminescence is dependent on the used cutting speed. This was already shown for PC in Figure 4.7.

It was roughly estimated that, with the previously described turning conditions for PSU, the luminescence disappeared at a cutting speed smaller than 2 m/s. From Figure 4.8 it follows that the luminescence appears at surface charges above 20 µC/m^2 for the used PSU. This is in reasonable agreement with the critical surface charge value of 26.4 µC/m^2, given in [130][3], before breakdown occurs above the surface.

4.4.2 Influence of feed rate

Figure 4.9 shows the measured surface charges for PMMA cut with different feed rates. The figure shows several measurements. The deviation on the measured signals is significant, however, the trend is clear: increasing feed rate results in an increasing charge generation. This can be ascribed to a larger damaged surface area [128].

---

[3] This charge was derived for a breakdown strength of air of $E = 3 \cdot 10^6$ V/m.

4.4.3 Influence of depth of cut

The curves shown in Figure 4.10 give the measured surface charges for different depths of cut after turning PSU. The gray curves and straight LSQ fit were derived for depth of cut $h = 50$ µm and the black curves and LSQ fit were derived for smaller depth of cut $h = 20$ µm. Notice the deviations for the 20 µm measurements.

From this figure it becomes clear that with a bigger damaged surface area, as a result of the bigger depth of cut, more charge is generated. This is the same response as for bigger feed rates.

4.4.4 Influence of humidity

The effect of humidity is known on surface charges: with high air humidities static electrification becomes less, while at low humidities static electrification occurs more easily. The amount of static electrification is dependent on the decay time of the generated charge. From Shashoua [119] it follows that with increasing relative humidity, the decay time of the charge present decreases by several orders.

From van Krevelen [83] it is known that the relative dielectric constant of hydrophilic polymers, like PMMA, is very dependent on the relative humidity (RH). This is mainly caused by the high relative dielectric constant of water ($\epsilon_r = 80$). In Table 4.3 it can be seen that for PMMA $2.6 < \epsilon_r < 3.7$. The lowest value is for dry environment and the highest value for wet conditions. The relative dielectric constant of hydrophobic polymers, like PS, is less susceptible to RH values.

Looking at Equation 4.4, given as $E = \sigma/\epsilon_0\epsilon_r$, it can be seen that with decreasing surface charge, the electric field strength decreases too. Decreasing electric field strength can also be obtained by an increasing relative dielectric constant ϵ_r. It is interesting to notice that both a decrease in surface charge and an increase in relative dielectric constant are a result of an increasing relative humidity. Thus, if one increases the relative humidity of the cutting environment, lower field strengths will be formed, resulting in less electrostatic tool wear. This effect on electrostatic tool wear is also known from industry: at higher RH values (70%), no significant electrostatic tool wear is observed [41].

To measure the influence of relative humidity on tribo-electric charging in cutting, a shielding was placed on the turning machine. In this turning environment humid air was applied and the RH value was measured with a hand-held hygrometer. The hygrometer had a measurement uncertainty of maximal 3% RH. Deviations in relative humidity within the shielding were determined to be within 5% RH. The uncertainty of the measured RH value at the cutting edge is therefore 8% RH.

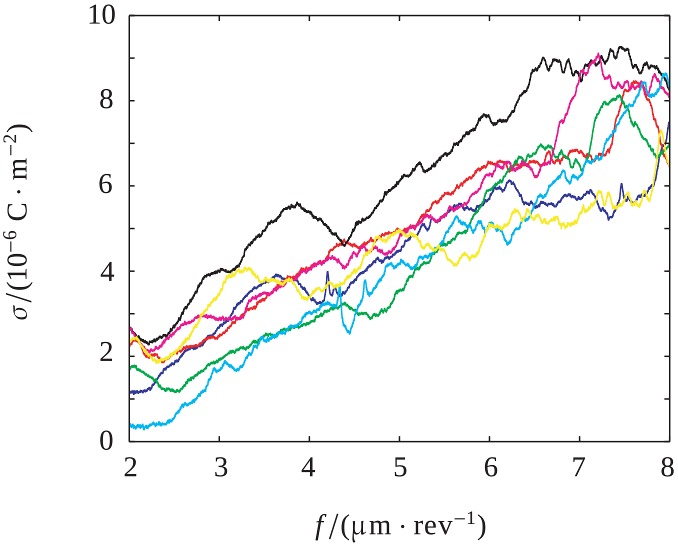

Figure 4.9: Several measured surface charges on PMMA for $v_c = 1$ m/s, $h = 20$ µm, $R = 1$ mm and $RH \approx 50\%$. Increasing feed rate results in an increasing surface charge.

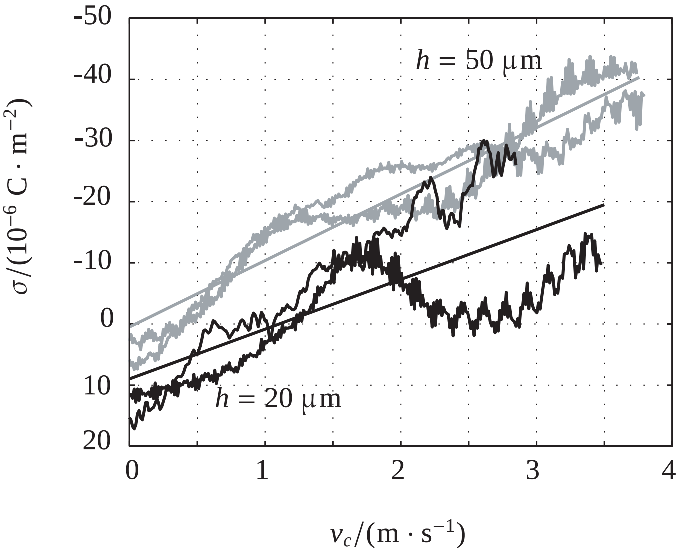

Figure 4.10: Measured surface charges on PSU for different depths of cut, $f = 20$ µm/rev, $R = 1$ mm and $RH \approx 50\%$. LSQ fits are given as a guide to the eye.

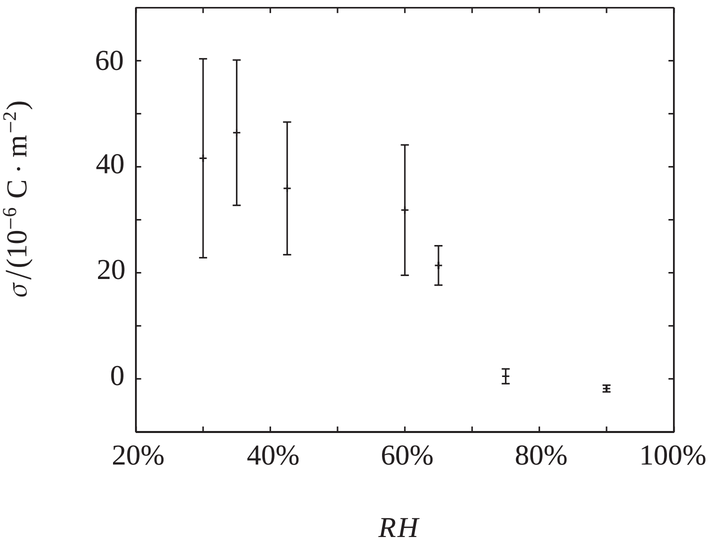

Figure 4.11: Influence of relative humidity on the measured charge during turning of PC.

Figure 4.11 shows the measured surface charges +/- one standard deviation against the relative humidity of the environment. It can be seen in this figure that at RH-values above 60% the charge present on the cut surface decreases rapidly to zero. Therefore, it can be expected that tribo-electric tool wear can be decreased significantly if an appropriate air humidity is chosen, preferably above 60% RH.

4.4.5 Influence of chain scission

Thermoplastic PMMA shows chain scission during cutting, see Table 3.3. Therefore it is interesting to find out whether chain scission contributes to the amount of charging. To investigate if chain scission contributes to the amount of charging, crosslinked PMMA grades were made. This was done from pure MMA to which EGDM (Ethylene Glycol Dimethacrylate) and initiators Trigonox C, AIBN and V70 were added. Such a combination results in crosslinking during polymerization. Before the liquid was put in an oven, it was mixed thoroughly and cast into a die to get plates. Different amounts of EGDM were added to get different crosslink densities.

Figure 4.12 shows the results of the surface charges for differently crosslinked PMMA grades, and the measured surface charge of the thermoplastic PMMA, used in this investigation.

The figure shows that with increasing crosslink density, the amount of charging increases as well. It was observed that all materials were cut with (semi)ductile chips. Although the exact mechanism of the charge generation is not known at the moment, it can be said that materials with higher crosslink densities show more charging during diamond turning. It can therefore be expected that materials

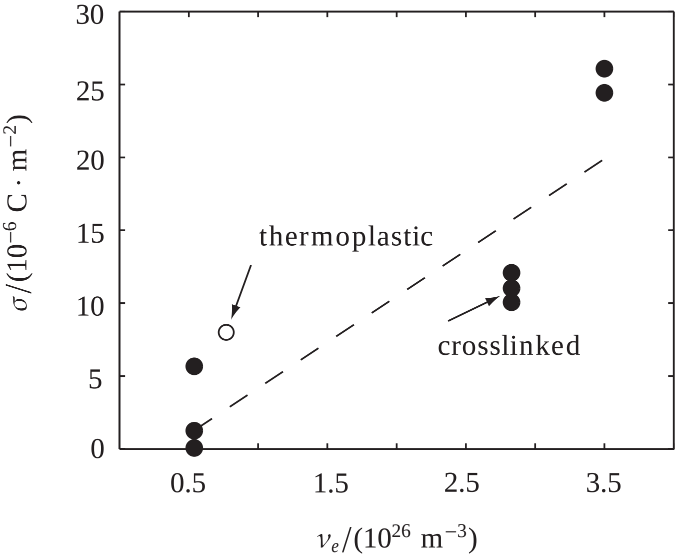

Figure 4.12: Measured surface charges for different polymers at $v_c = 1$ m/s, $f = 2.5$ mm/min and $h = 20$ µm; (●) denote the crosslinked PMMA grades, (○) denotes the thermoplastic PMMA grade.

with high crosslink densities are more likely to result in a dominant tribo-electric tool wear.

4.5 Tool life experiments

4.5.1 Expectations

In the previous sections a lot of measurements and observations have been presented. The question until now is: does tribo-electric tool wear occur during diamond turning of all polymers? To verify this, tool life experiments have to be performed. Dry cutting ($RH < 60\%$) has been performed on PMMA, PC and PSU. During diamond turning of PC and PSU luminescence was observed. It was shown in Section 4.3.2 that the luminescence had its origin in discharging. Therefore, a wet turning experiment was also performed on PC to find out whether a possible tribo-electric tool wear by discharging could be ruled out. Wet turning was performed by applying a water spray on the cutting zone. Table 4.4 summarizes the used conditions, observations and expectations for tribo-electric tool wear to occur during the tool life tests. The expectations will be explained next.

Grillo and Field describe in their work [131] that electrical processes do not play a significant role in polishing of diamond. They investigated this by subjecting different kinds of diamond to discharging from an electrode. No significant wear was observed. However, sparking can occur during diamond turning of polymers

Table 4.4: Summary of experimental findings.

Material	Condition	Luminescence observed?	Charging above $E_{crit} = 1$ kV/mm ?	Tribo-electric tool wear expected?
PMMA	dry	no	no	no
PC	dry	yes	yes	yes
PC	wet	no	no	no
PSU	dry	yes	yes	yes

and it can severely wear the cutting edge, see Figure 4.1.

Based on the results for charging at higher cutting speeds (Table 4.2) the energies given in Table 4.5 were derived using Equation 4.3 for electrons moving in a uniform electric field.

Table 4.5: Calculated impact energies of electrons during dry turning conditions.

Material	$\lvert E \rvert$	$\lvert U_e \rvert$
PMMA	900 V/mm	$1.4 \cdot 10^{-18}$ J (9 eV)
PC	3200 V/mm	$5.1 \cdot 10^{-18}$ J (32 eV)
PSU	4800 V/mm	$7.7 \cdot 10^{-18}$ J (48 eV)

It can be seen in Table 4.5 that turning of PMMA results in a calculated electron impact energy of 9 eV. It is known that for the second positive system of nitrogen in air by discharging, an energy of approximately 11 eV is needed [123, 132]. In Section 4.3 was described that no luminescence appeared during turning of PMMA. Therefore it can be concluded that the calculated electric field strengths are in accordance with the observations. For PC an energy of 32 eV is calculated. This is sufficient for exciting nitrogen [123], which is in accordance with the observed spectrum of Figure 4.3. PSU was also seen to result in luminescence during turning.

As discussed in the introduction of this chapter, two possible tool wear mechanisms can be present in case of tribo-electric charging in diamond turning of polymers:

1. Tool wear by a discharging mechanism.
2. Tool wear by impacting particles (electrons and/or ions) accelerated in the electric field.

Tool wear by discharging Tool wear by discharging can be split into two different phenomena. First, as described in the introduction, electrons may accumulate in the tool, creating a space charge that may eventually lead to an abrupt discharge starting from within the material. This way, a Lichtenberg figure is created. Second, a discharge in air that leads to chemically, oxidative reactive species, like peroxides and ozone, around the tool. A more detailed description of possible reactive species formed in discharging is given in Appendix H.

Experiments showed that in dry turning conditions both PC and PSU showed luminescence. Table 4.5 showed that the calculated electric field strengths (based on parallel capacitor equations) are high enough for discharging in air. However, for diamond it is known that it has a breakdown strength of $1 \cdot 10^8$ V/m – $20 \cdot 10^8$ V/m, or better said, 100 to 2000 times higher than air. Based on the calculations, this seems hard to achieve. However, inclusions or scratches may locally increase the electric field strength, resulting in Lichtenberg figures from discharging.

Tool wear by impacting particles Table 4.5 showed the calculated impact energies of electrons for a certain diamond turning process of PMMA, PC and PSU. Since it is an estimate based on plane capacitor theory the values can be considered to be underestimates. Also, no energies were calculated for ions. The main reason for this is that ions become important once a discharge is formed, such as in diamond turning of PC and PSU. During discharging no longer a uniform and homogeneous electric field can be assumed [133] and the electric field strength can increase significantly more than the calculated uniform field strength. In fact, the electric field can increase a factor 100 [111], indicating that even ions with their short mean free path length will posses sufficient energy (order 10^{-18} J) to result in dissociation of the diamond lattice with a bond dissociation energy of $1.2 \cdot 10^{-18}$ J.

Because of their longer mean free path length, the energies of electrons are sufficiently high for dissociation of carbon atoms from the diamond structure by impact. Also, because of the higher electric fields encountered *during* discharging, ions can have sufficient energy for ”eroding” the diamond surface by impact and dissociation.

Referring to Table 4.4, it was said that PMMA is not expected to result in tribo-electric tool wear. The reason for this is that the breakdown voltage is not reached, therefore no Lichtenberg figures and no strong oxidizing environment are expected.

PC and PSU in dry turning conditions can result in discharging, and therefore tribo-electric tool wear by discharging is to be expected. Lichtenberg figures could be present after turning and tool wear by an oxidizing environment created by the discharges too. Also, impingement of electrons and ions to dissociate diamond atoms can occur.

PC in wet turning conditions will not result in a sufficiently high electric field for discharging to occur, since no electrostatic charges are present. Neither will charged particles be accelerated to high impact energies. No tribo-electric tool wear is to be expected here.

4.5.2 Experiments and results

Tool life experiments were conducted on PMMA, PC and PSU. All materials were precision turned with a natural (type Ia) mono-crystalline diamond tool with rake and clearance plane orientation of (110) respectively (100). A nose radius tool ($R = 1$ mm) was used. A length of cut of 85 km was used[4], with depth of cut 25 µm and feed rate 20 µm/rev. The mean cutting speed was 6.6 m/s. Every material was cut with three tools to ensure tool wear reproducibility. It was found that all three tools had the same kind of tool wear after turning a certain material. This indicated that the observed tool wear was dependent on the tool-workpiece combination and not solely on the used tool.

Polymethylmethacrylate (PMMA)

Figure 4.13(b) shows schematically the worn tool geometry. Figure 4.13(a) shows an ESEM photo of the worn tool. It can be seen that diamond turning of PMMA results in a crater wear at the rake face. All diamond tools showed crater wear, but not all diamond tools showed the wear at the cutting edge, compare for example the tool used for turning PMMA shown in Figure 5.7(a) on page 133.

The heavily damaged cutting edge shows similarities with the Lichtenberg figure given in Figure 4.1, indicating that it is possibly a result of discharging. Why it occurred is not known, but it may have been caused by charges present at the surface prior to the cutting experiment started. Since it occurred on one tool only.

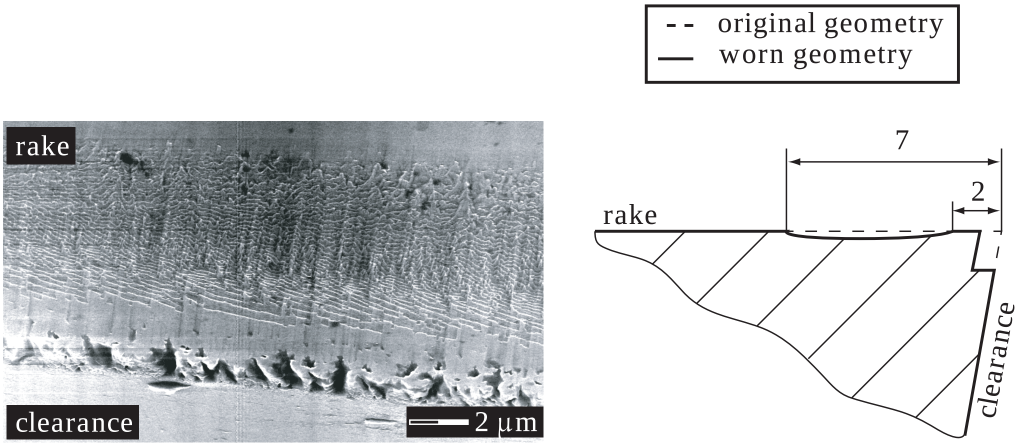

(a) (b)

Figure 4.13: ESEM picture of a worn diamond tool after cutting 85 km of PMMA (tilt = 30°). Dimensions are given in micrometers.

The crater has a pattern that shows similarities with oxidative etch patterns observed on diamond [134, 135]. Although discharging may result in an oxidizing environment, it is unlikely that this oxidative etch pattern occurred by a discharging mechanism. The reason for this is that a maximum chip thickness of 3.6 μm can be calculated using Equation 1.16, and assuming a contact length of eight times the uncut chip thickness [84], this results in a contact length of almost 30 μm. Comparing this value with the position of the maximum distance of the crater wear from the cutting edge, it can be stated that the observed oxidative etch pattern is not a result of an oxidative environment created by tribo-electric phenomena around the tool. This is confirmed by Brinksmeier et al. [20, 136] who showed that no ambient molecules, like oxygen, are present in the contact zone. The crater is formed on the diamond tool where the chip slides over the rake face. This is in accordance with the general observation in metal cutting, that crater wear occurs in the secondary shear zone at the rake face. This is generally the region where higher shear stresses and temperatures occur.

---

[4] A typical diameter for a blank that is used in the fabrication of spectacle lenses is 80 mm. Turning it with a feed rate of 5 µm/rev, results for a single stroke in a length of cut of 1 km.

Polycarbonate (PC)

Although both dry and wet turning conditions were applied on PC, the observed tool wear pattern for both turning processes was the same. Figure 4.14(b) shows schematically this wear pattern for the tool after dry turning. It can be seen that the cutting edge is worn by the formation of facets on both the rake and the clearance face. For the dry turning condition, the facet formed on the rake face has a length of 9 μm at the position of the tool where the largest chip cross-section occurred during turning.

The wet turning condition led to facets as well, although significantly less: the facet on the rake face extended for only 4 μm from the cutting edge. Examination with ESEM showed that the wear pattern looked the same as for the dry turning condition.

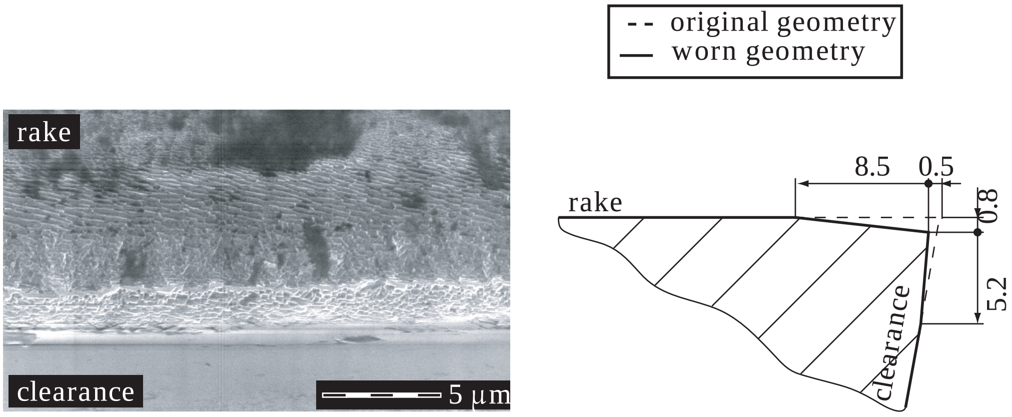

(a) (b)

Figure 4.14: ESEM picture of a worn diamond tool after cutting 85 km of PC (tilt = 30°). Dimensions are given in micrometers.

Figure 4.14(a) shows an ESEM picture of the worn diamond tool after dry cutting. Both the dry and wet turning condition did not result in Lichtenberg figures, although this could have been expected for the dry turning condition. Interesting to notice here is that the observed luminescence in the dry turning condition ceased within 5 km length of cut.

The observed wear pattern of Figure 4.14(a) is also formed by oxidative etching, just like the crater wear observed after turning PMMA. For the result after turning PC, the same reasoning holds as for the result after turning PMMA: the wear on the rake face is formed within the contact length of the chip. Therefore, chemical wear by discharging is not responsible for the observed oxidative etching pattern. Instead, the wear must have been formed by tribo-chemical processes.

Although less tool wear was observed during the wet turning condition, this does not mean that this was caused by the absence of tribo-electric tool wear. Since the wet cutting condition was created by applying a water spray on the cutting zone, this water must have cooled the cutting region considerably, lowering the chemical reaction rate for oxidative etching.

Polysulphon (PSU)

One of the first interesting things that was observed in the tool life experiments of PSU was the fact that luminescence was still observed after 50 km length of cut, while that for PC ceased within 5 km length of cut.

The second interesting thing is the appearance of Lichtenberg figures on the diamond tool. Figure 4.15(a) shows such a Lichtenberg figure observed on the diamond tool. Figure (b) shows a detail of this figure. It appears as if the discharge that resulted in the Lichtenberg figure, proceeded through the diamond tool. It may have originated at an inclusion or micro fracture in or at the surface of the diamond. Such a spot will result in an increased local electric field, creating a possibility for discharging to occur. This would mean that tools have to be manufactured without flaws, in order to prevent discharging from these spots.

Although Lichtenberg figures were observed after the tool life test, the remarkable thing is that the Lichtenberg tree shown in Figures (a) and (b) is positioned outside the actual cutting zone. Other trees were also observed outside the cutting zone, both on the tool side located at the cut surface as on the other side located at the uncut surface. This is shown in the inset of Figure (a), where a top view of the rake face of the diamond tool is given. The grey area represents the chip cross-section and the positions of the different Lichtenberg figures is shown here.

It was observed (not shown here) that Lichtenberg figures also damaged the cutting edge, just like the damage shown in Figure 4.1. It can be understood that when such a damaged cutting edge occurs by discharging outside the actual cutting zone, that it will result in a bad surface quality during contouring operations, which are often applied in industry.

The pattern shown in Figure 4.15(c) shows Lichtenberg patterns on the rake face, created behind the contact length of the chip. This pattern was only visible

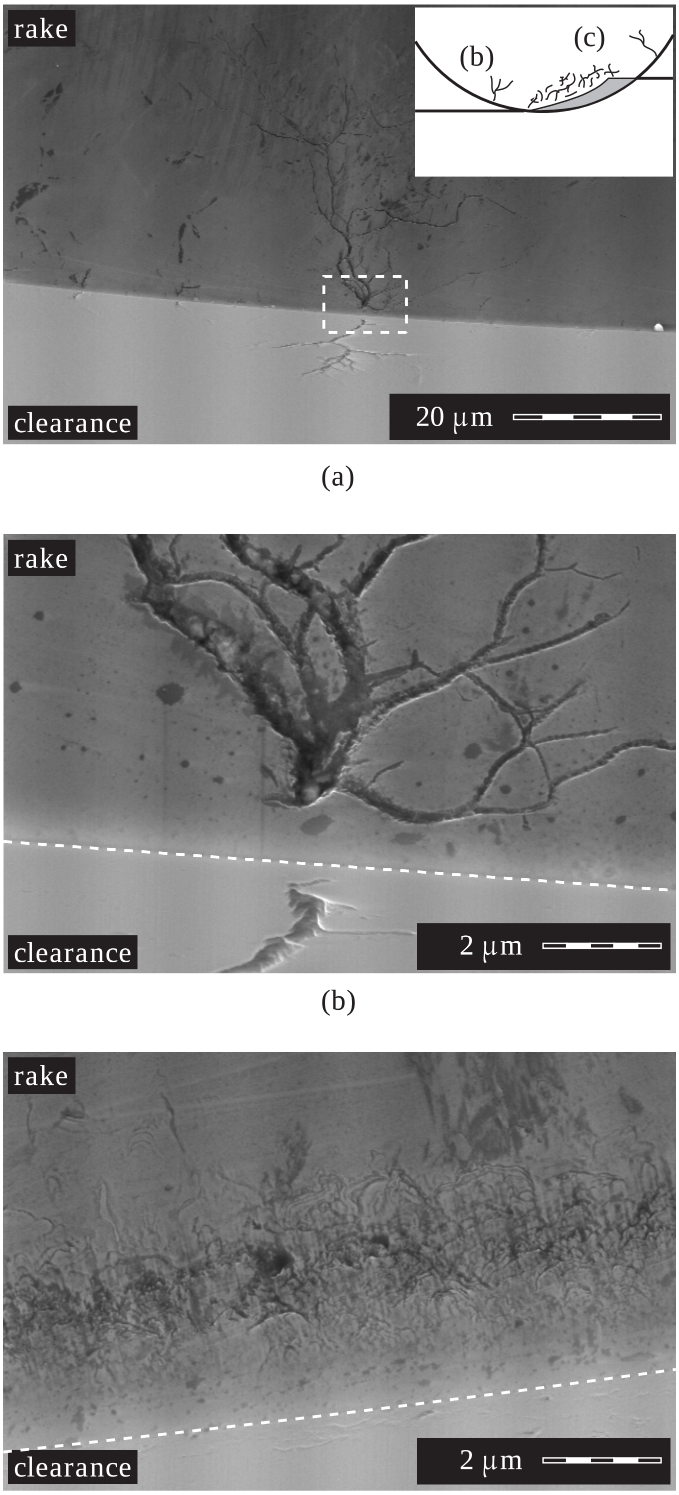
rake
(b)
(c)
clearance
20 µm
(a)
rake
clearance
2 µm
(b)
rake
clearance
2 µm
(c)

Figure 4.15: ESEM pictures of a worn diamond tool after cutting 85 km of PSU (tilt = 30°). The dashed box in figure (a) is given in more detail in figure (b). The inset in figure (a) shows the top view of the tool and the locations of the different Lichtenberg figures given in (b) and (c).

at the rake face and not at the clearance face. This indicates that the electric field strengths near the rake face were higher than near the clearance face.

In contrast to the observed wear patterns after cutting PMMA and PC, no chemical wear pattern was observed after turning PSU. This indicates that PSU results in another dominant tool wear mechanism than PMMA and PC during diamond turning.

4.5.3 Dominance of tribo-electric tool wear

Looking at the combined results of charging behaviour, luminescence observations and tool life experiments, it is interesting to notice that only PSU resulted in tribo-electric tool wear exhibited by Lichtenberg figures.

Some additional measurements showed that during turning a difference is present between the sign of the charge at the cut surface and that of the chip. For the low cutting speed, the chip removed from the PSU workpiece had an opposite sign with respect to the cut surface (the others were not measured). For high cutting speeds on PC, it was measured that the cut surface charged positive (see Section 4.2.2), while chip and diamond tool charged negative (see Section G.3.2 in the appendix). This implies that the charge generated at the back side of the chip (i.e. at the rake-chip interface) is charged more than the free side of the chip, else the electric field could not have been opposite with respect to the sign measured at the cut surface and thus the free chip side. For overlapping cuts, the charge on the surface to be cut is equal to the charge on the cut surface behind the tool. This can be concluded when decay times are considered. Decay times are given by [137]:

$$\tau = \epsilon_0 \epsilon_r R \tag{4.6}$$

Polymers typically have resistivity values of order 10^{14} Ωm [138], resulting in decay times of order 10^3 s. This means that the charge that is present on the cut surface will still be present at the uncut surface in the next revolution, as shown in Figure 4.16.

Based on these findings, it is assumed that in general, the situations given in Figure 4.16 can occur in polymer turning. It shows the possible charging systems during turning with overlapping cuts at higher cutting speeds. Figure 4.16(a) shows the situation as it will occur for PC and PMMA. Contrary to PC and PMMA, it is expected that for PSU the opposite signs should be used as given in Figure 4.16(b).

Based on Figure 4.16 it becomes clear that there are several possible discharge paths: 1) between front and back side of the chip, 2) between front side of the chip and rake face of the tool, and 3) between rake face and cut surface.

The latter option is not certain, because this depends on the surface charge present at the clearance face too. No measurements were performed on this, so the first two options are assumed to be possible. Notice here that discharging will

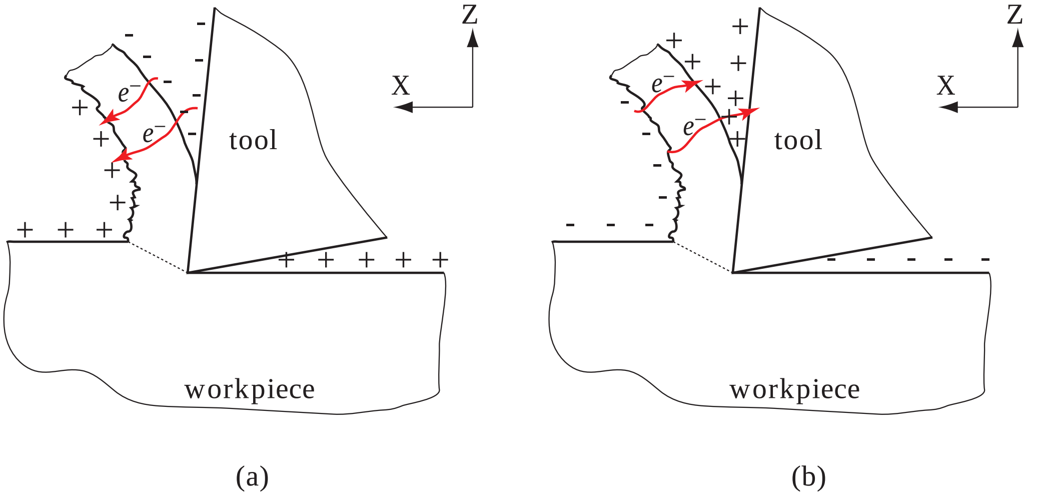

Figure 4.16: Charging in turning of (a) PC and PMMA, and (b) PSU at higher cutting speeds. All at normal relative humidities around 50%.

most probably not proceed through the chip, but around it, because of the lower relative dielectric constant of air.

Lichtenberg figures can be positive or negative [108, 139, 140]. The amount of branching may differ, depending on whether a positive or negative Lichtenberg figure is formed, see e.g. [139, 140]. Looking at the model given in Figure 4.16, it can be concluded that the Lichtenberg figures are the positive kind, i.e. starting at the anode (for PSU the diamond tool) to the cathode (in this case the front side of the chip).

It is known that positive Lichtenberg figures are more easily created than negative ones [133]. Also, for positive streamers a background field[5] is needed of 450 – 500 V/mm, while for negative streamers a background field of 1000 – 2000 V/mm is needed [139]. This may indicate why Lichtenberg figures are created in the diamond tool during turning of PSU, since the tool behaves as the anode and the chip as the cathode. For PMMA and PC, the tool behaves as a cathode, needing a higher electric field strength for the occurrence of negative Lichtenberg figures.

From Nasser and Loeb [141] it follows that the length of the longest branch of the (positive) Lichtenberg figure is proportional to the applied voltage of the anode [141]. In order to make an estimate, the length/voltage curves have to be known for the particular dielectric. These are dependent on e.g. the radius of the anode. The values needed for representation of the used turning setup were not found.

---

[5] Reference [139] mentions that streamers can propagate in fields lower than the inception field, but not lower than some critical minimum background field.

4.6 Tool life improvements

In Section 4.4.4 it was shown that with relative humidities above approximately 65% the amount of charging at the cut surface decreased significantly. Increasing relative humidity can decrease tribo-electric tool wear, since no charges are present anymore, so the electric field strengths will be small and breakdown will not occur. This is also known from industry [41]. Therefore, the best way to diminish tribo-electric tool wear is to apply a high relative humidity in the cutting environment. Besides a higher charge decay, it may also increase the relave permitivity of the polymer [83], raising it more to the value of the used diamond tool. Less charge will be generated then, since the distance in the tribo-electric series between the polymer and the diamond decreases. Although not tested, this can give interesting results for cutting polyacrylonitril (PAN), whose relative permitivity is very susceptible to changes in relative humidity; with increasing relative humidity its dielectric constant increases from approximately 3 to 6 [83]. Based on the tribo-electric series this should imply that with increasing relative humidity the amount of charging during diamond turning of PAM should become less, and even change sign at the highest relative humidity.

Also, it could be expected that the application of an electrically conductive (type IIb) diamond is capable of lowering tribo-electric tool wear. However, from [142] it followed that the application of a type IIb diamond led to more tribo-electric tool wear. This was ascribed to the fact that the tool acted as a ”lightning conductor”, thus becoming more easily damaged by the high amount of discharges taking place then.

Table 4.6 shows the process parameters that were investigated in this research and the influence these parameters had on the charging behaviour. When the amount of charge generated decreases, tribo-electric effects will becomes smaller, or may even disappear. Notice that the adaption of crosslink density ν_e will most probably only work for the same polymer grade, and not for different polymers.

Table 4.6: Overview of adaptable parameters for decreasing the amount of tribo-electric charging, and thus tribo-electric tool wear, during diamond turning of polymers.

parameter		charging
v_c	$<$	$<$
f	$<$	$<$
h	$<$	$<$
RH	$>$	$<$
ν_e	$<$	$<$

4.7 Conclusions

This chapter showed that tribo-electric tool wear *can* be dominant in diamond turning of glassy polymers and that it can severely damage the cutting edge. From the tool life experiment on PSU it followed that this damaged cutting edge by discharging occurred outside the actual cutting zone. Although this was not a problem during the face turning setup used in these experiments, during contouring operations, which are commonly used in the production of optics, this can be a problem. So even when a discharge originates at the cutting edge outside the actual cutting region, it can eventually result in a bad optical quality of the workpiece. Further, but less critical to the turning process is the occurrence of Lichtenberg figures caused by discharging behind the chip contact length. This damages the rake face, but it has little influence on the achievable surface quality after turning.

Based on the tribo-electric series only small differences are to be expected between different polymers. However, in Section 4.2 it was shown that there exist big differences in charging behaviour during diamond turning between the polymers used in this research. For differently crosslinked PMMA grades a relation between network density of the polymer and the amount of charging was found.

Section 4.4 described a lot of turning parameters that influenced the charging behaviour during diamond turning of polymers. It was shown in Section 4.4.1 that when the cutting speed was increased, the amount of charge generated increased too. It was observed during turning of PSU that when the surface charge exceeded approximately 20 $\mu C/m^2$, luminescence by discharging occurred. This is in agreement with the value of 26 $\mu C/m^2$ given by Kwetkus [130] for breakdown in air to occur.

Spectral analyses of the observed luminescence showed the occurrence of excited nitrogen N_2^*, ionized nitrogen N_2^+ and OH radicals. Although only OH radicals are directly capable of chemically wearing the diamond tool, the N_2^* and N_2^+ can be involved in reactions to produce OH radicals, as well as hydroperoxide and ozone, all oxidative species, capable of chemically wearing the diamond tool, which was described in Section 4.5.1 and Appendix H.

The tool life tests described in Section 4.5.1 have shown that two dominant tool wear mechanisms can be observed after diamond turning of some polymers:

1. tribo-chemical tool wear after turning PMMA and PC, and
2. Lichtenberg figures resulting from electric discharges after turning PSU.

The observed tribo-chemical tool wear after diamond turning PMMA and PC was caused by an oxidative etching process. Although discharging can lead to an oxidative environment, see Section 4.5.1, from contact length considerations and the observed tool wear after diamond turning PMMA and PC (the latter showing a facet at the cutting edge), it can be concluded that the wear does not have a tribo-electric origin, but rather a tribo-chemical origin. This will be described more explicitly in the next chapter.

The remarkable thing is that PC showed luminescence and therefore it was expected that tribo-electric tool wear should have been dominant. The reason for the absence of a dominant tribo-electric tool wear was found by the difference in the charging system in respect to PSU.

Measurements have shown that the signs of the charge generated at the back side of the chip and the rake face are opposite to the sign of the charge at the cut surface. The model given in Section 4.5.3 shows that discharging is most likely to occur between the front and back side of the chip, and/or the front side of the chip and the rake face of the tool.

Only the PSU resulted in Lichtenberg figures on the diamond tool after turning. Besides the highest amount of charging during turning, an additional explanation was given in Section 4.5.3, Figure 4.16. Here it was concluded that during turning of PSU, the tool behaves as an anode, creating the possibility of positive Lichtenberg figures to form. During turning of PMMA and PC the diamond tool behaves as a cathode. In that case, Lichtenberg figures are less likely to occur and a higher background field is necessary for the Lichtenberg figures. Obviously, the condition for creating Lichtenberg figures in the tool during diamond turning of PMMA and PC could not be reached for the given conditions.

Chapter 5

Tribo-chemical diamond tool wear

5.1 Introduction

The previous chapter discussed the possibility of tribo-electric tool wear during diamond turning of polymers. It was shown that of the investigated polymers only PSU resulted in tribo-electric diamond tool wear in the form of Lichtenberg figures. The tested PMMA and PC did not result in a dominant tribo-electric tool wear. Instead, tribo-chemical wear was found to be the dominant wear mechanism.

Figure 5.1 shows in more detail the tribo-chemically worn cutting edge of the diamond tool after turning 85 km PC. A wear pattern like this is also found in literature on oxidative etching of diamond [134]. Therefore, it was concluded that this wear was also a result of an oxidative etching process during diamond turning of the specific polymer.

The dashed line in Figure 5.1 indicates the position of the current, worn cutting edge. The upper part of the photo is the worn (etched) rake face with Miller indices (110), and the lower part the worn clearance face with indices (100). Figure 5.2 shows the planes of a mono-crystalline diamond. The tool wear has a layered pattern with step heights of approximately 30 nm. The lattice spacing of diamond is 0.356 nm [143], indicating that approximately 84 crystal lattices have been etched away per layer.

It was discussed in the previous chapter that the oxidative etch pattern, which is a chemical wear, was formed within the contact length of the chip on the rake face. Prior to discussing more results of the research about tribo-chemical wear in diamond turning of glassy polymers, a short overview of tribo-chemical wear is given.

Tribo-chemical wear of diamond tools is mainly known from diamond turning of steels, see e.g. [20, 65, 101, 102]. Generally chemical wear of diamond is described as the breaking of the tightly bonded diamond lattice. When this happens, a carbon atom of the diamond may diffuse into the workpiece, graphitize, react with oxygen to form CO or CO_2, or react with the workpiece to form a carbide,

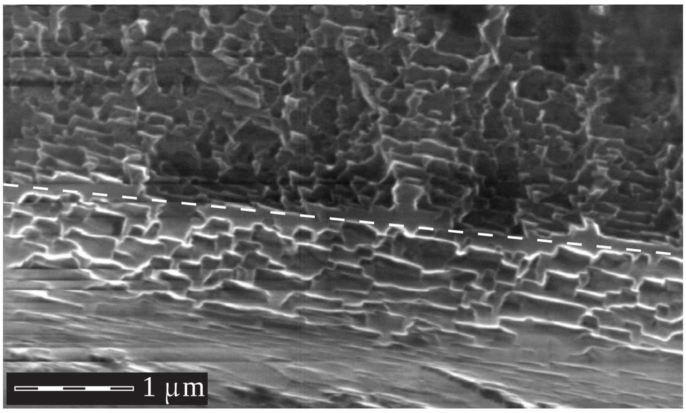

Figure 5.1: ESEM photo of a worn diamond cutting edge after turning 85 km PC. The dashed line indicates the position of the current (worn) cutting edge. Upper part of the photo is the worn (110) rake face, and the lower part the worn (100) clearance face.

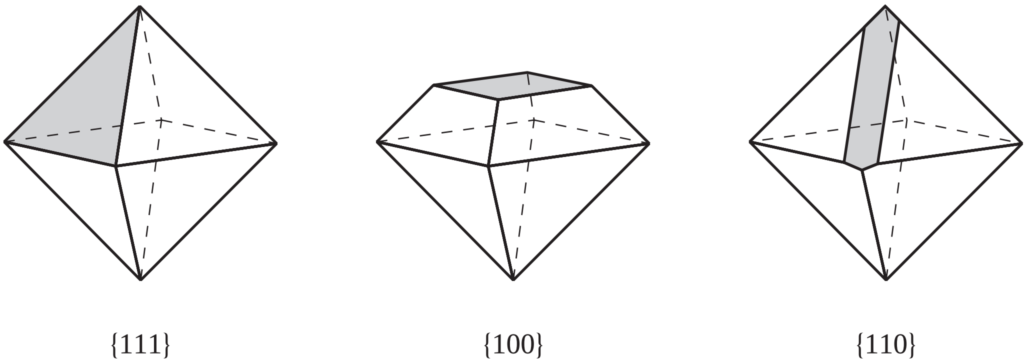

(a) (b) (c)

Figure 5.2: Crystal planes of a mono-crystalline diamond. The most abundant planes found in nature, are the {111} and {100} planes [134].

such as Fe_3C [65]. Oxidation of the diamond tool is generally described by the chemical reactions:

$$C(diamond) + O_2 \rightarrow CO_2 \tag{5.1}$$

and

$$2C(diamond) + O_2 \rightarrow 2CO \tag{5.2}$$

The best explanation for chemical tool wear during diamond turning of steels is given by the research work of Paul et al. [65]. They found that materials with unpaired d-electrons resulted in a relatively high amount of tool wear. The presence of unpaired d-electrons allows carbon-carbon breaking of the diamond lattice, followed by metal-carbon complex formation, resulting in excessive tool wear. Excessive tool wear means that during diamond turning of steels no good surface quality is reached anymore after 1 km length of cut [20, 136].

Based on this theory of unpaired d-electrons, Paul et al. [65] concluded that polymers should be diamond turnable without excessive chemical tool wear, since they do not have unpaired d-electrons. Figure 5.1 shows that the opposite is true for diamond turning of PC. Therefore, further investigation was performed on this kind of chemical tool wear.

Oxidative etching When diamond is heated in air it reacts with the oxygen and ”burns” away. Generally it is said that this reaction starts at approximately 500 °C [69]. In fact, this burning is a complicated process. It is strongly dependent on the conditions that are applied and the crystal plane that is oxidized. Oxygen can either work as a catalyst in transforming the diamond carbon-carbon bonds into graphite carbon-carbon bonds, or it can react with the diamond carbon to form carbon-dioxide or carbon-mono-oxide according to Equations 5.1 and 5.2. Also, the oxygen can react with the graphitized diamond to form CO_2 or CO [144].

Etching does not necessarily need molecular oxygen. Potassium nitrate and water are often used in researches about diamond etching [144, 145, 146]. Etching mechanisms may change depending on the presence of water. De Theije [145] found that {111} surfaces etch through a different mechanism whether pure oxygen is used or an oxygen/water mixture.

Chu et al. [146] propose the following reaction mechanism for the reaction of diamond with water for a {110} oriented diamond plane at temperatures above 800 °C:

$$C(diamond) + H_2O \rightarrow CO + H_2 \tag{5.3}$$

In this etching experiment no free oxygen was present.

Etching is crystal plane dependent. This means that the rate of etching depends on the combination of used etchant and crystal plane. O_2 is known to stabilize the {100} diamond plane during etching, since it is divalent. A {111} diamond plane can be stabilized by the presence of water, since it has only one dangling bond that can be stabilized by OH coming from the water. Divalent oxygen is known to result in chemical roughening of the {111} surface, since it cannot stabilize this surface with one dangling bond [134]. It leads too far to discuss all etching mechanisms. For further reading, see e.g. de Theije [134, 145].

5.2 Material selection

In the previous chapter three materials were tested for their influence on tribo-electric diamond tool wear, namely PMMA, PC and PSU. It was found that both PMMA and PC resulted in a tribo-chemical tool wear represented by oxidative etch patterns on the diamond tool. Figure 5.3 shows some selected polymers used for the experiments of this chapter. It can be seen in this figure that both PMMA and PC contain esters. PMMA has an ester side group in its monomeric unit, while PC has a (double) ester in its main chain monomeric unit. Therefore, the role of oxygen could be important.

To investigate the influence of polymer composition the polymers given in Figure 5.3 were chosen for their different functional groups and main chain compositions. This way the influence of chemical structure on dominancy of tribo-chemical tool wear during diamond turning could be investigated.

Although different polymer structures were used, all polymers were glassy, optical polymers, although PSU has a yellow shine due to the sulphur. Further, it was described in the introduction of Chapter 1 that PA and PU become more and more applied in spectacle lenses. PS is not used much for lenses because of its brittleness, but it is a glassy, transparent polymer that is often used in polymer research. For more detailed descriptions of the used polymers and their properties, the reader is referred to a general polymer handbook, such as [46].

PU and PA were selected for their hydrolysis properties. Esters are known to hydrolyze [147]. During hydrolysis of an ester, the ester is split into two parts according to the reaction given in Equation 5.5 on page 130. Possibly these products, one part is a carboxylic acid, can be chemically reactive to the diamond, or can work as catalysts. PU and PA have different activation energies for hydrolysis. The order of activation energy for hydrolysis is given as [147]:

$$\text{ester} < \text{urethane} < \text{amide} \tag{5.4}$$

showing that the resistance to hydrolysis, also called hydrolytic stability, increases in the order: ester, urethane, amide. Still, side groups can influence the order. From [147] it is known that amide bonds are 100 times more stable to hydrolysis than esters.

Polystyrene (PS) has a carbon backbone with a phenyl ($-C_6H_5$) functional side group. It was chosen since it has a relatively simple structure and no oxygen containing functional groups that may possibly result in oxidative etching of the diamond tool during turning.

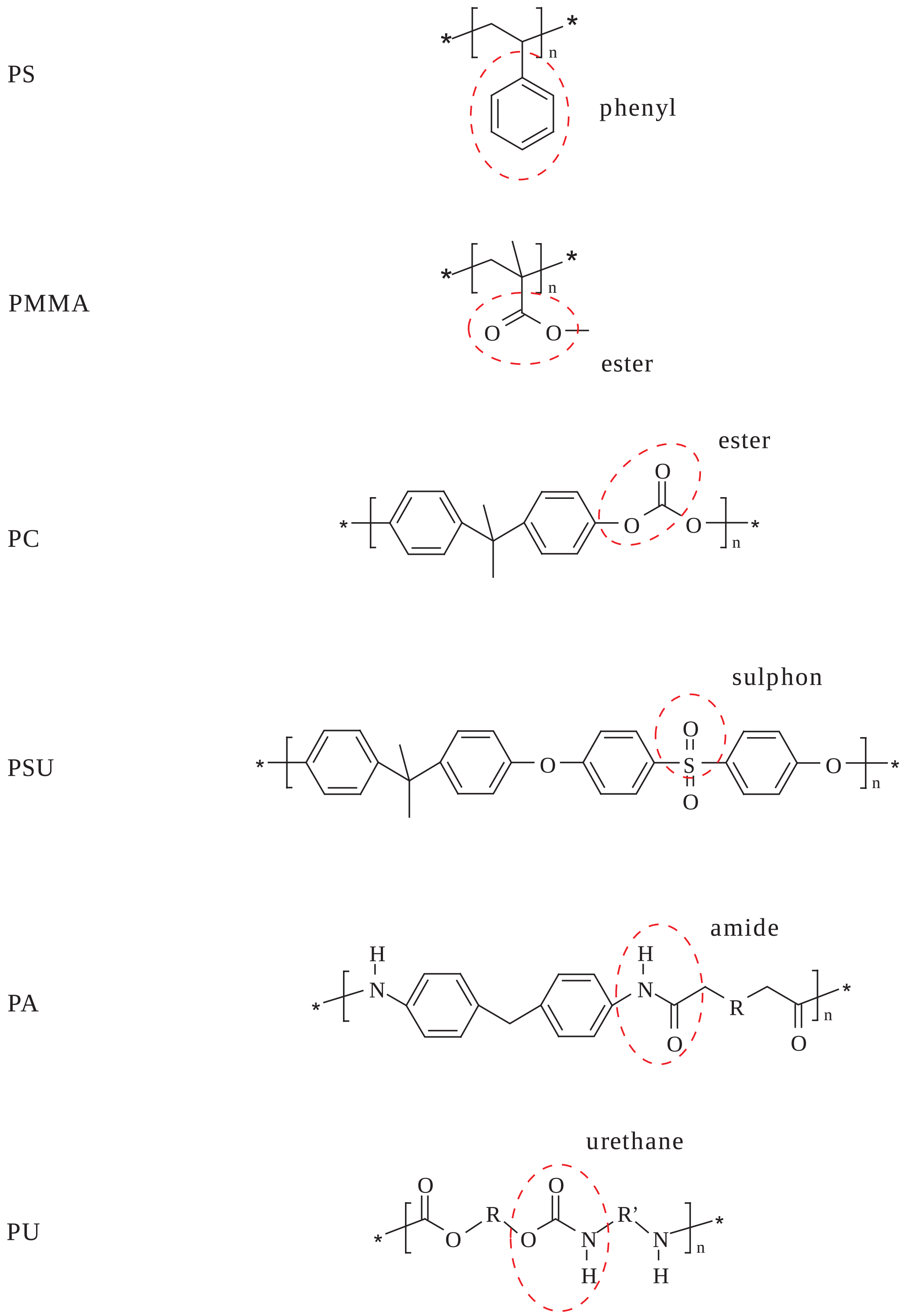
PS
phenyl
PMMA
ester
PC
ester
PSU
sulphon
PA
amide
PU
urethane

Figure 5.3: Used polymers for investigating dominant chemical tool wear mechanism. The dashed ellipses indicate the functional groups of interest.

Table 5.1: Used face turning conditions.

Parameter	Value
Tool material	natural diamond
Tool radius	1 mm
Rake	0°, (110) plane
Clearance	15°, (100) plane
Rotational speed	2880 rev/min
Feed rate	20 μm/rev
Depth of cut	20 μm
Chip removal	by vacuum cleaner no coolant applied
Relative humidity	50% - 60%

Polysulphon (PSU) has approximately the same backbone structure as PC, but it has no ester. Further, PSU has a double sulphone (S = O) group, which can indicate whether the double bonded oxygen is of importance for the observed chemical wear.

Tool life tests have been performed to validate the kind of tool wear that occurs, i.e. which one is dominant.

5.3 Experiments

A natural mono-crystalline diamond (type Ia) has been used for the turning experiments. To check for repeatability in the observed tool wear, several experiments were performed with three diamond tools cutting at the same time, with the same depth of cut and in the same workpiece. It was found that the observed tool wear was tool independent. This means that the wear was caused by the tool/workpiece combination and not solely by the used natural diamond tool. The used turning parameters are given in Table 5.1. Notice that a rotational speed is mentioned here, which implies a changing cutting speed as function of the radius of the workpiece. For PS, PMMA and PC the workpieces had a diameter of 70 mm. For PSU and PA the diameter was 77 mm, and for PU 53 mm.

For most tool life experiments a length of cut of 85 km was used, but for the PA and PU samples lengths of cut of 40 km were used, because of material availability. Although this influences the amount of tool wear, it does not influence the dominant tool wear mechanism for that tool/workpiece combination.

5.3.1 Results

Table 5.2 shows a summary of the results of the tool life experiments. It can be seen in this table that two different dominant tool wear mechanisms can be observed after diamond turning of different polymers. These two mechanisms are tribo-electric and tribo-chemical tool wear. Another possibility is that no tool wear occurs. This was observed for PS. The different material and wear combinations will be described next.

Table 5.2: Results of the tool life tests on different polymers, rotational speed 2880 rev/min, feed rate 20 μm/rev and depth of cut 20 μm.

Material	Functional group	Luminescence observed?	Tribo-electric tool wear?	Tribo-chemical tool wear?
PS	phenyl	no	no	no
PMMA	ester	no	no	yes
PC	ester	yes	no	yes
PSU	sulphone	yes	yes	no
PA	amide	no	no	yes
PU	urethane	yes	yes	no[a]

---

[a] The observed oxidative etch pattern is ascribed to an oxidative environment caused by tribo-electric effects, and it is therefore not considered as a tribo-chemical effect.

Polystyrene (PS)

PS is a remarkable material, since no tool wear is observed after 85 km length of cut. Figure 5.4(a) shows an ESEM picture of the rake face of the diamond tool. Since the tilt of the diamond was 0° the clearance face cannot be seen. Some round-off at the cutting edge appeared, but even after 85 km length of cut, superior surface qualities can be achieved. No luminescence was observed during turning.

Polymethylmethacrylate (PMMA)

The used cutting conditions did not result in luminescence during turning of PMMA, see Chapter 4. The tool wear shown in Figure 5.4(b) is formed within the contact length of the chip on the rake face, see Section 4.5.2. It shows an oxidative etch pattern with a mean step height of approximately 20 nm. This wear is similar to oxidative etch patterns found in literature [134]. The wear manifests itself as a crater wear.

All diamond tools showed crater wear, but not all diamond tools showed the wear at the cutting edge, compare for example the tool used for turning PMMA shown in Figure 5.7(a) on page 133.

The heavily damaged cutting edge shows similarities with the Lichtenberg figure given in Figure 4.1, indicating that it is possibly some result of discharging. Why it occurred is not known, but it may have been caused by charges present at

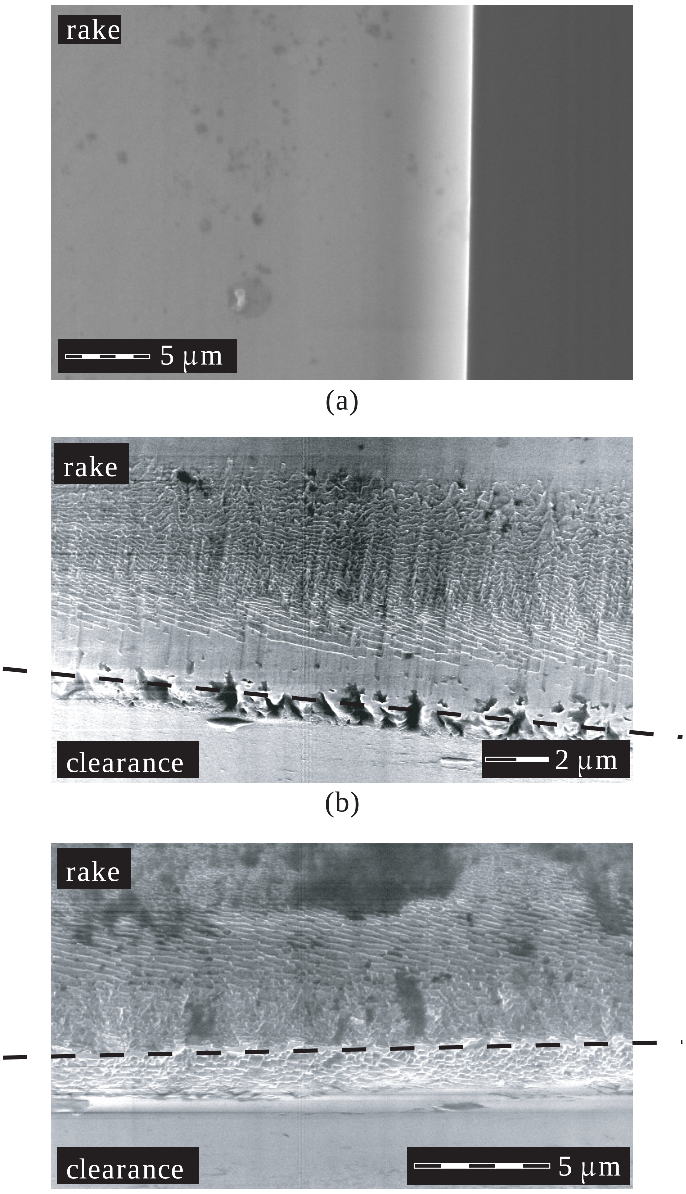
rake
5 μm
rake
clearance
2 μm
rake
clearance
5 μm

(a)

(b)

(c)

Figure 5.4: ESEM photos of used diamond tools after turning 85 km of (a) PS - tilt=0°, (b) PMMA - tilt=30°, and (c) PC - tilt=30°. The dashed line represents the actual cutting edge. For a description of the wear phenomena, see the main text.

the surface prior to the cutting experiment started, since it occurred on one tool only.

Polycarbonate (PC)

PC showed luminescence and it was therefore expected to see tribo-electric tool wear, see Chapter 4. However, as described in Section 4.5.2, no Lichtenberg figures were seen on the diamond tool, and the observed pattern shown in Figure 5.4(c), and in more detail in Figure 5.1, is ascribed to oxidative etching. It was described in Section 4.5.2 that the etch pattern on the rake face was formed within the contact length of the chip on the rake face. The sharp and nicely lapped cutting edge is replaced by a stepped pseudo cutting edge. The mean step height shown in this figure is approximately 30 nm, and it shows big similarities with the observed patterns in literature on oxidative etching of diamonds [134].

Polysulphon (PSU)

The results of the tool life experiment for diamond turning polysulphon were extensively described in the previous chapter, Section 4.5.2. For the overview, Figure 5.5(a) shows again the diamond tool after turning PSU. It was described in Section 4.5.2 that during diamond turning of PSU luminescence can be observed. The figure shows the Lichtenberg figures created during discharging on the rake face while turning for 85 km.

In Sections 4.5.2 and 4.5.3 it was discussed that the Lichtenberg figures originated behind the contact length of the chip on the diamond tool. Figure 4.16(b) showed that the Lichtenberg figures occur on the rake face where the chip leaves the rake face. No signs of tribo-chemical tool wear were found on this tool.

Polyamide (PA)

Figure 5.5(b) shows the cutting edge after turning PA for 40 km. Only little wear is observed on the diamond tool after this length of cut. The observed pattern shows steps, which can be a result of oxidative etching of diamond. Since no luminescence was observed during turning, it is assumed that this small amount of tool wear has a tribo-chemical origin. A tool life test with longer length of cut should give more details about the wear mechanism and if it really evolves as a stepped etch pattern.

Polyurethane (PU)

PU resulted in luminescence during turning. Figure 5.6(a) shows the resulting tool wear after diamond turning PU for 40 km. The arrows in this figure indicate the two different types of wear. The long arrow indicates a fractal-like geometry, indicating that tribo-electric tool wear occurred here. The short arrow indicates an etch pattern. The tool wear is shown in more detail in Figure 5.6(b), where

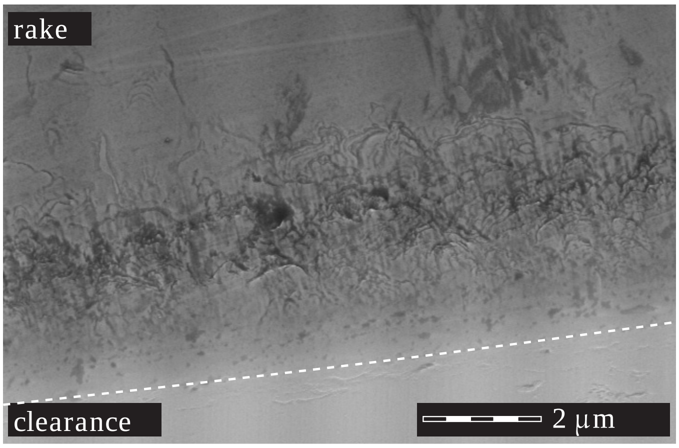

(a)

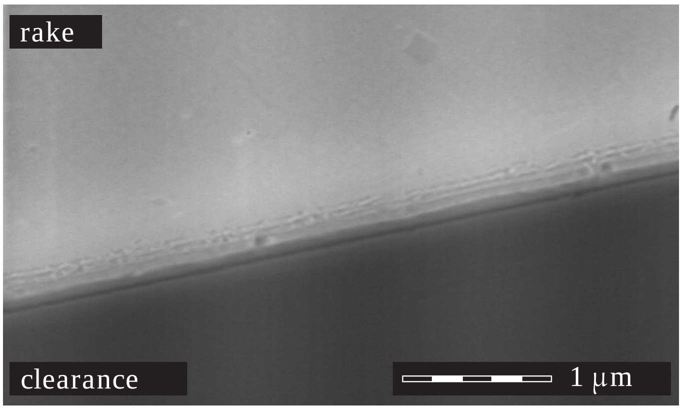

(b)

Figure 5.5: (a) ESEM photo of a worn diamond tool after turning 85 km of PSU (tilt=30°). The dashed line indicates the position of the cutting edge, and (b) shows an ESEM photo of a worn diamond tool after turning 40 km of PA (tilt=30°).

it can be seen that the fractal geometries evolve in an opposite direction with respect to the chip movement. Also, the etch pattern is positioned further away from the cutting edge than the Lichtenberg figures. This seems to indicate that tribo-electric tool wear was dominant, as will be explained next.

Figure 5.6(c) shows how these tool wear patterns may have originated. It was observed in a movie of the turning process that the chip ”wags” on the rake face; this is schematically shown by the dashed chip and the arrow in the figure. During this wagging the chip partly gets separated from the rake face. At that moment the electric field between rake face and chip back side may increase significantly. This is the region where the Lichenberg figures occur. This is supported by the research of Dickinson [148], who mentions that charge separation occurs readily during separation of dissimilar materials, e.g. crack propagation along a polymer-glass interface. The release of the wagging polymer chip from the rake face can

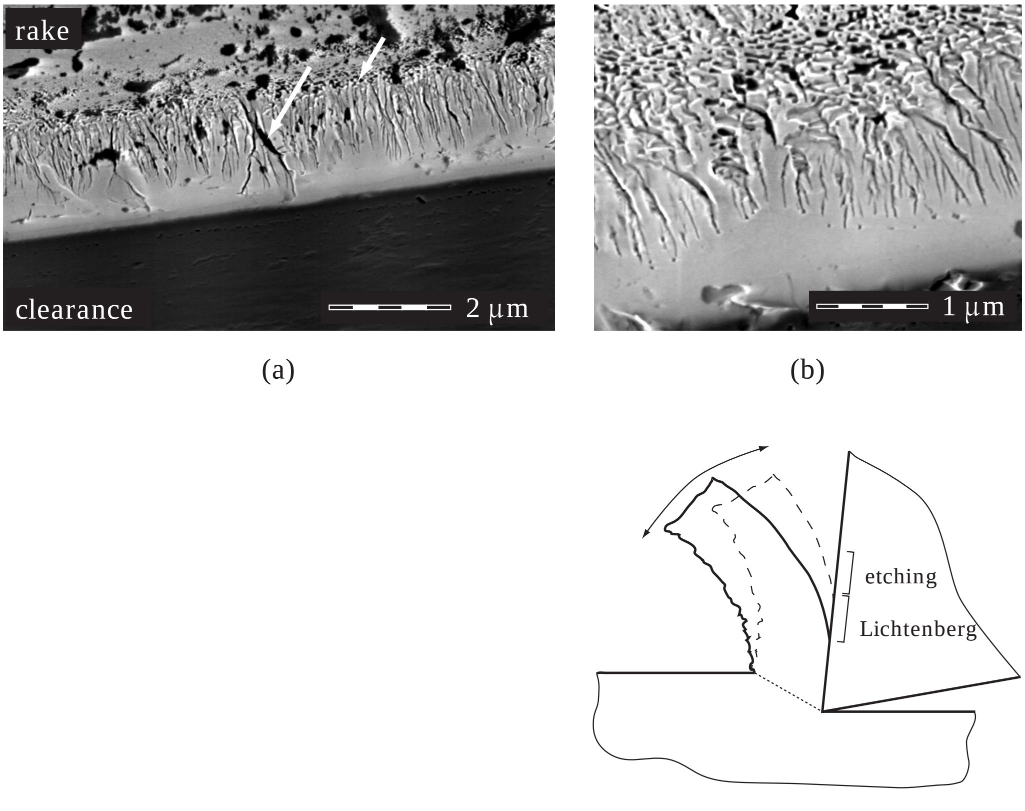

(a) (b)

(c)

Figure 5.6: ESEM photos of a worn diamond tool after turning 40 km of PU (tilt=30°). Figure (c) shows a schematic representation of the occurring wear.

also be considered as a crack propagation along a polymer-diamond interface. During this crack propagation the charge densities can be high enough to reach the breakdown strength of air. This is supported by the observed luminescence during turning. Notice that this wagging of the chip most probably occurred during the diamond turning of PSU too, see Section 4.5.2.

The etch pattern is also assumed to originate from a tribo-electric point of view: it is a result of the strong oxidizing environment that can be created during discharging in air, see Section 4.5.1 and Appendix H where the creation of oxidizing elements such as OH radicals, peroxides and ozone was described. This chemically reactive zone must occur in the zone where discharges are occurring, i.e. behind the contact zone of the chip on the rake face, as schematically given in Figure 5.6(c). Although not measured, it is expected that the electric field at the rake face during turning of PU was higher than during turning of PSU. This can be concluded by the absence of etch patterns on the diamond tool after turning PSU, see Figures 4.15 and 5.5(a), while they were present after turning PU.

5.3.2 Conclusions from experiments

From the turning experiments on the different polymers, it becomes obvious that different tool wear mechanism can be active, see Table 5.2. Looking at the chemical wear it appears that polymers with esters, like PMMA and PC, result in an oxidative etching mechanism. Clearly, it does not matter whether the ester is contained in a side group (PMMA) or in the main chain (PC) of the structural unit.

Diamond turning of PS did not result in any significant tool wear, indicating two things: 1) esters are important for chemical wear to occur, and 2) PS can be turned without excessive tribo-electric or tribo-chemical tool wear. Paul et al. [65] stated that polymers can be turned without diamond tool wear, since they do not have unpaired d-electrons. However, they did not take into account that other chemical process can be important during diamond turning of polymers. From the tested materials of this research PS seems to be the only one that obeys the conclusion of Paul et al.

Since PU resulted in a dominant tribo-electric tool wear it is difficult to conclude that hydrolysis is important in the tribo-chemical wear mechanism. However, based on the order of ease of hydrolysis, Equation 5.4, the little tool wear after turning PA supports the influence of hydrolysis.

PSU and PU result in a tribo-electric wear of the diamond tool. PSU resulted in Lichtenberg figures only, while PU resulted in Lichtenberg figures in combination with oxidative etch patterns caused by the reactive and oxidative environment from discharging, see Section 4.5.1. Why these differences occur, should be further investigated.

Influence of hydrolysis Notice that hydrolysis is discussed as being important for tribo-chemical tool wear to be dominant. However, hydrolysis means chain scission, even in PC. This can be seen in the (general) acidic hydrolysis reaction of an ester:

$$R(CO)OR' + H_2O \longrightarrow R(CO)OH + HOR' \tag{5.5}$$

with R and R′ parts of the main chain. However, chain scission was not measured in the GPC measurement. A reason for this is that the amount of chain scission caused by hydrolysis is too small to become detected in the small amount of chip material analyzed in the GPC measurement.

Using a chip width $b = 200\,\mu\text{m}$, and the diamond tool wear dimensions after turning PC as given in Figure 4.14, it can be estimated that approximately $1.02 \cdot 10^{-15}$ m^3 of diamond material is removed during the tool life test. This corresponds to a diamond mass $m = 3.6 \cdot 10^{-12}$ kg. Using

$$n = N_A \cdot \frac{m}{M} \tag{5.6}$$

with M the molar mass of the diamond (12 g/mol), it can be calculated that $1.8 \cdot 10^{14}$

diamond atoms have been removed in the wear process.

Assuming now that one chain scission of a PC molecule would result in a removal of one diamond carbon atom, this implies that $1.8 \cdot 10^{14}$ PC molecules are needed for this. Using Equation 5.6 again, and $M_n = 16$ kg/mol for the used PC, it can be calculated that $4.8 \cdot 10^{-9}$ kg of PC material is needed for the removal of the diamond atoms. Comparing this with the total amount of material cut in this tool life experiment, approximately $5.1 \cdot 10^{-2}$ kg, it can be seen that the cut polymer chains are only a very small fraction (order 10^{-7}) of the total amount of uncut polymer chains. This small difference will not be measured by GPC, indicating that hydrolysis may have occurred during diamond turning of PC.

Equation 5.5 showed the hydrolysis of an ester, forming a carboxylic acid R(CO)OH and an alcohol HOR′. Hydrolysis of esters is more likely to occur in aqueous solutions at higher temperature and in presence of a catalyst [147]. The catalyst can be an acid or a base. When a base is used, a carboxylate ion is formed instead of the carboxylic acid. Hydrolysis reactions of amides and urethanes can occur as well, although they have some different end-products.

One question at this moment is how a possible hydrolysis reaction should occur, since no acid or base, acting as a catalyst during the hydrolysis reaction, is explicitly added. These are needed for the hydrolysis to proceed. Energy is needed for hydrolysis too, but thermal energy will be supplied by the adiabatic heating in the shear zones during the turning process. As was shown in Chapters 2 and 3, temperatures may increase several decades during turning, up to a temperature of approximately 100 °C. In chemistry, every 10 K temperature rise means a two or three times higher reaction rate [147].

The exact influence of hydrolysis is not known, but based on the tool wear differences between ester-like polymers and polyamide the effect appears to be present. The importance of hydrolysis can be made clear if water has an important influence in the chemical wearing of the diamond tool. This will be described in the next section.

5.4 Influence of water on diamond tool wear

To find out what the influence of water is on the diamond tool wear, cutting experiments in two different environmental conditions were performed. The environments were created by placing a shielding around the turning machine and adding dry air respectively water vapor for the dry respectively wet turning experiment. The workpiece sample used for the dry turning experiment was heated in an oven at 105 °C for two days to remove absorbed water from the material. The workpiece sample used for the wet turning experiment was stored at normal room temperature and relative humidity of approximately 60%. Table 5.3 shows the used cutting conditions during the experiments.

No vacuum cleaner for chip removal has been used, nor a water spray for creating the wet environment, since these affect the temperature in the cutting zone. However, now and then, the chips were removed by switching the vacuum cleaner on for a short period.

Table 5.3: Turning conditions dry/wet experiment.

Condition	Value
Material	PMMA, ⌀60 mm
Tool material	natural diamond
Tool radius	1 mm
Rake	0°, (110) plane
Clearance	15°, (100) plane
Rotational speed	2000 rev/min
Feed rate	20 μm/rev
Depth of cut	20 μm
Length of cut	50 km
Chip removal	off
Temperature	22 ± 1 °C
RH in dry turning	7 %
RH in wet turning	79 %

Notice that only PMMA is tested in dry and wet turning conditions. The reason for choosing PMMA was, that PMMA results in a crater wear on the rake face of the diamond tool. This wear can easily be measured to get a quantitative value, in this case by interference microscopy.

5.4.1 Results

Figures 5.7(a) and (b) show the results for turning PMMA in a dry and a wet environments. It can be seen that in both turning conditions a crater wear is formed on the rake face of the tool. For dry turning conditions the crater is positioned at a distance of approximately 3.5 μm behind the cutting edge at the largest chip thickness. Here the width of the crater is approximately 5.5 μm. For wet turning conditions the crater is positioned nearly at the cutting edge (distance is less than 1 μm). Here, the width of the crater is approximately 10 μm.

The patterns in the craters were observed by ESEM, and they are the same for dry and wet turning experiments. For the wet turning conditions an ESEM photo showing the wear pattern in more detail is given in Figure 5.7(c).

Using Equation 1.17 for the width of the chip b, and stitching interferometry microscopy for the measurement of the width W and depth d of the crater, the volumetric wear V could be estimated. The dimensions of the crater wear and the volumetric wear of the diamond tool are given in Table 5.4.

The wet turning condition (RH=79%) led to a five times higher volumetric wear of the diamond tool. This is a significant difference, which indicates that the

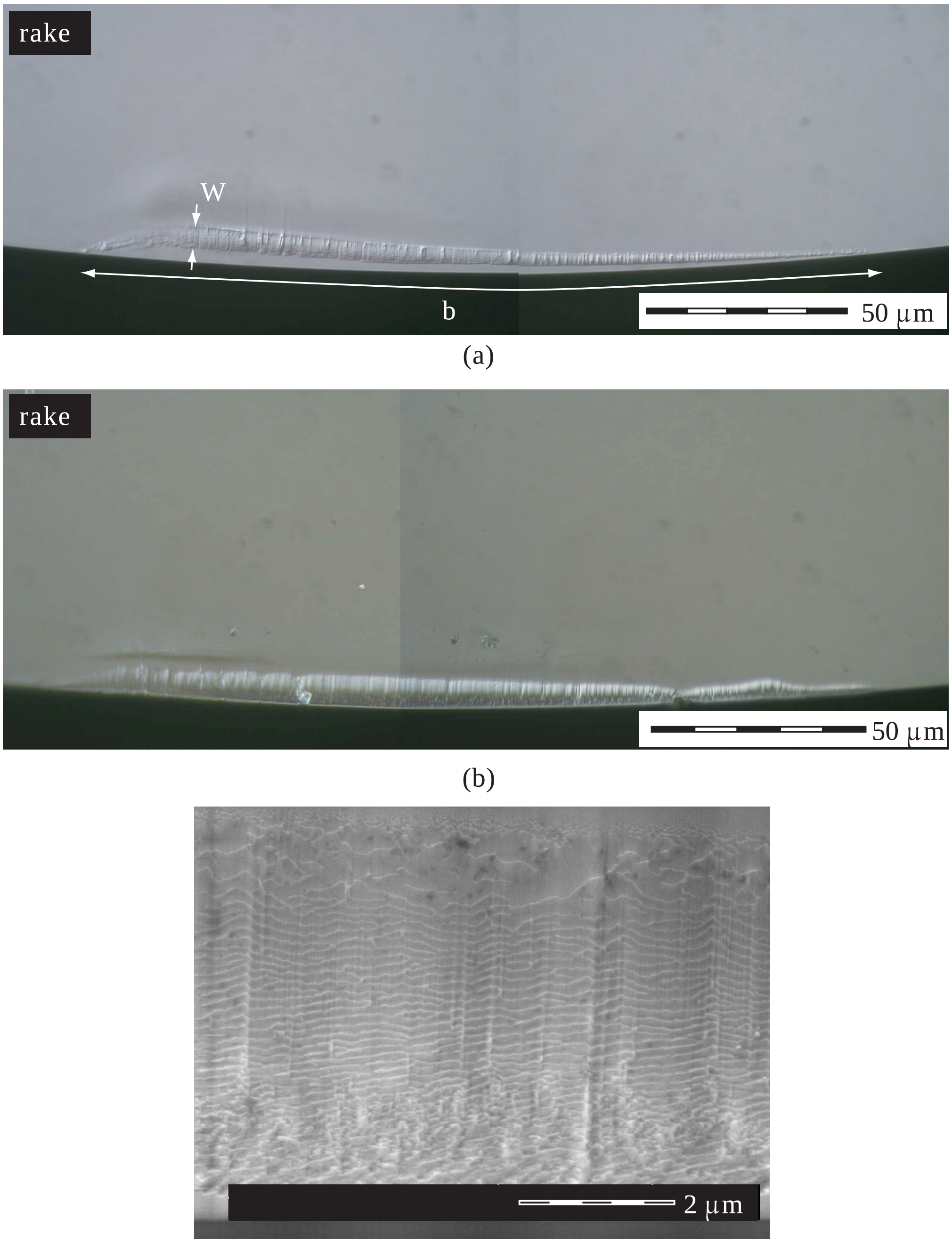

(a)

(b)

(c)

Figure 5.7: Nomarski DIC photographs of tool wear for (a) dry turning PMMA at *RH* = 7% and (b) wet turning PMMA at *RH* = 79%. Figure (c) shows an ESEM photo giving more detail of the wear pattern obtained in the wet turning process.

Table 5.4: Summary of wear dimensions and total volumetric wear for dry and wet turning conditions.

Environment	$W/\mu m$	$d/\mu m$	$b/\mu m$	$V/\mu m^3$
Dry cutting	5.5	0.15	200	41
Wet cutting	10	0.40	200	200

presence of H_2O promotes oxidative etching of the diamond tool during turning of this polymer.

Wilks and Wilks [69, Fig. 13.10] presented the effect of a water atmosphere on the volumetric removal rate during polishing. They showed an increase in volumetric removal rate when water is applied in the polishing process. This was tested for a {110} diamond surface, the same orientation as the rake face of the diamond tool. A similar effect was found for polishing in an ethanol atmosphere. Combining the results of the tool life tests of this chapter and the results mentioned in Wilks and Wilks [69], a water atmosphere can be assigned to be an important factor in increased volume removal rates for diamond {110} surfaces. However, polishing of diamond and wearing diamond in a turning process of polymers are two completely different processes, but still the influence of a water atmosphere is important to notice. The next section will describe a tribo-chemical wear mechanism for diamond turning of polymers.

5.5 Proposed tribo-chemical reaction mechanism

5.5.1 Creation of reactive elements

For etching to occur, reactive elements have to be present near the diamond. The previous section showed the importance of water on the resulting diamond tool wear. Also, in Section 5.3.2 hydrolysis was given as a possible contributor in the etching process of the diamond tool.

It was shown in Table 3.3 that PMMA exhibits chain scission during turning while PC does not. This means that during turning of PMMA radicals may be formed, while during turning of PC no radicals are formed. Although radicals may contribute to the wear process of the diamond tool during turning of PMMA, this is not the case for the wear process during turning of PC. Therefore it is assumed that the main wear mechanism is not dominated by radical reactions. Instead, an ionic mechanism will be proposed. The following reactions are assumed to contribute to the chemical wear process.

1. Auto-dissociation of water.

   Auto-dissociation of water is a natural process, also called auto-protolysis. Water, however pure, will have water molecules fallen apart in two ionic parts, given by the reaction:

$$H_2O \rightarrow H^+ + HO^- \tag{5.7}$$

It can be seen in this reaction that two reactive species originate from the dissociation, an acid (H^+) and a base (HO^-). The dissociation constant K_W is given by:

$$K_W = [H^+]\,[HO^-] \tag{5.8}$$

and is given as $K_W = 10^{-14}\ \mathrm{mol}^2/\mathrm{l}^2$ at ambient temperature (25 °C) and pressure. Looking at Equation 5.8, this means that $[HO^-] = \sqrt{K_W} = 10^{-7}$ mol/l. In water the concentration water molecules is $[H_2O] \approx 55.6$ mol/l. This indicates that there exists one HO^- ion on every $5.6 \cdot 10^8$ molecules H_2O. K_W is temperature dependent. The following relation is given by [149]:

$$\log K_W = -4471/T + 6.0875 - 0.01706 \cdot T \tag{5.9}$$

with T the temperature in K.

This means that at a temperature of 100 °C $K_W = 10^{-12.3}$. Looking at the concentration HO^-, it is now found that $[HO^-] = 7.1 \cdot 10^{-7}$ mol/l. This indicates that more auto-dissociation occurs at higher temperatures, so also in the turning process when water is present in the polymer.

2. Hydrolysis products.

It was discussed in Section 5.3.2 that hydrolysis may be important. This is supported by the results of the dry and wet turning experiment on PMMA. Equation 5.5 gave the (acidic) hydrolysis products of an ester as:

$$R(CO)OR' + H_2O \longrightarrow R(CO)OH + HOR' \tag{5.10}$$

with R and R′ parts of the chain structure. This way a carboxylic acid and an alcohol are formed. The carboxylic acid is a relatively strong acid[1], with acidity $pK_a \approx 5$. The alcohol is only little acidic with $pK_a \approx 16$ [147].

For the used polyamide the following hydrolysis reaction applies:

$$R'(CO) - (NH)R + H_2O \longrightarrow R'(CO)OH + H_2NR \tag{5.11}$$

It can be seen in this equation that for PA a carboxylic acid is formed too. However, this hydrolysis reaction needs a higher activation energy [147].

It is assumed that both $[HO^-]$ ions and products of the hydrolysis are present in the cutting zone under the influence of water and heat present in the turning process. The following section will describe the proposed reaction mechanism for the dominant chemical wear process in diamond turning of (some) polymers.

---

[1] Acidity is expressed as by the acid ionization constant K_a. This constant varies over a large range and therefore another scale is used: $pK_a = -\log K_a$. More generally, more negative pK_a values correspond to stronger acids and more positive pK_a values correspond to weaker acids.

5.5.2 Oxidative etching mechanism

The oxidation mechanism proposed here can be applied for diamond turning of polymers with and without chain scission. The reaction path is given by Equations 5.12-5.14, and it is an ionic based mechanism, since it is also applicable for diamond turning of PC, which does not result in radical formation by chain scission.

When tribo-chemical tool wear is dominant the proposed oxidative etching mechanism starts with a nucleophilic attack on the carbon of a carbonyl present at the diamond surface, see Equation 5.12. This nucleophile can be the HO^- coming from the auto-dissociation of water, or a nucleophile, like HOR′ coming from the hydrolysis reaction. HO^- is known to be a stronger nucleophile than the nucleophiles formed in the hydrolysis of esters and polyamides [147]. It is catalyzed by an acid, which can be the H^+ formed by the auto-dissociation of water, or it can be an acidic component formed in the hydrolysis of the polymer chain, as given in Equations 5.10 and 5.11. Obviously, the reaction in Equation 5.12 is reversible.

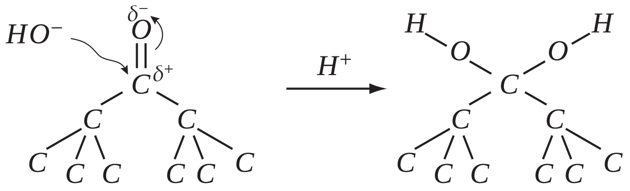

(5.12)

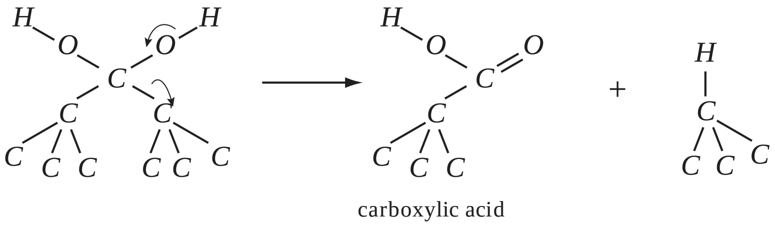

(5.13)

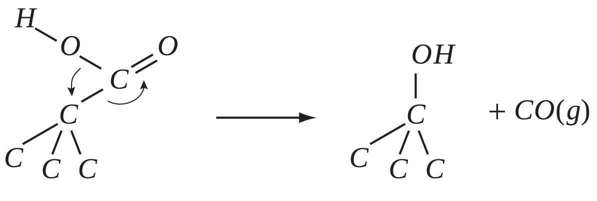

(5.14)

Subsequent scission of one diamond carbon-carbon bond results in one carboxylic acid at the diamond surface and one hydrogen terminated diamond carbon, see Equation 5.13. The latter will most likely be converted in an OH termination [150, 151]. The carboxylic acid will destabilize, removing one diamond carbon atom by desorption of carbon-monoxide (CO). Once the destabilized carboxylic acid liberates CO, it cannot return in its original form, and one carbon

Table 5.5: Bond energy calculation for the different reaction steps.

Equation		Bonds	Type	Bond energy
5.12	formed	$C-O$	ester	−353 kJ/mol
		$O-H$	OH	−466 kJ/mol
	broken	$C-O$	carbonyl	353 kJ/mol
Total				−466 kJ/mol
5.13	formed	$C-O$	carbonyl	−353 kJ/mol
		$C-H$	diamond	−416 kJ/mol
	broken	$C-C$	diamond	349 kJ/mol
		$O-H$	OH	466 kJ/mol
Total				46 kJ/mol
5.14	formed	$C-O$	$C-OH$	−353 kJ/mol
		$C-O$	CO	−300 kJ/mol
	broken	$C-C$	diamond	349 kJ/mol
		$C-O$	$C-OH$	353 kJ/mol
Total				49 kJ/mol

atom has been removed from the diamond surface.

A stable OH group is formed at the diamond surface. This is in accordance with the fact that (110) diamond surfaces etch to (111) faces [135], which will have an OH termination in the presence of water [134].

5.5.3 Discussion

Surely, the carbon-carbon bond breakage in Equation 5.13 is the most critical step, with a change in bond energy of 46 kJ/mol, see Table 5.5. Sufficient energy should be present during the turning operation to generate a destabilized carboxylic acid at the diamond surface. This energy can be provided by the temperature rise in the shear zone. Using the cutting force data of PMMA for $v_c = 3$ m/s from Table E.2, the generated power is

$$P_s = \eta \cdot F_s \cdot v_s = 2.4 \text{ W} \tag{5.15}$$

resulting in an energy consumption over the full length of cut of:

$$U = P_s \cdot \frac{L}{v_c} = 40 \text{ kJ} \tag{5.16}$$

Looking at the amount of material removed in the wet turning experiment, where the influence of the water atmosphere is substantial, it was given that 200 μm^3 diamond was worn during the turning process. It can be calculated, using Equation 5.6 that this is equivalent to $5.8 \cdot 10^{-11}$ mol carbon or $3.5 \cdot 10^{13}$ carbon atoms.

Looking at Table 5.5 it can be seen that for the removal of a diamond carbon atom by Equations 5.13 and 5.14, an energy of 95 kJ/mol is needed. Looking at the amount of worn diamond this required an energy of $5.5 \cdot 10^{-9}$ kJ. This is significantly less than the amount of thermal energy from the shearing process (40 kJ). Indicating that enough energy was present for the reactions to occur.

Another question is whether enough HO^- ions were available in the material that was cut, since the HO^- ions are considered to initiate the whole etching process.

From van Krevelen [83] it can be estimated that at $RH = 79\%$ the PMMA has a molar water content of approximately 0.1 mol/structural unit. PMMA with a structural molar weight of 88 g/mol than contains 1.8 g/mol water. Or, 100 g of PMMA contains 2 g water.

The total volume of material cut was $L \cdot f \cdot h = 2.0 \cdot 10^{-5}$ m^3, or 24 g. This amount of PMMA contained approximately 0.5 g water. This is equivalent to $1.6 \cdot 10^{22}$ water molecules. It was shown in Section 5.5.1 that for every $5.6 \cdot 10^8$ water molecules one HO^- is present. Therefore it can be said that at least $2.9 \cdot 10^{13}$ HO^- ions were present in the cut material. This is of the same order as the amount of carbon atoms removed. However, notice that at higher temperature more auto-dissociation occurs, as was shown in Section 5.5.1. Also the initiating step in the chemical wear process can be initiated by the less nucleophile ROH formed in the hydrolysis reactions. Therefore it can be concluded that enough nucleophiles were present for the observed chemical wear rate.

Some other findings contribute to the validity of the above mentioned tribo-chemical wear reactions. These are:

- Diamond turning of PS did not result in significant tool wear. Since PS is highly hydrophobic, hardly any water will be present in the material and hence little water will be present at the cutting edge. This way oxidative etching of the diamond tool by water will be absent, supporting the above water based etching mechanism. This suggests that the hydrophobicity of the material could be an important parameter to take into account besides environmental humidity and material chemistry.

- A tool life experiment was performed with a mono-crystalline (111)(111) diamond tool on PMMA. Only after 240 km length of cut a small noticeable tool wear could be observed. Examination of the tool by ESEM showed etch patterns.

  It is known that the (111) plane is H and/or OH terminated, therefore, it is unlikely that etching will start here, since a carbonyl is necessary for initiating the etching process, as given in Equation 5.12. In an oxygen/water environment the (111) plane etches at the step edges, where $C = O$ termination may be present, and it will etch towards an OH termination, which is a stable termination for the (111) plane. Therefore, when etching occurred on the (111) plane during the tool life test, this plane immediately became stabilized by the proposed oxidation mechanism. This supports the proposed etching mechanism as well.

- Mackey et al. [152] indicate that (110) diamond surfaces show more CO than CO_2 desorption, which is in accordance with the proposed reaction scheme given by Equations 5.12 to 5.14. They state that CO desorption comes from an ether ($C-O-C$), while it is here proposed to desorb from a carboxylic acid in Equation 5.14. The carboxylic acid in Equation 5.14, may also desorb to CO_2, resulting in an H-terminated surface, but since a lot of HO^- is present in the wet turning experiment, the proposed mechanism with desorption of CO, and formation of an OH terminated (111) plane seems likely to occur.

The above considerations indicate that the proposed etching mechanism can occur in diamond turning of (some) polymers. However, more research is needed to show the influence of hydrolysis on the tribo-chemical wear mechanism.

5.6 Conclusions

This chapter, Section 5.3.1, showed the results of tool life experiments on different glassy polymers. It was found that two types of diamond tool wear can be dominant: 1) tribo-electric tool wear, which was already described in more detail in Chapter 4, and 2) tribo-chemical tool wear. ESEM observations showed that the tribo-chemical wear of the diamond tool was caused by an oxidative etching mechanism.

Oxidative etching of the diamond tool occurred during diamond turning of easily hydrolysable polymers, like PMMA and PC. Polyamide (PA) which has a high stability against hydrolysis resulted in very little chemical tool wear. This indicated that hydrolytic stability can have an important effect on the amount of oxidative tool wear.

Since hydrolytic stability was assumed to be important, the influence of water should be important as well. This was confirmed by tool life experiments described in Section 5.4. These experiments showed that high relative humidity in the cutting environment led to more tool wear than low relative humidity. For the given conditions a five times higher volumetric wear was measured for diamond turning PMMA in a high relative humidity environment (RH 79%) than in a low relative humidity environment (RH 7%).

Since only PMMA results in a measurable chain scission during diamond turning and PC not, an ionic wear reaction mechanism is proposed. Based on the tool life experiments with different humidities and the influence of hydrolytic stability of the polymers turned, two chemical species were identified to be active in the oxidative etching mechanism. The first is the nucleophile HO^- formed by auto-dissociation of water, and the second is the less reactive nucleophile formed in the hydrolysis reaction, e.g. ROH.

Section 5.5 gave the full reaction mechanism for the tribo-chemical diamond tool wear, provided that tribo-chemical wear is dominant in polymer turning. The proposed mechanism is an ionic based mechanism, starting with a nucleophilic attack on the carbon atom of a carbonyl terminated diamond (110) surface. Subsequent scission of one diamond carbon-carbon bond results in a carboxylic acid and a hydrogen terminated diamond carbon. The latter will most likely be converted in an OH termination. The carboxylic acid will destabilize, removing one diamond carbon atom by desorption of carbon-monoxide (CO). Once the destabilized carboxylic acid liberates CO, it cannot return in its original form, and one carbon atom has been removed from the diamond surface.

Calculations have shown that sufficient energy is available in the turning process for these reaction mechanisms to occur. Further, it was calculated that the amount of initiators present, i.e. the nucleophiles, in the workpiece material was of the same order as the amount of diamond carbon atoms removed in the etching process. These calculations confirmed the proposed reaction mechanisms.

Further experiments showed that hydrophobic PS did not result in significant tool wear (neither tribo-electric, nor tribo-chemical) during diamond turning. Cutting a hydrophobic polymer means that water is absent near the tool tip, since no water is absorbed in the polymer. Therefore, no tribo-chemical wear can occur by auto-dissociated or hydrolysed species, supporting the proposed mechanism.

Another experiment confirming the proposed reaction mechanism was diamond turning PMMA with a (111) diamond tool. Even after 240 km no significant tool wear could be found on the diamond tool. Since the (111) surface of a diamond is H and/or OH terminated no etching will start here by the proposed nucleophiles, since they immediately stabilize the diamond surface.

It can generally be said that hydrophobic polymers will not result in a tribo-chemical diamond tool wear since no water is present at the cutting edge. Further, polymers with good hydrolytic stability will result in less tribo-chemical diamond tool wear than easily hydrolysable polymers. Also, the use of a (111) diamond tool instead of a (110) diamond tool is beneficial for the tool life during polymer turning.

Chapter 6

Conclusions and recommendations

The use of polymeric products for optical applications increases. The main reason for this is that optical polymers have beneficial properties over glass materials like better impact resistance and lower specific mass. The main objective of this research was to find out what parameters can be used or adapted to improve the precision turning process of polymeric optics. To investigate this, the research consisted of two parts: 1) the description of the precision turning process for achieving optical quality defined as $Ra < 5\,\text{nm}$, and 2) the description of the relatively high amount of diamond tool wear during precision turning of glassy polymers.

Chapter 1 gave an introduction about polymer behaviour and currently known literature about diamond turning of polymers. This literature generally relates the quality of the diamond turned surface to whether or not the glass transition temperature was reached during diamond turning. Smith [44] even made an estimate about the temperature rise in the shear zone, although she did not measure cutting forces, neither validated her calculations with temperature measurements.

From Smith's research it followed that polycarbonate cannot be cut to good optical quality since it cannot reach the thermal flow regime. To investigate the effect of cutting parameters another thermal model than that used by Smith was applied to actually visualize the temperature rise contours and to see what effect cutting conditions have on the temperature rise distribution in polymer turning. Some interesting results were seen, and not only for PC. The conclusions from this part of the research are described in Section 6.1.1

Section 6.1.2 describes the conclusions for the observed dominant diamond tool wear mechanisms found for diamond turning of glassy polymers.

Recommendations for the diamond turning process of polymers and future research on this topic are given in Section 6.2

6.1 Conclusions

6.1.1 Cutting mechanics

In Chapter 2 the thermal model derived by Komanduri and Hou was adapted for the application of turning polymers. The most important adaptation involved the addition of the parameter η, which incorporates the conversion ratio of mechanical work to heat. For metals this ratio is generally assumed to be 95%, but it was found in literature that for polymers this ratio can be as small as 50%. The consequence of this conversion ratio of mechanical work to heat in polymer turning is that the temperature rise is less than generally assumed in existing literature like [44].

For the implementation of the model, cutting force measurements were made on several glassy polymers, knowing PS, PMMA, PC and PSU. From the calculated temperature rises for the investigated cutting condition, it became clear that the cutting temperatures during polymer turning did not reach a temperature above T_g. The results were experimentally confirmed by temperature measurements during turning. The results described in this thesis are different from those of Smith [44]. The best reasons for this are: 1) only 50% of the mechanical work is actually converted into heat for polymers, and 2) a heat partition fraction to the chip of approximately 0.8[1], indicating that only little heat is conducted into the workpiece. Smith assumed a heat conversion of mechanical work to heat of 100% and a heat partition fraction to the chip of 0.6 [44]. Therefore it can be concluded that Smith overestimated the calculated temperatures. The results of the thermal model indicate that in the diamond turning process of polymers stress-activated flow has a significant contribution in the chip formation process. Further research on this subject is of interest.

Chapter 3 focused on changing cutting conditions and material properties. The thermal model derived in Chapter 2 was used for looking at the temperature profiles in the workpiece material during changing cutting conditions. It was found that an increase in cutting speed or a decrease in depth of cut does not have significant influence on the temperature rise in the primary shear zone. The thermal model indicated that a cutting speed of 3 m/s does not result in an additional temperature rise to reach the glass transition temperature. This is in contrast with literature on polymer turning [21, 44] that indicates that a higher cutting speed should bring the polymer in the thermal flow regime. In fact, at higher cutting speeds less heating of the material can occur due to the smaller heat diffusion of the polymer. This lowers the final cutting temperature in the shear zone. This was also found for the heat partition fraction of the workpiece for such a high cutting speed on PMMA; only 11% of the heat produced in the shear zone was conducted to the workpiece, while the rest was removed by the chip.

It was assumed by Smith [44] that a large negative rake could raise the adiabatic temperature rise significantly. However, the thermal model that Smith applied was not capable of determining this temperature rise. The thermal model used in this thesis was capable of doing this. Using this thermal model it was calculated that the application of a large negative rake angle ($\alpha = -20°$) led to a 30 K higher temperature rise than during turning of PC with zero rake angle. However, this was not enough for reaching T_g. For the investigated turning conditions it can be said that the thermal flow regime is not reached. These results also indicate that stress-activated flow in polymer turning cannot be neglected and this needs further research.

---

[1] This heat partition fraction was determined for a cutting speed $v_c = 0.3$ m/s. Smith used a heat partition fraction to the chip of 0.6 for that cutting speed.

Gel permeation chromatography (GPC) on collected chips and bulk workpiece material showed that the used PMMA grade formed chips by a chain scission and chain slip mechanism, while the used PC grade did not show any chain scission during turning. First, this indicates that it is not the value of the glass transition temperature that determines whether chain scission occurs in turning operations. Second, it can be said that the PC chip is formed by a ductile fracture mechanism.

Chapter 3 described that during turning of PC and PMMA different surface formation mechanisms are active. These appeared to be very susceptible to changes in cutting speed, depth of cut, and rake angle. It was found that for PC, a small non-zero rake angle or a small depth of cut decreases the surface roughness considerably when a faceted tool is used in plunge turning. In fact, the roughness value *Ra* could be decreased to approximately 10 nm for plunge turning.

However, application of a nose radius tool during diamond turning of thermoplastic polymers showed that these parameters do not have such a big influence as in plunge turning with a faceted tool. Therefore, it can be stated that the surface quality in precision turning of thermoplastic polymeric workpieces is rather determined by the ”footprint” of the tool left behind in the radial direction, than by surface characteristics formed in the tangential direction. However, for brittle polymers, like ADC, the tangential surface characteristics have a dominant influence.

Looking at the influence of changing thermo-mechanical history of a polymer, it can be concluded that this influence is marginal. Although cutting forces alter, which is explained by a changing initial yield stress, it was found that chip formation and surface quality are not influenced by a change in thermo-mechanical history.

PMMA was crosslinked to find out what the influence of crosslink density was on the achievable surface roughness. Although relatively high crosslink densities were achieved, no linear relation was found between crosslink density and *Ra* value. ADC with a crosslink density of 1.5 times more than the highest crosslink density created for PMMA had approximately a five times higher *Ra* value than the PMMA grade. This indicates that it is not only crosslink density that determines the resulting workpiece roughness after turning, but another material parameter, which still has to be determined.

Looking at the best conditions to reach good surface roughness values for optical applications, it can be concluded by Figure 3.15 that changing cutting speed does not yield a significant decrease in *Ra* value. The same can be concluded for depth of cut in Figure 3.16. However, decreasing the feed rate from 10 μm/rev to approximately 2 μm/rev has a significant effect for PC where the *Ra* roughness decreased from 60 nm to 20 nm, see Figure 3.17. For PMMA the effect was less pronounced. It can be concluded that the best approach to decrease surface roughness in polymer turning is to decrease the feed rate to small values of 2 μm/rev or less.

Depending on the polymer one can also try to change the rake angle. Figure 3.18 indicated that for ADC materials a large positive rake angle should be applied. For glassy polymers a small ($\approx 3^\circ$) positive or negative rake can be beneficial. However, the exact gain should always be investigated.

Since a lot of parameters were investigated and the effects were not always the same for different polymers, the following table summarizes the parameters that were investigated and whether that parameter can be adapted to improve the quality of the diamond turned workpiece. The table gives the best value that was found in this experimental work too. In general it can be stated that the demand of $Ra < 5$ nm for optical quality was not reached in this research. However, the next table can be used for further optimization.

Table 6.1: Investigated parameters and their influence for improving the diamond turning result for use with a nose radius tool; (+) positive effect, (+/-) effect has to be determined for the polymer to be cut, (○) no significant effect.

parameter	symbol	effect	best value
cutting speed	v_c	+/-	6 m/s
depth of cut	h	○	4 – 6 μm
feed rate	f	+	1 μm/rev
rake angle	α	+/-	$\approx 3^\circ$
rejuvenation	n.a.	○	n.a.
crosslink density	ν_e	○	n.a.

6.1.2 Diamond tool wear

One of the most important aspects of the application of precision turning in the manufacturing of optics is tool life, since this directly influences the cost of a product. In this research several diamond tool wear mechanisms were investigated for polymer turning.

Looking at adhesive, abrasive and thermal tool wear, it can be stated that none of these was responsible for the observed tool wear in this research. Adhesive wear always occurs on the softer material, which was in all cases the polymer. Abrasive tool wear can only be excluded after analysis of the workpiece material. This was done using EDX analysis on the used polymers.

Based on the findings of Chapters 2 and 3 it can be concluded that the temperature increase during diamond turning of glassy polymers is not high enough for thermal wear of the diamond to occur. A temperature above 500 °C in air is needed for the diamond to oxidize quickly. These temperatures are even higher for graphitization to occur. In polymer turning the temperature in the primary shear zone will generally not exceed 100 °C. Therefore it can be expected that thermal wear is not a dominant effect in diamond turning of polymers. However, notice that a higher temperature can increase chemical reaction rates.

Tool life experiments showed that the following can occur during polymer turning:

1. no significant diamond tool wear, as was observed for turning PS and PA, or
2. tribo-electric diamond tool wear can be dominant, as was observed for PSU and PU, or
3. tribo-chemical diamond tool wear can be dominant, as was observed for PMMA and PC.

Chapter 4 showed that tribo-electric tool wear manifests itself as Lichtenberg figures in the tool. These Lichtenberg figures are more likely to occur during diamond turning of polymers when the tool acts as the anode in the charged cutting system. In that case positive Lichtenberg figures are formed. That the anodic function of the tool is important was shown in the tool life experiment on PC. During diamond turning of PC, luminescence by discharging in air was observed, but the tool behaved as a cathode in the cutting system. The result was that not tribo-electric tool wear was dominant, but tribo-chemical tool wear.

Many parameters were found to influence charging and luminescence during turning. These parameters are cutting speed, feed rate and depth of cut. When these values are increased, charging increases as well. Relative humidity has the opposite effect: increasing relative humidity decreases charging, resulting in smaller electric field strengths, and thus less tribo-electric tool wear. Especially above a relative humidity of 65%, the charge in the cutting system decreased to zero; this indicates that when tribo-electric tool wear is dominant for dry turning conditions, it will not be dominant anymore at relative humidities above 65%.

The other dominant tool wear mechanism that can occur in diamond turning of polymers was tribo-chemical tool wear and was described in Chapter 5. It was found that this tribo-chemical wear of the diamond tool is caused by an oxidative etching mechanism. Notice that this tool wear mechanism wears the tool gradually, while tribo-electric tool wear can be very instantaneous. It appeared that polymers that are susceptible to hydrolysis, like PMMA and PC that have esters in their structural unit, are more prone to result in oxidative etching of the diamond tool. Further experiments showed that water is important in the wear behaviour.

A wear mechanism is proposed, and it is based on the experimental findings presented in Chapter 5. It starts with a nucleophile, which can be HO^- from the auto-dissociation of water, or another nucleophile resulting from the hydrolysis of the polymer, attacking a carbonyl group present at the (110) surface of the rake face. Some intermediate steps finally result in the desorption of carbon monoxide (CO). This way, the (110) rake face etches to a stable OH terminated (111) surface.

Calculations have shown that sufficient energy is available in the turning process for these reaction mechanisms to occur. Further, it was calculated that the amount of initiators present, i.e. the nucleophiles, in the workpiece material was of the same order as the amount of diamond carbon atoms removed in the etching process. These calculations confirmed the proposed reaction mechanisms.

6.2 Recommendations

The following recommendations can be made on the subject of precision turning of polymers.

6.2.1 Cutting mechanics

Stress activated flow appears to be important in the cutting process. However, a good description of the influence of stress activated flow during cutting of polymers is lacking and absent in literature. This may be further investigated, possibly by a finite element method, provided that an accurate failure criterium for the polymers can be formulated.

In Chapter 2 it was discussed that there was no linear relationship between cutting forces and initial yield stress for the investigated polymer. This is also known from Drescher's research on specific cutting forces [4]. He states that it is not only the initial yield stress that is important for the (specific) cutting force, but the combination of material ductility and strength. In this research, the relation between the mentioned combination and specific cutting forces was not investigated. For future research on polymers it seems interesting to investigate this relationship between specific cutting forces and the combination of material ductility and strength by using polymers with different thermo-mechanical histories; different thermo-mechanical histories will result in different ratios of ductility and strength.

Crosslinking of PMMA grades did not result in a linear relation between crosslink density and surface roughness value. This was expected and would have explained the influence of thermosetting properties on the turning behaviour of the hard-to-cut ADC material. This results indicates that it cannot be simply said that ”thermosets cannot be machined to optical quality”, since the highly crosslinked PMMA grade had a nearly optical quality. Therefore, it seems interesting to find out what other material parameter determines the outcome of the turning process. Possibly the relation between fracture strength and surface roughness value may yield a good correlation.

Most of the turning experiments were performed without any lubrication; generally a water spray is used for this. The precise effects of such a coolant or lubrication were not investigated. This can be done for process optimization in the field of improving surface quality and/or tool life.

6.2.2 Diamond tool wear

No tool life experiments were performed on the crosslinked PMMA grades described in Section 4.4.5. However, this is an interesting experiment, since the PMMA grade with the highest crosslink density has high enough surface charges for electric breakdown to occur. Tool life experiments on differently crosslinked polymer grades may change the dominant tool wear mechanism from tribo-chemical to tribo-electric.

Electrostatic measurements with an electrostatic voltmeter (EVM) were performed. This data was used for the calculation of the electrostatic charge present at the cut surface. The EVM could not be used for measuring and determining the electrostatic charge present on the chip, only its sign. For measuring the (net) charge present on the chip, an adapted setup with a Faraday cup can be used. The chip can be collected in the Faraday cup during cutting. In combination with the EVM, it will give a measure of the generated charge at the chip-tool interface.

If tribo-chemical tool wear is the dominant wear mechanism for a certain tool/workpiece combination, the use of a different tool material can be considered. The best option then is a mono-crystalline tool. Interesting here can be mono-crystalline aluminium oxide (Al_2O_3), called sapphire. It has a high negative Gibbs energy of formation [153], meaning that it has little affinity to chemical reactions, like oxidation. Whether it can achieve optical quality needs to be investigated.

The experiment with the (111)(111) diamond tool showed that the tool is very stable against chemical wear during precision turning of PMMA, which normally results in oxidative etching of the diamond tool. However, the cutting edge of a (111) tool cannot be made as accurately as the generally used (110) oriented tool. Looking at these results it seems very interesting to develop a manufacturing technique for creating sharp and accurate cutting edges on (111)(111) oriented diamond nose radius tools. Such a radius tool would not just have a (111) orientation on the clearance plane, but a continuously changing orientation to weaker orientation. The (110) orientation at the clearance face will then be located at approximately 54°. Although this may be a problem for small radii, large radius tools could benefit from such an orientation. Such tools could be used in fly-cutting operations.

Severe tribo-chemical tool wear occurred during diamond turning of polymers susceptible to hydrolysis. However, the exact influence of the hydrolysis in the wear process is not known yet, but it is worthwhile to investigate it for the development of easy turnable and new optical polymers. A possibility is to perform tool life tests on PU at high relative humidity, since the dominant tribo-electric tool wear will disappear, giving chance for tribo-chemical wear to become dominant. Combining this with tool life tests at different relative humidities will give more quantification of the tribo-chemical diamond tool wear.

Turning experiments in a different turning environment, such as an N_2 gaseous environment, can give additional insight in the reaction mechanism of the chemical tool wear, since water will be absent then.

6.2.3 Optical materials

Looking at the observed tool wear after turning Sil-O-Flex, a contact lens material that was described in Appendix F, it can be seen that the wear pattern has the same spacing as the feed rate. Tool wear optimization could be obtained by using a random feed rate during turning. This should be investigated, also with respect to achievable optical quality.

The results of a changing rake angle for diamond turning of ADC indicated that an increasing positive rake angle results in a decreasing surface roughness. Based on extrapolation of the ADC results in Figure 3.18, it seems interesting to investigate the achievable surface roughness for diamond turning with a rake angle of 20°.

Future optical polymers should have a high refractive index and Abbe number, hydrophobic properties, and result in the tool being the cathode during turning operations. Of course, hydrophobic properties cannot always be applied: the working of contacts is highly determined by moisture absorption. In that case the polymers should be developed such that the tool will act as the cathode.

Based on the tool life experiments and the description of current optical polymers, polyamide (PA) seems a very promising optical material for the application of the diamond turning process in the production of spectacle lenses.

Bibliography

[1] A. Hof and K. Mehlkopp. Process for manufacturing optical surfaces and shaping machine for carrying out this process. Patent WO9713603, 1997.

[2] K. Kawata, T. Enomoto, Y. Tani, Y. Lu, and M. Suzuki. Achievement of high flatness of work piece by polishing method utilizing polymer particles. In *Proceedings of EUSPEN*, volume 4, pages 109–110, Glasgow, 2004.

[3] V. Sinhoff and H.-P. Bolten. Rod-form micro-optic production process, e.g. for microlenses and micro-arrays. Patent DE19802976, 1999.

[4] J.D. Drescher. *Tool force, tool edge and surface finish relationships in diamond turning*. PhD thesis, North Carolina State University, Raleigh, 1992.

[5] M.J.M. Renkens. *Design of an axially controlled spindle unit for high precision diamond turning*. PhD thesis, Technische Universiteit Eindhoven, Eindhoven, 1997.

[6] P.J. Falter and T.A. Dow. *A diamond turning apparatus for fabrication on non-rotationally symmetric surfaces*, pages 187–201. Springer-Verlag, Berlin, 1988.

[7] M. Weck, J. Hennig, and O. Wetter. Long stroke fast tool servo with dynamic mass compensation and hydrostatic bearings. In *Proceeding of the International Topical Conference*, volume 1, pages 141–144, Aachen, Germany, 2003.

[8] C. F. Cheung and W. B. Lee. A theoretical and experimental investigation of surface roughness formation in ultra-precision diamond turning. *International Journal of Machine Tools and Manufacture*, 40(7):979–1002, 2000.

[9] J. Franse. Manufacturing techniques for complex shapes with submicron accuracy. *Reports on Progress in Physics*, 53:1049–1094, 1990.

[10] J.P.M.B. Vermeulen. *Ceramic optical diamond turning machine - design and development*. PhD thesis, Technische Universiteit Eindhoven, Eindhoven, 1999.

[11] Dr. W. Bos - Chemtura Corporation (Arnhem, NL). Personal communications.

[12] E. Hecht. *Optics*. Addison-Wesley Publishing Company, Massachusetts, 2 edition, 1987.

[13] Essilor International. Cahier d'optique oculaire, les materiaux. Essilor International, 1997.

[14] J.M. Elson, J.P. Rahn, and J.M. Bennett. Relationship of the total integrated scattering from multilayer-coated optics to angle of incidence, polarization, correlation length, and roughness cross-correlation properties. *Applied Optics*, 22(20):3207–3219, 1983.

[15] M. Riedl. Advances in single-point diamond turning provide improved performance for visible as well as ir optics. SPIE's OE-magazine, 2004.

[16] J.P.M.B. Vermuelen, P.C.J.N. Rosiëlle, and P.H.J. Schellekens. An advanced ceramic optical diamond turning machine - design and prototype development. *Annals of the CIRP*, 49(1):407–410, 2000.

[17] T.G. Gijsbers. De colath, een numeriek bestuurde draaibank met zeer hoge precisie. *Philips Technisch Tijdschrift*, 39(8):205–221, 1980. (in Dutch).

[18] S.P.F.C. Jaspers. *Metal Cutting Mechanics and Material Behaviour*. PhD thesis, Technische Universiteit Eindhoven, Eindhoven, 1999.

[19] S.P.F.C. Jaspers and J.H. Dautzenberg. Material behaviour in metal cuttings: strains, strain rates and temperatures in chip formation. *Journal of Materials Processing Technology*, 121:123–135, 2002.

[20] E. Brinksmeier and R. Gläbe. Advances in precision machining of steel. *Annals of the CIRP*, 50(1):385–388, 2001.

[21] J.W. Carr and C. Feger. Ultraprecision machining of polymers. *Precision Engineering*, 15:221–237, 1993.

[22] D.A. Lucca, P. Chou, and R.J. Hocken. Effect of tool edge geometry on the nanometric cutting of Ge. *Annals of the CIRP*, 47(1):475–478, 1998.

[23] M.Es. Abdelmoneim and R.F. Scrutton. Tool edge roundness and stable built-up formation in finish machining. *Transactions of the ASME - Journal of Engineering for Industry*, Nov:1258–1267, 1974.

[24] C. Arcona. *Tool force, chip formation and surface finish in diamond turning*. PhD thesis, North Carolina State University, Raleigh, 1996.

[25] N. Ikawa and S. Shimada. Cutting tool for ultraprecision machining. *Proceedings of the 3rd International Conference on Production Engineering*, pages 357–364, 1977.

[26] R.O. Scattergood. Cutting mechanics for ductile-regime machining. In *Proceedings of Principles of Cutting Mechanics*, ASPE Spring Topical Meeting, pages 17–20, Tucson, Arizona, apr 1993.

[27] H.K. Tönshoff, C. Arendt, and R. Ben Amor. Cutting of hardened steel. *Annals of the CIRP*, 49(2):547–566, 2002.

[28] M. Vahdati, K. Kishi, and Y. Ichida. Investigation on the cutting mode and behaviour of single crystalline silicon under single point diamond cutting. *International Journal of the Japan Society of Precision Engineering*, 29:128–133, 1995.

[29] W.S. Blackley and R.O. Scattergood. Ductile-regime machining model for diamond turning of brittle materials. *Precision Engineering*, 13(2):95–103, 1991.

[30] T. Shibata, E. Makino, M. Ikeda, A. Chiba, and M. Tanaka. Ductile-regime turning of quartz crystal. *Int. J. Japan Soc. Prec. Eng.*, 29(1):18–22, 1995.

[31] M.C. Shaw. *Metal cutting principles*. Oxford University Press Inc, New York, 1986.

[32] H. Ernst and M.E. Merchant. Chip formation, friction and high quality machined surfaces. *Transactions of the American Society of Metals*, 29:299–335, 1941.

[33] E.H. Lee and B.W. Shaffer. The theory of plasticity applied to a problem of machining. *Journal of Applied Mechanics*, dec:405–413, 1951.

[34] D.A. Lucca, R.L. Rhorer, and R. Komanduri. Energy dissipation in the ultraprecision machining of copper. *Annals of the CIRP*, 40(1):69–72, 1991.

[35] D.A. Lucca and Y.W. Seo. Effect of tool edge geometry on energy dissipation in ultraprecision machining. *Annals of the CIRP*, 42(1):83–86, 1993.

[36] T. Moriwaki. Experimental analysis of ultraprecision machining. *International Journal of the Japan Society of Precision Engineering*, 29(4):287–290, 1995.

[37] C.F. Cheung and W.B. Lee. *Surface generation in ultra-precision diamond turning: modelling and practices*. Professional Engineering Publishing Limited, London and Bury St. Edmunds, UK, 2003.

[38] D.J. Whitehouse. *Handbook of surface metrology*. Institute of Physics, Bristol, 1994.

[39] Y. Altintas and M. Weck. Chatter stability of metal cutting and grinding. *Annals of the CIRP*, 53(2):619–642, 2004.

[40] J.M. Oomen and J. Eisses. Wear of monocrystalline diamond tools during ultraprecision machining of nonferrous metals. *Precision Engineering*, 14(4):206–218, 1992.

[41] B. Wanders - Procornea (Eerbeek, NL). Personal communication.

[42] A. Kobayashi. Machining plastics - part 1. *Modern Plastics*, 40:110–120,174–175, 1963.

[43] G.C. Berry and T.G. Fox. The viscosity of polymers and their concentrated solutions. *Advances in Polymer Science*, 5:261–357, 1968.

[44] E.F. Smith. Single-point diamond turning of amorphous thermoplastic polymers. Master's thesis, North Carolina State University, Rayleigh, NC, 1989.

[45] L.C.E. Struik. *Physical aging of amorphous polymers and other materials*. Elsevier, Amsterdam, 1978.

[46] R.J. Young and P.A. Lovell. *Introduction to polymers*. Chapman & Hall, London, 1991.

[47] H.E.H Meijer and L.E. Govaert. Mechanical performance of polymer systems: the relation between structure and properties. *Progress in Polymer Science*, 30:915–938, 2005.

[48] H.G.H. van Melick. *Deformation and failure of polymer glasses*. PhD thesis, Technische Universiteit Eindhoven, Eindhoven, 2002.

[49] H.G.H. van Melick, L.E. Govaert, and H.E.H Meijer. Localisation phenomena in glassy polymers: influence of thermal and mechanical history. *Polymer*, 44:3579–3591, 2003.

[50] L.E. Govaert, P.H.M. Timmermans, and W.A.M. Brekelmans. The influence of intrinsic strain softening on strain localization in polycarbonate: modeling and experimental validation. *Journal of Engineering Materials and Technology*, 122:177–185, 2000.

[51] L.E. Govaert, H.G.H. van Melick, and H.E.H. Meijer. Temporary toughening of polystyrene through mechanical pre-conditioning. *Polymer*, 42:1271–1274, 2001.

[52] E.T.J. Klompen. *Mechanical properties of solid polymers*. PhD thesis, Technische Universiteit Eindhoven, Eindhoven, 2005.

[53] R.N. Haward and R.J. Young. *The physics of glassy polymers*. Chapman & Hall, London, 2 edition, 1997.

[54] S.M. Aharoni. On entanglements of flexible and rodlike polymers. *Macromolecules,* 16:1722–1728, 1983.

[55] B.H. Bersted. Entanglement network model relating tensile impact strength and the ductile-brittle transition to molecular structure in amorphous polymers. *Journal of Applied Polymer Science*, 24:37–50, 1979.

[56] J.E. Mark. *Polymer data handbook.* Oxford University Press, Oxford, 1999.

[57] A.K. van der Vegt. *Polymeren, van keten tot kunststof.* Delftse Universitaire Pers, Delft, 1996.

[58] P.I. Vincent. The tough-brittle transition in thermoplastics. *Polymer,* 1:425–444, 1960.

[59] B.H. Bersted and T.G. Anderson. Influence of molecular weight and molecular weight distribution on the tensile properties of amorphous polymers. *Journal of Applied Polymer Science*, 39:499–514, 1990.

[60] L.M. Nichilson, K.S. Whitley, T.S. Gates, and J.A. Hinkley. Influence of molecular weight on the mechanical performance of a thermoplastic glassy polyimide. *Journal of Materials Science,* 35:6111–6121, 2000.

[61] J.D. Ferry. *Visco-elastic properties of polymers.* John Wiley & sons Inc., New York, 1980.

[62] A. Kobayashi and K. Saito. On the cutting mechanism of high polymers. *Journal of Polymer Science,* 58:1377–1395, 1962.

[63] G. Boothroyd. *Fundamentals of metal machining and machine tools.* McGraw-Hill, New York, 1975.

[64] C. Feger and J.W. Carr. Viscoelastic behaviour and polymer machining. In *Annual Technical Conference Society of Plastics Engineers*, volume 50, pages 1965–1966, 1992.

[65] E. Paul, C.J. Evans, A. Mangamelli, M.L. McGlauflin, and R.S. Polvani. Chemical aspects of tool wear in single point diamond turning. *Precision Engineering*, 18:4–19, 1996.

[66] H.H. Hurt and D.L. Decker. Tribological considerations of the diamond single-point tool. In D.P. Brehm, editor, *Proceedings of SPIE,* volume 508, pages 126–131, 1984.

[67] K.G. Budinski. Tool wear in cutting plastic - abrasion or erosion? *Wear,* 233-235:362–371, 1999.

[68] J.E. Field. *The properties of diamond.* Academic Press, London, 1979.

[69] J. Wilks and E. Wilks. *Properties and applications of dimaond.* Butterworth-Heinemann Ltd., Oxford, 1991.

[70] S. Shimada, H. Tanaka, M. Higuchi, T. Yamaguchi, S. Honda, and K. Obata. Thermo-chemical wear mechanism of diamond tool in machining of ferrous metals. *Annals of the CIRP*, 53(1):57–60, 2004.

[71] G.W. Adams and R.J. Farris. Latent energy of deformation of bisphenol A polycarbonate. *Journal of Polymer Science. Part B, Polymer Science*, 26(2):433–445, 1988.

[72] Y.K. Godovsky. *Thermophysical properties of polymers.* Springer-Verlag, New York, 1992.

[73] M.C. Boyce, E.L.Montagut, and A.S.Argon. The effect of thermomechanical coupling on the cold drawing process of glassy polymers. *Polymer Engineering and Science*, 32(16):1073–1085, 1992.

[74] K. Horio and M. Nabeshima. Which of the material properties dominates surface roughness of diamond turned plastics. In *Proceeding of ASPE*, volume 22, pages 46–49, Arizona, 2000.

[75] S.N. Lavrynenko. Distinctive features of polymeric optical components precision machining. In *Proceedings of EUSPEN*, volume 1, pages 207–210, 1999.

[76] Y. Furukawa and N. Moronuki. Effect of material properties on ultra precise cutting processes. *Annals of the CIRP*, 37(1):113–116, 1988.

[77] R. Komanduri and Z.B. Hou. Thermal modeling of the metal cutting process - part 1 - temperature rise distribution due to shear plane heat source. *International Journal of Mechanical Sciences*, 42:1715–1752, 2000.

[78] R. Komanduri and Z.B. Hou. Thermal modeling of the metal cutting process - part 2 - temperature rise distribution due to frictional heat source at the tool-chip interface. *International Journal of Mechanical Sciences*, 43:57–88, 2001.

[79] R. Komanduri and Z.B. Hou. Thermal modeling of the metal cutting process - part 3 - temperature rise distribution due to the combined effects of shear plane heat source and the tool-chip interface frictional heat source. *International Journal of Mechanical Sciences*, 43:89–107, 2001.

[80] R.S. Hahn. On the temperature developed at the shear plane in the metal cutting process. In *Proceedings of First U.S. National Congress of Applied Mechanics*, pages 661–666, 1951.

[81] J.C. Jaeger. Moving sources of heat and the temperature at sliding contacts. In *Proceeding Royal Society of NSW*, volume 76, pages 203–224, 1942.

[82] D. Rosenthal. The theory of moving sources of heat and its application to metal treatments. *Transactions of ASME*, 68:849–866, 1946.

[83] D.W. van Krevelen. *Properties of polymers*. Elsevier Science, Amsterdam, 1997.

[84] T. Ueda, M. Sato, and K. Nakayama. The temperature of a single crystal diamond tool in turning. *Annals of the CIRP*, 40(1):41–44, 1998.

[85] H. Blok. Theoretical study of temperature rise at surfaces of actual contact under oiliness lubricating conditions. In *Proceedings of the General Discussion on Lubrication and Lubricants*, pages 222–235, 1938.

[86] A. Bejan and A.D. Kraus. *Heat transfer handbook*. Wiley, Chichester, 2003.

[87] H.O. Pierson. *Handbook of carbon, graphite, diamond and fullerenes*. Noyes Publications, Park Ridge, New Jersey, 1993.

[88] C.J. Pouchert. *The Aldrich library of infrared spectra*. Aldrich Chemical Company Inc., Wisconsin, 3 edition, 1981.

[89] A. Wei. Finite element analysis of localized heating in optical substrates due to e-beam patterning. In *BACUS Symposium on Photomask Technology*, volume 20, 2000.

[90] T. Moriwaki and K. Okuda. Machinability of copper in ultra-precision micro diamond cutting. *Annals of the CIRP*, 38(1):115–118, 1989.

[91] K. Feldman. Preliminary results, 2005. ETH Zurich.

[92] S.M. Schmalholz, Y.Y. Podladchikov, and J.-P. Burg. Control of folding by gravity and matrix thickness: implications for large-scale folding. *Journal of Geophysical Research*, 107:2005, 2002.

[93] D.W. Schmid and Y.Y. Podladchikov. Folding of a finite length power law layer. *Journal of Geophysical Research*, 109:B03407, 2004.

[94] C. Arcona and T.A. Dow. A new technique for studying the chip formation process in diamond turning. *Precision Engineering*, 18(2-3):157–160, 1996.

[95] G.M. Swallowe. *Mechanical properties and testing of polymers - an A-Z reference*. Kluwer Academic Publishers, Dordrecht, 1999.

[96] T.A. Tervoort. *Constitutive modelling of polymer glasses*. PhD thesis, Technische Universiteit Eindhoven, Eindhoven, 1996.

[97] T.A. Tervoort, E.T.J. Klompen, and L.E. Govaert. A multi-mode approach to finite, three-dimensional, nonlinear viscoelastic behavior of polymer glasses. *Journal of Rheology*, 40(5):779–797, 1996.

[98] T.A. Tervoort, R.J.M. Smit, W.A.M. Brekelmans, and L.E. Govaert. A constitutive equation for the elasto-viscoplastic deformation of glassy polymers. *Mechanics of Time-Dependent Materials*, 1(3):269–291, 1998.

[99] L. Zhang and H. Zhang. An approximate mechanics model for the orthogonal cutting of composites reinforced by unidirectional fibers. In C.A. van Luttervelt, editor, *Fourth CIRP International Workshop Modelling of Machining Operations*, pages 1–5. CIRP, 2001.

[100] J.D. Kim and I.H. Choi. Ultrasonic vibration turning of optical glasses. *Proceedings of the SPIE*, 2576:414–425, 1995.

[101] C. Evans. Cryogenic diamond turning of stainless steel. *Annals of the CIRP*, 40(1):571–575, 1991.

[102] J. Casstevens. Diamond turning of steel in carbon saturated environments. *Precision Engineering*, 5:9–15, 1983.

[103] S.N. Lavrynenko. Cutting tool wear mechanism in precision single-point diamond turning of optical and bioengineering polymers. In *Proceedings of EUSPEN*, volume 1, pages 241–244, 2003.

[104] G.P.H. Gubbels, G.J.F.T. van der Beek, A.L. Hoep, F.L.M. Delbressine, and H. van Halewijn. Diamond tool wear when cutting amorphous polymers. *Annals of the CIRP*, 53(1):447–450, 2004.

[105] A. Jacobs. Het modelleren van beitelslijtage. Master's thesis, Technische Universiteit Eindhoven, Eindhoven, 1997. WPA rapport nr. 310052 (in Dutch).

[106] H.J. Kiela. The influence of materials on surface quality in ultra-precision cutting of contact lenses. *Global Contact*, 21:26–27, 2001.

[107] V.R. Howes. The graphitization of diamond. *Proceedings of the Physical Society*, 80:648–662, 1962.

[108] F.H. Merrill and A. von Hippel. The atomphysical interpretation of lichtenberg figures and their application to the study of gas discharge phenomena. *Journal of Applied Physics*, 10:873–887, 1939.

[109] R.G. Brown. Time and temperature dependence of irradiation effects in solid dielectrics. *Journal of Applied Physics*, 38(10):3904–3907, 1967.

[110] N. Jonassen. *Electrostatics*. Chapman and Hall, London, 1998.

[111] Prof. Dr. Ir. G.M.W. Kroesen. Personal communication, apr 2006.

[112] J.L. Lauer, J.L. Shohet, and R.W. Hansen. Measuring vacuum ultraviolet radiation-induced damage. *Journal of Vacuum Science Technology A*, 21(4):1253–1259, 2003.

[113] E.M. van Veldhuizen. *Electrical discharges for environmental purposes*. Nova Science Publishers, New York, 2000.

[114] V.K. Sharma and R.A. Pethrick. Influence of tacticity on the triboelectric charging of polymethyl methacrylate. *Journal of Electrostatics*, 25:309–314, 1990.

[115] J.T. Dickinson, L. Scudiero, K. Yasuda, M.W. Kim, and S.C. Langford. Dynamic tribological probes: particle emission and transient electrical measurements. *Tribology Letters*, 3:53–67, 1997.

[116] D.M. Taylor, T.J. Lewis, and T.P.T. Williams. The electrokinetic charging of polymers during capillary extrusion. *Journal of Physics D: Applied Physics*, 7:1756–1772, 1974.

[117] L. Pérez-Trejo, J. Pérez-González, L. de Vargas, and E. Moreno. Triboelectrification of molten linear low density polyethylene under continous extrusion. *Wear*, 257:329–337, 2004.

[118] V.E. Shashoua. Static electricity in polymers, part 1: Theory and measurement. *Journal of Polymer Science*, 33:65–85, 1958.

[119] V.E. Shashoua. Static electricity in polymers, part 2: Chemical structure and antistatic behaviour. *Journal of Polymer Science: part A*, 1:169–187, 1963.

[120] A.I. Grabchenko, Verezub N.V., Lavrynenko S.N., Horvath M., and Mamalis A.G. Precision cutting of optical polymer components for bioengineering applications. *Journal of Materials Processing Technology*, 97:126–131, 2000.

[121] R.W.B. Pearse and A.G. Gaydon. *The identification of molecular spectra*. Chapman and Hall, London, 1984.

[122] J. Hecht. *The laser guidebook*. McGraw-Hill, New York, 1986.

[123] S. Badaloni and I. Gallimberti. *Basic data of air discharges*. Universita' di Padova, Padova, 1972.

[124] J. Fuhrmann, L. Nick, J.T. Dickinson, and L. Jensen. Photon emission during deformation of glass-fiber-reinforced bisphenol-a-polycarbonate. *Journal of Applied Polymer Science*, 48:2123–2133, 1993.

[125] Dr. Ir. E.M. van Veldhuizen. Personal communication, jun 2005.

[126] K. Nakayama and R.A. Nevshupa. Plasma generation in a gap around a sliding contact. *Journal of Physics D: Applied Physics*, 35:1.53–1.56, 2002.

[127] K. Nakayama. Triboemission of charged particles and resistivity of solids. *Tribology Letters*, 6:37–40, 1998.

[128] K. Nakayama, N. Suzuki, and H. Hashimoto. Triboemission of charged particles and photons from solid surfaces during frictional damage. *Journal of Physics D: Applied Physics*, 25:303–308, 1992.

[129] A. Kumar and M.M. Perlman. Sliding-friction electrification of polymers and charge decay. *Journal of Polymer Science, part B: Polymer Physics*, 30:859–863, 1992.

[130] B.A. Kwetkus, K. Sattler, and H.-C. Siegmann. Gas breakdown in contact electrification. *Journal of Physics D: Applied Physics*, 25:139–146, 1992.

[131] S.E. Grillo and J.E. Field. Investigation of the possibility of electrical wear by sparking in diamond polishing. *Wear*, 211:30–34, 1997.

[132] P.E. Frayssines, N. Bonifaci, A. Denat, and O. Lesaint. Streamers in liquid nitrogen: characterization and spectroscopic determination of gaseous filament temperature and electron density. *Journal of Physics D: Applied Physics*, 35:369–377, 2002.

[133] Y.P. Raizer. *Gas discharge physics*. Springer-Verlag, Berlin, 1991.

[134] F.K. de Theije. *Diamond surfaces - growth and etching mechanisms*. PhD thesis, Katholieke Universiteit Nijmegen, Nijmegen, 2001.

[135] Dr. F.K. de Theije - Philips (Eindhoven, NL). Personal communications.

[136] E. Brinksmeier, R. Gläbe, and J. Osmer. Ultra-precision diamond turning of steel molds. *Annals of the CIRP*, 55(1), 2006.

[137] R. Sharma, S. Trigwell, A.S. Biris, R.A. Sims, and M.K. Mazumder. Effect of ambient relative humidity and surface modification on the charge decay properties of polymer powders in powder coating. *IEEE transactions on industry applications*, 39(1):87–95, 2003.

[138] A.K. van der Vegt and L.E. Govaert. *Polymeren, van keten tot kunststof*. Delft University Press, Delft, 5 edition, 2003.

[139] M. Akyuz. *Positive streamer discharges in air and along insulating surfaces: experiment and simulation*. PhD thesis, Uppsala University, Sweden, 2002.

[140] J.C. Devins, S.J. Rzad, and R.J. Schwabe. Breakdown and prebreakdown phenomena in liquids. *Journal of Applied Physics*, 52(7):4531–4545, 1981.

[141] E. Nasser and L.B. Loeb. Impulse streamer branching from lichtenberg figure studies. *Journal of Applied Physics*, 34(11):3340–3348, 1963.

[142] D.A. Taminiau. Internal report Océ Nederland B.V., 1995.

[143] S.M. Sze. *Physics of Semiconductor Devices*. Wiley, New York, 2 edition, 1981.

[144] T. Evans and C. Phaal. The kinetics of the diamond-oxygen reaction. In *Proceedings of the 5th Conference on Carbon*, pages 147–153, Pennsylvania State University, 1962.

[145] F.K. de Theije, E. van Veenendaal, W.J.P. van Enckevort, and E. Vlieg. Oxidative etching of cleaved synthetic diamond {111} surfaces. *Surface Science*, 492:91–105, 2001.

[146] C.J. Chu, C. Pan, J.L. Margrave, and R.H. Hauge. F_2, H_2O, and O_2 etching rates of diamond and the effects of F_2, HF, and H_2O on the molecular O_2 etching of (110) diamond. *Diamond and Related Materials*, 4:1317–1324, 1995.

[147] F.A. Carey. *Organic chemistry*. McGraw-Hill, New York, 5 edition, 2003.

[148] J.T. Dickinson. Fractoemission. *Encyclopedia of Materials: Science and Technology*, pages 3254–3256, 2004.

[149] M. Whitfield. Electroanalytical chemistry of sea water. In J.P. Riley and G. Skirrow, editors, *Chemical Oceanography*, chapter 20. Academic Press, New York, 2 edition, 1975.

[150] C.J. Hartley and H.L. Shergold. The aging of aqueous diamond suspensions. *Chemistry and Industry*, pages 224–227, mar 1980.

[151] A.W. Phelps. Aqueous surface chemistry of diamond grains. In *Papers Presented to the 29th Annual Lunar and Planetary Science Conference*, Houston, Texas, 1998. Lunar and Planetary Science Institute.

[152] B.L. Mackey, J.N. Russel, J.E. Crowell, P.E. Pehrsson, B.D. Thoms, and J.E. Butler. Oxygen adsorption on the (110)-oriented diamond surface. *Journal of Physical Chemistry B*, 105:3803–3812, 2001.

[153] D.A. Taminiau. Interface conditions in precision cutting of steel. Ph.D. thesis (unpublished).

[154] D.A. Lucca and R.L. Rhorer. Aspects of surface generation in orthogonal ultraprecision machining. *Annals of the CIRP*, 43(1):43–46, 1994.

[155] D.A. Taminiau and J.H. Dautzenberg. Bluntness of the tool and process forces in high-precision cutting. *Annals of the CIRP*, 40(1):65–68, 1991.

[156] Dr. H. van Halewijn - Diamond Tools Group. Personal communication, 2004.

[157] A. Bejan. *Heat transfer*. John Wiley & Sons, Inc, New York, 1993.

[158] A. Coehn. Über ein Gesetz der Electricitätserregung. *Annalen der Physik und Chemie*, 64:217–232, 1898.

[159] D.M. Taylor and P.E. Secker. *Industrial electrostatics: fundamentals and measurements*. Research Studies Press Ltd., Somerset, England, 1994.

[160] M.A. Noras. Non-contact surface charge/voltage measurements - capacitive probe/principle of operation. Trek Application Note - number 3001, 2002.

[161] M.A. Noras. Non-contact surface charge/voltage measurements - field meter and voltmeter methods. Trek Application Note - number 3002, 2002.

Appendix A

List of used Nomenclature, Acronyms and Symbols

A.1 Abbreviations

ADC	allyl diglycol carbonate, like CR39, RAV7 or Nouriset
AFM	atomic force microscope
BUE	built-up edge
DIC	differential interference contrast
EDX	energy dispersive X-ray
ESEM	environmental scanning electron microscope
EVM	electrostatic volt meter
MRR	material removal rate
PA	polyamide
PC	poly(bisphenol carbonate)
PDI	Poly Dispersity Index ($PDI = M_w/M_n$)
PMMA	polymethylmethacrylate
PS	polystyrene
PSU	polysulphon
PU	polyurethane
RH	relative humidity
RMS	root mean square
SEM	scanning electron microscope
TIS	total integrated scatter

A.2 Symbols

roman	description	unit
A	amplitude	m
A	(surface) area	m^2
b	width of cut	m
B	heat partition fraction	–
Bi	Biot number	–
c	specific heat capacity	$J \cdot kg^{-1} \cdot K^{-1}$
c_l	specific heat capacity for polymer below T_g	$J \cdot kg^{-1} \cdot K^{-1}$
c_s	specific heat capacity for polymer above T_g	$J \cdot kg^{-1} \cdot K^{-1}$
C	capacitance	F
C	stiffness	$N \cdot m^{-2}$
C_∞	characteristic ratio	–
d	depth	m
d	diameter	m
d	thickness	m
E	electric field strength	$V \cdot m^{-1}$
E	Young's modulus	$N \cdot m^{-2}$
f	feed rate	$m \cdot rev^{-1}$
f	frequency	s^{-1}
F	force	N
F_c	(main) cutting force	N
F_f	frictional force at rake face	N
F_n	normal force	N
F_R	resultant force	N
F_s	shear plane force	N
F_{sn}	shear plane normal force	N
F_t	thrust force	N
h	heat transfer coefficient	$W \cdot m^{-2} \cdot K^{-1}$
h	depth of cut	m
h_c	chip thickness	m
h_{cu}	uncut chip thickness	m
H	hardness	$N \cdot m^{-2}$
H	height (general)	m

K_0	modified Bessel function of the second kind of order zero	–
l	bond length	m
l_i	distance from origin to segmental line heat source	m
L	length (general)	m
L	length of cut	m
L	length of line heat source	m
L_c	contact length of chip on rake face	m
L_s	length of the shear plane	m
$L_{thermal}$	distance between adjacent thermal layers	m
m	mass	kg
$\dot{m}$	mass rate	$\mathrm{kg \cdot s^{-1}}$
M	molar mass	$\mathrm{kg \cdot mol^{-1}}$
M_0	molecular weight of a monomer	$\mathrm{kg \cdot mol^{-1}}$
M_c	critical molecular weight ($M_c \approx 2M_e$)	$\mathrm{kg \cdot mol^{-1}}$
M_e	molecular weight between entanglements	$\mathrm{kg \cdot mol^{-1}}$
M_n	number averaged molecular weight	$\mathrm{kg \cdot mol^{-1}}$
M_w	weight averaged molecular weight	$\mathrm{kg \cdot mol^{-1}}$
n	number	–
n	refractive index	–
n_e	number of bonds between entanglements	–
Nu	Nusselt number	–
p	pressure	$\mathrm{N \cdot m^{-2}}$
P_s	shearing power	W
$\dot{q}$	heat flux ($\dot{Q}/A$)	$\mathrm{W \cdot m^{-2}}$
$\dot{q}_l$	heat liberation intensity of a line heat source	$\mathrm{W \cdot m^{-1}}$
$\dot{q}_{pl}$	heat liberation intensity of a plane heat source	$\mathrm{W \cdot m^{-2}}$
$\dot{q}_{pls}$	heat liberation intensity of shear plane heat source	$\mathrm{W \cdot m^{-2}}$
$\dot{q}_{point}$	heat liberation intensity of a point heat source	W
Q	electric charge	C
Q	(quantity of) heat	J
$\dot{Q}$	heat rate (power)	W
r	radius (general)	m
r	end-to-end distance	m
r_c	chip thickness ratio ($=h/h_c$)	–
r_n	cutting edge radius	m
R	distance between point M and segmental line dl_i	m

R	electric resistivity	Ωm
R	tool nose radius	m
Ra	Ra roughness value	m
R_{co}	thermal contact resistance	$m^2 \cdot K \cdot W^{-1}$
Re	Reynolds number	–
Rq	RMS roughness value	m
Rt	peak-vally roughness value	m
t	time	s
t	Celsius temperature	°C
T	temperature	K
T_g	glass transition temperature	K
T_m	melt temperature	K
u	speed of sound	$m \cdot s^{-1}$
U	energy	J
v	velocity	$m \cdot s^{-1}$
v_c	cutting speed	$m \cdot s^{-1}$
v_{chip}	chip velocity	$m \cdot s^{-1}$
v_s	shear velocity	$m \cdot s^{-1}$
V	potential	V
V	volume	m^3
V_d	Abbe number	–
W	width (general)	m
X	X-coordinate of point M in the moving coordinate system	m
X_i	projection of R on X-axis	m
y	y-coordinate of point M in the moving coordinate system	m
y_i	projection of R on y-axis	m
z	z-coordinate of point M in the moving coordinate system	m
z_i	projection of R on z-axis	m

greek	**description**	**unit**
α	rake angle	–
β	friction angle ($\beta = F_f/F_n$)	–
γ	clearance angle	–

γ	shear strain	–
$\dot{\gamma}$	shear strain rate	s^{-1}
δ	spring-back	m
ϵ	emissivity	–
$\dot{\epsilon}$	strain rate	s^{-1}
ϵ_r	relative dielectric constant	–
ϵ_{true}	true strain	–
η	work to heat conversion ratio	–
θ	valence angle	°
Θ (Θ_M)	temperature rise (at point M)	K
$\overline{\Theta}_{chip}$	mean temperature rise in chip	K
Θ_{sp}	temperature rise at shear plane	K
κ	thermal diffusivity	$m^2 \cdot s^{-1}$
λ	thermal conductivity	$W \cdot m^{-1} \cdot K^{-1}$
λ	wavelength	m
λ_e,λ_i	mean free path of electron, ion	m
λ_{max}	maximum extension ratio	–
μ	friction coefficient	–
ν_e	chain/entanglement density	$\text{chains} \cdot m^{-3}$
ρ	density	$kg \cdot m^{-3}$
σ	surface charge	$C \cdot m^{-2}$
σ	stress	$N \cdot m^{-2}$
σ_y	yield stress	$N \cdot m^{-2}$
σ_t	ultimate tensile stress	$N \cdot m^{-2}$
σ_{true}	true stress	$N \cdot m^{-2}$
τ	shear stress	$N \cdot m^{-2}$
τ	decay time	s
τ_y	shear yield stress	$N \cdot m^{-2}$
φ	hindrance angle of polymeric segments	°
φ	shear angle	°
Φ	angle of oblique moving heat source	°
ω	rotational frequency	s^{-1}

A.3 Values of some fundamental constants

symbol	**description**	**value**
N_A	Avogadro’s number	$6.0221367 \cdot 10^{23}\ mol^{-1}$
R	universal gas constant	$8.3145\ J \cdot mol^{-1} \cdot K^{-1}$

greek	description	value
ϵ_0	absolute dielectric constant in vacuum	$8.85 \cdot 10^{-12}$ F $\cdot$ m^{-1}
σ	Stefan-Boltzmann constant	$5.67051 \cdot 10^{-8}$ W $\cdot$ m$^{-2} \cdot$ K^{-4}

Appendix B

Cutting edge measurement

Although several references are known about cutting edge radius values of the mono-crystalline diamond tool, e.g. [4, 20, 22, 154, 155], for this research a verification measurement was performed too.

Several measurement techniques are known, such as direct examination by optical or scanning electron microscopy, replication techniques that have to be examined again by the previous methods, or scanning microscopy. A good reference for these methods is given by Drescher [4].

An atomic force microscope (AFM) was chosen for the measurements, because of its high resolution (sub-nanometer). For the measurements the tool was positioned under the AFM, on a special tool holder, enabling the possibility of adjusting the angle of the rake and clearance plane of the tool. This is important, since the used AFM tip has a maximum tip angle of 25°. This means that the tool faces always have to be positioned at an angle smaller than 65°. For most tools, this isn't a problem, unless a large positive clearance or rake angle is used.

Figure B.1 shows schematically the used setup. The angle ζ, which determines the measurement angles for the rake and clearance face can be calculated by

$$\zeta = \frac{90^\circ + \gamma - \alpha}{2} \tag{B.1}$$

with α the rake angle of the tool and γ the clearance angle. Using this angle the rake and clearance face can always be measured.
The used measurement strategy is:

1. Measure a calibration grid, for determining the AFM tip radius.
2. Position the AFM tip near the cutting edge and perform a scan.
3. Process the measurement data, i.e. AFM tip deconvolution.

Processing the measurement data involves two aspects: 1) determination of the radius of the AFM tip, which is necessary for deconvolution of the tip geometry from the cutting edge measurement, and 2) determination of cutting edge radius. Figure B.2 shows a measurement of a newly lapped diamond cutting tool.

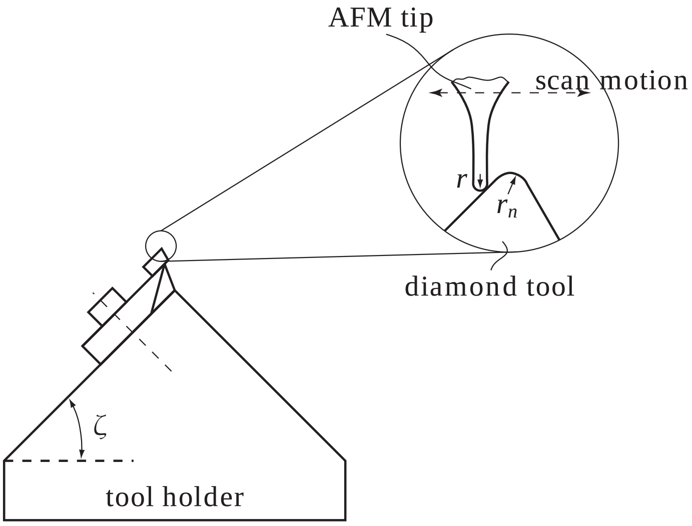
AFM tip
scan motion
r
r_n
diamond tool
ζ
tool holder

Figure B.1: Schematic representation of measurement setup.

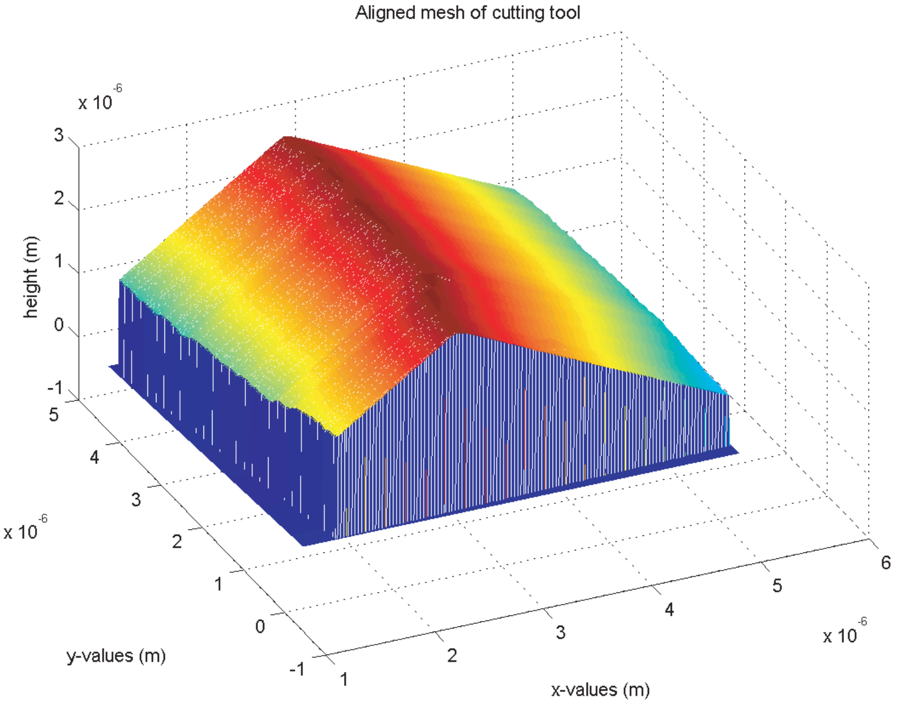

Figure B.2: Measured cutting edge of a newly lapped tool. The estimated cutting edge radius is 36 nm with an estimated standard deviation of 12 nm.

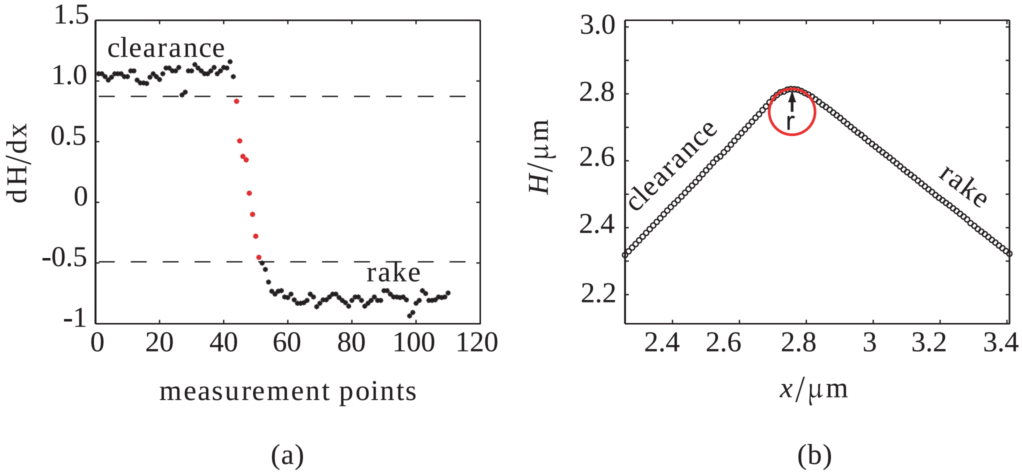

Figure B.3: Figure (a) shows the gradients of the cross-section shown in (b). In (b) the corresponding radius fit applied is shown as well.

The radius is determined on every scan line across the cutting edge. To do this, the cutting edge is leveled in respect to the base plane and rotated for alignment along the y-axis. Doing this, every scan line can be used for evaluation of the cutting edge radius. This gives, depending on the measurement resolution, a huge amount of values for the cutting edge radius.

The radius estimation is started by evaluating the derivatives between consecutive measurement points of each measurement line across the edge. Since the angles ζ, α and γ are known, the corresponding derivatives are known and can be used as boundaries for the estimation of the radius fit. This can be seen in Figure B.3, where the points between the dashed lines are deviations from the gradients of the two diamond faces, and should therefore belong to the cutting edge radius. Only these points are used for the least square radius fit.

For the sharp tool, a mean radius fit was obtained of 36 nm with a standard deviation of 12 nm. This is the radius after deconvolution of the AFM tip, which was determined to be 27 nm. The value of 36 nm is in good accordance with values reported in literature [4, 20, 22].

Worn diamond tool Figure B.4 shows the cutting edge of a worn diamond tool. The tool was used for turning PC with a length of cut of 100 km. Although the measurements do not totally overlap, it may be obvious that a significant tool wear occurred. The AFM measurement is in agreement with the observed tool wear in Figure 4.14.

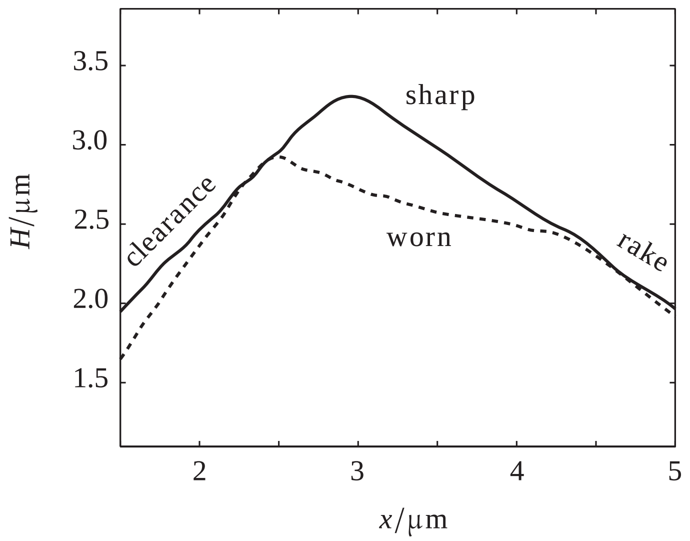

Figure B.4: AFM measurements of a sharp tool and a worn tool.

Appendix C

Material Properties

In this appendix several material properties are listed that are used in this thesis. Table C.1 gives some material properties of the polymers that were mainly used for the thermal modelling. Table C.2 gives some data known for diamond.

Table C.1: Some material properties of several polymers.

	PC	PMMA	PS	PSU
Property				
density in 10^3 kg/m^3	1.20	1.18	1.05	1.24
speed of sound in m/s	2350	2370	2600	2350
Mechanical properties				
E-modulus in MPa	2100	3300	3300	2450
yield stress in MPa	70	115	100	75
Thermal properties				
glass transition temperature in °C	150	110	95	190
thermal conductivity in W/(m · K)	0.193	0.193	0.142	0.22
specific heat capacity in 10^3 J/(kg · K)	1.20	1.38	1.21	1.0
thermal diffusivity in 10^{-8} m^2/s	13.5	11.8	11.1	17.7
$L_{thermal}$ in 10^{-11} m	5.8	5.0	4.3	5.0
Electrical properties				
dielectric constant	2.6-3.0	2.6-3.7	2.6	3.1
breakdown strength in 10^6 V/m	n.a.	n.a.	n.a.	39

Table C.2: Some material properties of diamond.

Property	
density in kg/m^3	3500
Thermal properties	
thermal conductivity in $W/(m \cdot K)$	500-2000
heat capacity in $J/(kg \cdot K)$	504
thermal diffusivity in $10^{-4}\ m^2/s$	4-11
Electrical properties	
dielectric constant	5.5
breakdown strength in $10^6\ V/m$	100-2000

Appendix D

Calibration of diamond tool with embedded thermocouple

The developed tool with embedded thermocouple has a certain distance between point of measurement and point of applied temperature (i.e. the cutting edge). Therefore a calibration procedure is needed to determine the error between applied temperature at the cutting edge and measured temperature at the thermocouple.

D.1 Calibration

The embedded thermocouple tool is used to measure the temperature at the tool tip. To get the relation between the measured thermocouple temperature and the actual cutting edge temperature a calibration procedure is applied. The main thought of the calibration procedure consists of the existence of a constant heat flow during the turning process of polymers from the primary shear zone to the diamond tool via the cutting edge. For most thermoplastic polymers a continuous chip is formed during the turning process. This means that a continuous and constant heat source can be assumed in the primary shear zone. A calibration procedure should account for this. It is assumed that the process of pressing the embedded thermocouple tool to an aluminium heated cylinder is comparable with the turning process of polymers. The reason for this is that aluminium has a relatively high thermal diffusivity compared to polymers. Because of this high thermal diffusivity a constant and continuous heat flow from the interior of the heated cylinder to the tool is achieved, just like the turning process.

However, when the tool is pressed against the aluminium cylinder, a different (thermal) contact resistance occurs than that during polymer turning. For solid interfaces the thermal contact resistance is given as [86]:

$$R_{co} = \left[1,45 \cdot \lambda_s \left(\frac{p}{H} \right)^{0,985} \frac{\left| \overline{\tan \delta} \right|}{\sigma_s} \right]^{-1} \tag{D.1}$$

with

$$\lambda_s = \frac{2 \cdot \lambda_1 \cdot \lambda_2}{\lambda_1 + \lambda_2} \tag{D.2}$$

the harmonic mean thermal conductivity and

$$\sigma_s = \sqrt{\sigma_1^2 + \sigma_2^2} \tag{D.3}$$

the RMS roughness and $\left|\overline{\tan\delta}\right|$ the average asperity angle. If the conditions are not known, it can be assumed that $\sigma_s / \left|\overline{\tan\delta}\right| = 5 - 9\ \mu\text{m}$ [86].

Table D.1 gives the thermal contact resistances of diamond and workpiece material for diamond turning of aluminium and of PMMA. The values for the aluminium cutting were derived from Ueda [84], and the values for the PMMA cutting were derived from Chapter 2. For the hardness it is assumed that $H = 3\sigma$. It can be seen in the table that the thermal contact resistance for the diamond-aluminium pair is three orders smaller than that for the diamond-PMMA pair.

Table D.1: Calculated thermal contact resistances.

	Aluminium	PMMA
$\lambda_1/(\text{W} \cdot \text{m}^{-1} \cdot \text{K}^{-1})$	237	0.2
$\lambda_2/(\text{W} \cdot \text{m}^{-1} \cdot \text{K}^{-1})$	500[a]	500[a]
$\lambda_s/(\text{W} \cdot \text{m}^{-1} \cdot \text{K}^{-1})$	322	0.4
p/GPa[b]	1.2	0.492
H/GPa	1.0	0.345
$R_{co}/(\text{m}^2 \cdot \text{K} \cdot \text{W}^{-1})$	$8.9 \cdot 10^{-9}$	$6.1 \cdot 10^{-6}$

[a] Synthetic diamond has a thermal conductivity of approximately 500 W/(m · K).

[b] Contact pressure is assumed to be given by $p = F_c/(b \cdot h)$.

Thinking in electrical circuitry the following analogy can be found:

$$\Theta = \dot{q} \cdot R_{co} \tag{D.4}$$

This means that when a certain temperature is applied at the cutting edge the heat flow $\dot{q}$ is larger for the diamond-aluminium pair than for the diamond-PMMA pair. This implies that a diamond tool that touches an aluminium cylinder during the calibration will have a larger heat flow into the tool, heating up more than during the actual polymer turning process. This will result in a smaller error between applied temperature at the cutting edge and the measured temperature of the embedded thermocouple. Therefore, it seems to be best to press the tool against an aluminium cylinder for a constant heat flow, but with a thin polymer

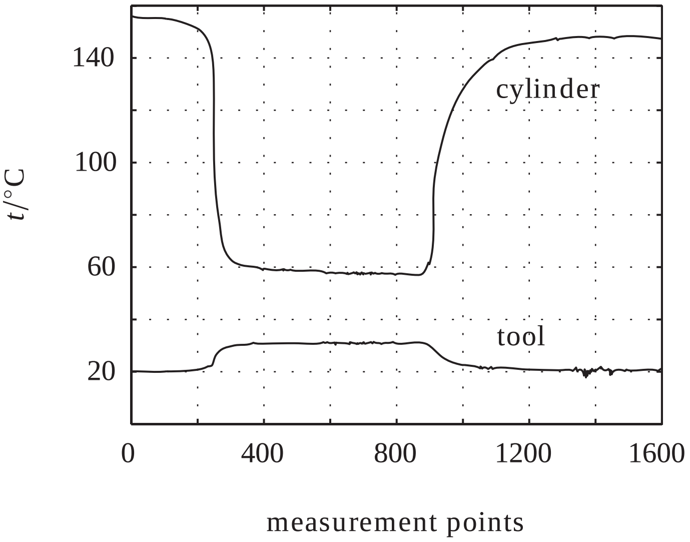

Figure D.1: Response of thermocouples during calibration procedure.

layer between diamond tool and aluminium cylinder to ensure the same thermal contact resistance.

The used self-adhesive J-type thermocouple has a thin shielding made from an insulating material like the cut polymers. This means that approximately the same contact resistance is achieved during calibration as during the actual turning process of a polymer.

The calibration procedure is executed as follows: an aluminium cylinder is heated in an oven to a temperature of 250 °C and kept here for a day to achieve a good homogeneous temperature profile in the cylinder. On the surface of the cylinder a self-adhesive J-type thermocouple is fixed. This thermocouple has a small time constant of less than 0.3 s, which is good for temperature measurements of continuous cutting operations over longer times in combination with a quick response at the beginning of the cutting operation.

When the cylinder is removed from the oven it starts cooling immediately. The embedded thermocouple tool is pressed against the thermocouple that is attached to the cylinder. Figure D.1 shows the response of both the fixed thermocouple at the cylinder and the embedded thermocouple in the tool for a temperature of approximately $150°C$ of the aluminium cylinder.

It can be seen in this figure that the temperature at the surface of the cylinder decreases rapidly when the diamond tool is touched. The reason for this is that diamond has a very good thermal diffusivity becoming a heat sink as soon as it touches the cylinder. Using this touching procedure the error estimates between measured temperature and applied temperature at the cutting edge were found. This is depicted in Figure D.2.

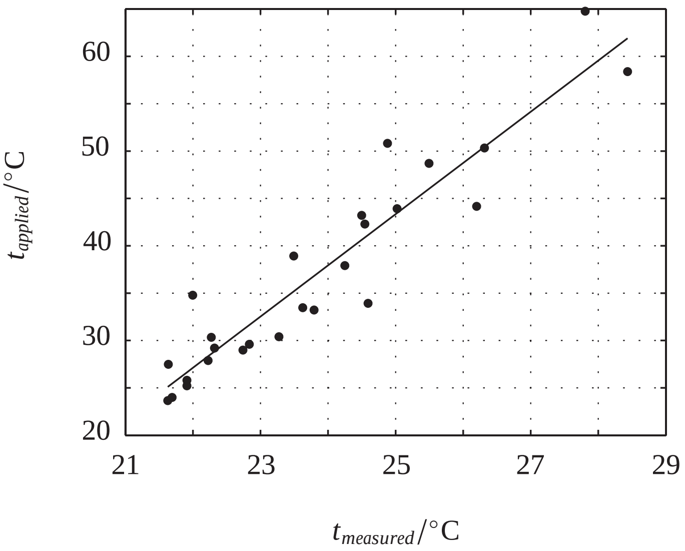

Figure D.2: Calibration curve for the embedded thermocouple tool.

D.2 Error sources

It may be questioned how accurate the above described calibration method is. Therefore this section will describe and estimate some errors that may not be taken into account during calibration, e.g forced convection of a vacuum cleaner that is used for the chip removal.

D.2.1 Conduction to tool shank

Diamond has a high thermal conductivity of approximately 1000 W/(m · K) [69], although it is approximately 500 W/(m · K) for synthetic diamond [156] that was used for the embedded thermocouple tool. It has to be noted here that the thermal conductivity of the diamond is very temperature dependent, but from literature [44] it is known that the temperature during precision turning of polymers approximates T_g, which is generally not more than 150 °C, and therefore the temperature dependence is small. Since diamond a high heat conduction value it is expected that the heat conduction to the tool shank contributes a lot to the heat loss of the diamond tool during cutting. An estimation is made here and Figure D.3 shows the schematic setup for this calculation. The arrows indicate the direction of heat transfer, while the gray plane indicates the plane of interest.

Before calculating the heat conduction through the diamond it is necessary to know if a uniform temperature distribution occurs in the diamond. This can be estimated using the Biot number (Bi), which is the ratio of surface convective resistance and internal conductive resistance, or:

$$Bi = \frac{h \cdot L}{\lambda} \tag{D.5}$$

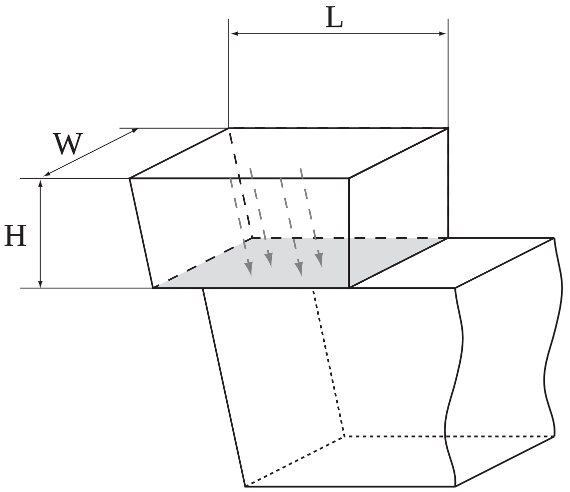

Figure D.3: Heat conduction to tool shank. Dimensions of the tool are $L \times W \times H = 4 \times 1 \times 1\ \text{mm}^3$.

where h is the heat transfer coefficient, L the characteristic length and λ the thermal conductivity. For forced convection a maximum heat transfer coefficient of $h = 250\ \text{W}/(\text{m}^2 \cdot \text{K})$ will be assumed and for the characteristic length the height H of the diamond tool. This leads to

$$Bi = \frac{250 \cdot 1 \cdot 10^{-3}}{500} = 5 \cdot 10^{-4} << 1 \tag{D.6}$$

which leads to the conclusion that a uniform heat profile can be assumed in the diamond.

For conduction the Fourier law of heat conduction is used, which is given as

$$\dot{Q} = \frac{\lambda \cdot A \cdot \Theta}{L} \tag{D.7}$$

with $\dot{Q}$ heat flow, λ thermal conductivity, A the contact surface, defined as $L \times W$, L the characteristic length, which is here assumed to be equal to the height H of the tool and Θ the temperature rise, which is assumed to be 130 K. For the heat conducted through the diamond the following can be calculated.

$$\dot{Q} = \frac{500 \cdot 4 \cdot 10^{-6} \cdot 130}{1 \cdot 10^{-3}} = 260\ \text{W} \tag{D.8}$$

This indicates that a lot of heat is transported by heat conduction from the rake face of the diamond tool to the tool shank.

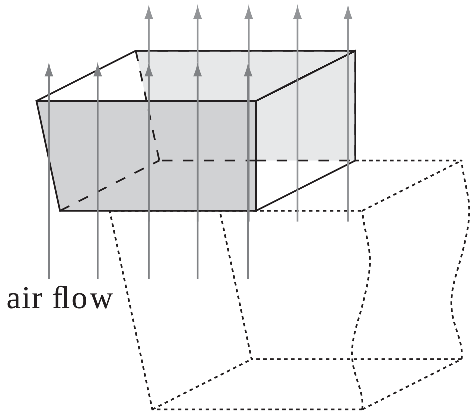

Figure D.4: Forced convection along diamond tool. Dimensions of the tool are $L \times W \times H = 4 \times 1 \times 1\ \mathrm{mm}^3$.

D.2.2 Forced convection

One of the first errors that may significantly attribute to differences between actual temperature and the measured temperature after correction, is the influence of the vacuum cleaner used for removal of the chip. If the chip is not removed during turning, it will damage the fragile threads of the thermocouple. The vacuum cleaner causes a forced convection, which means that the air movement causes an additional cooling that is not measured in the above described calibration procedure.

Difference has to be made between natural convection and forced convection. In forced convection the Reynolds number becomes important, i.e. laminar or turbulent flow. This is important since heat transfer functions change when a flow changes from laminar to turbulent and vice versa [157]. Figure D.4 shows the model used for estimation of heat loss due to forced convection.

From [157] it follows for the overall Reynolds number

$$Re = \frac{v \cdot L}{\nu} \tag{D.9}$$

with v the speed of the air flow, which is estimated as being at least 15 m/s, L a characteristic length, which is here the tool height H and ν the kinematic viscosity (in air at $293\,\mathrm{K} : \nu = 1.5 \cdot 10^{-5}\ \mathrm{m^2/s}$). Using these values a Reynolds number of $Re = 10^3$ can be calculated for the system. This indicates that a laminar flow can be assumed for the following calculations.

For a laminar flow on a uniform plane heat source the overall Nusselt number gives the ratio of actual heat transferred by a moving fluid to the heat transfer that would occur by conduction, or

$$\overline{Nu} = \frac{\dot{q}(convection)}{\dot{q}(conduction)} \tag{D.10}$$

It can then be calculated with [157]

$$\overline{Nu} = 0.664 \cdot Pr^{1/3} \cdot Re^{1/2} \tag{D.11}$$

For a Prandtl number of 0.72 of air at room temperature [157] this leads to $\overline{Nu} = 19$. A Nusselt number of order unity would indicate a sluggish motion little more effective than pure fluid conduction. A large Nusselt number means very efficient convection. From the calculated value the heat transfer coefficient can be calculated with

$$h = \frac{\overline{Nu} \cdot \lambda}{L} \tag{D.12}$$

leading with $\lambda = 0.024\ \mathrm{W/(m \cdot K)}$ for air to $h = 456\ \mathrm{W/(m^2 \cdot K)}$. Notice that this value is relatively high, since the convective heat transfer coefficient for forced convection is generally defined as $50 < h < 250$. The average heat flow $\dot{Q}$ can then be calculated as

$$\dot{Q} = h \cdot A \cdot (T - T_\infty) \tag{D.13}$$

with $A = 2 \cdot H \cdot L$ (there are two side faces of the tool), T the temperature of the tool, which is here assumed to be 150 °C, maximum heat transfer coefficient $h = 250\ \mathrm{W/(m^2 \cdot K)}$ and T_∞ the room temperature of the air. This leads to

$$\dot{Q}_{forced\ convection} = 0.26\ \mathrm{W} \tag{D.14}$$

D.2.3 Radiation

Radiation energy can be calculated with the aid of the Stefan-Boltzmann law, which states the relation between radiation energy and temperature of a black body as

$$\dot{q} = \sigma \cdot T^4 \tag{D.15}$$

with σ the Stephan-Boltzmann constant. For a ”gray body” with surface A and emissivity ϵ the heat rate can be calculated with

$$\dot{Q} = A \cdot \epsilon \cdot \sigma \cdot T^4 \tag{D.16}$$

Figure D.5 shows the faces where radiation energy will be lost when the diamond tool becomes heated. It is assumed that the bottom surface of the diamond tool loses heat by conduction to the tool shank only. Therefore only five faces will be losing heat by radiation.

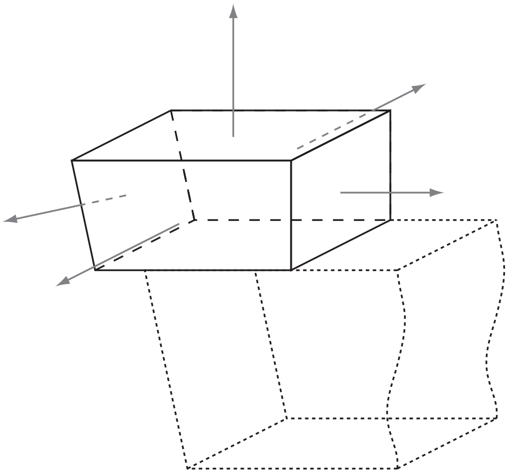

Figure D.5: Radiation losses at faces of diamond tool. Dimensions of the tool are $L \times W \times H = 4 \times 1 \times 1\ \text{mm}^3$.

The heat loss by radiation of a diamond tool at temperature 150 °C and with (worst case) emissivity $\epsilon = 1$ can now be estimated as

$$\dot{Q}_{radiation} = 14 \cdot 10^{-6} \cdot 1 \cdot \sigma \cdot (423 - 293)^4 = 227 \cdot 10^{-6}\ \text{W} \tag{D.17}$$

From this it becomes clear that the heat loss by radiation is very small.

D.2.4 Total heat loss

Summarizing the sections about heat losses for a uniform temperature rise at the rake face of 130 K, the following table can be made.

Table D.2: Summary of heat losses

Heat loss method	heat flow in W
Conduction	$2.6 \cdot 10^{2}$
Forced convection	$2.6 \cdot 10^{-1}$
Radiation	$2.3 \cdot 10^{-4}$

It follows from this table that heat conduction through the tool is the most important heat transfer, and that heat losses due to forced convection and radiation are negligible. This means that the thermocouple in the tool can measure most of the heat that is produced at the cutting edge.

D.2.5 Heat transport by chip movement

Sections D.2.1 to D.2.3 calculated the possible amount of heat losses of the diamond tool for an assumed temperature rise of 130 K at the rake face. From these estimations it followed that the heat conducted through the diamond is the biggest loss in the system. A heat loss of 260 W was calculated for that given temperature rise.

However, is this heat actually entering the diamond tool through the thermal contact resistance R_{co}? Using Equation D.4 and the calculated thermal contact resistance for diamond on PMMA a heat flux $\dot{q}_{co} = \Theta / R_{co} = 2.1 \cdot 10^7\ \mathrm{W/m^2}$ can be calculated for $\Theta = 130\ \mathrm{K}$. This indicates that less heat is entering the diamond tool at the rake face than that can be conducted by the diamond tool for this temperature rise, see Section D.2.1.

The heat flux of the chip was given by Equation 2.16 as

$$\dot{q} = \rho \cdot c \cdot v_{chip} \cdot \overline{\Theta}_{chip} \tag{D.18}$$

Using the data of PMMA given in Appendices C and E for a cutting speed of 3 m/s results in a heat flux of the chip $\dot{q} = 1.9 \cdot 10^8\ \mathrm{W/m^2}$.

Comparing these to heat fluxes indicates that only 11% of the total heat present in the volume of the chip is entering the diamond tool for the assumed temperature rise and cutting speed.

Appendix E

Cutting force data

This appendix presents the cutting force data used in this thesis. Before the measurement data is presented, an overview of the used cutting force equations is given.

The shear angle is defined as (Equation 2.10):

$$\tan\varphi = \frac{h\ \cos\alpha}{h_c - h\ \sin\alpha} \tag{E.1}$$

which can be rewritten as $\tan\varphi = h/h_c = r_c$ for zero rake angle.

The relation between cutting forces was given in Figure 1.6. The resultant force vector F_R can be resolved according to:

$$\vec{F_R} = \vec{F_c} + \vec{F_t} = \vec{F_s} + \vec{F_{sn}} = \vec{F_f} + \vec{F_n} \tag{E.2}$$

Using Figure 1.6, the following geometrical relations can be derived:

$$F_s = F_c \cos\varphi - F_t \sin\varphi \tag{E.3}$$

$$F_{sn} = F_c \sin\varphi + F_t \cos\varphi \tag{E.4}$$

$$F_f = F_c \sin\alpha + F_t \cos\alpha \tag{E.5}$$

$$F_n = F_c \cos\alpha - F_t \sin\alpha \tag{E.6}$$

The shear velocity is given by:

$$v_s = v_c \cdot \frac{\cos\alpha}{\cos(\varphi - \alpha)} \tag{E.7}$$

The following table gives the cutting force data used as input for the thermal models of Chapters 2 and 3.

Table E.1: Cutting data of experiments of Chapter 2.

Material	$v_c/(\mathrm{m\cdot s^{-1}})$	$h/\mu\mathrm{m}$	b/mm	r_c	α	φ	F_c/N	F_t/N	$F_R/\ \mathrm{N}$	F_s/N	$v_s/(\mathrm{m\cdot s^{-1}})$	F_f/N
PS	0.26	10	0.5	0.57	0°	30°	1.27	0.64	1.91	0.78	0.30	0.64
PMMA	0.28	10	0.5	0.67	0°	34°	2.46	0.63	3.09	1.69	0.34	0.63
PC	0.27	10	0.5	0.61	0°	31°	2.20	1.35	3.55	1.19	0.32	1.35
PSU	0.27	10	0.5	0.50	0°	27°	2.10	1.42	3.52	1.23	0.30	1.42

Table E.2: Cutting data of experiments of Chapter 3.

Material	$v_c/(\mathrm{m\cdot s^{-1}})$	$h/\mu\mathrm{m}$	b/mm	r_c	α	φ	F_c/N	F_t/N	$F_R/\ \mathrm{N}$	F_s/N	$v_s/(\mathrm{m\cdot s^{-1}})$	F_f/N
PC - set 1	0.3	10	0.80	0.60	0°	31°	3.20	2.05	5.25	1.69	0.35	2.05
PC - set 2	0.3	5	0.74	0.58	0°	30°	1.30	0.65	1.95	0.80	0.35	0.65
PC - set 3	0.3	2	0.80	0.56	0°	29°	0.83	0.51	1.34	0.47	0.34	0.51
PC - set 4	3.0	10	0.80	0.63	0°	32°	2.85	1.65	4.50	1.53	3.55	1.65
PC - set 5	3.0	2	0.80	0.63	0°	32°	0.67	0.37	1.04	0.37	3.55	0.37
PC - set 6	0.3	10	0.75	0.65	3.6°	34°	2.00	1.03	3.03	1.08	0.36	1.03
PC - set 7	0.3	10	0.72	0.59	−3.6°	30°	2.25	1.40	3.65	1.27	0.35	1.40
PC - set 8	0.3	10	0.80	0.57	−20°	24°	5.00	4.80	9.80	2.60	0.33	4.77
PMMA - set 1	0.28	10	0.5	0.67	0°	34°	2.46	0.63	3.09	1.69	0.34	0.63
PMMA - set 4	2.99	10	0.5	0.67	0°	34°	1.89	0.47	2.36	1.31	3.60	0.47

Appendix F

Tool wear during turning of Sil-O-Flex

This appendix describes the results of tool life experiments on Sil-O-Flex, a contact lens material. This material is known to result in a lot of diamond tool wear.

Sil-O-Flex is known as a contact lens material and composed of Si and MMA. The silicon is added for a higher oxygen permeability. Compare Sil-O-Flex with an oxygen permeability of 17 versus PMMA with a value of only 0.2. The addition of fluorine (F) to the base material may increase the oxygen permeability even more to values above 50.

A reference was found [105], indicating that these silicon particles are present in the form of hard abrasive particles, most probably as SiO_2 or SiC, capable of causing abrasive diamond tool wear by a continuous impact on the tool.

For the tool wear research, it was interesting to find out how such an abrasive tool wear looked like. Therefore a turning experiment was performed on a Sil-O-Flex workpiece material. Prior to cutting, an EDX-analysis was performed for determining what elements were present in the workpiece material.

Figure F.1 shows the results of the EDX analysis. Figure (a) shows the analyzed area with dimensions $30.2 \times 23.6\ \mu m^2$. Figure (b) shows the distribution of carbon C (K shell) atoms, figure (c) that of oxygen O (K shell) and figure (d) that of Si (K shell). It can be seen that these elements are distributed randomly, which also proves that the material is amorphous and not crystalline. From the EDX analysis it becomes clear that Si is present, but not whether is it bonded as e.g. SiC or SiO_2.

Table F.1 summarizes the results of the EDX analysis. The table shows some weight percentage of the element aluminium too. Whether this element was present in the Sil-O-Flex, or that it occurred from the underlying sample holder is not known. It can be seen that the weight percentages of carbon and oxygen atoms are high, which is normal for polymers, but that they are lowered by the high amount of silicon added to the material.

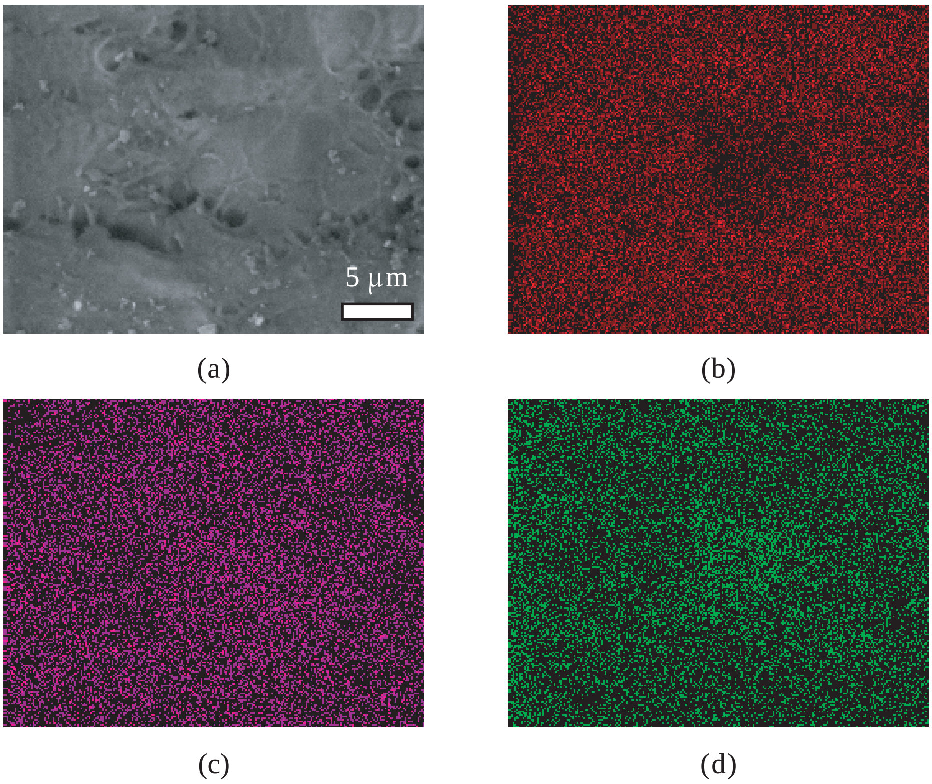

(a) (b)

(c) (d)

Figure F.1: EDX measurements of Sil-O-Flex. Figure (a) shows the measurements spot, (b) carbon atoms, (c) oxygen atoms and (d) silicon atoms.

Table F.1: Weight percentages of elements in Sil-O-Flex.

	C (K)	O (K)	Si (K)	Al (K)
wt %	48.49	25.73	24.91	0.87

F.1 Experiment and results

For the tool life test, a Sumitomo synthetic diamond tool, with nose radius 0.6 mm was used. The workpiece diameter was 12.7 mm. As cutting conditions a constant rotational speed of 1500 rpm was used, in combination with a feed rate of 1 µm/rev and a depth of cut of 20 µm. A length of cut of 15 km was taken in face turning operation without coolant.

Figure F.2 shows the results of the tool life test. It can be seen that a battlemented cutting edge occurs. Figure F.2(b) shows that the distance between the battlements is approximately 2 µm and that a peak appears in between the two. The distances between the mids of the peaks and the battlements was measured to be 1 µm equal to the used feed rate.

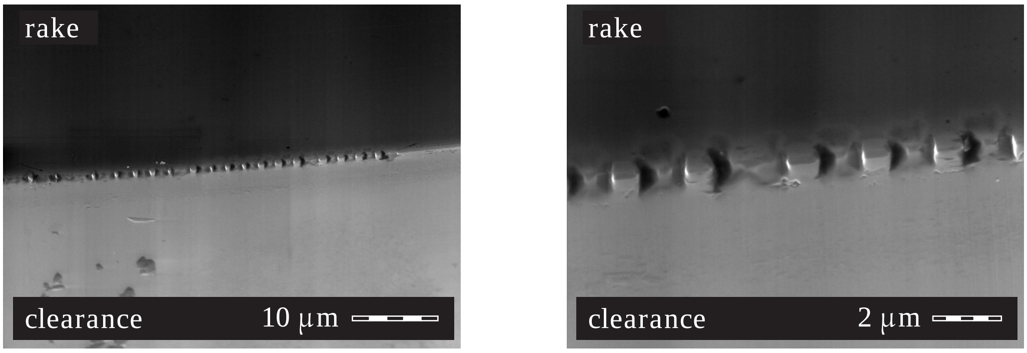

(a) (b)

Figure F.2: Observed tool wear of diamond tool after 15 km turning of Sil-O-Flex. A battlemented cutting edge occurs.

To investigate whether the occurrence of the pattern showed a correlation with the used feed rate, another tool life test was performed with a feed rate of 2.5 µm/rev. Indeed, the created pattern with the battlements and peaks in between, shifted to distance of 2.5 µm. This indicates that the wearing process is dependent on the feed rate, possibly influenced by the rills left by the tool imprint during overlapping cuts.

Appendix G

Electrostatic measurements

G.1 Electrostatics

G.1.1 Static electrification

When two materials are brought into contact, a charge transfer will occur, whether these materials are conductors or insulators. In daily life, only the effects of insulators will be experienced, since charge decay is slow and the materials hold their charges for long periods of time. Whether the materials charge positive or negative depends on the contacting materials, i.e. the contact pair.

A rubbing contact is not necessary for electro-static charging, but rubbing increases the contact area, resulting in more charge generation. Electrostatic charging of differently contacting materials was well described by Coehn [158]. Whether a material charges positive or negative, can be seen in the tribo-electric series. Table G.1 gives some values that are relevant for this thesis. However, besides contacting materials, also the area of the the rubbing surface is of importance [118]

Table G.1: Relative permittivities of several materials. If $\epsilon_1 < \epsilon_2$, then material 1 with ϵ_1 will charge negative against material 2.

+	
Material	**Permittivity**
Diamond	5,5
Poly(methyl methacrylate)	2,6 - 3,7[a]
Polycarbonate	2,6 - 3,0[a]
Polysulfone	3.1[b]
-	

---

[a] From Ref. [83].

[b] Product information Ultrason S2010 (BASF).

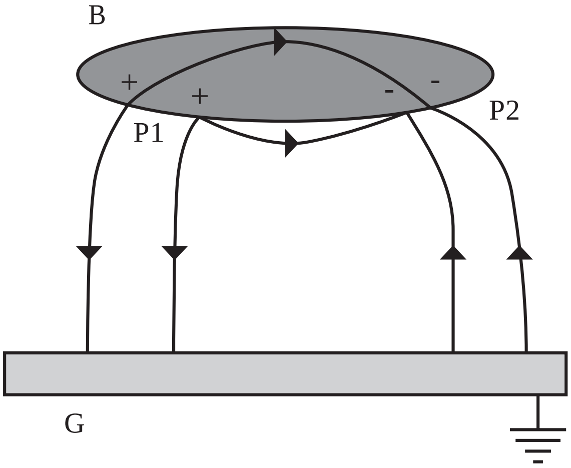

Figure G.1: Schematic representation of an electric field around an insulator. Surface charges usually vary from point to point on the surface.

G.1.2 Electrostatics of charged insulators

The electrostatic charge of an (insulated) conductor can be described by:

$$Q = C \cdot V \tag{G.1}$$

with Q the charge of the system, C the capacitance of the system and V the electric potential. From this equation it becomes clear that as long as the capacitance of the system is unknown, the charge cannot be measured by the electric potential. The capacitance is determined by the conductor's size and shape, and its relative placement to other conductors and ground.

Figure G.1 shows a charged insulator. The electric field conditions can differ from point to point on an insulator. The reason for this is that charge cannot move over the surface of the insulator, because of long decay times. This results in a non-uniform charge distribution on insulators. In fact, as depicted in Figure G.1, the polarity of the charge can even be different from point to point. For the shown insulator the surface potential at a given point can be calculated by:

$$V_{P_i} = \int_{P_i}^{G} E\,da \tag{G.2}$$

with E the field strength between point P_i and ground G and a the path of the electric field between these points. From this figure it becomes cleat that the insulator can have a changing voltage in its interior. The above should make it clear that an insulator cannot be described by a single voltage.

The electric field is defined as the change of potential per distance:

$$E = \frac{V}{d} \tag{G.3}$$

For a plane capacitor with surface A and thickness d the capacitance of the system is defined as:

$$C = \frac{\epsilon \cdot A}{d} \tag{G.4}$$

Combining equations G.1 and G.4 the following relation can be derived for the electric potential:

$$V = \frac{Q \cdot d}{\epsilon \cdot A} \tag{G.5}$$

If it is assumed that a uniformly charged insulator exists, equation G.5 can be rewritten as:

$$V = \frac{\sigma \cdot d}{\epsilon} \tag{G.6}$$

or

$$\sigma = \epsilon \frac{V}{d} \tag{G.7}$$

with σ the charge density, defined as $\sigma = Q/A$. Reliable quantitative measurements of insulators can only be performed on uniformly charged free insulative sheets, Figure G.2(a), and on uniformly charged sheets backed by a grounded conductor, Figure G.2(b).

G.2 Measurement of electrostatic charging

G.2.1 Non-contacting voltmeter

Figure G.2 shows the use of a non-contacting voltmeter that can be used for field strength measurements. Figure (a) shows the voltmeter when measuring a uniformly charged free sheet that is fully insulated from the environment.
In this case equating Equations G.3 and G.6 leads to

$$V = E \cdot d = \frac{\sigma}{\epsilon} \cdot d \tag{G.8}$$

meaning that the measured voltage is linear with the distance between sheet and voltmeter at constant surface charge. Therefore voltage cannot be used as a measure for the surface charge, unless the distance between sheet and voltmeter is accurately known.

The situation shown in Figure G.2(b) is more applicable. It shows a uniformly charged insulator disk between a grounded backing electrode and a free grounded electrode, which in this case is a (shielded) non-contacting voltmeter. The

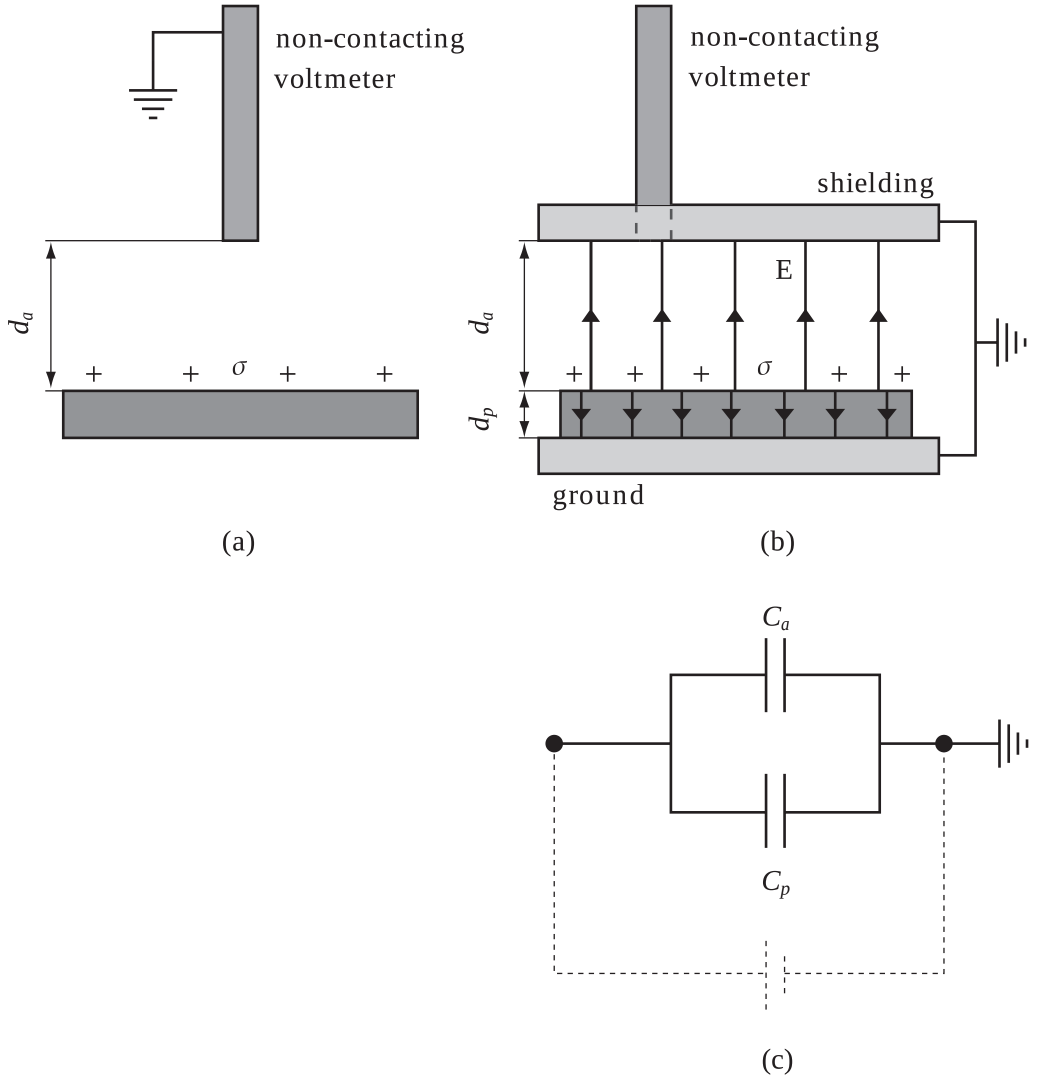

Figure G.2: Schematic of non-contacting voltmeter; (a) in use at a uniformly charged free insulative sheet, (b) a more realistic setup for measurements, and (c) the electric diagram showing the parallel system of this setup.

reason for its better applicability is that a uniform electric field is generated by the grounded backing electrode. If the backing electrode was not used the field lines might not be parallel to each other, which results in a (measured) fluctuating electric field. This setup is also used in this research, where an aluminium workpiece holder is used for the polymer workpiece. During the measurements the workpiece holder works as the backing electrode.

The system in Figure G.2(b) can be modeled as two parallel capacitances[1] [159]. This is schematically given in Figure G.2(c), where the dashed lines indicate how a battery should be placed to obtain an electrical system that clearly shows the parallel setup. For this system the substituting capacitance is given as:

---

[1] The subscripts 'a' respectively 'p' are used for denoting air respectively polymer.

$$C = C_p + C_a \tag{G.9}$$

$$C = \frac{\epsilon_0 \cdot \epsilon_p \cdot A}{d_p} + \frac{\epsilon_0 \cdot \epsilon_a \cdot A}{d_a} \tag{G.10}$$

$$C = \frac{\epsilon_0 \cdot \epsilon_p d_a + \epsilon_0 \cdot \epsilon_a d_p}{d_p \cdot d_a} \cdot A \tag{G.11}$$

By using equation G.1 the surface charge can be derived as:

$$Q = C \cdot V \tag{G.12}$$

$$Q = \epsilon_0 \cdot A \cdot V \cdot \frac{\epsilon_p d_a + \epsilon_a d_p}{d_p \cdot d_a} \tag{G.13}$$

$$\sigma = \epsilon_0 \cdot V \cdot \frac{\epsilon_p d_a + \epsilon_a d_p}{d_p \cdot d_a} \tag{G.14}$$

Using Equation G.8 the electric field strength E between insulator and grounded electrode is then described as:

$$E = \frac{V}{d_a} = \frac{\sigma}{\epsilon_0 \epsilon_a} \tag{G.15}$$

G.2.2 Vibrating electrostatic voltmeter

From Equation G.15 it becomes obvious that the measured surface potential is dependent on the accuracy of the determination of the distance d_a in figure G.2(b). To overcome this problem, Lord Kelvin proposed in 1898 an electrostatic voltmeter based on an oscillating probe and this was made by Zisman in 1932 [160]. The working of this probe is depicted in Figure G.3.

The decrease in potential over the air gap d_a is

$$V = \left| V_p - V_s \right| = \frac{Q}{C} \tag{G.16}$$

where V_p is the voltage of the probe and V_s the voltage of the surface to be measured. The capacitance of the system with non-oscillating probe is described by Equation G.4. When the probe oscillates over a distance

$$d(t) = d_a + a \cdot \sin(\omega t) \tag{G.17}$$

with a and ω the amplitude respectively the circular frequency ($\omega = 2\pi f$) of the vibration and t time, than the capacitance of the system changes with the oscillation as [161]:

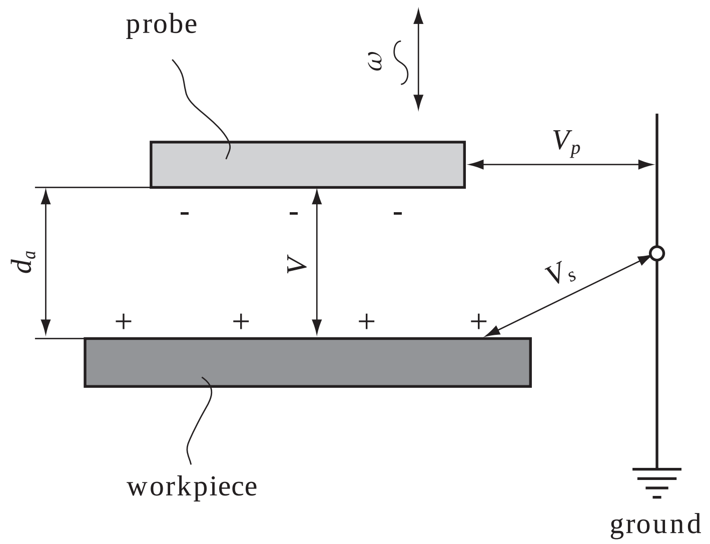

Figure G.3: Principle of the vibrating electrostatic voltmeter.

$$C = \frac{\epsilon \cdot A}{(d_a + a \cdot \sin(\omega t))} \tag{G.18}$$

When the probe oscillates, an electric current flows to or from the surface to the probe. This current $I = dQ/dt$ can now be described using equations G.16 and G.18 as:

$$I = \frac{dQ}{dt} = -V \cdot \epsilon \cdot A \cdot \frac{a\omega \cdot \cos \omega t}{(d_a + a \cdot \sin \omega t)^2} \tag{G.19}$$

For achieving electrostatic voltage measurements the voltmeter will nullify the current by nullifying the potential difference V by adapting the probe voltage V_p to the surface voltage V_s. Recording this voltage V_p will then be a direct measure for the surface potential.

For the electrostatic voltage measurement experiments a Monroe Electronics Electrostatic Voltmeter (type 244A) in combination with a high resolution end-viewing Kelvin probe (type 1017AEH) was used. It was chosen for its distance independency [161] as described before.

G.3 Measurement results of electrostatic charging

G.3.1 Electrostatic charges after turning with 1 m/s

Figure G.4 shows the measured surface charges versus workpiece radius after cutting with a diamond tool with tool nose radius 1 mm and rake and clearance face orientation (110) respectively (100). A constant cutting speed $v_c = 1$ m/s , feed rate $f = 2.5$ mm/min and depth of cut $h = 20$ µm were used.

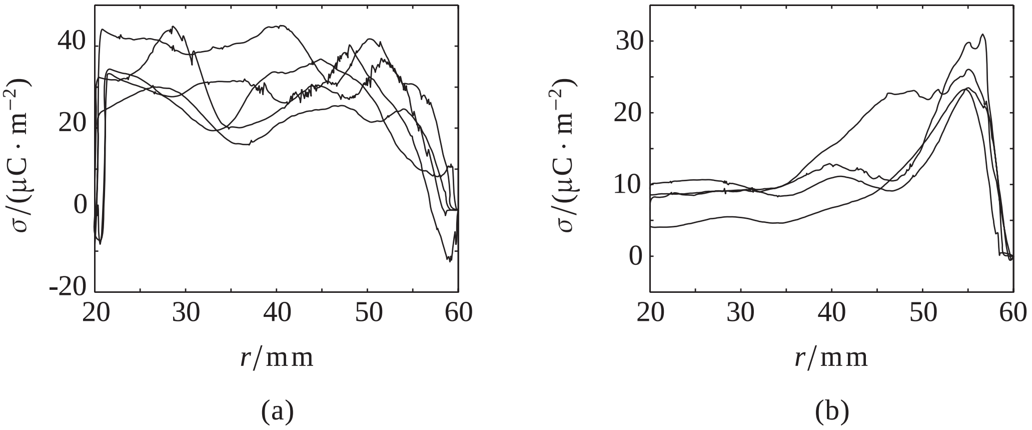

Figure G.4: Measured surface charges during turning of (a) PC, respectively (b) PMMA, with $v_c = 1$ m/s, $f = 2.5$ mm/min and $h = 20$ µm.

G.3.2 Signs of charges on chip and tool

Figure G.5 shows the measured potential of the chip that was produced during turning of PC with cutting conditions $v_c = 1$ m/s, $f = 2.5$ mm/min and $h = 20$ µm. In order to measure the chip potential the chip was sucked into the vacuum cleaner. Since a stable, continuous chip is formed during turning of PC it was possible to retract the vacuum cleaner from the cutting zone during cutting. This way it became possible to measure the surface potential of the chip with the EVM. It can be seen that the chip charges negatively for PC. For PMMA, such a test was not possible, since a semi-continuous, fragile chip was produced in the given cutting conditions.

For measuring the sign of the produced charges on the diamond tool the EVM probe was moved over the tool. Figure G.6 shows the results of these measurements for PC and PMMA. The diamond tool is given on true scale with respect to the diagram. Notice that only the sign of the charge can be determined and the relative amount of charging of the tool after turning PC respectively PMMA. It can be seen that PC results in more charging of the diamond tool and that the diamond's electric field extends far outside the true diamond tool region.

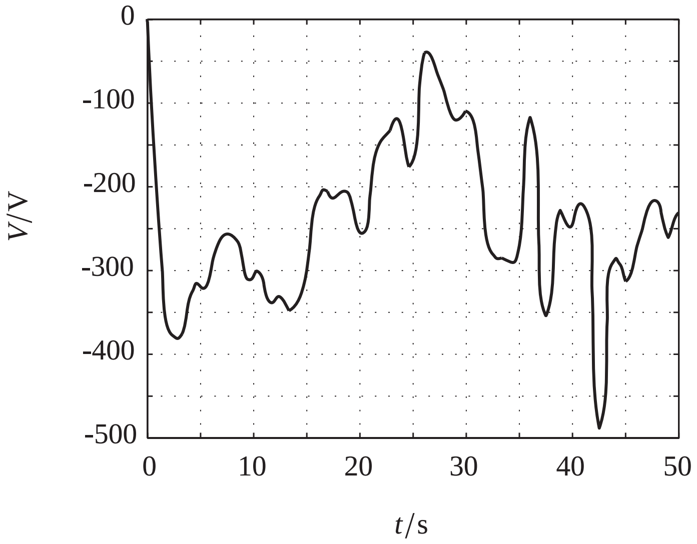

Figure G.5: Measured chip potential during turning of PC at $v_c = 1$ m/s, $f = 2.5$ mm/min and $h = 20$ µm.

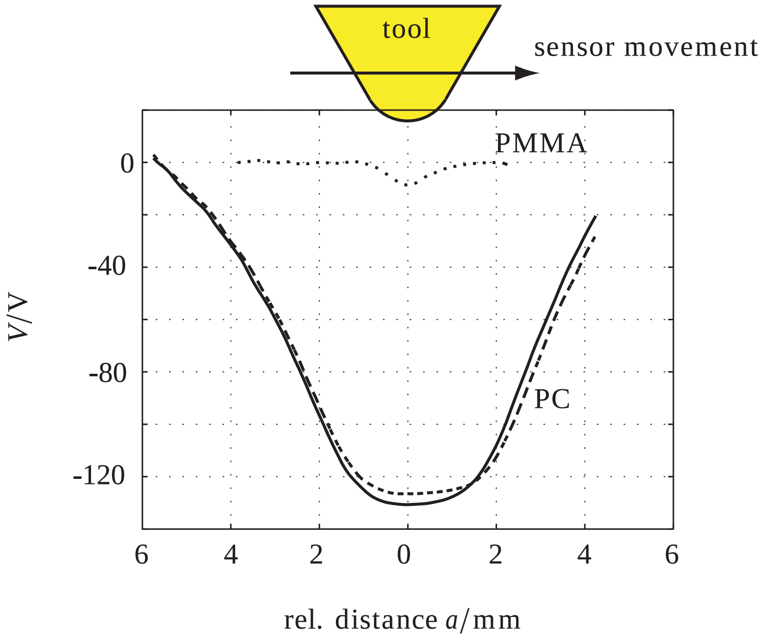

Figure G.6: Measured potentials after turning PC and PMMA with $v_c = 1$ m/s, $f = 2.5$ mm/min and $h = 20$ µm. The tool is given on scale with the figure.

Appendix H

Discharge chemistry

This appendix describes in short what chemically reactive species can occur during discharging. It was described in Chapter 4 that luminescence occurred during diamond turning of polycarbonate (PC) and polysulphon (PSU). No luminescence was observed during diamond turning of polymethylmethacrylate (PMMA). The origin of several chemical species is found in the measured spectrum of the luminescence during diamond turning of PC, see Section 4.3.2.

From [113] it is known that excited molecules can dissociate. This would lead to reactive radicals by the following physical-chemical equations.

Excitation of nitrogen (N_2) by electron collision [113]:

$$e + N_2 \overset{+\,\mathrm{eV}}{\rightarrow} N_2^* + e \tag{H.1}$$

with N_2^* the excited nitrogen and e an electron. In [113] it is shown that excited particles, which are here the excited nitrogen molecules, can be significant in processes of radical formation. The following reactions are given:

$$N_2^* + H_2O \rightarrow N_2 + HO\bullet + H\bullet \tag{H.2}$$

where $\bullet$ denotes a radical. This may result in hydroperoxide according to the reaction:

$$H\bullet + O_2 \rightarrow HOO\bullet \tag{H.3}$$

The hydroperoxide is a very reactive species and can be formed quickly.

The excited nitrogen can also be involved in another reaction path to create OH radicals:

$$N_2^* + O_2 \rightarrow N_2 + O(^1\Delta) + O \tag{H.4}$$

The $O(^1\Delta)$ product, which is excited atomic oxygen, is then involved in the production of $HO\bullet$ by hydrogen abstraction from H_2O according to:

$$O(^1\Delta) + H_2O \rightarrow 2HO\bullet \tag{H.5}$$

However, other reactions may deplete the $O(^1\Delta)$ product as well. These reactions involve O_2, N_2 and H_2O, but they produce less reactive products. The possibility of these reactions to occur is bigger, because of higher concentrations of these products, but the rate of hydrogen abstraction from water, necessary in Equation H.5, is high, only little water is necessary for creating a lot of OH radicals [113]. The $O(^1\Delta)$ may also be involved in the production of ozone through [125]:

$$O(^1\Delta) + O_2 \rightarrow O_3 \tag{H.6}$$

which may more readily occur than Equation H.5, because of the bigger cross-section of O_2.

The positive N_2^+ ion that was observed in the measured spectrum of the luminescence during turning of PC (see Section 4.3.2) is produced by direct ionization of nitrogen. With an ionization potential of 15.7 eV [123] it is possibly produced in the reaction:

$$N_2 + e \overset{+\,\mathrm{eV}}{\rightarrow} N_2^+ + 2e \tag{H.7}$$

Next the N_2^+ can be involved in the creation of OH radicals through the following reaction [113]:

$$\begin{aligned} N_2^+ + H_2O &\rightarrow H_2O^+ + N_2 && \text{(H.8)} \\ H_2O^+ + H_2O &\rightarrow H_3O^+ + HO\bullet && \text{(H.9)} \end{aligned}$$

The efficiency of these reactions is concerned with the low ionization potential of water and the high bond energy of the hydroxonium ion (H_3O^+) [113].

Negative oxygen ions can be produced by attachment of electrons in the collision with oxygen molecules via

$$2O_2 + e \overset{+\,\mathrm{eV}}{\rightarrow} O_2^- + O_2 \tag{H.10}$$

and

$$O_2 + e \overset{+\,\mathrm{eV}}{\rightarrow} O^- + O \tag{H.11}$$

Another oxygen ion that can be formed in discharging by direct ionization during turning of PC is:

$$O_2 + e \overset{+\,\mathrm{eV}}{\rightarrow} O_2^+ + 2e \tag{H.12}$$

with an appearance potential of 12.1 eV [123]. Probably due to its weak emission intensity [125], this has not been detected in the measured spectrum. Badaloni [123] mentions that the O_2^+ ion is relatively stable. Unless it will encounter an O^- to produce ozone according to:

$$O_2^+ + O^- \rightarrow O_3 \tag{H.13}$$

Ozone may create, just like OH radicals, a strong oxidizing environment [113]. Another way of ozone generation was already given in Equation H.6, but it can also be formed by [113]:

$$O_2 + O + M \rightarrow O_3 + M \tag{H.14}$$

where M is a third particle. The reaction rates may be high if the temperatures in the discharge are sufficiently high.

The above equations show that a lot of reactive chemical products can be formed in the environment *during* discharging; even more are mentioned in [113]. It is known that peroxides and ozone can work as oxidizing species, which means that diamond tools cannot only be damaged by Lichtenberg figures as described in Chapter 4, but also by an oxidizing environment created by the discharging.

Curriculum vitae

Guido Gubbels was born on March 21st, 1976 in Urmond, the Netherlands. After obtaining his Atheneum (B) degree at *het Bisschoppelijk College* in Sittard in 1994, he commenced his study of Mechanical Engineering at the Eindhoven University of Technology. In 1998 he worked on his internship named ”Development of an apparatus for applying diffusive brain injuries to rats”. During his study he was in the board of the *Eindhovense Studenten Film en Foto vereniging* (ESFF) Dekate Mousa. In June 2000 he obtained his Master’s Degree in the Precision Engineering group. His Master’s project was about Precision turning of polycarbonate (PC) and CR39. From this project the Ph.D. project ”Diamond turning of glassy polymers” was started. He worked on his Ph.D. project from August 2000 till August 2005. In October 2005 he started working at Vision Dynamics in Eindhoven, and was seconded to TNO Science and Industry in Delft, where he currently works as a researcher on optical fabrication technology in the Opto-Mechanical Instrumentation division.

References

Journals

- G.P.H. Gubbels, G.J.F.T. van der Beek, A.L. Hoep, F.L.M. Delbressine, H. van Halewijn,”Diamond tool wear when cutting amorphous polymers”, *Annals of the CIRP*, vol. 53(1), 447-450, (2004)

Proceedings

- G.P.H. Gubbels, G.J.F.T. van der Beek, F.L.M. Delbressine, P.H.J. Schellekens,”Electrostatic tool wear in diamond turning of amorphous polymers”, *Proceedings of the 4th Euspen International Conference*; Glasgow, United Kingdom, 97-98, (2004)

- G.P.H. Gubbels, F.L.M. Delbressine, L.E. Govaert, P.H.J. Schellekens,”Precision cutting of glassy polymers: influence of aging on the cutting process”, *Proceedings of SPIE*; Editors: R. Geyl, D. Rimmer, L. Wang, Saint Etienne, France, 111-121, (2003)

Dankbetuiging

Terugkijkend naar de afgelopen vijf jaar zijn er toch veel mensen die mijn dank verdienen. In het bijzonder mijn promotor professor Piet Schellekens. Zonder hem zou dit onderzoek nooit mogelijk zijn geweest. Ook zijn brede kennis is een belangrijke inspiratiebron en bijdrage voor dit onderzoek geweest. Verder bijzondere dank aan mijn twee co-promotoren. Frank Delbressine stond dagelijks klaar en Leon Govaert was nooit te beroerd om mee te denken over dit polymerenvraagstuk.

Ook de leden van de kerncommissie, professor G. Kroesen (TU/e), professor D. Schipper (UT) en professor B. Karpuschewski (Universität Magdeburg) wil ik bedanken voor hun tijd en waardevolle bijdragen aan mijn dissertatie.

Tijdens mijn promotietijd heb ik veel tijd samen doorgebracht met mijn kamergenoten Maarten Jansen, Suzanne Cosijns en Bastiaan Knarren. Dat privé en werk gescheiden moeten zijn is gelukkig niet waar. Fijnere collega's en vrienden kon ik me niet wensen. Datzelfde geldt voor mijn ”buurman” Alper Tiftikçi. Ook Edwin Bos, mijn laatste kamergenoot wil ik bedanken voor de gezellige tijd.

Willie ter Elst en Erik Homburg wil ik bedanken voor hun ondersteuning bij de vele draaiproeven. Verder wil ik alle andere collega's bedanken voor de fijne tijd die ik bij Precision Engineering heb gehad.

Diverse studenten ben ik erkentelijk voor hun werk, maar bijzondere aandacht verdienen Jeroen van Assen en Gert-Jan van der Beek. Beiden hebben een belangrijke bijdrage geleverd in het slijtageonderzoek. Jeroen in het bijzonder bedankt voor de leuke discussies en de zeer goede aanzet in het slijtageonderzoek. Ook de Doesburgse mosterdsoep zal ik niet vergeten. Gert-Jan wil ik bedanken voor de grote hoeveelheid uitgevoerde metingen.

Verder wil ik Sjaak Cauwenberg en Simon Plukker bedanken voor hun hulp bij diverse draaiproeven. Ab Kneppers wil ik bedanken voor de nodige apparatuur/spullen uit de ”oude doos” die mij nogal van pas kwamen in het verspaningsonderzoek. Marc van Maris verdient zeer veel dank voor zijn handige (E)SEM trucjes. Kees Meesters en Hans van Griensven wil ik bedanken voor de gezelligheid, de interesse en de nodige assistentie op tribologiegebied. Jules Kierkels wil ik bedanken voor zijn assistentie bij de GPC metingen.

Verder heeft het slijtageonderzoek veel fysische en chemische aspecten omvat. Hiervoor was ik aangewezen op hulp van diverse mensen buiten de faculteit werktuigbouwkunde: Eddy van Veldhuizen van de faculteit Natuurkunde, Helger van Halewijn van de Diamond Tools Group, Wim Bos van Chemtura Corporation en Femke de Theije van Philips (High Tech Campus). Met name de laatste twee wil ik danken voor hun zeer waardevolle bijdrage op het gebied van de chemische slijtagebeschrijving.

Tolé Hoep van Océ Technologies wil ik bedanken voor het gebruik van de elektrostatische voltmeter en zijn uitgebreide interesse. Contour Fine Tooling wil ik bedanken voor het snelle relappen en voor het meedenken. Martin Bouman van Flir Systems wil ik bedanken voor het gebruik van de IR camera.

Senter-Novem wil ik bedanken voor de verleende subsidie in het kader van het IOP Precisie Technologie. De bijeenkomsten waren gezellig en nuttig. Alle begeleidingscommissieleden wil ik bedanken voor hun interesse en bijdragen in het onderzoek.

Mijn ouders en schoonouders wil ik hartelijk danken voor hun interesse in mijn onderzoek. Tevens wil ik mijn schoonouders bedanken voor de tijd die ik achter hun computer door heb mogen brengen om mijn dissertatie verder af te kunnen ronden in de laatste maanden.

Mijn belangrijkste steun, toeverlaat, motivatie- en inspiratiebron in de afgelopen jaren was Astrid. Vooral jouw geduld bij iedere keer ”het is bijna af” was geweldig. Zonder jou had ik deze laatste regel nooit gehaald!